2009-08-11

A System Level Approach to D-Fiber Electric Field Sensing

Joshua Monroe Kvavle
Brigham Young University - Provo

A SYSTEM LEVEL APPROACH TO D-FIBER ELECTRIC FIELD SENSING

by

Joshua Monroe Kvavle

A dissertation submitted to the faculty of

Brigham Young University

in partial fulfillment of the requirements for the degree of

Doctor of Philosophy

Department of Electrical and Computer Engineering

Brigham Young University

December 2009

BRIGHAM YOUNG UNIVERSITY

GRADUATE COMMITTEE APPROVAL

of a dissertation submitted by

Joshua Monroe Kvavle

This dissertation has been read by each member of the following graduate committee and by majority vote has been found to be satisfactory.

Date	Stephen M. Schultz, Chair
Date	Aaron R. Hawkins
Date	Gregory P. Nordin
Date	Michael D. Rice
Date	Richard H. Selfridge

BRIGHAM YOUNG UNIVERSITY

As chair of the candidate's graduate committee, I have read the dissertation of Joshua Monroe Kvavle in its final form and have found that (1) its format, citations, and bibliographical style are consistent and acceptable and fulfill university and department style requirements; (2) its illustrative materials including figures, tables, and charts are in place; and (3) the final manuscript is satisfactory to the graduate committee and is ready for submission to the university library.

Date

Stephen M. Schultz
Chair, Graduate Committee

Accepted for the Department

Michael J. Wirthlin
Graduate Coordinator

Accepted for the College

Alan R. Parkinson
Dean, Ira A. Fulton College of
Engineering and Technology

ABSTRACT

A SYSTEM LEVEL APPROACH TO D-FIBER

ELECTRIC FIELD SENSING

Joshua Monroe Kvavle

Department of Electrical and Computer Engineering

Doctor of Philosophy

This dissertation presents the novel creation of a hybrid D-fiber electro-optic polymer electric field sensor. The sensor is made by removing a portion of the cladding from a D-shaped optical fiber, thus exposing the core to interaction with external stimulus. Then, an electro-optic polymer is deposited, partially replacing the core of the fiber. Next, the polymer is poled to endow it with electro-optic properties. This sensor is packaged in order to restore its mechanical strength. Because D-fiber is not intrinsically compatible with standard optical equipment it is fusion spliced to standard polarization maintaining fiber. Finally the sensor is tested for electro-optic sensitivity.

The hybrid D-fiber electric field sensors designed and fabricated in this work meet the requirements of mechanical strength, temporal stability, minimal perturbation of the electric field by the sensor, and a small and flexible cross-sectional area so that it can be embedded into the device under test. A fully packaged hybrid electro-optic polymer D-fiber electric field sensor which is capable of detecting electric fields

of 50 V/m at a frequency of 6 GHz is produced. The sensor's electro-optic response is shown to be temporally stable. Additionally, the sensor is physically robust, and physically and electrically non-intrusive.

This work also adds a thorough understanding of the design and fabrication of D-fiber waveguides with a polymer material deposited in the core. Several new fabrication techniques are developed and presented. A path to greater electric field sensitivity is outlined for future research.

ACKNOWLEDGMENTS

I publicly acknowledge the hand of God in my life, including the opportunity and means to pursue a doctorate degree. Literally none of this would have been possible without Him.

I thank my dear wife Candice, for inspiring, encouraging, supporting, and loving me. I would not have had the confidence or the desire to better myself in this way without her. My parents have been a source of support and encouragement through all of my schooling, and I thank them for that. I also thank my grandparents, especially my Grandpas Slay and Kvavle, whose interest in engineering and science have impacted my life.

Brigham Young University has been the ideal place to carry out my undergraduate and graduate education. The University's emphasis on learning in the light of faith has enriched my education and life. Throughout my graduate and undergraduate studies Dr. Stephen Schultz has been an excellent mentor. I thank him for his encouragement and for the opportunity to carry out research under his tutelage. I never dreamed I would have been capable of pursuing an advanced degree, and I would not have been able to do so without his support and willingness to teach me. I also thank Dr. Richard Selfridge, Dr. Aaron Hawkins, and Dr. Greg Nordin for the opportunities that I have had to collaborate with them on various research projects, and for their expertise and willingness to mentor me.

I have worked with many people throughout my research, and want to thank in particular Eric Johnson, who helped me to achieve the preliminary results which have formed a basis for the rest of my research. I also would like to thank Earl Parsons, Krystle Thiel, Jonathan Young, Efrain Gutierrez, and Andrew Sieler for their help in

this work. I am thankful for the opportunity to work alongside Tyson Lowder and Rich Gibson, their camaraderie has enhanced my graduate studies and research.

I would like to thank the Test Resource Management Center Test and Evaluation/Science and Technology Program for their financial support. This work is funded through U.S. Army Program Executive Office for Simulation, Training and Instrumentation. I would also like to thank AFL Telecommunication, Fujifilm Dimatix, and KVH Industries for their donations in support of this research.

Table of Contents

List of Tables

List of Figures

Chapter 1

Introduction

1.1 Electric Field Sensing

Interest in electric fields was first documented at least two thousand years ago with the ancient Greek philosopher Thales of Miletus' (623 - 546 B.C.) discovery that rubbing fur and amber together endowed amber with the power to attract lightweight objects. It was this experiment which later led to the invention of the word *electricity* which is derived from the word amber (*elektron* in Greek) [1]. Interest in electricity and electric fields has continued to increased since its initial discovery.

Electricity has become a means of supplying energy, performing computation, transmitting information, discovering more about our surroundings, and learning more about the structure of our bodies. Many other applications are being discovered and implemented every day. Another application of the use of electric fields is the high power microwave (HPM) weapon. These high power directed electric fields can be used to destroy circuit boards, or interfere with electronic equipment operation. There are at least two reasons for interest in HPM weapons. One, by understanding how an HPM weapon works it is possible to protect electronic equipment more effectively. Two, there are combat situations where a weapon that could be used to disrupt electronic equipment could save human lives.

Since electric fields are not directly observable, a method of sensing the HPM electric fields is required. The most common method for sensing electric and magnetic fields is to use D-dot and B-dot probes which are pictured in Figure 1.1. These sensors are typically to large to place inside the circuits which are under test, and even if they could be placed inside, their metallic parts would perturb the fields they are intended to measure. These two difficulties have spawned interest in alternative techniques for

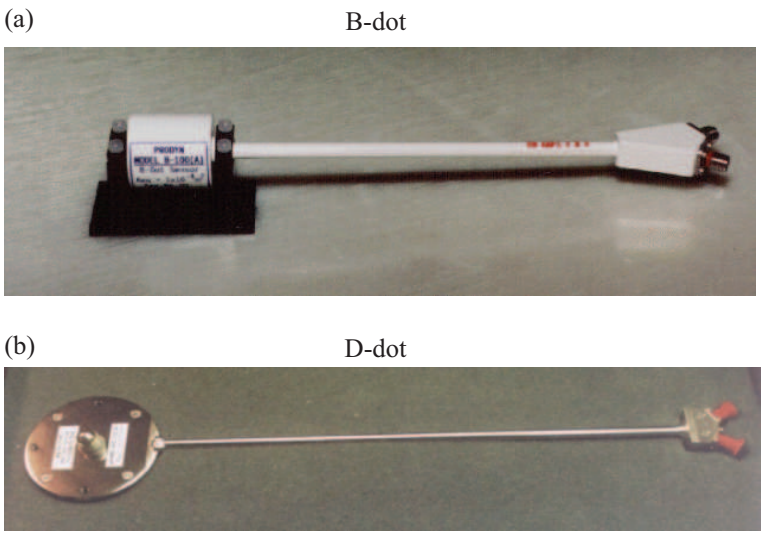

Figure 1.1: Traditional metallic (a) magnetic and (b) electric field sensors, which are too large to embed into a device under test and whose metal components perturb the fields they are intended to measure.

electric field sensing. The optimal sensor for this application includes qualities such as mechanical strength, temporal stability, minimal perturbation of the electric field by the sensor, and a small and flexible cross-sectional area so that it can be embedded into the device under test.

One area of research which has focused on fulfilling the requirement for these type of electric field sensors is the electro-optic (EO) sensor. The idea behind this sensor is that an electric field can induce an optical effect which can then be measured and the electric field information extracted. This transduction from electrical to optical signals generally makes use of the linear electro-optic effect. While various electric-field sensors have been developed which have made used of the linear electro-optic effect [2, 3, 4, 5, 6, 7], none have been shown to fully satisfy all of the requirements for the optimal HPM electric field sensor.

1.2 D-fiber Sensing Platform

In-fiber sensors are an effective platform for sensing various physical parameters. Among this category of sensors, D-fibers have been successfully used to make various in-fiber devices, where a strong interaction with the light in the core is desir-

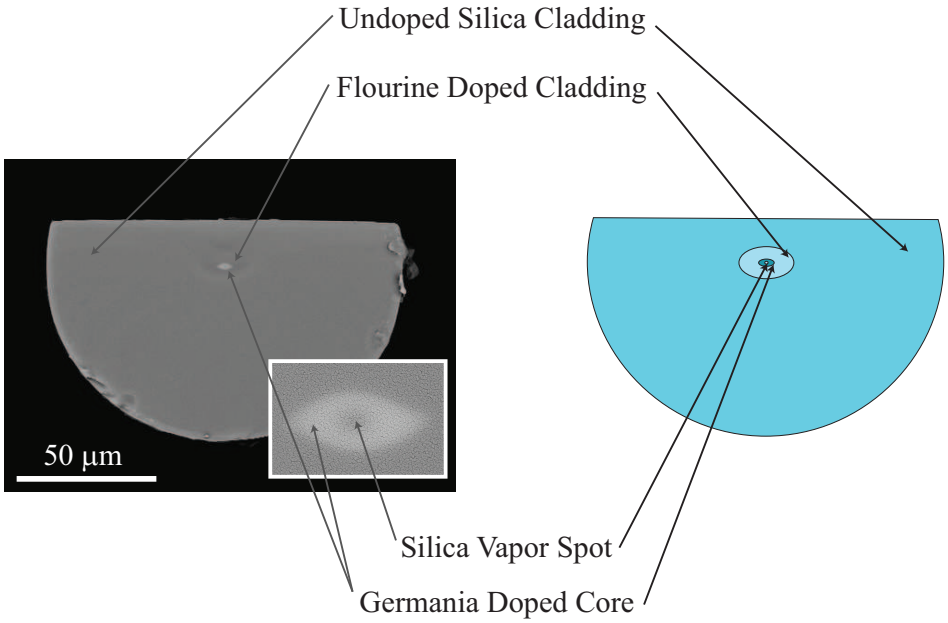

Figure 1.2: D-fiber that consists of a Germania-doped core ($n_{core} = 1.4756$) surrounded by a fluorine doped depressed cladding ($n_{fluorine} = 1.441$) and an undoped super cladding covered ($n_{cladding} = 1.444$). The undoped silica vapor spot ($n_{vapor\ spot} = 1.444$) is also visible in the zoomed inset image of the fiber core.

able. D-fiber sensors are effective, because the core is positioned close to the edge of the cladding. This cladding shape enables access to the light in the core of the fiber without destroying the physical integrity of the fiber. Figure 1.2 shows a D-shaped optical fiber (D-fiber), which is produced by KVH Industries, that is used as the device platform. Various sensors based on the D-fiber platform have been reported such as high temperature sensors [8], strain sensors [9], chemical sensors, [10] and electric field sensors [11, 12]. Some of the advantages of such sensors are their high bandwidth, low optical loss, and inherently small and flexible cross-section.

This work applies the advantages of D-fiber sensors to the challenge of sensing the high speed electric fields characteristic of HPM weapons. The sensor is designed and fabricated with mechanical strength, temporal stability, minimal perturbation of the electric fields, and a small and flexible cross-sectional area in mind. Figure 1.3 shows the concept of how a compact D-fiber electric field sensor can be threaded into the circuitry of a device during HPM weapon testing. The sensors small cross-section,

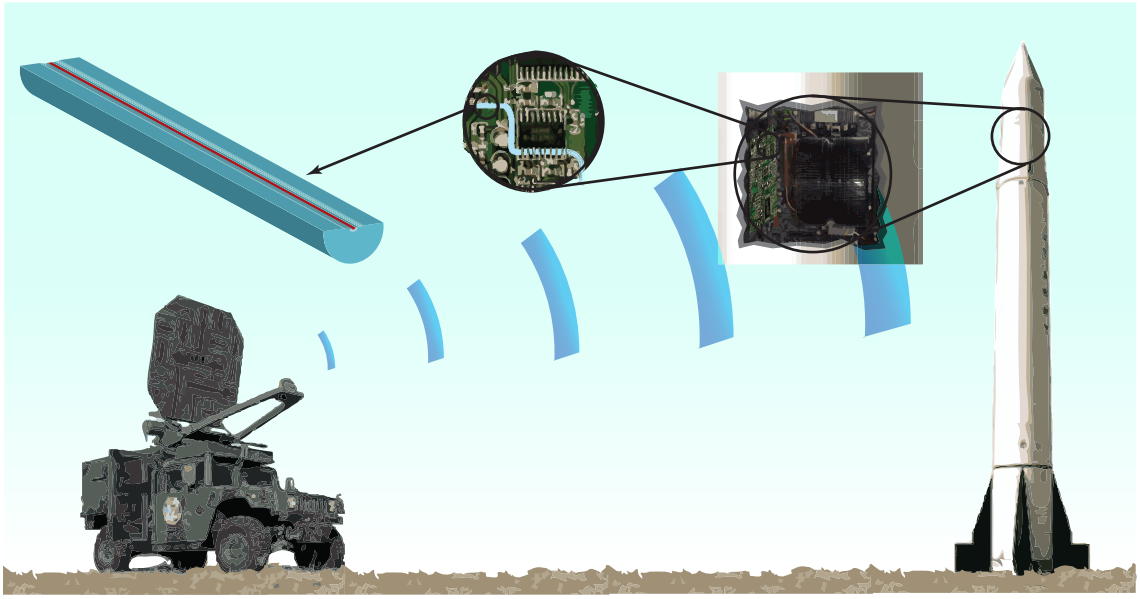

Figure 1.3: Illustration of how a D-fiber optical sensor can be used for the measurement of HPM weapons

ability to carry a signal over great distances, large bandwidth, temporal stability, non-electrically perturbing nature, and EO sensitivity, make the D-fiber sensor a promising platform for HPM weapon testing.

1.3 Hybrid EO Polymer D-fiber Sensors

The key to creating an in-fiber E-field sensor from D-fiber is producing a section of fiber in which the effective index of refraction of the core varies with applied electric field. The two most common methods used to achieve this EO response are to make the Germania-doped glass itself nonlinear [13] or to create a section of the optical fiber with a hybrid guiding region consisting of part glass and part poled EO polymer. Since the induced EO effect in Germania-doped glass is fairly small, it is more practical to use the EO polymer/D-fiber hybrid waveguide approach.

The fabrication of low loss EO D-fiber hybrid waveguides requires a sequence of sensitive processes. First, the fiber cladding must be etched away so that the core is exposed to interaction with the EO polymer. Second, an EO polymer must be deposited, replacing the portion of the fiber where the core was removed. Next, that

polymer must be poled in order to align the chromophore molecules which are contained in the polymer. Finally the fiber must be packaged to protect the fragile etched portion of the fiber from damage. Details about specific methods and innovations in each area of processing are included throughout this work.

1.4 Dissertation Outline/Contributions

The final product reported from this work is a fully packaged hybrid EO polymer D-fiber electric field sensor which was used to detect electric fields of 50 V/m with a modulation frequency of 6 GHz at an off-site location. The sensor is physically robust, and physically and electrically non-intrusive, and exhibits a temporally stable EO response.

The overarching purpose of design, fabrication, and testing of an electric field sensor was only possible by the successful integration of a variety of undergirding subsystems. These subsystems can be broken down into four main areas, (1) materials, (2) waveguide, (3) system, and (4) supporting technology. Figure 1.4 maps out how each of these subsystems relate to one another. The flow of the illustration goes from the micro level materials at the top, through the waveguide level of complexity, to the whole system level sensing scheme at the bottom. The chapter number where each subsystem is described in detail is included for each inset image. A brief description of each of the areas of research along with a bulleted list of relevant contributions in each areas follows.

1.4.1 Materials

The EO response of the sensors in this work is derived from poled EO polymers. Therefore, one main area of research and development in this work is with regard to the poling and characterization of EO polymers. Electro-optic polymer of the guest-host type used in this work must be poled in order to be sensitive to electric fields. Chapter 2 describes the theory and the experimental techniques used to pole electro-optic polymers which are deposited in the core of a D-fiber. Since poling efficiency is not directly observable, the effectiveness of the poling technique being used must

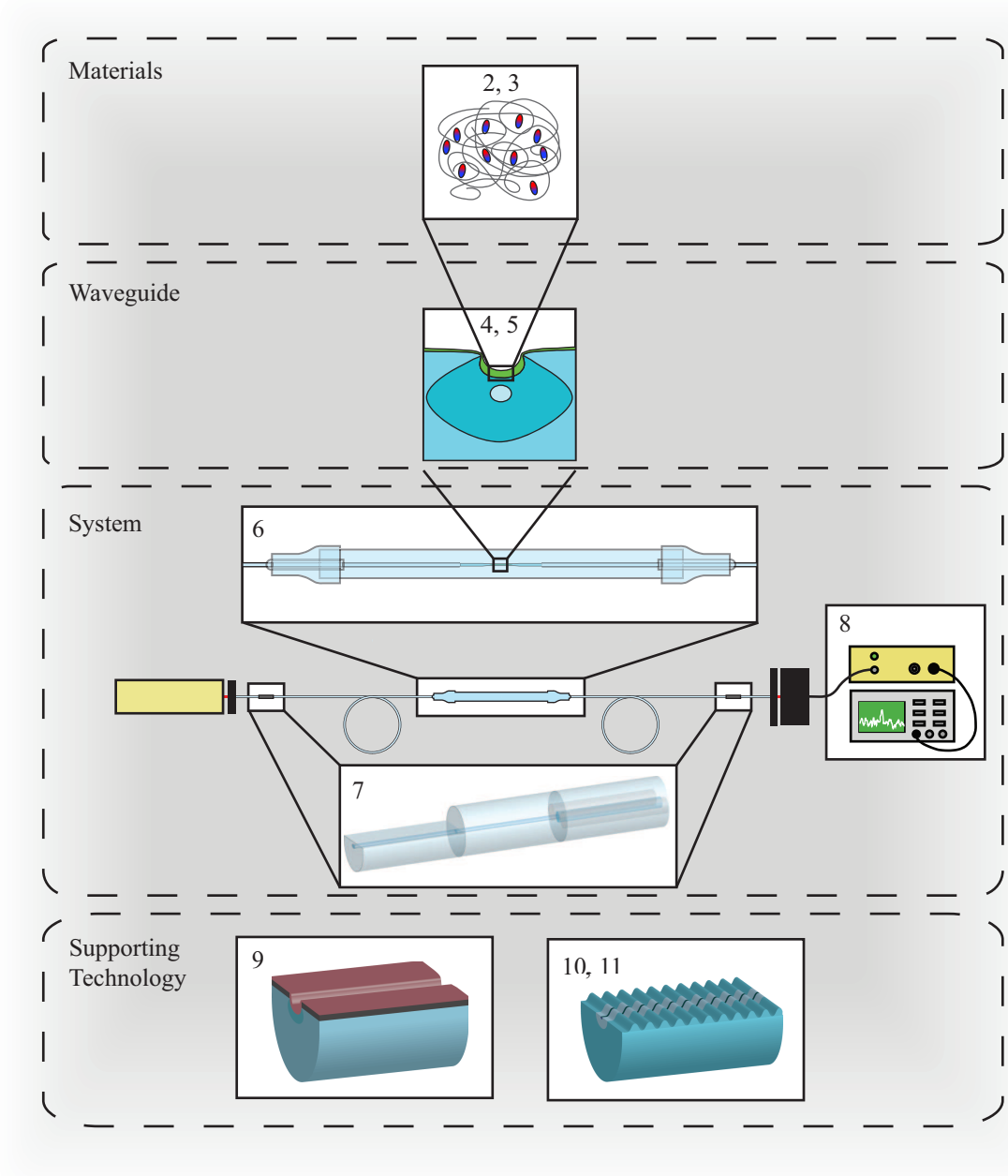

Figure 1.4: An illustration of the system level view of the D-fiber electric field sensors presented in this dissertation with a icon representing each chapter of the dissertation, (2) poling of electro-optic polymers, (3) in-situ second harmonic generation, (4) waveguide design, (5) polymer deposition, (6) sensor packaging, (7) D-fiber fusion splicing, (8) device testing, (9) fiber photolithography, (10) E-beam written fiber Bragg gratings, (11) the Vernier grating interrogation scheme.

be tested indirectly through another means. Chapter 3 presents an experimental technique for determining the effectiveness of a poling recipe as well as the theoretical underpinnings of the nonlinear optical effects relevant to this technique. Relevant research contributions include,

- the demonstration of an effective hybrid waveguide poling process[1, 3, 4], and
- the implementation of an in-situ second harmonic generation testing setup to characterize poling efficiency.

1.4.2 Waveguide

With a method in place for efficiently poling EO polymers, the next step is to form a hybrid D-fiber waveguide with the EO polymer material. Hybrid EO polymer D-fiber waveguide can translate the change in electric fields to a change in optical power. More optical power confinement in the EO polymer region of the waveguide results in higher device sensitivity. However, the sensor must balance insertion loss with confinement in order to maximize sensitivity by ensuring that the device operates in single mode and that the transition between unetched fiber to the device region results in good mode matching. Chapter 4 analyzes the theoretical background related to single mode fiber waveguides, and describes a method for designing high confinement low loss hybrid waveguides.

Once a workable design is obtained, the fiber must be fabricated to meet the design. D-fiber presents a variety of fabrication challenges due to its flexible substrate and high contrast topographies. Chapter 5 presents a method that is used to accurately and efficiently deposit polymer to form a hybrid polymer/fiber waveguide by means of ink-jetting with a commercial materials printer. This method improves upon the traditional spin-casting approach, and the two methods are compared. The contributions related to this work are,

- the acheiving of a greater understanding of the guiding characteristics of the D-fiber hybrid waveguide[4], and
- the development of D-fiber compatible polymer deposition methods[3].

1.4.3 System

The hybrid D-fiber waveguide, once fabricated is ready to be tested to verify that it is electrically sensitive. The device region of the sensor undergoes a variety of process which weaken its mechanical strength. Chapter 6 describes the details of a packaging design that has proven effective in increasing the robustness of the D-fiber hybrid waveguide sensor as well as other tests used to show the non-intrusive nature of the sensor and its packaging. After packaging, the D-fiber sensor must be connected with standard equipment before it can be tested. Chapter 7 presents background related to the polarization maintaining connection of optical fiber with fusion splicing, and the application of this technique to the low loss connection of D-fiber to PANDA fiber by means of an E-fiber bridge splice. The fusion spliced, packaged sensor is then tested to determine the effectiveness of the design and fabrication techniques, and to determine in what ways they need to be improved. Chapter 8 outlines the testing methods that were used to characterize sensitivity and reports testing results of various sensors which were fabricated.

- the development of a technique for low loss D-fiber fusion splicing[2],
- the design of a compatible packaging technique for a D-fiber optical sensor and the testing of its mechanical strength[4],
- the demonstration of the electrically non-intrusive nature of the D-fiber sensor by comparing it to the perturbation of thin metal wires inserted into a resonant waveguide[4], and
- the demonstration of effective E-field sensor testing and evaluation for both DR1/PMMA and AJL8/APC hybrid D-fiber waveguides[1, 4],

1.4.4 Supporting Technology

Even though relatively high electric fields are present during the testing of HPM weapons, it is necessary for the sensor to be able to detect changes in electric fields down to the 1 V/m range or less. Thus, there is a constant push to greater

sensitivity. Various exploratory technologies were developed in this work to address the need of greater sensitivity. Chapter 9 describes a method that was used to lithographically pattern electrodes and other structures on the surface of a D-fiber. These electrode structures can be used to obtain high electro-optic coefficients as described in (2.7). In an effort to increase sensitivity by using another sensing scheme, Chapter 10 presents the use of surface relief fiber Bragg gratings to detect electric fields. Chapter 11 shows how these surface relief fiber Bragg gratings can be used to obtain a device with greater electro-optic sensitivity by combining one or more grating structures to form resonances. Some of the key contributions in these areas are,

- the development of an embedding technique for making a planar substrate from a D-shaped fiber, and the fabrication of various photolithographically patterned structures on the surface of an embdedded D-fiber,
- the fabrication of SR-FBG's with E-beam lithography and ion beam milling, and
- the theoretical demonstration of Vernier scheme for electric field sensing and preliminary experimental results toward Vernier sensing.

1.4.5 Publications

Where applicable, each specific contribution listed above is noted with the number of the publication in which that contribution is published. The publications are listed below in chronological order.

1. E. K. Johnson, J. M. Kvavle, R. H. Selfridge, S. M. Schultz, R. Forber, W. Wang, and D. Y. Zang, *Electric Field Sensing With a Hybrid Polymer/Glass Fiber*, Applied Optics, vol. 46, no. 28, pp. 6953-6958, (2007).
2. J. M. Kvavle, S. M. Schultz, R. H. Selfridge, *Low Loss Elliptical Core D-fiber to PANDA Fiber Fusion Splicing*, Optics Express, Vol. 16, No. 18, pp. 13552-13559, (2008).

3. J. M. Kvavle, S. M. Schultz, R. H. Selfridge, *Ink Jetting of AJL8/APC for D-fiber Electric Field Sensors*, Applied Optics, (Submitted 06-12-09, In Peer Review)

4. J. M. Kvavle, J. Young, E. Gutierrez, S. M. Schultz, R. H. Selfridge, *Robust, Non-Intrusive In-Fiber Electric Field Sensors*, IEEE Sensors, (To Be Submitted)

1.4.6 Appendices

In addition to the main content, further information is included in the appendices of this work. Appendix A details various fabrication processes used in this work. Appendix B includes some useful MATLAB code that was used for the modeling in this work. Appendix C describes the method used to accurately model the guiding characteristics of a D-fiber hybrid waveguide by translating SEM cross-sectional images into refractive index profiles for BeamProp or FimmWave. Appendix D includes a detailed summary of the factors contributing to electric field sensitivity of the hybrid waveguides. Finally, Appendix E describes the RIE in-situ monitoring technique which was used to controllably remove polymer from the flat of a fiber.

Chapter 2

Poling of Electro Optic Polymers

2.1 Introduction

For some time there has been great interest in electro-optic (EO) polymers due to their high electro-optic coefficients, relatively low cost compared to EO crystals, low material dispersion, and straightforward processibility[14, 15, 16]. EO polymer also exhibit minimal phase mismatch between microwave signals and optical signals, allowing for EO modulation frequencies in the terahertz regime [17].

This chapter focuses on some basic chemistry dealing with electro-optic polymer and addresses how these polymer obtain their electro-optic sensitivity. Details about the specific poling methods and results at BYU are also outlined.

2.2 The Linear Electro-Optic Effect

The linear electro-optic effect was first discovered in 1893 by Friedrich Carl Alwin Pockels (1865 - 1913). As a result it is often referred to as the Pockels effect and the material coefficients describing its strength are often referred to as Pockel's coefficients. Pockels noticed that by applying an electric field to a birefringent material, it changed the refractive indices of the material in proportion to the strength of the applied electric field.

The linear electro-optic effect is a second order non-linear optical process which requires that the electro-optic material exhibit non-centro-symmetry, or long range order. The connection between second-harmonic generation, another non-linear electro-optic effect, and the linear electro-optic effect is described in Section 3.2.3.

Because the linear electro-optic effect requires non-centro symmetry, it is often found in crystals such as lithium niobate. However, other materials which exhibits

non-centro symmetry can also produce a significant electro-optic effect. In polymers, for example, the alignment of chromophores with large hyperpolarizabilities can produce electro optic coefficients in the 100 pm/V range.

The electric field dependent bulk index of refraction of an electro-optic material can be expressed as

$$n(E) = n + a1E + a2E^2 + ... \tag{2.1}$$

However, it is more common to use the impermeability of the material

$$\eta(E) = \eta_0 + \mathbf{r}E + \mathbf{s}E^2 + ..., \tag{2.2}$$

where $\eta = \frac{1}{n^2}$, $\mathbf{r}$ are the Pockels coefficients and $\mathbf{s}$ are the Kerr coefficients. The Pockels effect is proportional to field while the Kerr effect is proportional to the quadratic of the electric field. In most cases $\mathbf{r}E \gg \mathbf{s}E^2$ and all other higher order terms. This first term is called the linear electro-optic effect. With only the linear electro-optic effect being considered the impermeability can be expressed in matrix form as

$$\begin{bmatrix} \Delta\eta_1 \\ \Delta\eta_2 \\ \Delta\eta_3 \\ \Delta\eta_4 \\ \Delta\eta_5 \\ \Delta\eta_6 \end{bmatrix} = \begin{bmatrix} r_{11} & r_{12} & r_{13} \\ r_{21} & r_{22} & r_{23} \\ r_{31} & r_{32} & r_{33} \\ r_{41} & r_{42} & r_{43} \\ r_{51} & r_{52} & r_{53} \\ r_{61} & r_{62} & r_{63} \end{bmatrix} \begin{bmatrix} E_x \\ E_y \\ E_z \end{bmatrix}. \tag{2.3}$$

The electro-optic tensor is of the form [18],

$$\mathbf{r} = \begin{bmatrix} 0 & 0 & r_{13} \\ 0 & 0 & r_{13} \\ 0 & 0 & r_{33} \\ 0 & r_{13} & 0 \\ r_{13} & 0 & 0 \\ 0 & 0 & 0 \end{bmatrix}, \tag{2.4}$$

where the z-axis is the poling direction. Therefore, if the applied electric field is also in the $\hat{z}$ direction, the index ellipsoid can be calculated to be

$$\underbrace{\left(\frac{1}{n_o^2}+r_{13}E_z\right)}_{\frac{1}{n_x^2}}x^2+\underbrace{\left(\frac{1}{n_o^2}+r_{13}E_z\right)}_{\frac{1}{n_y^2}}y^2+\underbrace{\left(\frac{1}{n_o^2}+r_{33}E_z\right)}_{\frac{1}{n_z^2}}z^2=1. \tag{2.5}$$

The index of refraction in the EO polymer for the $\hat{y}$ and $\hat{z}$ directions are

$$\begin{aligned} n_y &= \left(\frac{1}{n_o^2}+r_{13}E_z\right)^{-\frac{1}{2}} \\ &= n_o\left(1+n_o^2 r_{13}E_z\right)^{-\frac{1}{2}}, \end{aligned} \tag{2.6}$$

and

$$\begin{aligned} n_z &= \left(\frac{1}{n_o^2}+r_{33}E_z\right)^{-\frac{1}{2}} \\ &= n_o\left(1+n_0^2 r_{33}E_z\right)^{-\frac{1}{2}}, \end{aligned} \tag{2.7}$$

respectively. Because typical values of the Pockels coefficients are in the range of $10^{-12}m/V$, $n_o^2 r_{13}E_z \ll 1$ and $n_o^2 r_{33}E_z \ll 1$ for any practical applied electric field. Because $(1+\Delta)^{-\frac{1}{2}} = 1-\frac{1}{2}\Delta$ for $\Delta \ll 1$, Eq. 2.6 and 2.7 can be simplified to

$$n_y = n_o - \frac{1}{2}n_o^3 r_{13}E_z, \tag{2.8}$$

and

$$n_z = n_o - \frac{1}{2}n_o^3 r_{33}E_z. \tag{2.9}$$

Taking a closer look at the r_{33} coefficient we find that the it is related to the molecular hyperpolarizability, β by the following relation,

$$r_{33} = N\left\langle cos^3\theta\right\rangle 2F\beta/n^4, \tag{2.10}$$

where N is the number of chromophores, $\langle cos^3\theta \rangle$ is the noncentrosymmetric order parameter, F is the field factor which takes into account the dielectric properties of the material, and n is the index of refraction of the material. The order parameter is influenced by the poling field strength, the chromophore dipole moment, and the thermal energy of the material. Therefore, to obtain the highest electro-optic effect a large number of chromophores, and a large hyperpolarizability are desirable. The number of chromophore can only be increased up to a certain point before intermolecular forces dominate and the order parameter becomes smaller. Thus, for each type of chromophore and polymer combination there exist an optimal chromophore loading level where the r_{33} is maximized and the intermolecular forces are minimized [19].

2.3 Electro-Optic Polymer

2.3.1 Polymers

Alone, the electro-optic chromophore would not be compatible with the fabrication of an electro-optic device. There are at least two reasons for this. First, because the chromophores cannot be it mixed and deposited to cannot form a uniform film. Second, when chromophores are packed too tightly their neighboring chromophore molecules would cancel out any of their polar characteristics, thus making them loose their electro-optic potential. However, by combining a smaller amount of chromophore with a larger amount of polymer, an electro-optic polymer is created. The electro-optic polymer will then have some of the characteristics of its polymer and some characteristics of its chromophore.

At the molecular level, polymers are simple molecules which are linked to make one very long chain. Amorphous polymers, like the ones used in this work, interweave and wrap around one another to form a tangled mess of molecules. These polymer chains are constantly moving and vibrating. Depending on the makeup of the polymer, the chains will move more or less at a particular temperature. The temperature at which the polymer chains begin to move easily is called the glass transition temperature of the polymer, or T_g.

2.3.2 Guest-Host Polymer Systems

In general EO polymers are not intrinsically electro-optic. Also, in most cases the polymer part of the EO polymer is not actually electro-optic at all. Rather, the chromophore, which is sensitive to electric fields, is mixed with a polymer host. That combination of guest chromophore and host polymer can be poled to form an electro-optic material. Often these type of polymers are referred to as *guest-host* polymers [20, 21]. Several other categories of EO polymer systems include side-chained, main-chained, crosslinked, hyperbranched, dendritic, and organic-inorganic hybrid polymers [14]. While various systems offer some advantages, the guest-host system is the simplest to implement. Making a guest-host polymer system only involves obtaining and mixing two separate components which then diffuse into one another to form a uniform matrix.

2.3.3 Spaghetti Analogy

A guest-host EO polymer system can be thought of as spaghetti with meatballs. The polymer chains are like spaghetti noodles and the chromophores are like meatballs distributed throughout the spaghetti. Below the T_g of the material, The polymer chains surround and restrict the movement of the chromophores, which are initially randomly oriented. An illustration of the guest-host polymer system is in Figure 2.1. When heated above the T_g of the polymer, the chromophores can move around and reorient themselves as in Figure 2.1(b). Thus a common method to permanently reorient the chromophore molecules is to heat the EO polymer to the glass transition temperature and then apply a field while lowering the polymer temperature back down to below the T_g [22].

There exist various methods of aligning or "poling" the chromophores of a guest-host polymer system. The two most common ways are corona poling, and contact poling. Section 2.4 describes the theory behind corona poling. Section 2.5 addresses the specific challenges of poling a D-shaped fiber with DR1/PMMA as the EO polymer. Section 2.6 discusses the additional challenges associated with corona

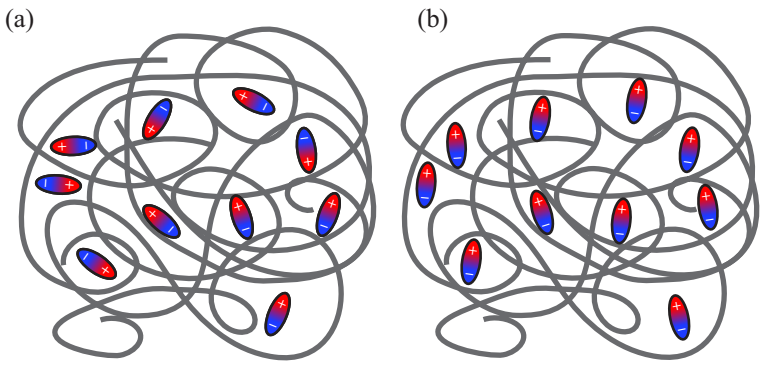

Figure 2.1: Illustration of an (a) un-poled polymer matrix, and a (b) poled polymer matrix

poling AJL8/APC. Section 2.7 describes a method where contact poling is used to pole AJL8/APC and reports the challenges and results.

2.4 Corona Poling

The corona poling technique is well documented and has been successfully used to pole a variety of materials. There are several articles that describe its use in poling electro-optic polymers [22, 23, 24, 25], and piezo-electric materials [26], and in making electrets [27, 28].

The basic idea behind corona poling is that a strong field is necessary in order to induce a rotational force on the polar chromophore molecules so that they align themselves all to one direction. In corona poling that field is applied due to the accumulation of charges on the surface of the sample, and a corresponding opposite charge is built up on the ground electrode. Figure 2.2 illustrates the corona poling process. First a needle or wire is used to create a location where ionization can occur. Usually the wire or needle has a very small diameter so that the voltage is all concentrated to one line or point in space. In the case of the needle, which is the method used in this work, the point is located on the tip of the needle. A smaller diameter tip results in a more concentrated voltage which makes ionizing the air much easier.

Two processes occur when a high voltage is applied to the needle and the bottom electrode is grounded. First, the air surrounding the needle is ionized. The

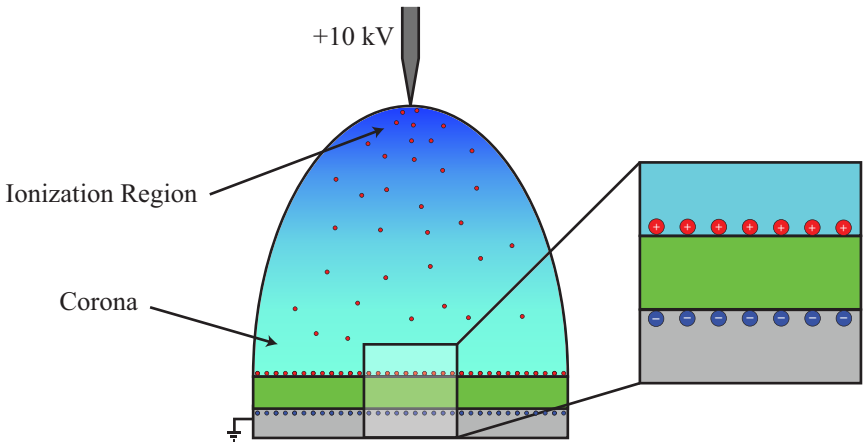

Figure 2.2: Illustration of corona poling of electro-optic polymer on a grounded substrate

needle is set at such high positive potential that electrons in the surround air are literally ripped off creating positively charged ions. The concentration of ionized air is higher just surrounding the needle. Second, once ionized these air molecules begin to accelerate toward the sample surface as the electric field generated by the needle and ground plane begin to act on them. The molecules eventually reach the sample surface where they remain. As more ions are deposited the sample surface reaches a point where no more ions can be deposited because the electrostatic forces between ions become stronger than the electric field's pull.

Once the saturation point is reached, the electric field across the sample is constant, and is related to the electric field from the sheet of charges on the sample surface and the distance over which the field is applied. The surface upon which the charges rest is not conductive and the ions have decreased mobility. Their decreased mobility makes it so that if there is a localized defect in the sample surface, the electric field across the sample in another area is unaffected. Another advantage of corona poling is that it only requires one electrode since the ions on the surface are themselves the source of the electric field. It has also been said that corona poling allows for poling near the breakdown voltage of the dielectric material [29].

2.4.1 Damage From Corona Poling

Since ions are constantly being accelerated toward the sample surface, corona poling often causes damage to the surface of a sample. Figure 2.3 contains optical microscope images of an sample before and after poling, as well as an image of a sample which was protected with a glass cover slip during the poling of the sample.

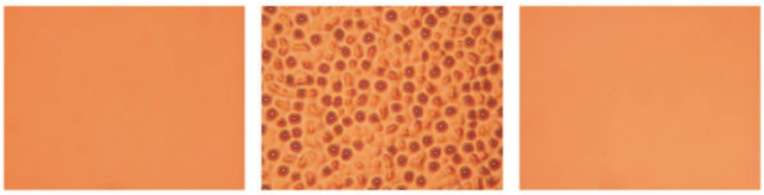

Figure 2.3: Cover glass protects the (a) unpoled polymer from (b) the damage that poling can cause creating (c) an optically smooth poled polymer.

Another method that reduces poling damage is to use Nitrogen as the poling gas, as described in Section 3.3.4.

2.4.2 Corona Needle Corrosion

After a time, the process of ripping off electrons during corona poling starts to affect the corona needles being used. One result is that the corona needle become dull. Figure 2.4 shows two corona needles, one which is new, and one which has been used extensively. Another unexpected process is that there is significant corrosion of the needle which resembles a coral reef! It is believed that this corrosion is the result of a chemical process that is intensified with the heat which is used to raise the polymer to the glass transition temperature. The composition of the corrosion is unknown, but is probably a combination of the molecules present in ambient air,

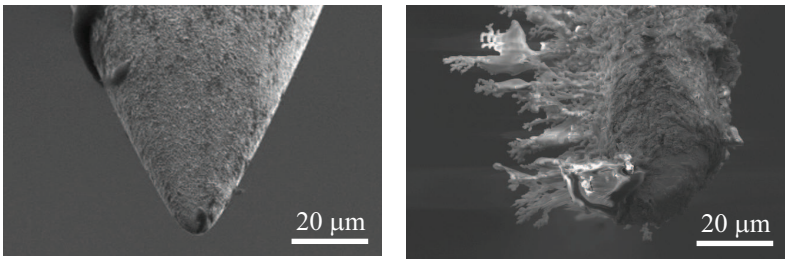

(a) (b)

Figure 2.4: SEM images of (a) new corona needle and (b) corroded corona needle

which is mostly oxygen and nitrogen. Because of this corrosion it is imperative to replace the corona needles regularly.

One practical effect of corroded needles is that the ion current generated by the needle is significantly reduced. As the ion current is reduced, the poling efficiency drops. A new corona needle positioned about 1 cm above the surface of the sample, with a corona voltage of 10 kV, generates a slight blue glow that can be see around the needle if the lights are turned off. A slightly audible crackling noise can also be heard. No blue glow, and minimal crackling is detectable with corroded needles.

2.5 Corona Poling a Hybrid DR1/PMMA Fiber Core

Many researchers use Disperse Red 1 (DR1) and Poly(methyl methacrylate) (PMMA) as a means to quantify their methods of poling, or second harmonic generation, as well as to compare its electro-optic coefficient with other materials. Figure 2.5 illustrates the chemical structure of the DR1 molecule. Note that DR1 has a smaller molecular weight (314 GPC) compared to many other chromophores in recent publication (650-850 GPC) [30].Among the reasons for the common usage of DR1/PMMA is that it is commercially available for a low price. It is also simple to mix into a guest-host system. Usually a high molecular weight PMMA ($\tilde{9}$96,000 by GPC) is used since higher molecular weight polymers exhibit higher glass transition temperatures.

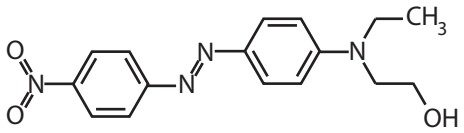

Figure 2.5: Molecular structure of disperse red 1

2.5.1 Formation of a Planar Poling Geometry

The basic corona poling process is not amenable to poling a polymer located in the fiber core. The primary reason for this incompatibility is that the positive charges build up on the substrate rather than just on the flat surface of the fiber resulting in the high electric field not being across the hybrid waveguide. In order to overcome this deficiency, there needs to be a surface parallel to the ground electrode onto which the charges build up and the fiber needs to be placed between these parallel surfaces as shown in Fig. 2.6.

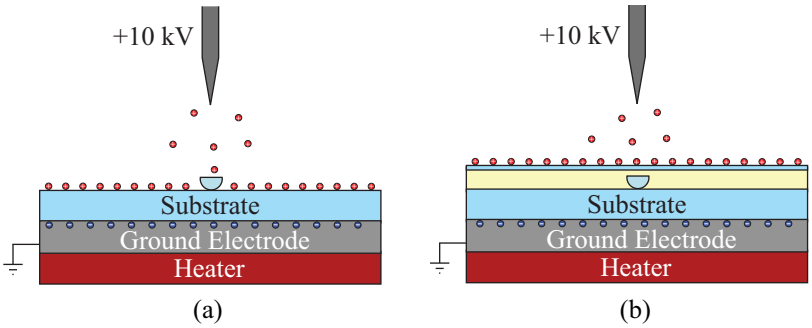

Figure 2.6: Illustration showing how the D-fiber is embedded in epoxy and cover glass to provide a structure that is compatible with corona poling.

Figure 2.7 shows the basic process used to create a structure that is compatible with corona poling. The hybrid waveguide section of the fiber is placed on a copper electrode. A layer of LS-6140 NuSil Silicone low index epoxy (Carpinteria, CA) is then deposited on to the fiber and a glass microscope coverglass is pressed over the fiber to create the parallel surface. This coverglass also protects the polymer from being damaged during the poling process. To protect the fiber where the protective

jacket has been removed and where the fiber touches the edges of the cover glass, low index epoxy is placed along the entire length of the striped region and a protective tubing is put on the fiber and attached to the cover glass.

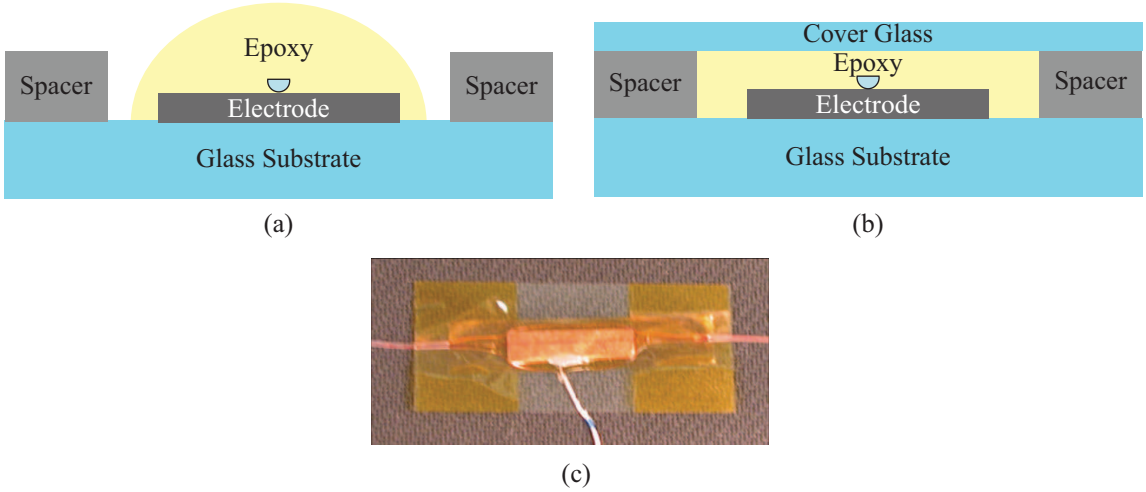

Figure 2.7: Illustrations of the basic planarization process which consists of (a) depositing epoxy over a D-fiber that is placed on top of a copper electrode and (b) pushing a glass coverglass over the fiber resulting in an embedded sensor as shown in (c).

2.5.2 Some Embedding Considerations

Note that the poling efficiency is related to how much field is applied across the fiber during poling. The poling field is dependent upon charge density as well as the distance between charges. Therefore, it is imperative that the thickness of the epoxy is minimized for the best poling efficiency. Some of the most efficient sensors have been fabricated with very thin epoxy, on the order of the thickness of the fiber. Figure 2.8 shows two SEM images of the epoxy that was used to embed a fiber for poling. The fiber has been removed from both to show the shape of the location where the fiber was embedded. Figure 2.8(a) was a very efficient electric field sensor, while Figure 2.8(b) was not as efficient.

It is also very important to ensure that the fiber polarization axes which are aligned to the flat of the D-fiber are aligned to the poling direction. If the angle

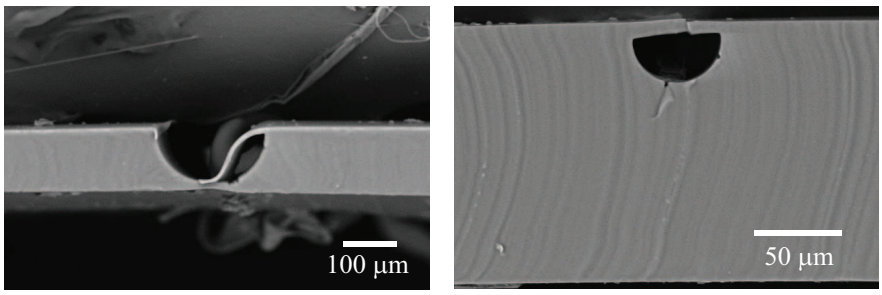

Figure 2.8: SEM cross-sectional images of silicone based epoxy used to embed D-fibers for poling. (a) The fiber embedded with a thickness of 62 μm was more efficient than (b) the fiber embedded with a thickness of 296 μm.

is rotated the poling efficiency will be diminished. The optimal embedding process, thus involves correct alignment of the flat of the D-fiber and a minimum thickness of epoxy for embedding. Both of these objectives can be obtained by carefully aligning the angle of the fiber before embedding and then applying force to the cover slip during the curing of the epoxy. The method used to obtain the very thin epoxy in Figure 2.8(a) is shown in Figure 2.9. First, the spacers are permanently attached to a glass slide. The electrode is then place between the spacers, and the fiber is aligned flat side up on the electrode. A small amount of epoxy used to cover the fiber and the electrode. The cover slip is then placed carefully over the epoxy so that no air bubbles form, and a magnet is placed on the top of the cover slip. The attraction between the magnet and the steel plate causes a constant downward force on the coverslip during curing. If the fiber angle is slightly incorrect, the force of the coverslip on the flat of the D-fiber help to rotate it to the proper angle.

The choice of epoxy, Nusil LS-6140, used for embedding was selected primarily for its index of refraction. Another advantage is that even after curing, the epoxy is soft, and the fiber can be removed from the epoxy after poling. It has been observed that this polymer tends to have components which settle after a while. Therefore, before embedding a fiber for poling it is important to ensure that each part is premixed well before mixing the parts together. Inefficient poling will result from poorly mixed parts. It is also important to accurately mix the 1:1 ratio. This can be done, most

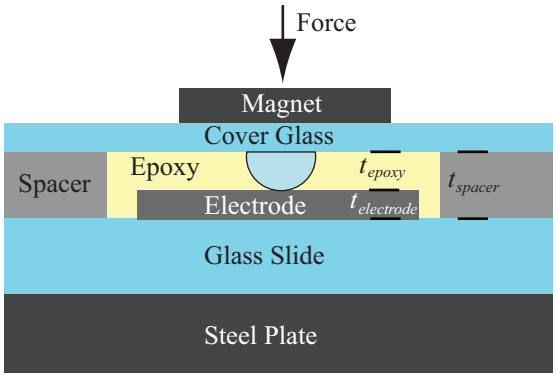

Figure 2.9: Illustration of the optimal embedding technique for D-fiber corona poling. The thickness of the epoxy (t_{epoxy}) and the thickness of the electrode ($t_{electrode}$) should be equal to the spacer thickness (t_{spacer}).

accurately, by weighing the drops on a milligram accurate scale. Generally 100 mg of each part is more than enough to embed a fiber.

2.6 Corona Poling a Hybrid AJL8/APC Fiber Core

Though DR1/PMMA is a good guest-host polymer for demonstrating the EO effect, its r_{33} coefficient at communications wavelengths is only around 4 pm/V. Additionally, PMMA has a low glass transition temperature (T_g = 100°C), which results in a polymer which is not temporally stable at room temperature.

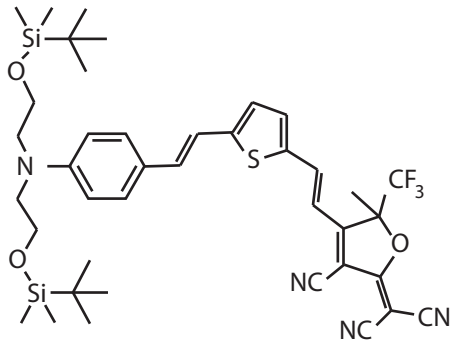

Figure 2.10: Illustration of the molecular structure of AJL8

Various other combination of chromophore and polymer have been attempted. One combination that has shown promising results is AJL8/APC, where AJL8 is the guest chromphore and APC, or amorphous polycarbonate, is the host polymer. Figure 2.10 shows the chemical structure of AJL8. This chromophore was designed and synthesized at the University of Washington, for its high hyperpolarizability. Various devices have been fabricated using AJL8/APC such as ring resonators [31], and Mach-Zehnder modulators [32]. AJL8/APC has also been found to be temporally stable when heated to 85 °C for over 500 hours [33]. The temporal stability of AJL8/APC is derived from the much higher glass transition temperature, (T_g = 140°C) of APC. The more rigid polymer backbone of APC is the source of its higher glass transition temperature.

Since AJL8/APC is a guest host polymer, it is simple to prepare. Figure 2.11 is a photo of a small quantity of AJL8, which is mixed in solution with commercially available APC. In the crystalline form, AJL8 is dark red, very similar to DR1, but when mixed in solution with APC and an organic solvent, the color turns green. Not all commercially available APC is usable as a host polymer. Therefore, its optical properties, such as loss, should be tested before use.

Figure 2.11: Photo of synthesized AJL8 in its crystalline form.

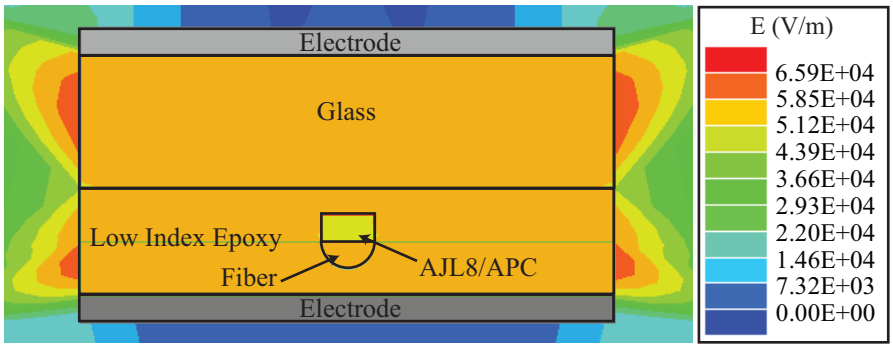

Figure 2.12: Electrostatic model for corona poling a fiber.

As in the case of DR1/PMMA poling of hybrid core fibers, the hybrid core AJL8/APC fiber must also be encapsulated for poling. Initially the only difference in poling the two materials was to adjust the poling temperature from 100°C for DR1/PMMA to 140°C for AJL8/APC.

After fabricating sensors with AJL8/APC it was found that the obtained r_{33} coefficient was not as high as expected. One reason for this decreased performance is that AJL8/APC is a more conductive than DR1/PMMA. By obtaining a SEM cross-section image and modeling the resulting index profile in Beamprop, it was estimated that an electro-optic coefficient obtained was probably only around 7 pm/V. The r_{33} coefficient of DR1/PMMA was measured to by to about 4 pm/V.

2.6.1 Conductivity of AJL8/APC

The erroneous assumption was that all materials involved in the embedding of the fiber, as well as the EO polymer and fiber itself were essentially perfect dielectrics. Thus, the poling fields could be modeled with a simple two-dimensional solution to Laplace's equation. The electric permittivity, voltage, and distances would therefore determine the electric field during poling. Figure 2.12 illustrates the field distribution using an electrostatic model. The AJL8/APC layer thickness is greatly exaggerated for the purpose of more easily seeing the field distribution in the film. Note that the higher permittivity of the AJL8/APC polymer results in a slightly lower electric field, but the difference is not enough to cause concern.

However, it was determined later that AJL8/APC is slightly more conductive than DR1/PMMA and the glass and epoxy used in the embedding process. By factoring conductivity into the model, it was determined that most of the field will drop across the lower conductivity materials.

Whereas a perfect dielectric structure can be modeled as a series of parallel capacitors as in Figure 2.13(a), a slightly conductive material must be modeled as a capacitor in parallel with a resistor which is then in series with another capacitor and resistor as in Figure 2.13(b). The behavior of the resistors dominate in the steady state operation of a voltage applied to a conductive material. The result is a voltage divider where the majority of the field drop across the larger resistor.

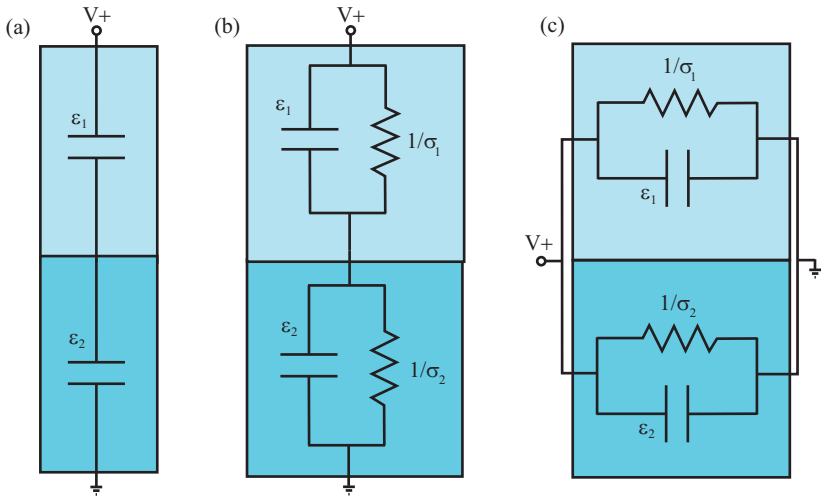

Figure 2.13: Circuit diagram for (a) corona poling a perfect dielectric (b) corona poling a slightly conductive material and (c) in-plane poling of a slightly conductive material.

Ansoft's Maxwell SV is a free modeling software package that can be used to model electrostatic field distributions. It also includes a DC Conduction field solver where the electric potential is calculated based on the physical model and boundary conditions, and the electric field is derived from the electric potential.

Figure 2.14 illustrates a simple case where a voltage is applied across two slabs of low conductivity materials which sandwich a slab of higher conductivity material.

The red shading denotes the highest field and the blue denotes the lowest field. No field is dropped across the higher conductivity material. It was assumed that the higher conductivity material has a conductivity on the order of the conductivity of AJLS102/APC as reported in [34]. The lower conductivity material was assumed to be glass and its conductivity was obtained from [35].

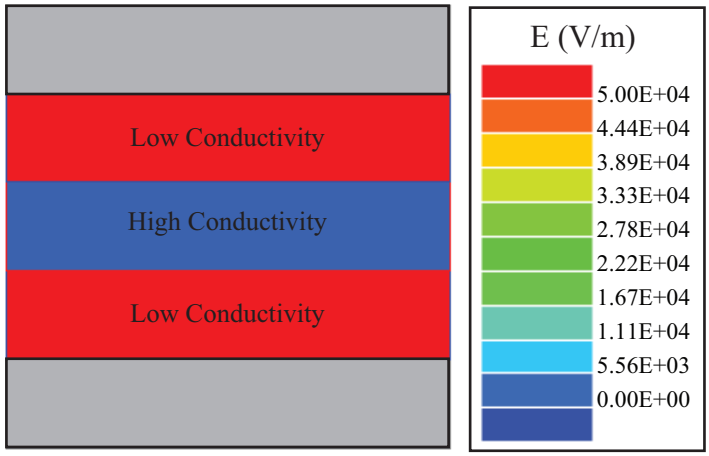

Figure 2.14: Slab of higher conductivity material between lower conductivity material. All of the field drops across the low conductivity materials.

Figure 2.15 illustrates the electric field distribution for a corona poled fiber using the DC conduction model. As in the case of a simple slab structure, the higher conductivity AJL8/APC also has no electric field dropping across it. In reality the corona poling of an embedded optical fiber is most likely a combination of both the electrostatic and DC conduction models.

2.7 In-line Contact Poling of a Hybrid AJL8/APC Fiber Core

This phenomenon in relation to the poling of conductive EO polymers is observed in [34], and their solution is the in-plane electrode poling configuration. The in-plane electrode structure effectively puts the resistors in parallel as illustrated in Figure 2.13(c). The result is an improved poling field across the EO polymer due to equal voltage in each branch.

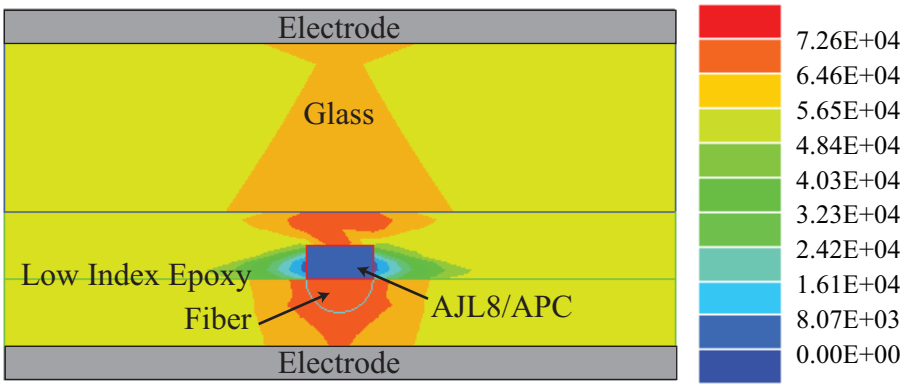

Figure 2.15: Illustration of the electric field present in the polymer during the standard corona poling process.

If In-plane electrodes are used with a partially etched out core, the result is better, but still, most of the field will drop across the gap between the sharp edges of the groove, as shown in Figure 2.16. The field in the polymer itself is a little over half of the maximum field.

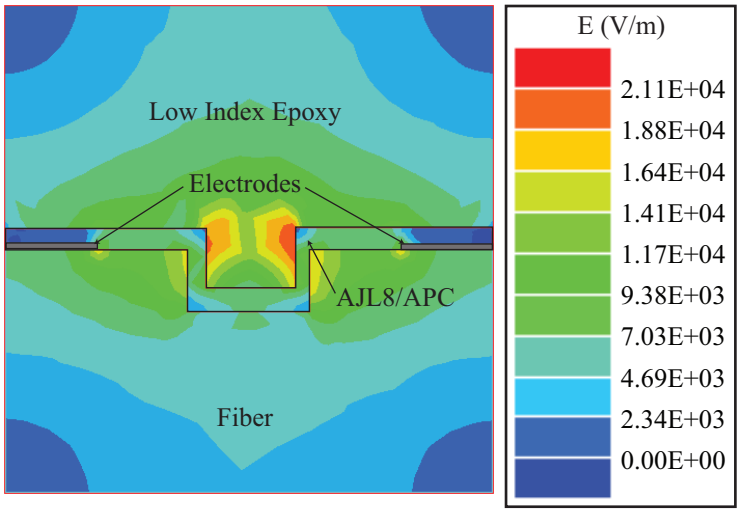

Figure 2.16: DC conduction model of partially etched fiber hybrid core with APC/AJL8

This case would still be much better that the current corona poling configuration, but the optimal poling structure for maximum electric field is one where the AJL8/APC is flat on the surface of the fiber.

Figure 2.17 illustrates the fields when the polymer is flat on the surface of the fiber, and is only curved due to the curve of the fluorine doped etch region. The field is much more uniform. This more uniform field makes it more likely that a higher field can be applied to the polymer before dielectric breakdown.

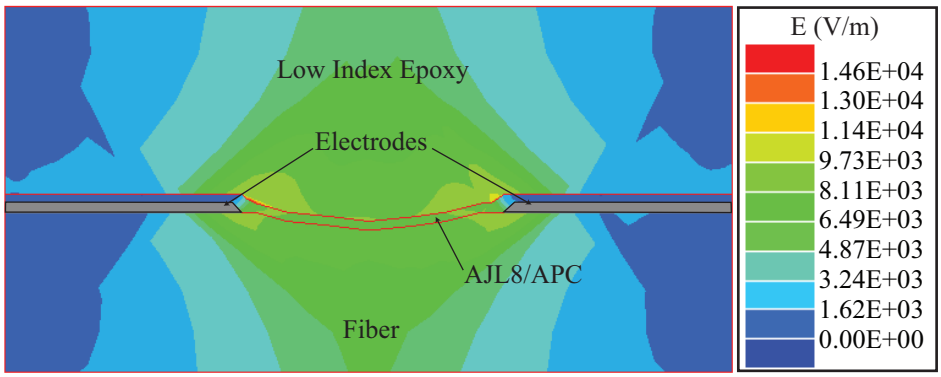

Figure 2.17: Illustration of the optimal poling conditions with the DC conduction model.

In plane electrodes are the optimal choice for poling a more conductive polymer with less conductive materials which surround it. The conductances are then in parallel, and the electric fields are less conductivity dependent.

2.8 Conclusions

The challenges of poling an electro-optic polymer deposited in the core of a D-fiber have been addressed by the of corona poling a D-fiber which has been embedded into a low index material, thus making a uniform planar surface for the charges to accumulate. For slightly higher conductivity materials, this method is insufficient to maximize the electro-optic coefficients of the poled polymer. Rather, an in-plane electrode poling method can be used to apply the electric field in parallel.

Simulations indicate the the electric field distribution using in-plane electrodes is much more ideally suited to the poling high conductivity polymers.

Future work should focus on continuing work with the patterning of in-place electrodes on the surface of an embedded fiber, and then depositing the polymer, and a barrier layer to avoid air breakdown. All of these materials must be compatible with the high poling temperatures (145 °C) associated with AJL8/APC poling. A 5x improvement in device sensitivity can be obtained from an optimal poling configuration.

Chapter 3

In-Situ Second-Harmonic Generation

3.1 Introduction

Corona poling of EO polymers aligns the chromophore molecules in a guest-host polymer chromophore system. The resulting orientational order of the chromophore makes a material in which second-order nonlinear effects can be observed. The nonlinear optical effect of interest in electric field sensing is the Pockel's Effect, or the linear electo-optic effect. Another very common nonlinear optical effect is second-harmonic generation (SHG). Because the change in the molecular orientation occurs at the microscopic level, it is difficult to directly determine if the polymer is poled. Therefore, it is necessary to use an indirect method to measure the orientational order, or non-centro-symmetry of an EO polymer.

One of the most straight-forward methods of quantifying the orientational order of an EO polymer is to measure the SHG. SHG takes advantage of a particular non-linear optical phenomenon first observed in 1961 by Franken *et al.*, and will be described in further detail in the following section [36].

This chapter focuses on some of the theory behind SHG, and then goes on to describe the specific experimental setup that was built to monitor the the SHG of a sample during the corona poling process. It will be shown that in-situ SHG is an effective method in determining optimal parameters for corona poling EO polymers.

3.2 Background

3.2.1 Qualitative Description of SHG

Second-harmonic generation is the process by which two photons of frequency ω_1 are combined into one photon of frequency ω_2, where ω_2 is twice the frequency of ω_1. Figure 3.1 illustrates this point. At the molecular level the two photons are absorbed by an atom or molecule. That absorption causes the energy level of the molecule to be raised by two virtual energy levels. After a time the molecule will return to its ground state by emitting a photon of twice the frequency of those absorbed.

The process of SHG is a non-linear process because it depends on the square of the electric field. Thus, SHG can only be measured in the presence of very high electric fields, and was only observed after the invention of the first Laser.

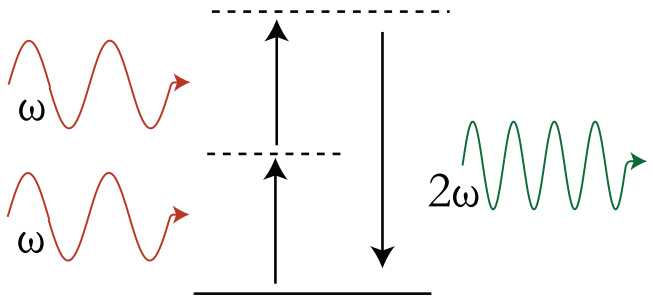

Figure 3.1: Diagram of SHG where two photons combine to raise the energy level of an molecule which then releases that energy in the form of one photon of twice the frequency

However, even with high powered lasers, second order nonlinear processes are only highly efficient in a non-centro symmetric medium because of phase matching requirements[37]. If the material is composed of molecules with random orientation, the phases of each of the second harmonic waves will eventually add together to cancel one another in deconstructive interference. On the other hand, if they are all aligned, they will add constructively and the phase matched SHG signal can then be detected. Figure 3.2 illustrates the two cases.

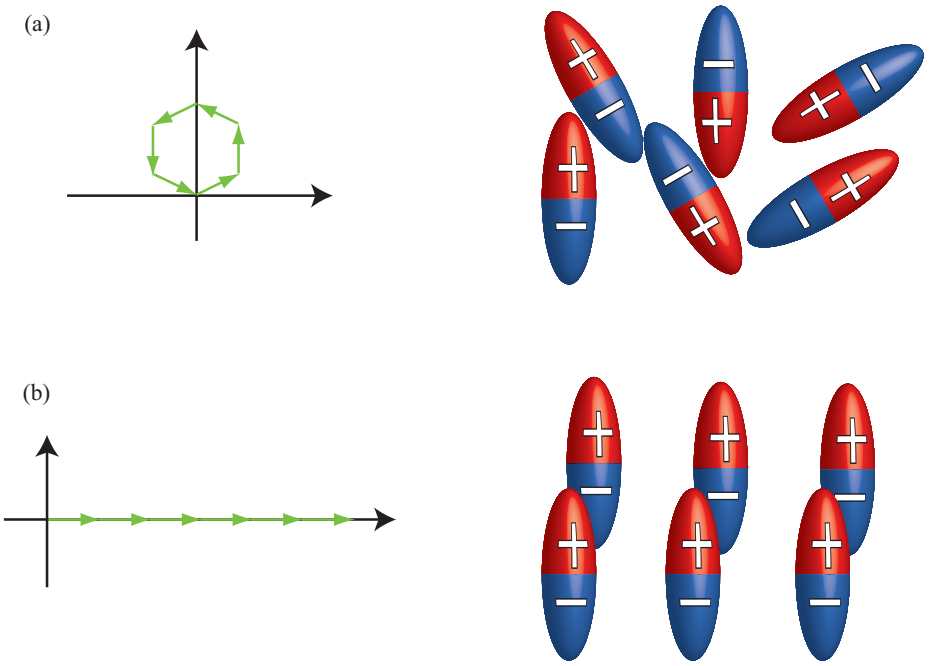

Figure 3.2: a.) The vector representation of material polarization components adding out of phase with each other, and a corresponding illustration showing a randomly oriented material. b.) The vector representation of components adding in phase with each other, and a corresponding illustration of the non-centro symmetry molecule matrix that could satisfy the phase matching conditions.

3.2.2 Theoretical Description of SHG

Now examine the theory of second-harmonic generation as treated in Boyd's *Nonlinear Optics* [38] will be examined. First let us consider how the polarization, $\tilde{P}$, of a material is influenced by an electric field, $\tilde{E}$. The polarization of a material is another word for the dipole moment per unit volume, and should not be confused with the polarization of light. We see in equation 3.1 that they are related by multiplying $\tilde{E}$ by ϵ_0, which is the permittivity of free space, and $\chi^{(1)}$, which is known as the linear susceptibility,

$$\tilde{P}(t) = \epsilon_0 \chi^{(1)} \tilde{E}(t). \tag{3.1}$$

It is common to use the polarization of a material to describe non-linear processes as in equation 3.1 because a time varying polarization can become the source for new electric field components.

The linear susceptibility is a term that indicates how much the polarization of a material is affected by a given electric field, or how susceptible the material is to a change in dipole moment. Therefore, if a material is very susceptible to electric fields it will have a larger χ value.

However, Equation 3.1, does not include any information about non-linear susceptibility, so we must expand it in a power series as follows:

$$\begin{aligned}\tilde{P}(t) &= \epsilon_0 \left[\chi^{(1)}\tilde{E}(t) + \chi^{(2)}\tilde{E}^2(t) + \chi^{(3)}\tilde{E}^2(t) + \ldots\right] \\ &\equiv \tilde{P}^{(1)}(t) + \tilde{P}^{(2)}(t) + \tilde{P}^{(3)}(t) + \ldots. \end{aligned} \tag{3.2}$$

Now we see that there are terms that describe both the second- and third-order nonlinear optical susceptibilities. For SHG we are interested in the second-order term $\chi^{(2)}$. Note that there are two major assumptions in equation 3.2. We assume that $\tilde{P}$ and $\tilde{E}$ are scalar quantities. We also assume that the affect of the electric field on the polarization of the material is instantaneous, which also implies that the medium is lossless and dispersionless.

Let us now consider the process of SHG. First we take the electric field for a laser beam,

$$\tilde{E}(t) = Ee^{i\omega t} + c.c., \tag{3.3}$$

which is incident upon a polymer film for which the second-order susceptibility $\chi^{(2)}$ is nonzero. If we substitute that electric field into into equation 3.2 and solve for $\tilde{P}^{(2)}$, we obtain the following,

$$\begin{aligned}\tilde{P}^{(2)} &= \epsilon_0\chi^{(2)}\left[Ee^{i\omega t} + c.c.\right]^2 \\ &= \epsilon_0\chi^{(2)}\left[\underbrace{E^2e^{i2\omega t}}_{second-harmonic} + \underbrace{2EE^*e^{i\omega t}}_{zero-order} + c.c.\right]. \end{aligned} \tag{3.4}$$

Now, we use this time dependent polarization to drive the non-homogeneous wave equation of the form,

$$\nabla^2 \tilde{E} - \frac{n^2}{c^2}\frac{\partial^2 \tilde{E}}{\partial t^2} = \frac{1}{\epsilon_0 c^2}\frac{\partial^2 \tilde{P}^{NL}}{\partial t^2}. \tag{3.5}$$

It can be shown that by substituting equation 3.4 into equation 3.5 that the second-harmonic term results in radiation at the second-harmonic frequency. The zero-order frequency term, however, results in no radiation since the second time derivative disappears.

3.2.3 Relationship of SHG to Pockel's Effect

By carefully measuring the amount of SHG from a particular EO polymer sample, it is possible to obtain an accurate idea of the potential strength of the Pockel's effect in that material, since both are dependent upon the $\chi^{(2)}$ term in equation 3.1. Even though it is often called the linear electro-optic effect, the Pockels effect is still a nonlinear process governed by the same theory that was used to describe SHG.

In the case of SHG we found that the polarization had a $\tilde{E}(\omega)^2$ dependence as in equation 3.4. In the case of the linear electro-optic effect we find that it has an $\tilde{E}(\omega)\tilde{E}(0)$ dependence. The $\tilde{E}(\omega)$ comes from the field created by the light in the material, and the $\tilde{E}(0)$ comes from the DC electric field that is applied to the material. Thus, the polarization of the material changes based on the two interacting fields, and the result is an electric field dependent material index of refraction, $\eta(\tilde{E})$ [39].

3.3 Experimental Results

Various researchers have used SHG to determine the effectiveness of their poling technique. Some use SHG after poling [22, 40],while some measure the SHG during the poling process, often called in-situ monitoring, to obtain additional information [41, 23, 24, 42, 43, 44]. This work was already well established when we

began work with corona poling and SHG as a means to determine the effectiveness in poling. Our efforts focused on replicating their results so that we would have the same tools for characterization of poling.

Our first use of SHG involved corona poling a sample and then measuring the SHG after poling to see how well the sample was poled. The next stage of research called for a more complex experimental setup that provided additional information that was then used to further optimize the poling process. This more complex experimental setup was used to characterize various chromophore-polymer combinations. Additionally, one of the experimental setups also allowed for feedback control of the corona current.

The following subsections of this chapter focus on the results obtain for various polymer and chromophore combination and by various experimental setups.

3.3.1 Post Poling SHG of DR1/PMMA

In our initial SHG experiments DR1/PMMA was the material of choice, due to it's availability. A sample is prepared by spin casting a polymer solution of DR1, PMMA, and cyclohexanone onto a double wide glass slide. The sample is then cured for 15 minutes at 90 C on a hotplate. The sample is then poled according to the process described in the chapter on corona poling. After the sample is poled, it is testing in the first experimental setup illustrated in Figure 3.3. The YAG Laser emits a 25 mJ, 7 ns pulse at a wavelength of 1064 nm which is expanded in the diverging lens to prevent burning through the filters. Next, the light from the laser is focused using a standard 17 cm focal length lens. The YAG laser uses a flash lamp to generate the the pulse, so that light is eliminated by using a 1064 nm pass filter. The sample is placed at the focal point of the beam to create a small interaction point of high power. This high power region is necessary in order to achieve appreciable non-linear effects. The 1064 nm portion of the beam is then filtered out with a 532 nm pass filter and the only photons that then reach the photo-multiplier tube (PMT) are the ones generated by second harmonics.

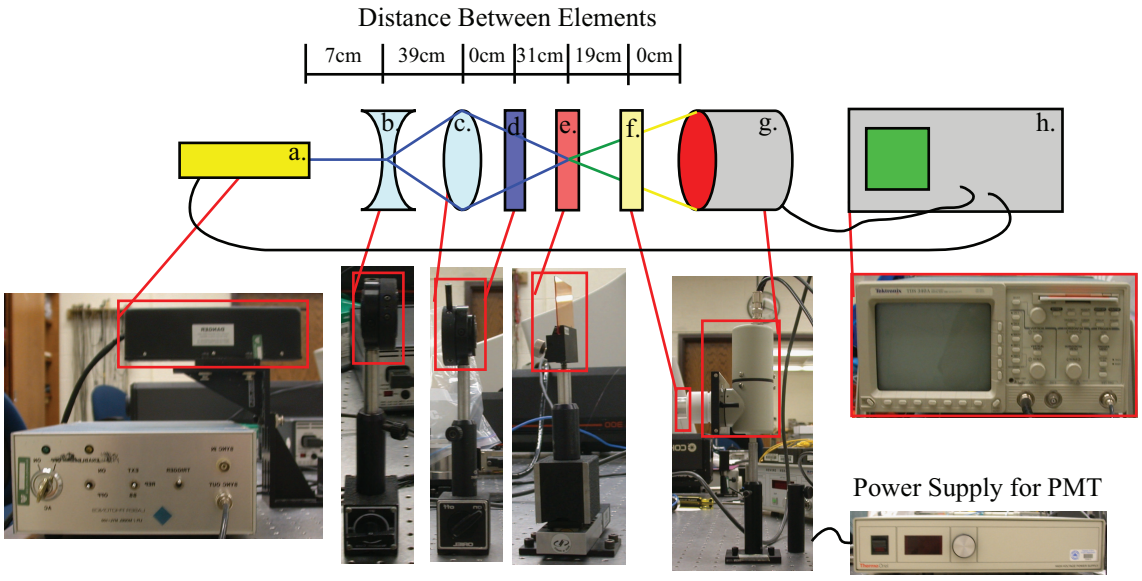

Figure 3.3: Simple SHG setup used to determine the presence of SHG after poling. a.) Nd:YAG laser, b.) diverging lens, c.) focusing lens (17 cm focal length), d.) 1064 nm pass filter, e.) sample, f.) 532 nm pass filter, g.) photo multiplier tube, h.) oscilloscope (Tektronix TDS 340A)

The SHG photons create a current pulse in the PMT, but it is translated into a voltage signal when the current is fed into the oscilloscope. The oscilloscope triggers on the sync signal from the YAG laser and records the voltage pulse. The amplitude of the pulse is then taken to be related to the strength of the SHG. A screen-shot of an SHG pulse recorded on a Tektronix TDS 340A oscilloscope is shown in Figure 3.4.

Notice that the signal is a negative. That is because the signal from the PMT is a negative current pulse. This particular screen-shot in Figure 3.4 shows a fairly small SHG response. The voltage only dips down to 25 mV, whereas a well poled sample shows a dip on the order of 160 mV. Also note in the screen shot the long straight line immediately preceding the voltage pulse. This is simply an artifact of the trigger input from the laser and can be ignored.

This simple setup also helped to experimentally confirm that DR1/PMMA does not maintain its non-linearity very well. We performed an experiment where we tested the SHG signal with no sample in the sample holder. Then, a test was performed with an unpoled sample in the sample holder. Next, the sample was poled

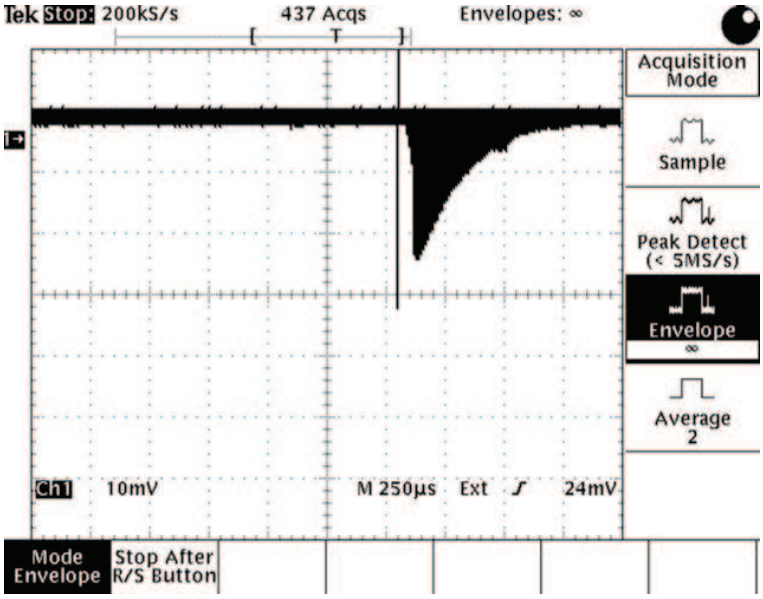

Figure 3.4: Screen capture of a DR1/PMMA SHG pulse

and tested. Finally, the sample tested four days after it was initially poled. Figure 3.5 plots the pulses obtained with these four test cases.

Note that there is still a small SHG signal even when there is no sample in the sample holder. This signal results from the fact that our optical filters do not perfectly block all undesirable wavelengths. The SHG signal when nothing is in the sample holder is a basis for determining the proper bias voltage for the PMT. The no sample SHG signal level should be just distinguishable above the noise for good SHG signal contrast.

The SHG signal is measurable when an un-poled sample is tested. This is due to the fact that at such high fields there will be a small amount of SHG. Another possible cause is that the sample is sparking slightly. It is important to verify that the sample is positioned slightly off of the focus of the lens, otherwise the high power of the laser will actually ablate the film, and a spark will be visible to the naked eye. This spark is not SHG.

Not surprisingly, the highest SHG signal is obtained with a poled sample. This signal is about seven times higher than the sample when it was measured four days

after poling. This confirms the fact that DR1/PMMA is not temporally stable as Mortazavi observed [22].

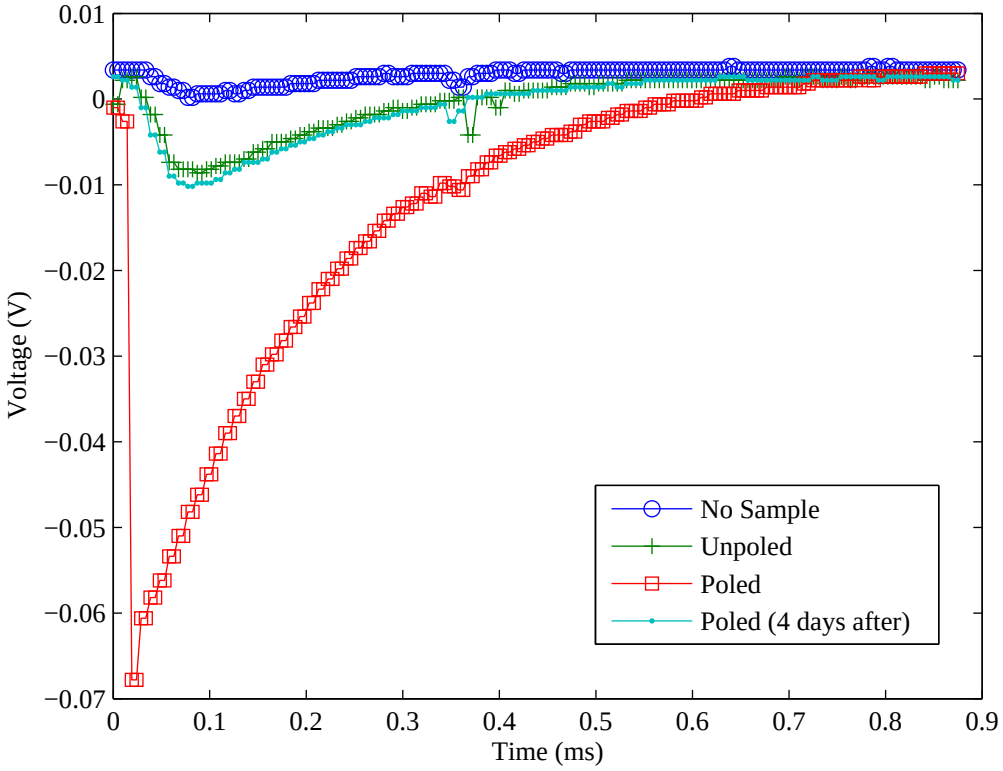

Figure 3.5: Plot of SHG for no sample, un-poled sample, poled sample, and four day old sample.

3.3.2 In-Situ SHG of DR1-PMMA

Testing for the SHG signal from a sample after poling is good because it indicates how well the sample has been poled. If more information is desirable, or if the optimal poling conditions are completely unknown, it is helpful to measure SHG while the sample is being poled.

An experimental setup that was assembled for the purpose of performing in-situ SHG is illustrated in Figure 3.6.

A more detailed view of the corona poling part of the setup is shown in Figure 3.7.

The in-situ experimental setup involves several additional layers of complexity over the simple setup described in the previous section. First, the setup records real-time data using a LabView interface. Second, the SHG signal is reflected from a mirror-polished copper electrode [42]. Third, it allows for corona current feedback control [28]. Fourth, the setup also records the temperature of a reference sample during poling [42, 43, 44]. Finally, it enclosed in a Plexiglas box with quartz windows so that the poling atmosphere can be controlled [23, 28, 26].

As in the simple experimental setup, a sample is prepared by spin casting a polymer solution of DR1, PMMA, and cyclohexanone onto a double wide glass slide. The sample is then cured for 15 minutes at 90 C on a hotplate. A function generator is set to a 1 Hz frequency to with the YAG laser, and the oscilloscope are synced. The YAG laser emits a 25 mJ, 7 ns pulse at a wavelength of 1064 nm which is expanded in the diverging lens to prevent burning through the filters. An iris is used to block most of the flash lamp light from the YAG laser. Next, the light from the laser is focused using a standard 17 cm focal length lens. The remaining portion of the YAG laser flash lamp is eliminated by using a 1064 nm pass filter. The sample is placed in the corona poling setup, so the light is directed down towards the sample with a mirror, and once it passes through the sample, is reflected back up with the polished ground electrode. The angle of the mirror is chosen so that the light has a clear path to and from the sample. The 1064 nm portion of the beam is then filtered out with a 532 nm pass filter and the only photons that then reach the photo-multiplier tube (PMT) are the ones generated by second harmonics. The PMT then transmits that pulse to the oscilloscope which triggers on the function generator signal. LabView retrieves the pulse data from the oscilloscope.

While this SHG signal is being recorded, a LabView controlled 10 kV voltage source is connected to the corona needle, and the control grid is connected to a 2 kV voltage source. The copper plate in the corona poling setup, also used to reflect the SHG, is connected to ground through a current amplifier so that the corona current

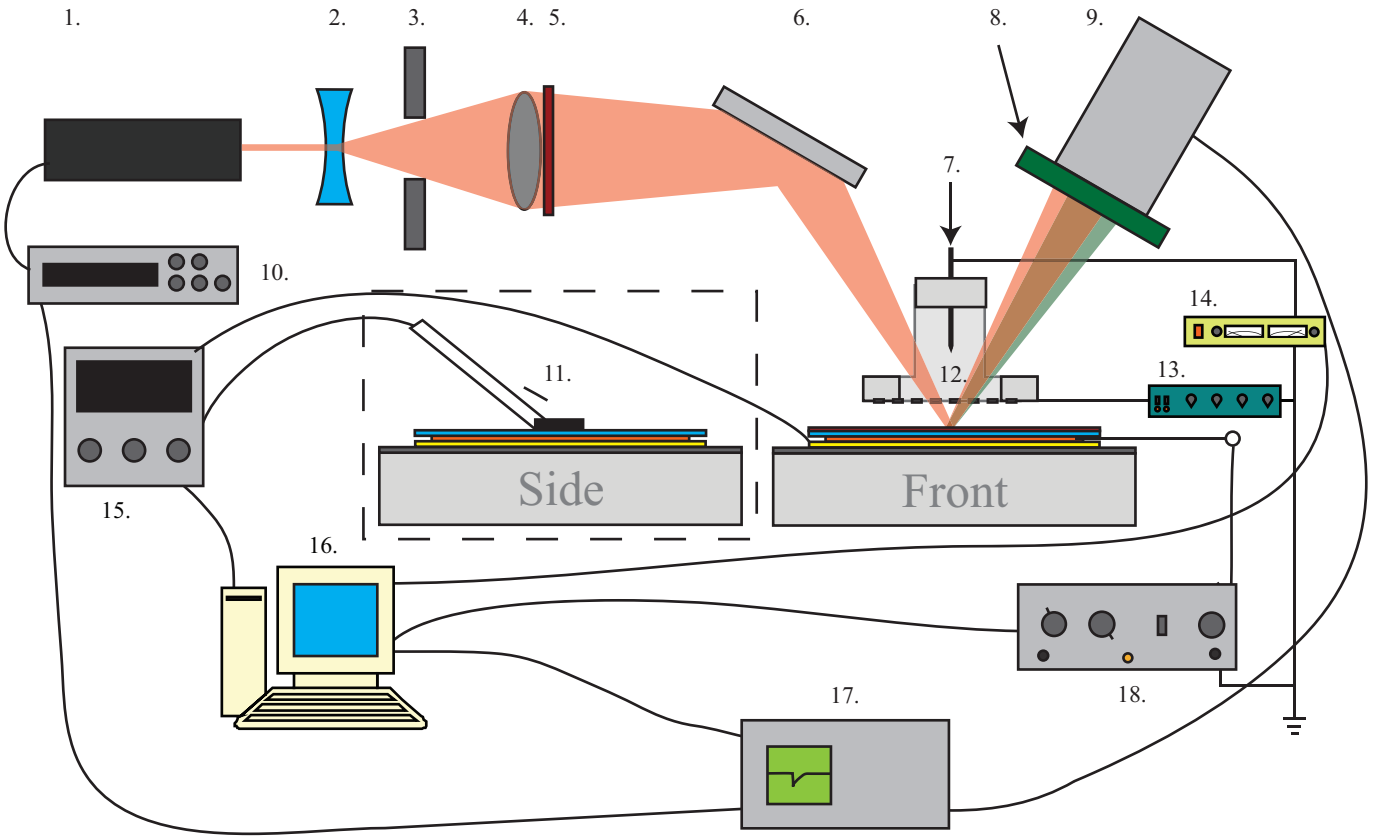

1. YAG Laser, 1 Hz, 25mJ, 7 ns
2. Diverging Lens to Expand the Beam
3. Iris to block the flash lamp
4. Focusing Lens
5. 1064nm Narrowband Filter
6. Mirror to direct beam down to sample.
7. Corona Needle for Poling
8. 532nm Narrowband Filter
9. Photo Multiplier Tube
10. Function Generator
11. K type Thermocouple
12. Control Grid
13. Control Grid High Voltage Source (2 kV)
14. Corona Needle High Voltage Source (10 kV)
15. Temperature Controller
16. Labview Interface.
17. Oscilloscope for detecting and recording SHG Pulses
18. Current Amplifier

Figure 3.6: In-situ SHG experimental setup with labels identifying each component.

can be measured. A temperature controller heats the sample and monitors the temperature of a reference sample. Using a reference sample eliminates interference with the sensitive voltage signal between the dissimilar materials of the thermocouple and the inherently interfering process of corona poling.

One of the most important aspects of this setup is the LabView interface of the temperature controller, the oscilloscope, the current amplifier, and the high voltage source. This interface makes it possible to record temperature, corona current, corona voltage, and SHG data simultaneously. Each of these signals is synced using a function generator and internal LabView programming. LabView writes these values to a file, which is plotted as in Figure 3.8.

Figure 3.8 plots both the SHG signal and the temperature of the sample on separate axes. The high voltage is applied to the corona needle throughout the experiment. The SHG signal first rises as the chromophores begin to align when the PMMA is heated enough to allow them to freely move. As the temperature increases further, the orientational order is eliminated by the increased kinetic energy of the PMMA molecules due to temperature. As the temperature cools the PMMA molecules lose some of their kinetic energy and the SHG returns because the chromophores are again free to move in the applied electric field. It is thus possible to determine the optimal poling temperature range from that plot since we can determine the point at which the SHG began to increase and decrease.

From this analysis it was determined that 95 C is a good poling temperature for PMMA/DR1 since the SHG signal is highest at that point.

Several factors contribute to make it difficult to make quantitative measurements of SHG in this experimental setup. First, the YAG laser does not have very good shot to shot uniformity. Second, each sample has a different polymer thickness, which affects the phase matching conditions of the SHG. Finally, optical alignment of the beam through the lenses, filter, and mirrors affect the intensity of light that is transmitted to the PMT. There was an observable difference from day to day in the SHG intensity of a sample. It is difficult to use the same sample to try and eliminate some of this variability as well, because the samples are slightly damaged

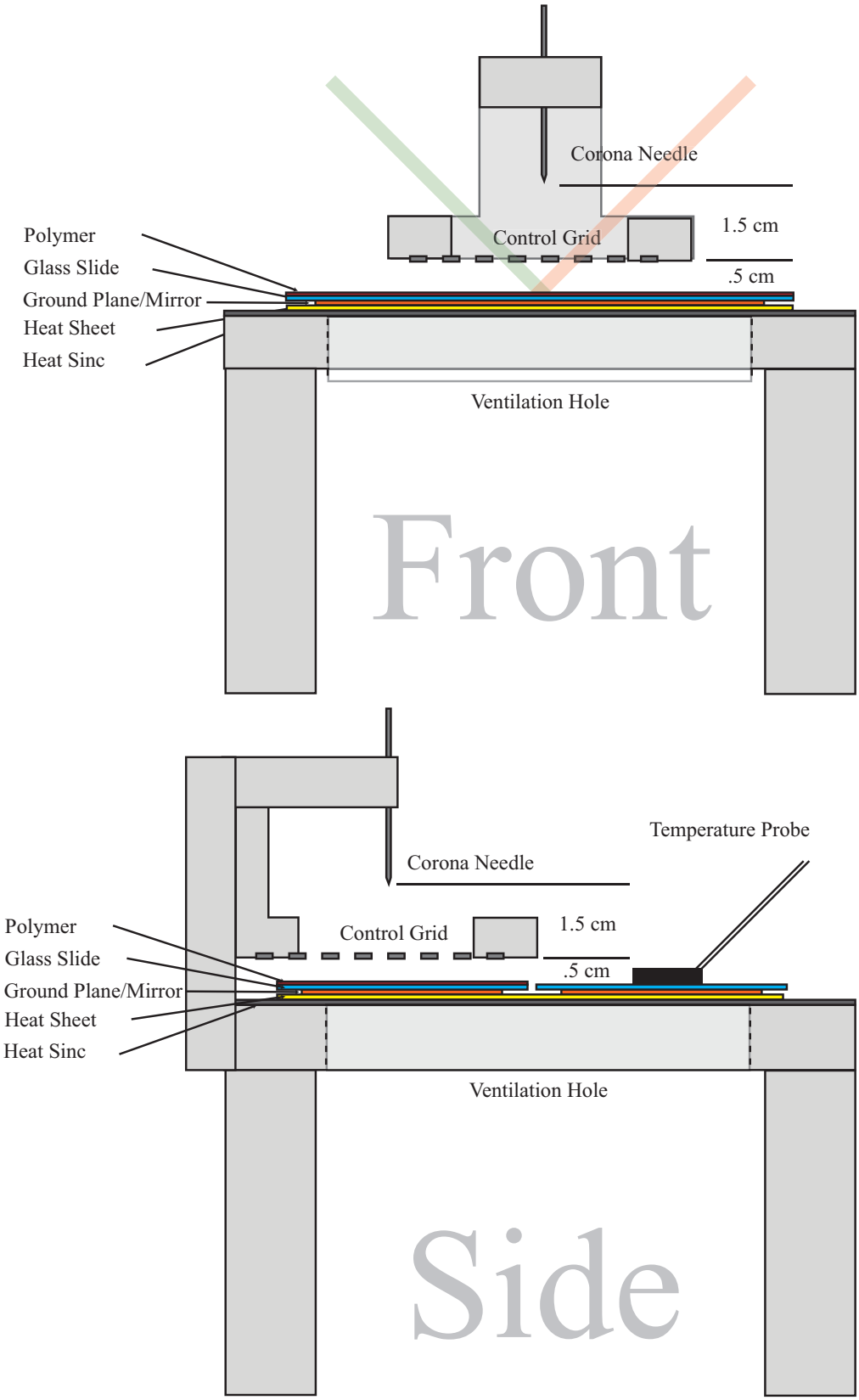

Figure 3.7: A detailed view of the corona poling stand used for in-situ SHG.

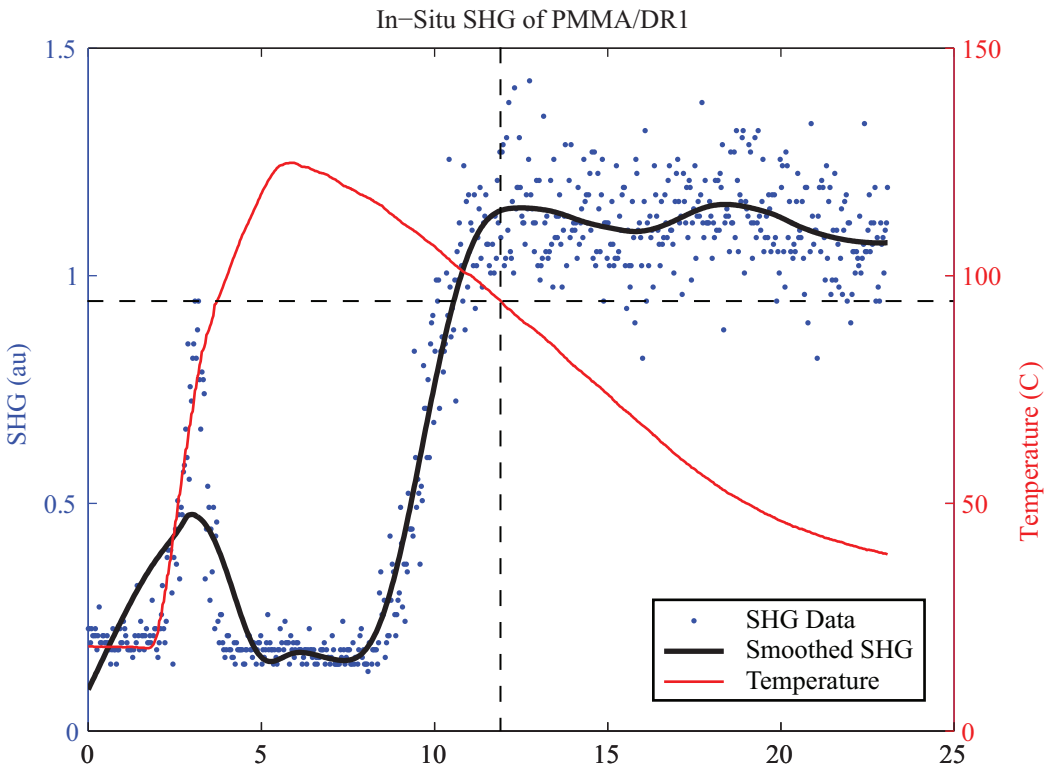

Figure 3.8: Two y-axis In-Situ SHG plot of SHG response for a PMMA/DR1 sample.

in the corona poling process. A qualitative analysis is the most productive use of this experimental setup due to these factors.

3.3.3 Constant Current Corona Poling

Often is is desirable to maintain a constant current during corona poling [28]. The constant current method of corona poling increases charge uniformity, and by keeping the current constant it is possible to focus on other parameters to maximize poling efficiency. To keep the current constant, it is necessary to adjust the voltage of either the corona needle or the control grid in a corona triode configuration. The advantage of adjusting the control grid is that the control grid voltage can be used to determine the surface potential of the sample being poled.

The corona poling setup used for in-situ monitoring was either the simple point to plane corona poling configuration, or the corona triode configuration depending

on the desired experiment. In the description of constant current poling it will be assumed that the corona triode was used.

By using a corona triode the ionized gas that acts as the corona poling charges are accelerated towards the sample surface. The efficiency of the poling becomes greater since a greater percentage of the total charges contribute to the poling field is greater.

Two high voltage sources were used with the corona triode setup for constant corona current. The 10 kV supply was wat set to between 0 and 10 kV with a labview interface. The 2 kV source was connected to the control grid and was manually set.

In order to understand how the corona current can be kept constant it must be noted that the corona current is related to corona voltage and temperature, among other things. First, the corona current is proportional to the corona voltage. Figure 3.9 plots the corona current as the corona needle voltage is increased in increments of 1 kV. The spikes in the corona current are due to arcing through or around the sample. Notice that they occur regularly when the corona voltage is changed, and could be cause by a current spike in the high voltage source itself. In this experiment the control grid was kept constant at 1.5 kV.

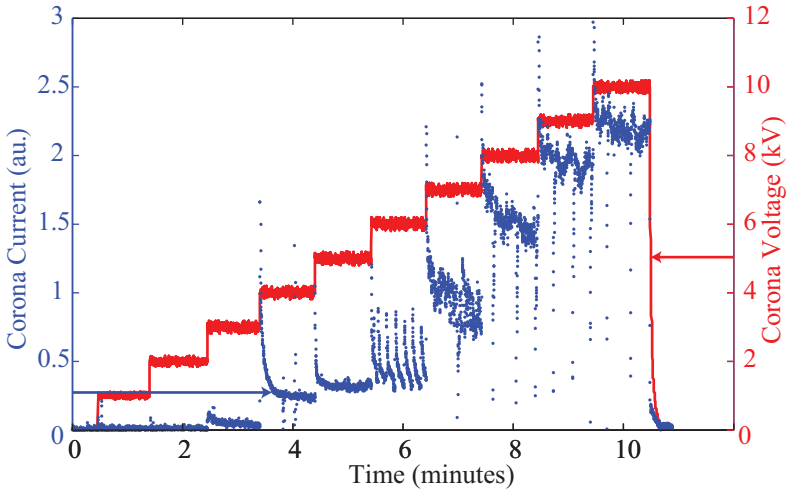

Figure 3.9: Corona current vs. corona voltage for corona triode with a control grid set at 1.5 kV.

Notice that when the voltage was set to 1 kV and 2 kV there is no corona current above the noise floor. One reason for that is the voltage on the needle needs to be high enough to produce enough potential to separate the gas from one of its electrons. Another reason is that the electric field between the needle and the control grid had an opposite polarity until the voltage on the needle was higher than the control grid. Finally, the current amplifier used in this experiment was adjusted so that it would not go beyond its maximum output voltage for the highest current levels, therefore due to its limited dynamic range, some of the lower signals may have been lost.

The next factor in controlling the corona current is to recognize that temperature affects the amount of corona current. Figure 3.10 plots the temperature of a sample with a measured corona current. The voltage on the corona needle was set to 6 kV and the control grid was set to 1 kV so that no corona current was presnet at room temperature. The sample was then heated and then cooled back down to room temperature, all while measuring thecorona current. The current follows the temperature surprisingly close. There is a spike in the current at about 2 minutes due to an experimental error.

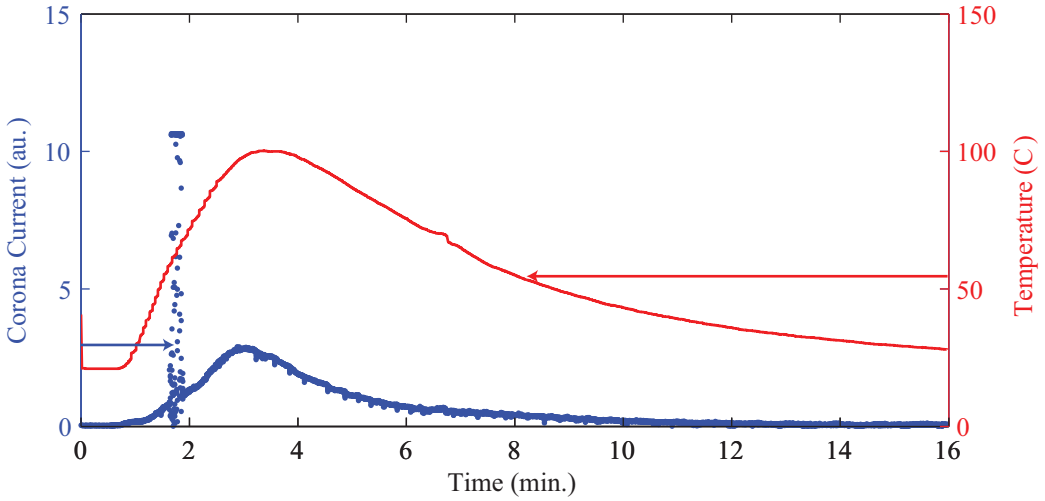

Figure 3.10: Corona current vs. temperature for a needle voltage of 6 kV and a control grid voltage of 1 kV.

During corona poling of electro-optic polymers, the sample temperature is raised to just below the glass transition temperature of the material. Since corona current is temperature related, the corona voltage on the needle must compensate for the change in temperature to maintain a constant current. This is accomplished with a simple feedback control. The corona current is measured and the voltage on the high voltage corona needle is either increased or decreased depending on the corona current for that iteration. The measurement and adjustment loop repeats throughout the duration of the poling.

Figure 3.11 show the temperature, corona voltage, and corona current recorded during the in-situ SHG monitoring of a sample that was poled. The corona current was set to be 1 μA as measured from the trans-impedance amplifier during this poling process. Notice how initially there is low current, which causes the voltage to increase until it almost reaches 10 kV. By that time the temperature of the sample increases enough that the current is now larger than the desired setting. The corona voltage thus decreases until it reaches a steady state at 1 μA again. If it were important to only approach but never exceed a current value of 1 μA, a better starting value voltage could be chosen, or a more sophisticated feedback loop could be implemented.

Besides this initial "ringing," the corona current stays fairly constant during the poling process. The corona voltage responds by increasing and decreasing to maintain the constant current as the temperature changes.

Intuition indicates that for a higher corona current a higher corona voltage is necessary. Figure 3.12 illustrates this point by plotting the corona voltage for four different corona current settings. PMMA/DR1 samples were poled where the only parameter that was changed was the corona current setting.

3.3.4 In-Situ SHG in a Nitrogen Environment

The Corona Poling of electro-optic polymer takes advantage of the fact that ions are accelerated in an electric field toward the sample surface where they collect. Those ions, along with their couterparts in the ground electrode, are the source of the actual poling field. The ions are generated by stripping of the electrons from

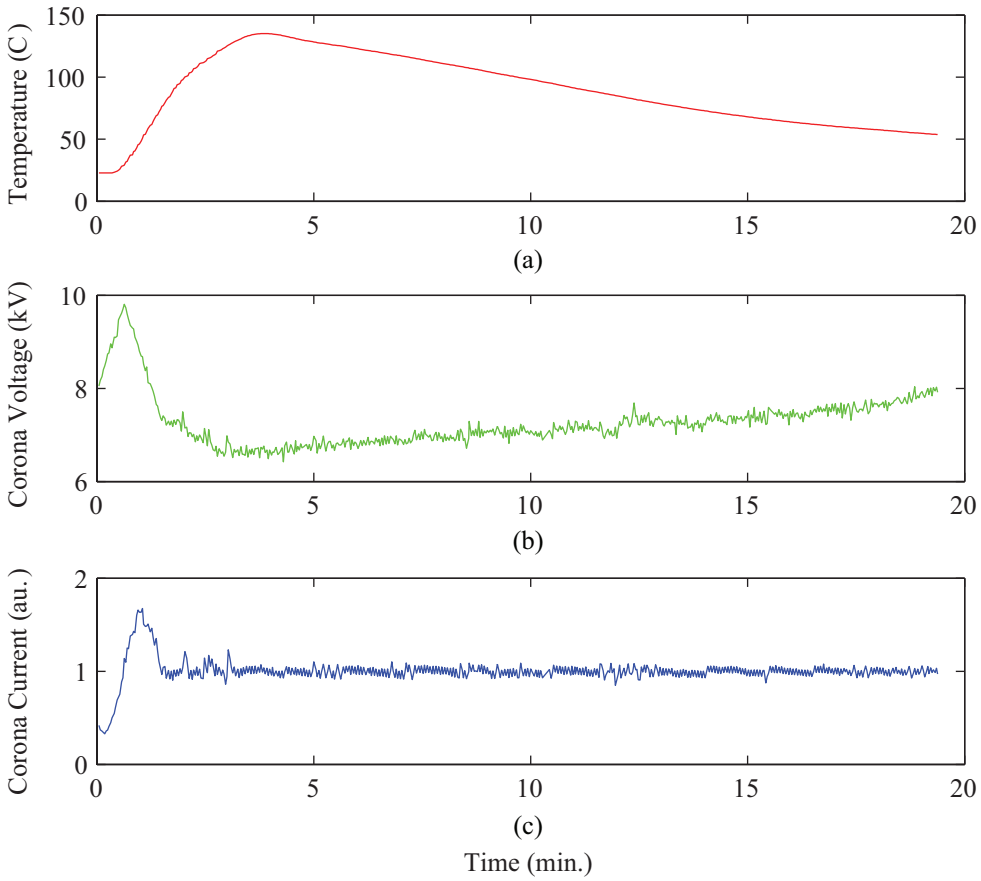

Figure 3.11: Plots of (a) temperature, (b) corona voltage, and (c) corona current during in-situ SHG poling of a PMMA/DR1 sample

the environment around the corona needle. Therefore, if the poling environment is ambient air composed of 78% Nitrogen, 21% Oxygen, and less than 1% of Argon and Carbon Dioxide, some of these various ions will be present on the surface of a sample being poled. Nitrogen, and Argon are both fairly inert, while carbon dioxide is moderately reactive. However, Oxygen is highly reactive, and will forms compounds with almost any other element.

About twenty percent of the poling ions in an ambient enviroment are reactive, and will chemically react with the compound toward which they are accelerated. This process is analogous to the reactive ion etching process common to CMOS fabrication. In essence, corona poling of ambient air is like making your own mini RIE. This is generally not a desirable effect in the corona poling process.

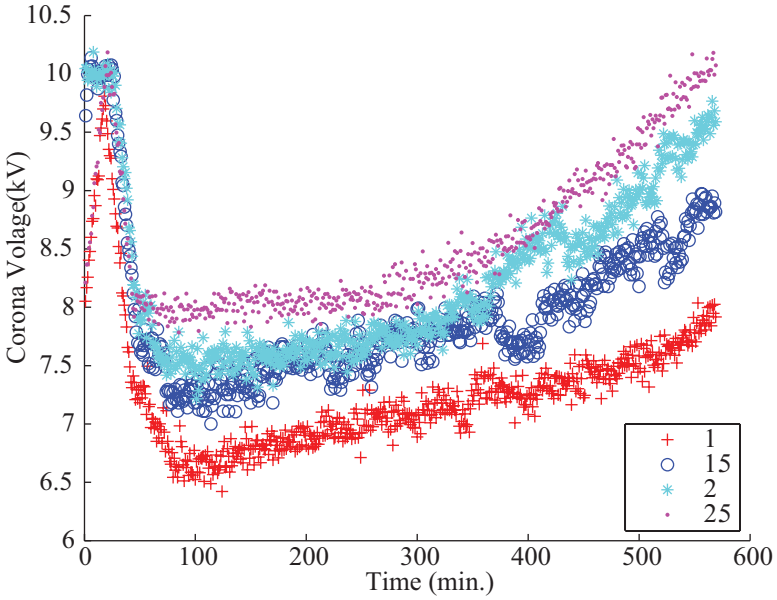

Figure 3.12: Plot of corona voltage for multiple corona current settings with the same poling recipe

Various solutions to this oxygen problem have been proposed, such as using a removable barrier [29], as well as using an inert poling atmosphere[23]. Both techniques have been used in the optics lab with success.

In the in-situ SHG experimental setup the inert atmosphere solution was chosen to reduce the damage to a sample. Nitrogen was pumped into an enclosure illustrated in Figure 3.13 and the ambient air was displaced by the incoming nitrogen. The YAG laser light and the SHG output are angled into the enclosure through quartz windows.

The advantages of using nitrogen instead of ambient air are best shown by contrasting two PMMA/DR1 samples which were poled in nitrogen and air respectively. Both were poled with 1 au. of corona current, and the same temperature recipe, but the results are much better for the nitrogen environment. Figure 3.14.

3.3.5 In-Situ SHG of DR1/s-BPVE

With the ability to measure SHG while poling a sample, it was possible to explore the poling characteristics of other materials. In collaboration with Tetramer,

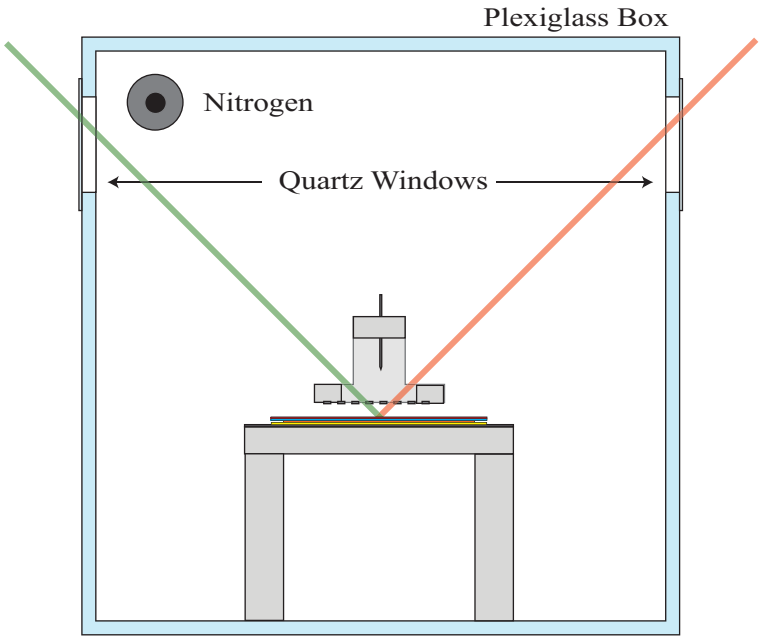

Figure 3.13: Illustration of plexiglass enclosure for in-situ SHG with a nitrogen environment

a Clemson University spin-off company, another type of polymer was evaluated for its poling characteristics.

While various chromophores and polymers were used in this collaborative effort, DR1/s-BPVE will be addressed here as being representative of the collaboration.

Since chromophores are polar by nature, if the host polymer is doped with chromophores to a certain level the EO effect is dramatically decreased. The cause of this is agglomeration, or the attaching of one chromophore to another chromophore.

Sulfonated BisPhenylVinylEther, or s-BPVE, is a polymer. Clemson University has found s-BPVE to be useful in the production of fuel cells due to its proton conducting capability [45]. Tetramer determined that due to the chemistry of the polymer, that greater chromophore doping would be possible. This is because of the ionic interactions of the sulphonated groups which are attached to the BPVE polymer chain. It was theorized that these ionic interactions would allow for greater loading levels by decreasing agglomeration.

Tetramer did not know what the glass transition (T_g) temperature of the polymer was when they sent it. The standard technique used by many chemists

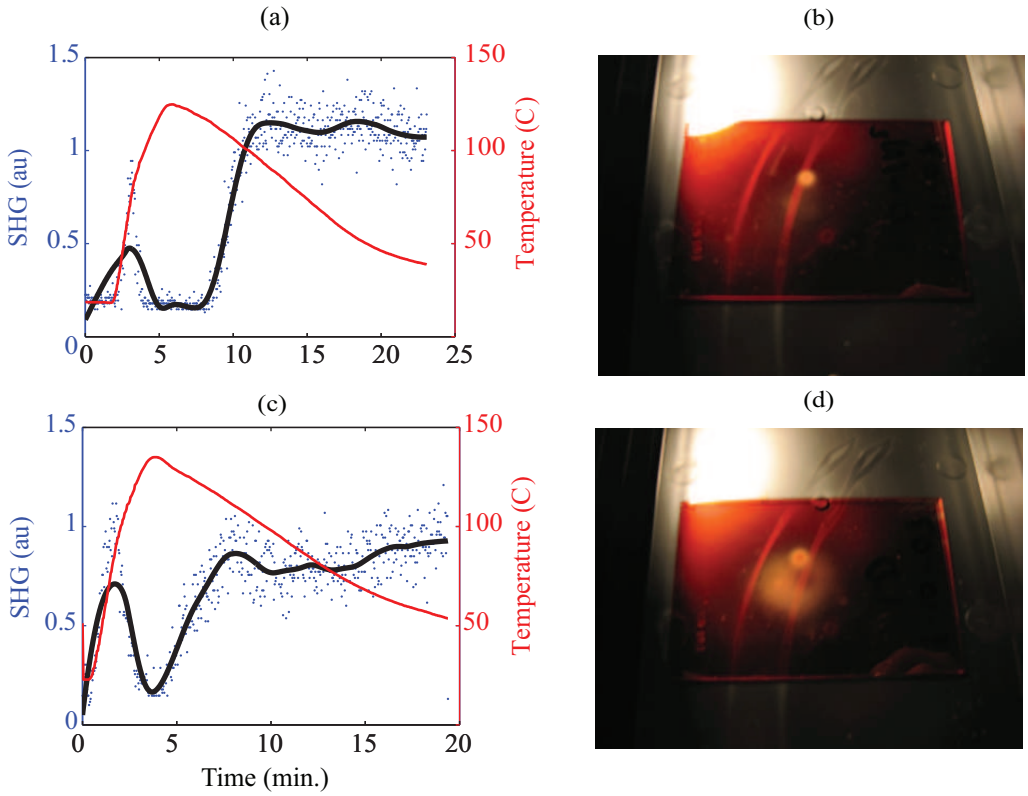

Figure 3.14: (a) Plot of the in-situ SHG of PMMA/DR1 with nitrogen environment and a maximum smoothed SHG value of 1.1. (b) A photograph of the PMMA/DR1 the sample in (a). Note the damaged spot in the middle of the sample. (c)Plot of the in-situ SHG of PMMA/DR1 with an ambient air environment and a maximum smoothed SHG value of .9 (d) A photograph of the PMMA/DR1 the sample in (c). Note that in addition to the damaged spot in the middle of the sample, there is a larger diamter hazy region which was damaged during the poling in ambient air.

to determine the T_g of a material is called differential scanning calorimetry (DSC). Unfortunately DSC didn't work well with s-BPVE due to the strong ionic chemistry of the polymer.

In-situ monitoring of the SHG signal for s-BPVE was a great option since the SHG signal would be present as the temperature approached the T_g of the polymer. Then it could be determined what the optimal poling temperature for s-BPVE was.

An in-situ SHG poling process was performed with a sample that was coated with 50% wt./wt. DR1 with s-BPVE as the host polymer. It was estimated that the T_g of the polymer was around 140 C, so the temperature was set to 140 C for this

particular experiment. Other experiments used poling temperatures of 160 C with similar results.

In Figure 3.15 the SHG signal remains very weak throughout the entire poling process. Compared to the DR1/PMMA samples previously mentioned the maximum SHG signal for s-BPVE was almost twenty times less. Even though the DR1/PMMA samples were 20% wt./wt. they still exhibited a larger SHG.

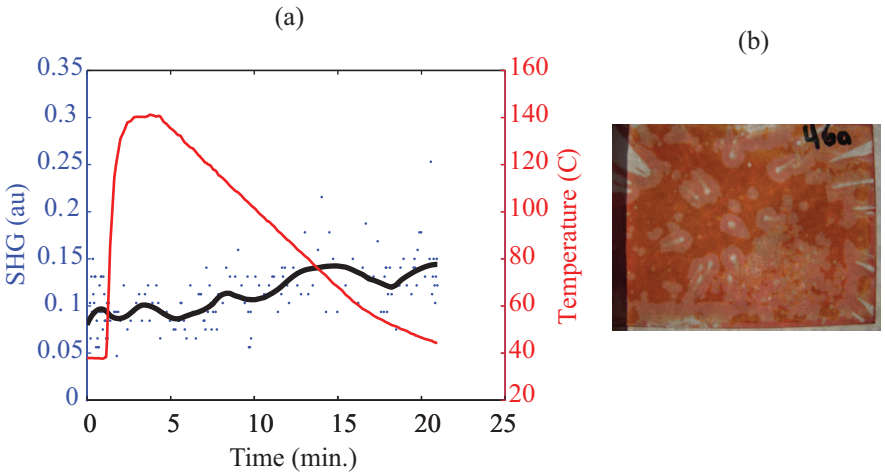

Figure 3.15: (a) In-situ SHG plot of DR1/s-BPVE with a DR1 loading level of 50% wt./wt. (b) A photograph of the s-BPVE sample that was tested. Notice that there are areas where the polymer didn't wet to the surface of the slide.

Phase matching can be eliminated as a cause of the lower SHG due to the fact that both the s-BPVE and the PMMA host polymer films were close to the same thickness. The index of refraction of both materials is also on the same order. Therefore, it is unlikely that the reasons for the lower SHG signal is phase matching.

Chromophore agglomeration is also not likely to be the cause of the lower SHG, since a poor film quality is indicative of agglomeration and can be seen with simple optical microscopy. While the film quality was not uniform over the whole sample due to wetting problems, the localized film quality of the DR1/s-BPVE sample in Figure 3.15 was good.

After several other experiments it was determined that the reason for the low SHG even for highly doped s-BPVE was that the polymer itself is designed to conduct protons. During the corona poling process it is the building up of charges on the surface of a polymer that create the electric field which induced the oriental ordering of the chromophores. If the polymer itself conducts those charges, almost no field will be held across the polymer.

The determination that s-BPVE does not make a good host polymer was obtained in part due to a good in-situ SHG test that allowed greater information of the entire poling process to be obtained. Had in-situ SHG not been used in the poling process, the reason for no post-poling SHG would have been very difficult to determine. It would have involved many more experiments and much more time just to determine that s-BPVE was not a good candidate as a host in a guest-host EO polymer configuration.

3.3.6 In-Situ SHG of AJL8/APC

Research into fabricating electric field sensors based on AJL8/APC as the EO polymer was commenced with the University of Washington. Previous to the collaboration with UW, PMMA was the only host polymer for which good results had been obtained. AJL8/APC offered several advantages over DR1/PMMA. Therefore it was important that we be able to transfer our corona poling technology to the poling of a new polymer. Though AJL8/APC had already been shown to be a good EO polymer [33], it had not yet been used as part of a corona poled hybrid fiber core.

In-situ SHG of AL8/APC was determined to be a good technique whereby we could confirm successful poling and identify the optimal poling temperature. Researchers at UW had already given us an optimal temperature range of between 135 to 145 C as a starting place.

Figure 3.16 shows the SHG obtained from an AJL8/APC sample during poling. The maximum SHG level is higher than for the highest DR1/PMMA sample poled, but not as high as expected since the r33 of AJL8 is around 33 pm/V, and DR1 is only around 4 pm/V.

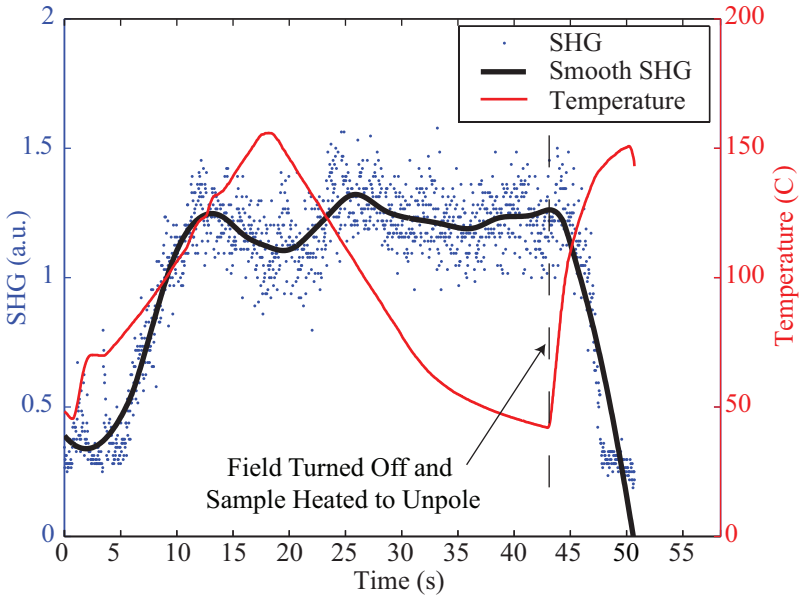

Figure 3.16: In-situ SHG of AJL8/APC polymer. The sample was poled, and then unpoled.

The main point of this experiment was to determine if AJL8/APC was poling or not, and at what temperature, so the relative level of SHG were less important. Notice in Figure 3.16 how the temperature range is much higher than is require for PMMA. The reason for that temperature increase is that APC has a higher T_g than PMMA, which is what makes APC a more temporally stable EO polymer host.

3.4 Conclusions

In-situ SHG was used as a tool to determine whether a sample was poled or not, and was useful in optimizing the poling recipe for several different EO polymers. It also helped determine that s-BPVE is not a good EO polymer. AJL/APC was poled in the in-situ SHG setup and information about its poling recipe was thus obtained.

In future EO polymer research, the in-situ monitoring setup is an indispensable tool in verifying and determining poling recipes. At times when no other EO results are working, in-situ SHG can help to eliminate some of the problems since it is another

way to determine the non-linearity of an EO polymer, besides blindly trying to test devices until one works.

Chapter 4

Design of Hybrid Polymer D-fiber Waveguides

As in any research effort whose purpose it is to fabricate devices, it is desirable to have a good understanding of the theory behind the device operation. While it is possible to determine the optimal device design by the brute force of experimental experience, an accurate understanding of the physics informs and complements the knowledge gained by experiment alone.

Work presented in [46] was not reproducible when the work for this dissertation began. Low loss high confinement DR1/PMMA sensors were finally produced by varying the fabrication parameters, reducing the variability between samples, and finally arriving at the proper recipe over a period of over two years time. At that time it was a mystery as to why these particular sensors were low loss. The purpose of this chapter is apply theory to the design of a hybrid D-fiber waveguides, so that the formation of a hybrid waveguide with a variety of materials, and fiber dimensions is possible.

Based on the theoretical understanding outlined in this chapter, various low loss sensors have been produced with losses around 1 dB and a confinement of around 7% for an AJL8/APC hybrid D-fiber waveguide. The entire design and fabrication process with AJL8/APC D-fiber hybrid waveguide sensors was less than three months, demonstrating the effectiveness of a good theorical model. These successful design principles take the mystery out of low loss D-fiber waveguide fabrication. The theory developed in this chapter also explains why the DR1/PMMA recipe that was experimentally obtained was low loss.

This chapter includes background related to electro-magnetic waves, and their propagation in symmetric and asymmetric dielectric slabs. Since this work relies

on optical fibers, theory related to optical fiber wave propagation, and D-fiber wave propagation is addressed. Since a full parametric analysis of hybrid waveguides is impractical due to their complexity, an asymmetric dielectric slab model matching the structure of a hybrid waveguide is used to gain intuition concerning each of the major impact factors in the design of a hybrid D-fiber waveguide. Along with the asymmetric slab results, the modeling results of actual fabricated fibers are considered and compared to the asymmetric slab. The chapter concludes with several designs for D-fiber hybrid waveguides with maximum optical power confined to the polymer and minimum insertion loss.

4.1 Background

4.1.1 Maxwell's Equations

Maxwell's equations were established by James Clerk Maxwell (1831-1879) in 1873, and since then have been found to govern a wide variety of electromagnetic (EM) phenomenon including the propagation of light in optical fibers. The equations themselves are the unification of laws discovered by Michael Faraday (1791-1867), Karl Friedrich Gauss (1777-1855), and Andre-Marie Ampere (1775-1836). Maxwell's equation can be written in various forms, and are included here in their differential form.

$$\text{Faraday's induction law:} \quad \nabla \times \bar{E}(\bar{r},t) = -\frac{\partial \bar{B}(\bar{r},t)}{\partial t}, \tag{4.1}$$

$$\text{Ampere-Maxwell law:} \quad \nabla \times \bar{H}(\bar{r},t) = \frac{\partial \bar{D}(\bar{r},t)}{\partial t} + \bar{J}(\bar{r},t), \tag{4.2}$$

$$\text{Gauss' law for electricity:} \quad \nabla \cdot \bar{D}(\bar{r},t) = \rho(\bar{r},t), \text{ and} \tag{4.3}$$

$$\text{Gauss' law for magnetism:} \quad \nabla \cdot \bar{B}(\bar{r},t) = 0, \tag{4.4}$$

where,

$$\begin{aligned}
\bar{E}(\bar{r},t) &= \text{electric field strength (volts/m)},\\
\bar{B}(\bar{r},t) &= \text{magnetic flux density (webers/m}^2\text{)},\\
\bar{H}(\bar{r},t) &= \text{magnetic field strength (amperes/m)},\\
\bar{D}(\bar{r},t) &= \text{electric displacement (coulombs/m}^2\text{)},\\
\bar{J}(\bar{r},t) &= \text{electric current density (amperes/m}^2\text{), and}\\
\bar{\rho}(\bar{r},t) &= \text{electric charge density (coulombs/m}^3\text{).}
\end{aligned}$$

Since the derivation of waves which satisfy Maxwell's equations is so fundamental to EM, the treatment leading to analytical solutions for various waveguides can be found in almost every book on EM. The books referenced for this chapter are [47, 48, 49, 50, 51, 52]. Even though the following derivation of the wave equation is common, the significance of Maxwell's contribution merits its repetition.

Equations 4.1 - 4.4 are a set of coupled, partial differential equations that have been proven to accurately predict EM phenomenon. Before an analytical solution to these equations can be obtained, various approximations and boundary conditions need to be applied to describe the situation of interest.

For example, this treatment focuses on EM waves which propagate in a waveguide. Therefore, assumptions and simplifications must be made in order to obtain an analytical solution for even a simple waveguide. The properties and dimensions of the waveguide, as well as the incident EM fields will determine the solution to Maxwell's equations.

4.1.2 The Wave Equation

First, it must be assumed that the medium through which the fields are propagating are both free of charges, and are non-conductive. It is also assumed that our fields are linear, and spatially independent. With those assumptions we can simplify

Equations 4.1 - 4.4 to

$$\nabla \times \bar{E}(\bar{r},t) = -\frac{\partial \bar{B}(\bar{r},t)}{\partial t}, \tag{4.5}$$

$$\nabla \times \bar{H}(\bar{r},t) = \frac{\partial \bar{D}(\bar{r},t)}{\partial t}, \tag{4.6}$$

$$\nabla \cdot \bar{D}(\bar{r},t) = 0, \text{ and} \tag{4.7}$$

$$\nabla \cdot \bar{B}(\bar{r},t) = 0. \tag{4.8}$$

The constitutive relations can be used to couple the equations so that they can be simplified further by relating $\bar{D}$ to $\bar{E}$ and $\bar{B}$ to $\bar{H}$, leaving only the $\bar{E}$ and $\bar{H}$ terms.

$$\bar{D}(\bar{r},t) = \bar{\epsilon}\bar{E}, \tag{4.9}$$

$$\bar{B}(\bar{r},t) = \bar{\mu}\bar{H}, \tag{4.10}$$

where $\bar{\epsilon}$ is the permittivity of the material and $\bar{\mu_0}$ is the permeability of free space.

$$\nabla \times \bar{E}(\bar{r},t) = -\mu_0 \frac{\partial \bar{H}(\bar{r},t)}{\partial t}, \tag{4.11}$$

$$\nabla \times \bar{H}(\bar{r},t) = \bar{\epsilon}\frac{\partial \bar{E}(\bar{r},t)}{\partial t}, \tag{4.12}$$

$$\nabla \cdot \bar{E}(\bar{r},t) = 0, \text{ and} \tag{4.13}$$

$$\nabla \cdot \bar{H}(\bar{r},t) = 0. \tag{4.14}$$

Now, using Equations 4.11 - 4.14 it is possible to obtain an equation which relates only one variable. It is most common to solve for $\bar{E}$ and then by symmetry derive $\bar{H}$. Solutions to equations like the wave equation are much more manageable when further simplifications can be made. One common simplification when solving for analytical solutions is to assume that the fields are monochromatic. That assumption along with the superposition principle allows us to solve a greater variety of problems that would be too difficult to solve otherwise.

First, take the curl of Equation 4.11, and commute the curl and partials derivative. Then substitute Equation 4.12 in for the curl of $\bar{H}$. Then combine partial derivatives.

$$\begin{aligned}
\nabla \times \left(\nabla \times \tilde{E}(\bar{r})\right) &= \nabla \times \left(-\mu_0 \frac{\partial \tilde{H}(\bar{r})}{\partial t}\right), \\
&= \nabla \times \left((-\mu_0 \frac{\partial \tilde{H}(\bar{r})}{\partial t}\right), \\
&= -\mu_0 \frac{\partial \left(\nabla \times \tilde{H}(\bar{r})\right)}{\partial t}, \\
&= -\mu_0 \frac{\partial \left(\bar{\epsilon} \frac{\partial \tilde{E}(\bar{r})}{\partial t}\right)}{\partial t}, \text{ and} \\
\nabla \times \left(\nabla \times \bar{E}(\bar{r})\right) &= -\mu_0 \bar{\epsilon} \frac{\partial^2 \tilde{E}(\bar{r})}{\partial t^2}. \qquad (4.15)
\end{aligned}$$

Now apply the vector identity $\nabla \times \left(\nabla \times \bar{A}\right) = \nabla \left(\nabla \cdot \bar{A}\right) - \nabla^2 \bar{A}$ to the left hand side of Equation 4.15.

$$\nabla \times \left(\nabla \times \tilde{E}(\bar{r})\right) = \nabla \left(\nabla \cdot \tilde{E}(\bar{r})\right) - \nabla^2 \tilde{E}(\bar{r}). \qquad (4.16)$$

The first term on the right hand side of Equation 4.16 can be eliminated by substituting in Equation 4.13 leaving Equation 4.17.

$$\nabla \times \left(\nabla \times \tilde{E}(\bar{r}, t)\right) = -\nabla^2 \tilde{E}(\bar{r}, t). \qquad (4.17)$$

Equation 4.17 is then substituted back into Equation 4.15 and results in the following equation,

$$-\nabla^2 \tilde{E}(\bar{r}) = -\mu_0 \bar{\epsilon} \frac{\partial^2 \tilde{E}(\bar{r})}{\partial t^2}, \qquad (4.18)$$

which is referred to as the wave equation or the Helmholz equation. The wave equation is often written as

$$\nabla^2 \tilde{E}(\bar{r}) - \mu_0 \bar{\epsilon} \frac{\partial^2 \tilde{E}(\bar{r})}{\partial t^2} = 0. \qquad (4.19)$$

This can be further simplified by applied the derivatives for time harmonic fields,

$$\nabla^2 \tilde{E}(\bar{r}) + \omega^2 \mu_0 \bar{\epsilon} \tilde{E}(\bar{r}) = 0. \tag{4.20}$$

The wave equation is a fairly common type of elliptical partial differential equation. One of the main characteristics of elliptical PDE's is that their solutions propagate. That is one of the reasons Maxwell's equations are so elegant, because their solutions match exactly what had been observed experimentally. Because these propagating solutions were so well known in the differential equation community, many solutions had already been obtained by the time that Maxwell's equation were found to describe the propagation of EM fields.

We can also assume that the equation is separable, or that each independent variable can be described separately. Thus we can assume that solutions to the wave equation are of the form

$$\tilde{E}(\bar{r}) = \tilde{E}(x)\tilde{E}(y)\tilde{E}(z). \tag{4.21}$$

4.1.3 Single Mode Slab Waveguides

An infinite number of solutions of the form (4.21) can be obtained from Equation 4.19. Real world problems include initial conditions as well as boundary conditions which restrict the solutions. The obtained solutions describe the possible EM waves that can exist in that particular system. The term *mode* is often used to describe a possible solution to the wave equation based on boundary conditions. The prescribed initial conditions would then indicate which of the possible modes actually exist in the waveguide.

A term *single mode* waveguide refers to the kind of system where, independent of the initial conditions, only up to one mode can exist in the waveguide. Obviously not all systems operate in single mode, therefore it is necessary to design a waveguide for single-mode operation. The simplest type of optical waveguide, which can offer insight into the propagation of light in an optical fiber, is the dielectric slab waveguide.

A dielectric slab waveguide is simply a slab of dielectric material surrounded by media of a lower refractive index.

As was previously mentioned, boundary conditions are necessary to define the system and thus determine how the fields will propagate. It is assumed that no charges are present at the surface between the boundaries. In the case of a dielectric slab both the normal and tangential boundary conditions,

$$\bar{E}_{1t} = \bar{E}_{2t}, \text{ and} \tag{4.22}$$

$$\epsilon_1 \bar{E}_{1n} = \epsilon_2 \bar{E}_{2n}, \tag{4.23}$$

must be considered.

Exact solutions to the wave equation can be made with these boundary conditions, if the permittivity of the material, the wavelength of light, and the dimensions of the waveguide are known.

Figure 4.1 illustrates, where $n1 > n2 > n3$, and the guided mode is $\hat{y}$ polarized, making it a transverse electric or TE wave.

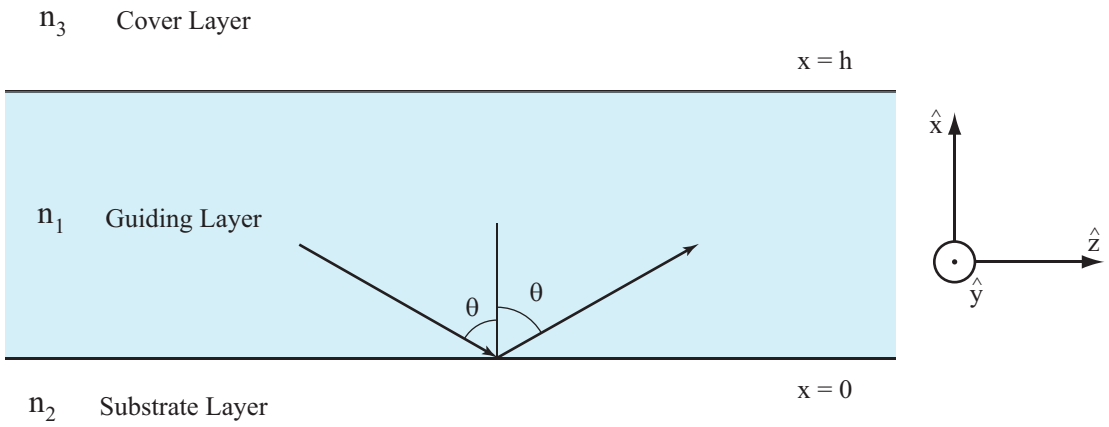

Figure 4.1: Illustration of a dielectric slab waveguide

The scalar wave equation for each layer is thus,

$$\nabla^2 E_{yi}(x,z) - n_i^2 k_0^2 E_{yi}(x,z) = 0, (i = 1,2,3), \tag{4.24}$$

and the solutions are of the form,

$$E_{yi}(x,z) = E_x exp(-j\beta z), (i = 1,2,3), \tag{4.25}$$

where i indicates the layer number, and β is the propagation constant. Combining Equations 4.24 and 4.25, we obtain,

$$\frac{d^2 E_i}{dx^2} + \left[n_i^2 k_0^2 - \beta^2\right] E_i = 0. \tag{4.26}$$

Now, based on what we know about our structure and what we expect the electric fields to be like in each layer we assume a solution for each layer. First, we know that the electric field in layer 1 will be guiding. We know that they electric field in layers 2 and 3 will be evanescent, or decaying. Therefore, we use the following solutions as trials

$$E_1 = E\ cos\kappa x - \phi, \tag{4.27}$$

$$E_2 = E'\ exp(\gamma x), \text{and} \tag{4.28}$$

$$E_3 = E''\ exp\left[-\delta(\gamma x)\right], \tag{4.29}$$

where ϕ is the relative phase, and the constants κ, γ, and δ are defined as

$$\kappa = \sqrt{(n_1^2 k_0^2 - \beta)}, \tag{4.30}$$

$$\gamma = \sqrt{(\beta - n_2^2 k_0^2)}, \text{and} \tag{4.31}$$

$$\delta = \sqrt{(\beta - n_3^2 k_0^2)}. \tag{4.32}$$

We further constrain these solutions by applying the boundary condition that both the fields and their first derivatives must be continuous across the boundaries between

layers 1 and 2 and layers 1 and 3. First we take the boundary at $x = 0$, between layer 1 and layer 2, where we find that,

$$E' = E\ cos\left(\phi\right), \tag{4.33}$$

and matching the field derivatives gives,

$$\gamma E' = -\kappa E\ sin\left(-\phi\right). \tag{4.34}$$

By dividing Equation 4.34 by Equation 4.33, the field amplitudes cancel and we obtain

$$tan\ \phi = \frac{\gamma}{\kappa},\ \text{or}\ \phi = tan^{-1}\ \left(\frac{\gamma}{\kappa}\right). \tag{4.35}$$

Now for the boundary between Slab 1 and Slab 3 at $x = h$.

$$E'' = E\ cos\left(\kappa h - \phi\right). \tag{4.36}$$

$$\delta E'' = -\kappa E\ sin\left(\kappa h - \phi\right). \tag{4.37}$$

Dividing Equation 4.37 by Equation 4.36 the following relation is obtained

$$tan\ \left(\kappa h - \phi\right) = \frac{\delta}{\kappa}. \tag{4.38}$$

Valid solutions, therefore, must satisfy Equations 4.33-4.38, but most importantly the trigonometric relations in Equations 4.35 and 4.38. Subsequently, each field amplitude can be determine by solving Equations 4.36 and 4.33.

The trigonometric identity,

$$tan\ \left(A - B\right) = \frac{\left(tan\ A - tan\ B\right)}{\left(1 + tan\ A\ tan\ B\right)}, \tag{4.39}$$

allows us to simplify the two main equations. First we convert the LHS of Equation 4.38 to

$$tan\ (\kappa h - \phi) = \frac{[tan\ \kappa h - tan\ \phi]}{[1 + tan\ \kappa h\ tan\ \phi]}. \tag{4.40}$$

Thus, Equation 4.38 becomes

$$[tan\ (\kappa h)\ -\ tan\ \phi][1 + tan\ (\kappa h)\ tan\ \phi] = \frac{\delta}{\kappa}. \tag{4.41}$$

Then substituting Equation 4.35 into Equation 4.41, we obtain,

$$[tan\ (\kappa h) - \frac{\gamma}{\kappa}][1 + tan\ (\kappa h)\ \frac{\gamma}{\kappa}] = \frac{\delta}{\kappa}, \tag{4.42}$$

which becomes,

$$tan\ (\kappa h) = \frac{\kappa\,[\gamma + \delta]}{[\kappa^2 - \gamma\delta]}. \tag{4.43}$$

Equation 4.43 can now be used to solve for the supported modes of this waveguide. Sometimes equations like this are called eigenvalue equations, in this case β is the eigenvalue, because κ, γ, and δ are all dependent upon it. Each value of β that satisfies this equation will represent a supported mode. Each value of β is related to what it called the effective index of the mode by the following relation,

$$\beta_\nu = \frac{2\pi n_{eff\nu}}{\lambda_0}, \tag{4.44}$$

where ν is the mode number, $n_{eff\nu}$ is the effective index of the mode, and λ_0 is the free space wavelength. The effective index is the bulk index of refraction of a material which would give the same propagation constant and phase velocity as the waveguide it describes.

With an understanding of what β is, and with an eigenvalue equation that can be solved for it, we can proceed. This particular eigenvalue equation is transcendental, meaning that we cannot solve for β analytically. However, there are various numerical methods available to us for solving equations of this type. One method that was used before computers were readily available was to plot each side of the equation with β

as the independent variable. Figure 4.2 plots the left hand side of the equation and the right hand side of the equation for a range of values of β. Table 4.1.3 records the physical parameters of the problem which is solved.

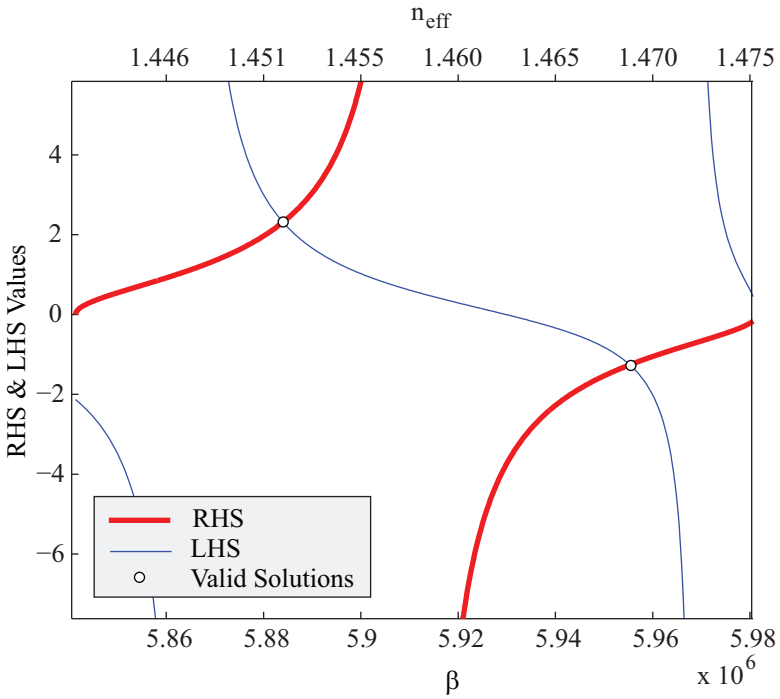

Figure 4.2: Plot of the solutions for the symmetric and anti-symmetric modes of a dielectric slab waveguide

Table 4.1: The Physical Parameters Used for the Calculation in Figure 4.2

Physical Parameter	Value
λ	1550 nm
n1	1.476
n2	1.441
n3	1.441
Waveguide Thickness	4 μm

There are two valid solutions to the eigenvalue equation (4.43) with the physical parameters in Table 4.1.3. The zero order solution has an $n_{eff} = 1.469$ and is a symmetric solution. The first order solution is antisymmetric with an $n_{eff} = 1.452$. Both of these solution are between the indices of the guiding regions and the cladding region of this waveguide. Figure 4.3 illustrates the shape of the zero and first order modes for a dielectric slab. There is a cosinusoidal field inside the waveguide and exponentially decay fields outside of the guiding region. The exponentially decaying portion of the mode is often called the evanescent field.

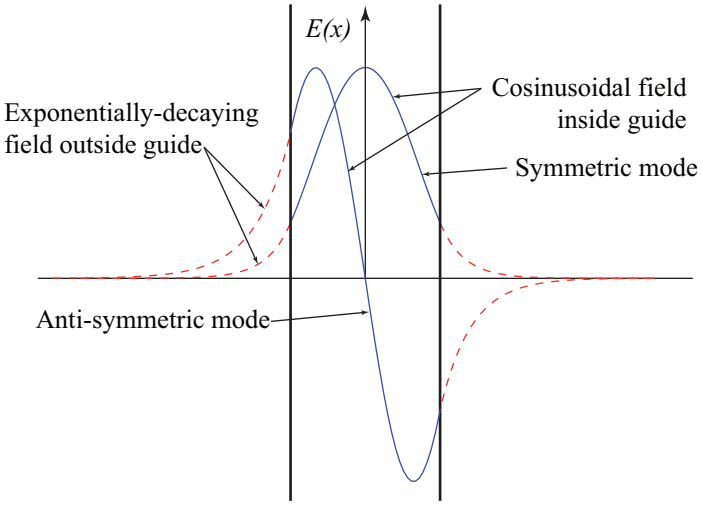

Figure 4.3: Illustration of the symmetric and anti-symmetric modes fields of a dielectric slab waveguide.

One powerful tool in designing single mode waveguides is to plot the effective index of the mode verses what is often called normalized frequency, or the V-parameter. The physical parameters which describe the waveguide with normalized frequency is given by

$$V = k_0 a \left(n_1^2 - n_2^2\right)^{1/2} = \frac{2\pi}{\lambda}\ a\ NA, \tag{4.45}$$

where k_0 is the wavenumber, λ is the free-space wavelength, a is the thickness of the slab, and $NA = \sqrt{(n_1^2 - n_2^2)}$ is the numerical aperture. A plot can be generated with

the V parameter which then indicates the thickness, and index of the slab that will support only one mode at a particular wavelength. Figure 4.4 plots n_{eff} of the mode for the slab waveguide described in Table 4.1.3 verses the V parameter.

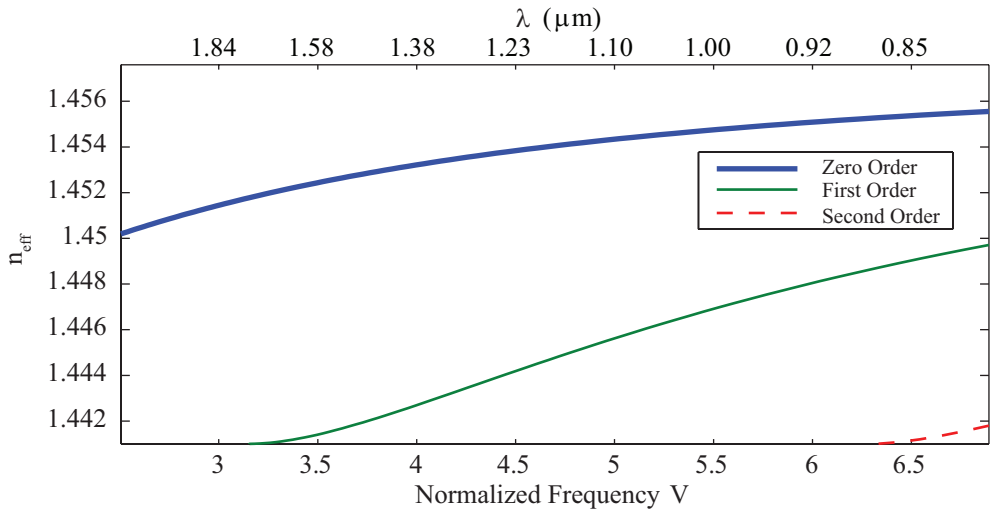

Figure 4.4: Plot of normalized frequency vs. effective index for a dielectric slab ($n_1 = 1.4756$, $n_2 = 1.441$, $n_3 = 1.441$, $h = 4e-6$ μm). A dashed line is used to mark the V-number which corresponds to a wavelength of 1550 nm. This waveguide supports two modes at a wavelength of 1550 nm.

4.1.4 Asymmetric Multi-Layer Dielectric Slab

The hybrid waveguide structure of interest in this chapter more closely resembles a multi-layer dielectric slab than a single layer symmetric one. The numerical method of solving for the guiding modes of the multilayer slab is slightly different than the symmetric slab and more information about the method used in this section can be obtained by referring to [53]

Figure 4.5 shows the multilayer slab structure under consideration. Air surrounds a layer of polymer which is deposited on the core layer on the top of the cladding layer. Table 4.1.4 records the parameters used in the multiple-layer slab calculation. As in the case for the symmetric dielectric slab the effective index for the asymmetric multiple-layer slab is modeled for a range of V parameters. Figure 4.6

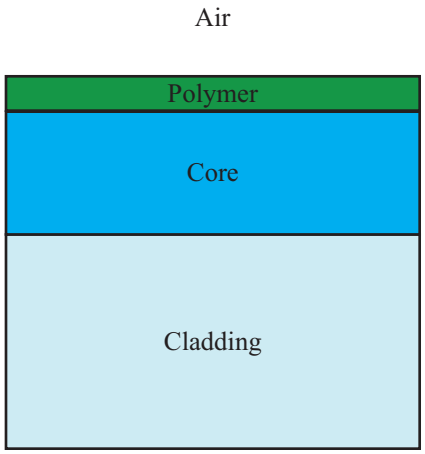

Figure 4.5: Illustration of the multiple slab structure used in this section

plots the results. Note that in the case of a symmetric slab, the fundamental mode never reaches cutoff, but in the asymmetric slab case, there is a hard cutoff.

Table 4.2: Multiple Layer Slab Modeling Parameters

Physical Parameter	Value
Core Thickness	2 μm
Polymer Thickness	.55 μm
Core Index	1.4756
Polymer Index	1.6
Cladding Index	1.441 μm

Another interesting observation is to see what happens to the mode shape in an asymmetric multi-layer waveguide when the wavelength is decreased. In Figure 4.7 there are three electric fields plotted for different wavelengths. As the wavelength decreases the confinement to the polymer layer increases. However, as Figure 4.6 shows, as the V parameter increases, or as wavelength decreases, the waveguide begins to support multiple modes. The asymmetric slab cutoff, single mode, and multi-mode regions are analogous to the same regions in the hybrid waveguide structure discussed later in the chapter.

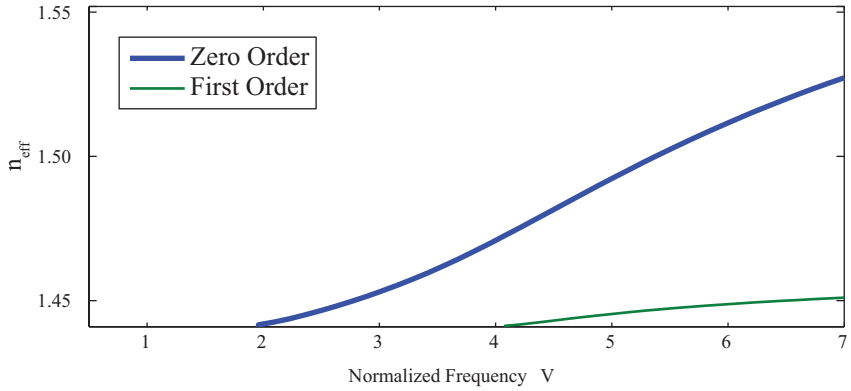

Figure 4.6: Plot of n_{eff} for a multiple layer slab as a function of the V parameter.

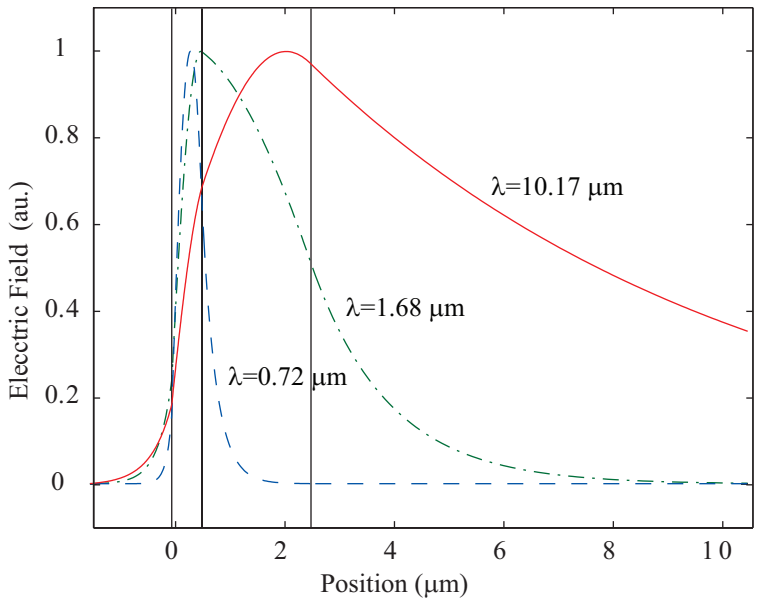

Figure 4.7: Diagram of how the mode shape changes as the wavelength is decreased in a multi-layer dielectric slab waveguide.

4.1.5 Optical Fiber Waveguides

Though the hybrid waveguide shares some common characteristics with asymmetric slabs, it an in-fiber device based on elliptical core optical fiber. Thus, it is instructive to consider the guiding characteristics of optical fiber. As in the case for dielectric slab waveguides, the optical fiber waveguide supports optical modes. However, the wave solutions for the optical fiber are more complex due to their cylindrical geometry. Figure 4.8 illustrates the geometry of an optical fiber. The core, or the light guiding region of the optical fiber, has a higher index of refraction than the cladding.

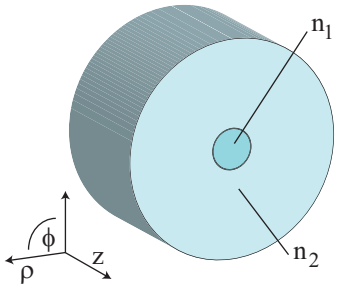

Figure 4.8: Illustration of the geometry of an optical fiber.

Theory/Derivation of Modes

Taking advantage of its cylindrical geometry, the wave equation for an optical fiber can be written as,

$$\frac{\partial^2 E_z}{\partial \rho^2} + \frac{1}{\rho}\frac{\partial E_z}{\partial \rho} + \frac{1}{\rho^2}\frac{\partial^2 E_z}{\partial \phi^2} + \frac{\partial^2 E_z}{\partial z^2} + n^2 k_0^2 E_z = 0, \tag{4.46}$$

where n is the index of refraction of the fiber, and is defined as follows,

$$n = \begin{cases} n1; & \rho \leq a, \\ n2; & \rho > a. \end{cases} \tag{4.47}$$

Equation 4.46 relates only the axial component, E_z, of the electric field. Equations for each of the five other components can be written, but it is customary to obtain E_ρ,H_ρ,E_ϕ, and H_ϕ in terms of E_z and H_z. To solve for E_z

The solution to Equation 4.46 is obtained through the separation of variables approach [48], and with some simplifications can be written as,

$$E_z = \begin{cases} AJ_m(p\rho)exp(im\phi)exp(i\beta z); & \rho \leq a, \\ CK_m(q\rho)exp(im\phi)exp(i\beta z); & \rho > a, \end{cases} \tag{4.48}$$

where the J_m and K_m functions are Bessel functions, and the p's and q's are defined by,

$$p^2 = n_1^2 k_0^2 - \beta^2, \text{ and} \tag{4.49}$$

$$q^2 = \beta^2 - n_2^2 k_0^2. \tag{4.50}$$

The magnetic field can be solved in a similar way and the result is identical, except for the coefficients.

$$H_z = \begin{cases} BJ_m(p\rho)exp(im\phi)exp(i\beta z); & \rho \leq a, \\ DK_m(q\rho)exp(im\phi)exp(i\beta z); & \rho > a. \end{cases} \tag{4.51}$$

By solving for the other four components, applying boundary conditions, and performing some non-trivial algebra, the following result is obtained,

$$\left[\frac{J_m^{'}(pa)}{pJ_m(pa)} + \frac{K_m^{'}(qa)}{qK_m(qa)}\right]\left[\frac{J_m^{'}(pa)}{pJ_m(pa)} + \frac{n_2^2}{n_1^2}\frac{K_m^{'}(qa)}{qK_m(qa)}\right] \tag{4.52}$$

$$= \frac{m^2}{a^2}\left(\frac{1}{p^2} + \frac{1}{q^2}\right)\left(\frac{1}{p^2} + \frac{n_2^2}{n_1^2}\frac{1}{q^2}\right). \tag{4.53}$$

Numerical Solutions for Optical Fiber Waveguide

This equation can then be solved numerically as was the case with the dielectric slab waveguide. One useful equation in solving for solutions is the relationship between a Bessel function and its derivative [54]. Where F_ν is a Bessel function of an

integer order, the relation is as follows,

$$F'_{\nu}(z) = -F_{\nu+1}(z) + \frac{\nu}{z}F_{\nu}(z). \tag{4.54}$$

Solutions for various wavelengths and various Bessel function orders result in a V vs. b plot which describes the guiding characteristics of an optical fiber. Figure 4.9 shows the v vs. b plot for a standard optical fiber with the parameters included in Table 4.1.5. This result matches well with the results indicated in [48]. Figure 4.9 is plotted with the normalized propagation constant because that is the standard in the literature. The effective index is more useful when considering the design of a hybrid waveguide, and so in all other cases the effective index is used in this chapter. The normalized propagation constant is directly related to n_{eff} by

$$n_{eff} = n_{cladding} + b(n_{core} - n_{cladding}). \tag{4.55}$$

Table 4.3: The Physical Parameters Used for the Calculation in Figure 4.9

Physical Parameter	Value
λ	1550 nm
n1	1.4509
n2	1.444
Core Diameter	4.11 μm

Figure 4.9 contains a substantial amount of information about the way that light travels in a waveguide. Each line represents a different possible mode. The slope of each line is also related to waveguide dispersion of the fiber. This plot also contains information about the single mode operating point for the fiber. The HE_{11} term in Figure 4.9 is the fundamental mode. The first mode to be supported after the fundamental mode is the TE_{01} mode. This mode has a cutoff at $V = 2.405$. when

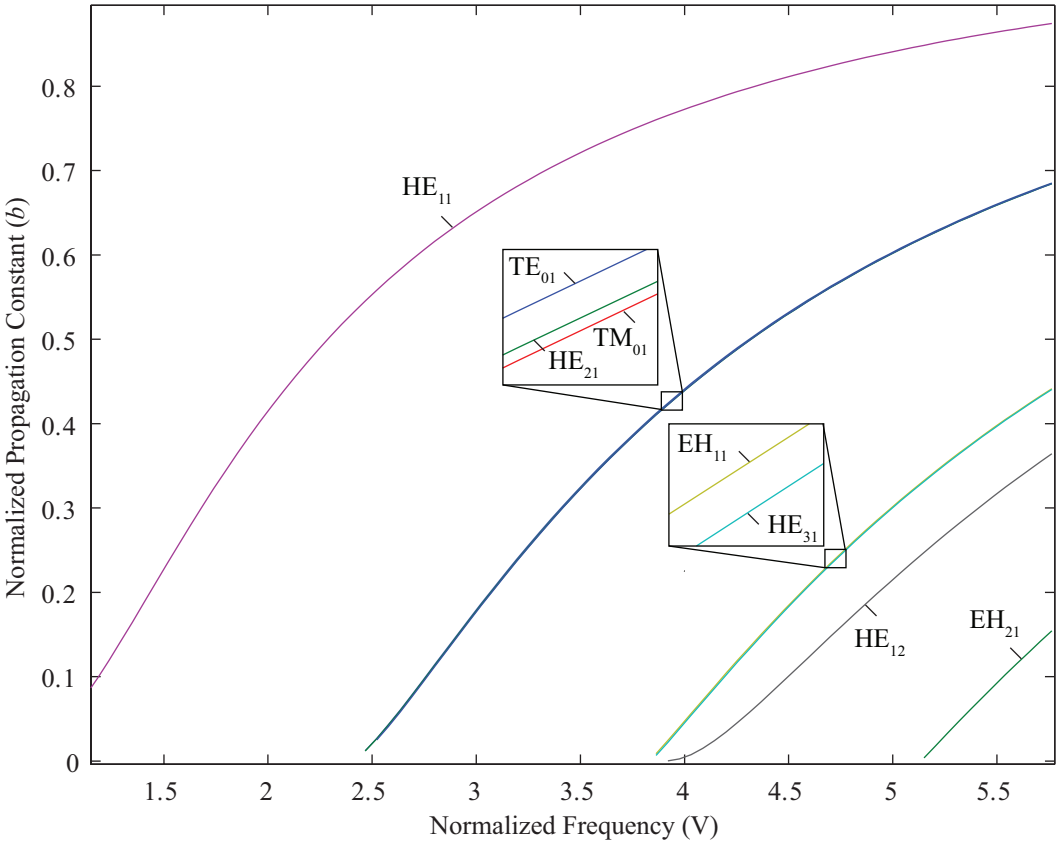

Figure 4.9: Plot of the normalized propagation constant vs. the Normalized frequency for an optical fiber whose physical parameters are included in Table 4.1.5.

designing a fiber to be single mode at a particular wavelength Equation 4.45 must be solved so that the $V \leq 2.405$.

4.1.6 D-fiber Elliptical Waveguides

The standard elliptical core of a D-fiber waveguide supports two orthogonal polarization states due to geometrical birefringence. In this analysis a waveguide which supports one mode in each polarization state will be referred to as single mode.

As with all types of fiber waveguides the supported modes in the waveguide can be analyzed with an V vs. n_{eff} plot as in Figure 4.11. Figure 4.10 was generated using BeamProp to calculate the effective index of the mode for increasing wavelengths, the V parameter was then calculated from the physical parameters of the fiber and the wavelength used.

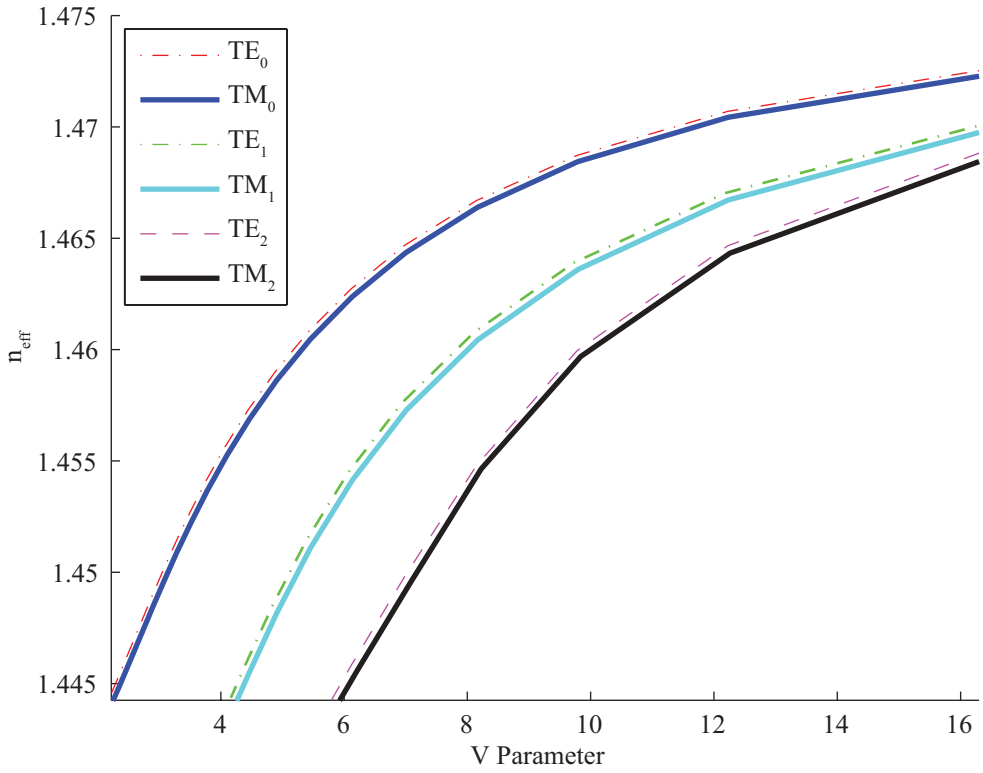

Figure 4.10: Plot of n_{eff} vs. V for an unetched D-fiber

Unfortunately, the V parameter in the case of D-fiber waveguides is not as useful as it is with other circular core fiber for three reasons. First the core does not have a constant diameter due to its elliptically shaped core. Second, for the purposes of this research, the core and cladding physical parameters are fixed. Third, we can no longer assume a design where the cutoff is at $V = 2.405$ for the elliptical core D-fiber waveguide. For these reason it is much more useful to relate the guiding characteristics of a mode with the wavelength, rather than the V parameter. As the waveguide core is partially filled with polymer, the guiding characteristics are even more complicated. Figure 4.11 show a plot of n_{eff} vs. wavelength for the same waveguide as in Figure 4.10. The plots are powerful in conveying information about which modes are supported at a particular wavelength, as well as the confinement of the mode to the core.

Figure 4.11 was generated using BeamProp to model the effective index of the mode for both TE and TM modes for a range of wavelengths. An SEM image was

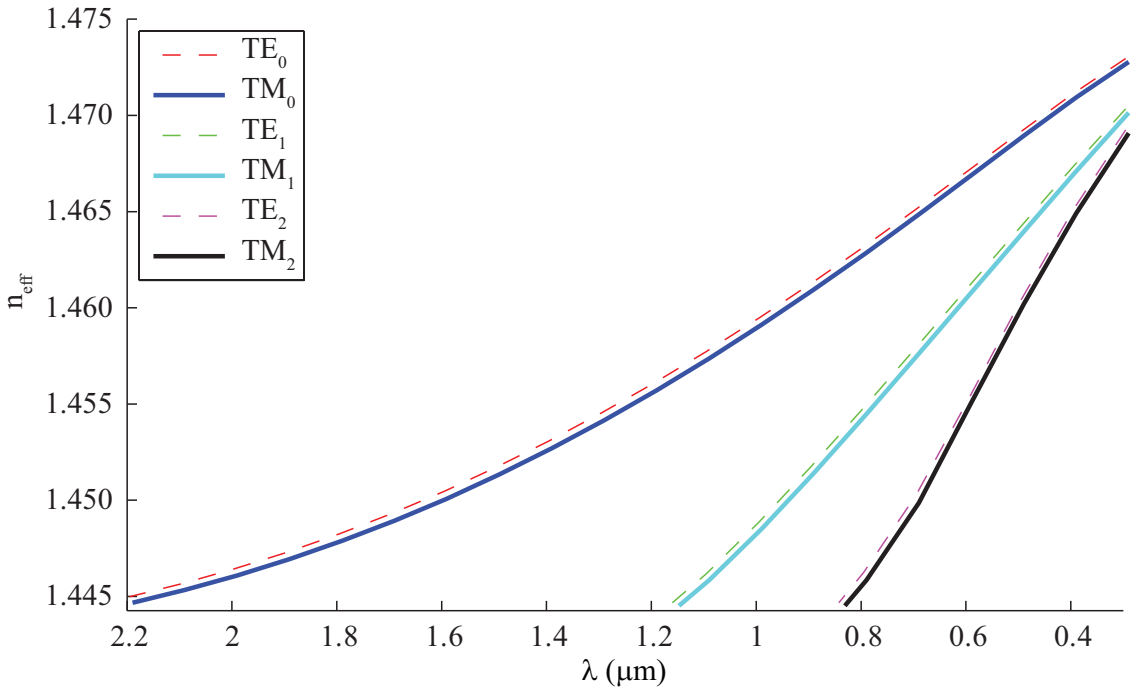

Figure 4.11: Plot of n_{eff} vs. λ for an unetched D-fiber

taken of an unetched D-fiber, and then an index profile was generated by mapping out the cladding, core, and vapor spot in Adobe Illustrator. Each component was imported into MATLAB and assigned the proper index of refraction value. The full index profile was then exported and prepared for BeamProp. A BeamProp mode finder function was used to calculate the effective index of each mode at a given wavelength. The effective indicies were then plotted vs wavelength with a reversed wavelength axis to match conventional V vs. b plots. The first and second order modes are cutoff at 1.2 um and .8 um respectively. A mode is cutoff when the n_{eff} at that wavelength is lower than the cladding of the fiber (n=1.444).

4.1.7 Hybrid Polymer D-fiber Waveguides

Like the original elliptical core of the D-fiber, the hybrid core of the electric field sensor also supports two eigenmodes with the dominant electric field component in the $\hat{y}$ and the $\hat{z}$ directions as pictured in Figure 4.12. Each of these eigenmodes is characterized by an effective index of refraction (N_y and N_z), from which the group

velocity of the mode can be derived. Since the polymer is electro-optic, its bulk indices of refraction, n_y and n_z, change with applied electric field, thus changing the effective indices of refraction of an eigenmode.

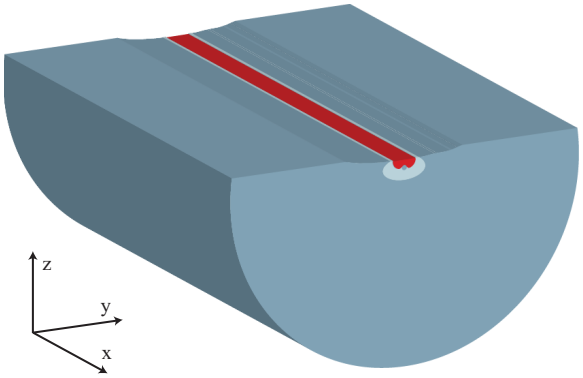

Figure 4.12: The hybrid waveguide supports two eigenmodes with the dominant electric field component in the $\hat{y}$ and the $\hat{z}$ directions.

Section 2.2 includes a more detailed description of the influence of an electric field on the anisotropic refractive index of an electro-optic polymer. The change in the effective indices of refraction (ΔN_y and ΔN_z) of the modes when in the presence of an electric field are related to the index of refraction of the polymer as in the following equations

$$\Delta N_y = -\frac{1}{2} n_o^3 r_{13} E_z \Gamma, \tag{4.56}$$

and

$$\Delta N_z = -\frac{1}{2} n_o^3 r_{33} E_z \Gamma, \tag{4.57}$$

where Γ is a fitting factor that relates the bulk indices of refraction of the polymer to the effective index of a mode. The factors relate the amount of light confined to the polymer portion of the hybrid waveguide, and must be determined numerically for complex structures like core-replaced fibers. The change in the effective index of refraction of the modes results in a change in the fiber birefringence as given by

$$\Delta B = \Delta N_y - \Delta N_z = \frac{1}{2} E_z n_o^3 \left(r_{33} - r_{13}\right) \Gamma, \tag{4.58}$$

where Γ is a fitting factor that relates the change in the bulk indices of refraction of the polymer to the change in the birefringence and depends on the amount of light confined to the polymer portion of the hybrid waveguide.

If equal power is launched into each of the eigenstates the resulting electric field is given by,

$$\vec{E} = E_0 \left[\hat{y} e^{j(wt - k_o(L_T N_{y,0} + L_H \Delta N_y) + \Phi)} + \hat{z} e^{j(wt - k_o(L_T N_{z,0} + L_H \Delta N_z) + \Phi)} \right], \tag{4.59}$$

where $k_o = 2\pi/\lambda$, λ is the free space wavelength, $N_{y,0}$ and $N_{z,0}$ are the effective indices of the waveguide eigenmodes without any applied electric field, L_T is the total length of the optical fiber, and L_H is the length of the hybrid core section. After the common phase terms between the two modes are removed the equation becomes

$$\vec{E} = E_0 \left[\hat{y} + \hat{z} \exp j \left(k_o L_H \left(\Delta N_y - \Delta N_z \right) + k_o L_T \left(N_{y,0} - N_{z,0} \right) \right) \right]. \tag{4.60}$$

Using Eq. 4.58 and substituting ϕ_o for the built in retardation, we obtain

$$\phi_o = k_o L_T \left(N_{y,0} - N_{z,0} \right), \tag{4.61}$$

and the electric field becomes

$$\vec{E} = E_0 \left[\hat{y} + \hat{z} \exp j \left(\phi_o + k_o \Delta B L_H \right) \right]. \tag{4.62}$$

The sensitivity of the device is thus determined by $r_{13} - r_{33}$ and the values of n_o and Γ. For a given polymer-chromophore combination, the value of n_o is constant and the values of r_{13} and r_{33} are determined by how effectively the polymer is poled as well as the intrinsic hyperpolarizability of the chromophore being used. With an effective procedure for poling in place, the Pockels coefficients are fairly constant. The sensitivity is then dependent upon Γ. The value of Γ can be increased by increasing the ratio of polymer to glass in the hybrid waveguide. However, the waveguide should be designed to maximize the modal power concentrated in the polymer, while

maintaining single mode operation and low loss coupling between the unetched and etched regions.

4.2 Design of Hybrid D-fiber Waveguide

The ultimate purpose of the hybrid D-fiber waveguide is to detect electric fields in the most efficient manner possible. There are two major factors which should be considered in this design.

First, the fiber should have the lowest insertion loss possible. Consider the electric field sensor connected in the polarizer analyzer configuration. First assume that the optical power reaching the photodector is maximized at 1 μW when no electric field is present. Now, assume that the electric field which is applied is sufficient to cause a full π phase shift in the sensor, resulting in almost no optical power reaching the optical power detector. The sensor had a swing of close to 100% of its initial optical power. If a sensor with an optical power output of 1 mW with the same electric field sensitivity were tested with the same configuration, the swing would be 1000 times 100% of the first sensor, thus increasing the sensitivity by 1000x. Thus, device sensitivity scales linearly with output power, and smaller total signal amplitudes result in modulation signal which are also smaller.

The second major factor in device sensitivity, as explained in Section 8.1, is the E_π of a sensor. The factors that contribute to minimize the E_π are the length of the sensing region, the electro-optic coefficients, and the amount of optical power confined to the polymer.

The length can be adjusted by simply etching and depositing polymer in a longer region. However, the fabrication becomes impractical if the devices are too long. In this dissertation the device regions are 1.5 to 2 cm long.

The electro-optic coefficients are determined by the chromophore used in the EO polymer as well as the poling efficiency. Chapter 2 describes more about how to obtain high electro-optic coefficient values with D-fiber poling.

The factor of greatest concern in this chapter is the confinement of optical power to the electro-optic polymer, and is referred to as confinement in this chapter.

Along with trying to maximize confinement, waveguide loss both in the device and transition regions will be considered. Thus the design aims to minimize loss and maximize polymer confinement. Devices which are currently practical to fabricate will be considered. Some device designs which are not currently practical, but which are possible, will also be considered.

An etched D-fiber with polymer deposited in the core can be thought of as three separate waveguides as illustrated in Figure 4.13. The first section is the input waveguide which provides optical power through which sensing can occur. Since the input waveguide is an elliptical core fiber waveguide operating in single mode at 1550 nm, it will only provide or support one mode in each polarization state. The second region of the fiber device is the etched portion where polymer has been deposited in contact with the fiber core, forming a new hybrid polymer glass core waveguide structure. This is the portion of the device where sensing actually occurs. The output section is identical to the input section. Workable hybrid D-fiber waveguides must operate in single mode in the device section in order to best match modes with the input and output sections.

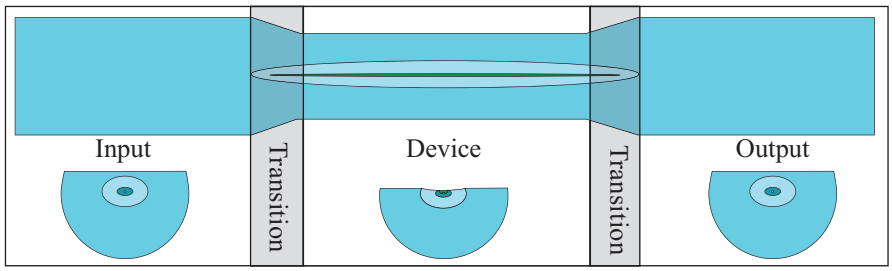

Figure 4.13: Illustration of various Device Regions in a D-fiber Electric field sensor

It should be noted that between the input and device regions of the hybrid core device, there is a region where the fiber passes from the original unetched waveguide to the device waveguide. This conversion between the two is referred to as the transition region of the fiber waveguide.

4.2.1 Confinement and Loss

Confinement of optical power to the polymer portion of a hybrid waveguide results in a stronger response to a given electric field. Generally speaking, in these hybrid waveguide devices, higher optical power confined to the polymer region results in higher insertion loss. Thus, it is necessary to balance these two factors in order to maximize overall device sensitivity.

Both confinement and loss are influenced by several interdependent factors. Confinement depends on the etch depth, the polymer thickness, and the index of refraction of a polymer. Loss depends upon how closely the mode from the unetched portion matches the supported modes of the devices region.

The hybrid waveguide must also operate in the single mode regime, otherwise all of the power that couples into the higher order mode will be lost when it is coupled back into the output section of the waveguide. The transition between input to the device region, and then from the device region to the output also influences the insertion loss of a hybrid waveguide device.

4.2.2 Design Variables

The purpose of this chapter is to design highly sensitive low loss hybrid polymer fiber waveguides. In the design and fabrication of D-fiber waveguides there are parameters which are fixed, and parameters which can be adjusted to suit the design. The dimensions of the core of the D-fiber are fixed based on the fabrication process that occurs during the drawing of the fiber at KVH industries. Therefore, device designs are constrained to working within those dimensions. Another limiting parameter is the shape of the groove which is formed by the chemical etching process as a portion of the core is removed.

The parameters which can be changed in the design of a hybrid core device are the amount of the core which is etched away, and the thickness of the polymer in the core of the fiber, and the index of refraction of the polymer in the core. The etch depth and the polymer thickness can be adjusted in the fabrication process. The polymer index of refraction must be adjusted by a complex synthesis process that is

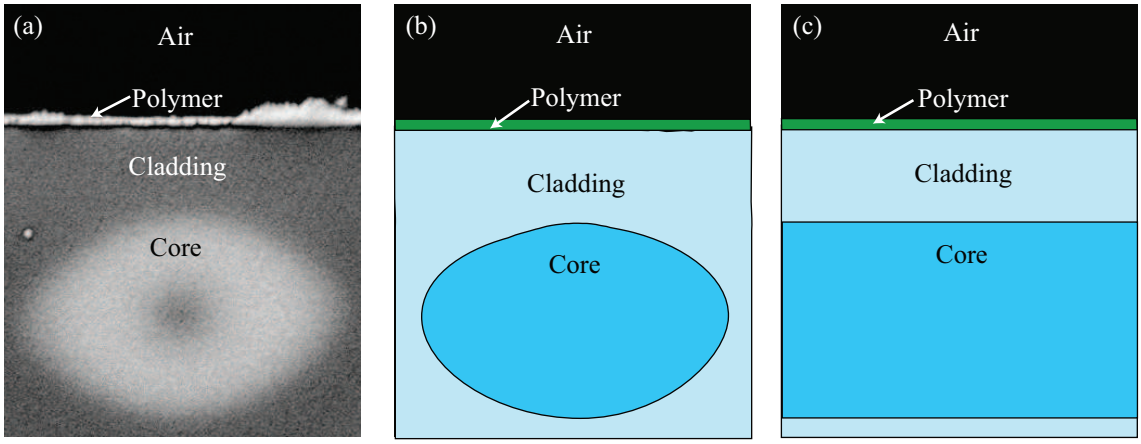

Figure 4.14: An illustration of how a (a) SEM cross-sectional image can be converted into a (b) index profile for modeling, and how that modeling can be simplified further into a (c) multilayer dielectric slab.

beyond the capabilities of this lab, but can be done by collaborators at the University of Washington.

In order to obtain the optimal design of a hybrid waveguide the waveguides guiding characterists for a variety of parameters must be obtained. However, the complex structure of the hybrid waveguide makes it impossible to analytically solve for guiding solutions. The modes must be solved numerically using a numerical modeling program like BeamProp or Fimmwave. Even with a powerful computer and an efficient tool for modeling the waveguide, the construction of an accurate model is time consuming. Fortunately, a multilayer dielectric slab can be used as a bridge toward understanding the trends that affect the hybrid waveguide. Figure 4.14 illustrates how one particular SEM cross-section can be converted into an accurate index profile structure, and then how that can be simplified further and represented by a dielectric slab.

As each design variable is considered, trends will be extrapolated from multiple layer slab mode calculations. The knowledge of principles gained by the modeling of a multilayer slab apply to the asymmetric hybrid waveguide structure. These principles will be highlighted in simulations that were performed based on fabricated hybrid waveguide structures.

4.2.3 Etch Depth

To understand the effect of etch depth on polymer confinement, first, let us consider a multilayer dielectric slab like the one shown in Figure 4.14c. The multi-layer slab will be modeled as if it were an etched fiber with a layer of polymer deposited on the surface. Figure 4.15 shows a filmstrip of how the slabs are "etched" until the "core" of the multilayer slab is completely etched away leaving only a guiding polymer layer. Note how the electric field is gradually pulled up into the polymer layer as the etch depth increases, resulting in higher confinement as the fiber is etched deeper. Figure 4.16 plots the effective index of the fundamental and second order mode as a function of etch depth. The cladding in the model begins with a thickness of 4 μm and the core with a thickness of 2 μm. Note how there are two distinct regions of slope. In the first region the slope is increasing and the effective index also increases as the cladding layer is etched away. Then when the cladding is completely removed and the core begins to be etched, the effective index increases slightly and then decreases dramatically as the core becomes smaller and smaller. The first order mode is cutoff at just past an etch depth of 2 μm.

The first area of interest is the effect of the etch depth on the amount of power that is confined to the polymer. The confinement is calculated by summing the amount of optical power in the polymer region and dividing that by the total electric field in the modeling window. Figure 4.17 plots the optical power confinement as a function of etch depth in microns. As the cladding is removed the confinement increases with a very small increasing slope. Then once the core is breached, the power increases linearly until the core and polymer slab combination no longer strongly support the mode, and the mode becomes weakly guiding. At that point the confinement drops rapidly. The maximum confinement was 37.3% and was obtained from a combination of slabs with about half a micron of "core" material and half a micron of polymer. The next area of interest is the insertion loss of the slabs. One way to approximate loss is to perform an overlap integral with the power in an "unetched" waveguide with the combination of slabs that is of interest. In this case an overlap integral of the electric field when the slabs were "unetched" was overlapped

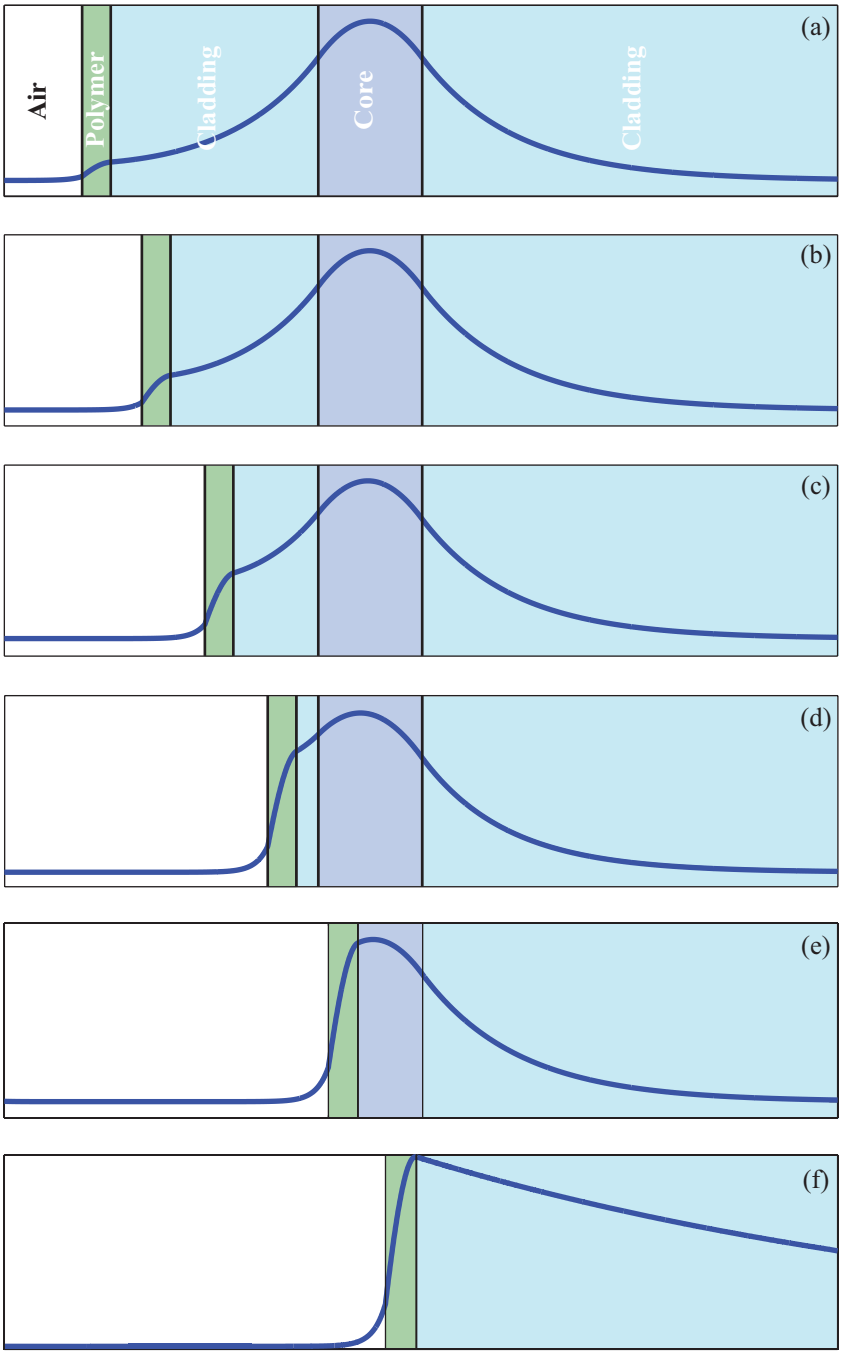

Figure 4.15: A series of illustrations of multiple slabs with of the electric field profile of the fundamental mode superimposed on the slab layers. The slabs start out by simulating a fiber which has a polymer layer, cladding and core layer. The cladding and core are "etched" away from (a) through (f).

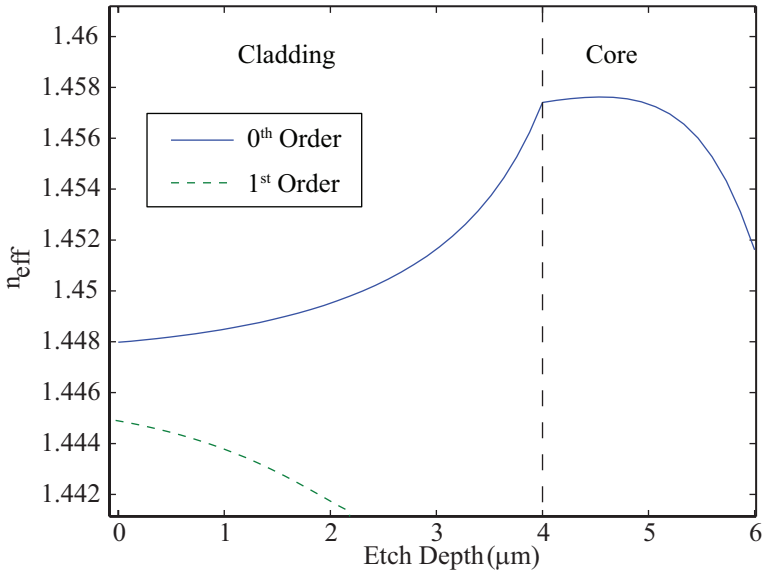

Figure 4.16: Plot of the effective index of a mode as a function of etch depth. The cladding layer began with a thickness of 4 μm and the core with a thickness of 2 μm.

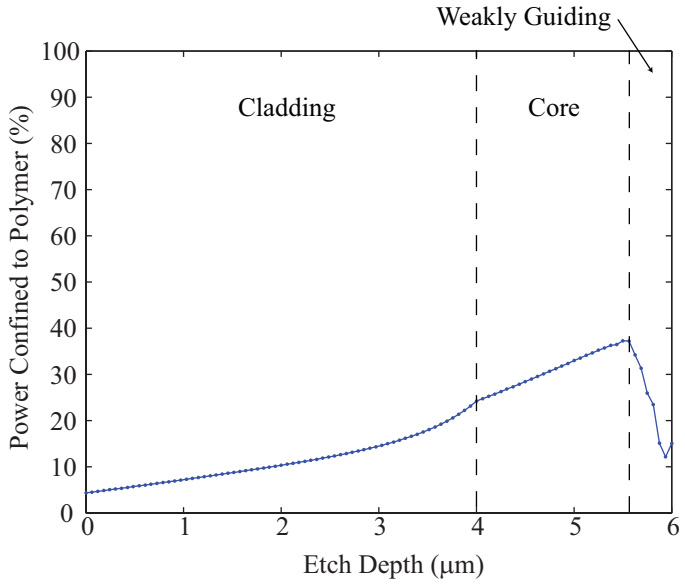

Figure 4.17: Plot showing the amount of optical power confined to a polymer slab for varying etch depths. In the region where the cladding layer is being etched the confinement increases with a slightly increasing slope, once the core is breached the confinement increases linearly until the mode become more and more weakly guiding at which point it drops dramatically.

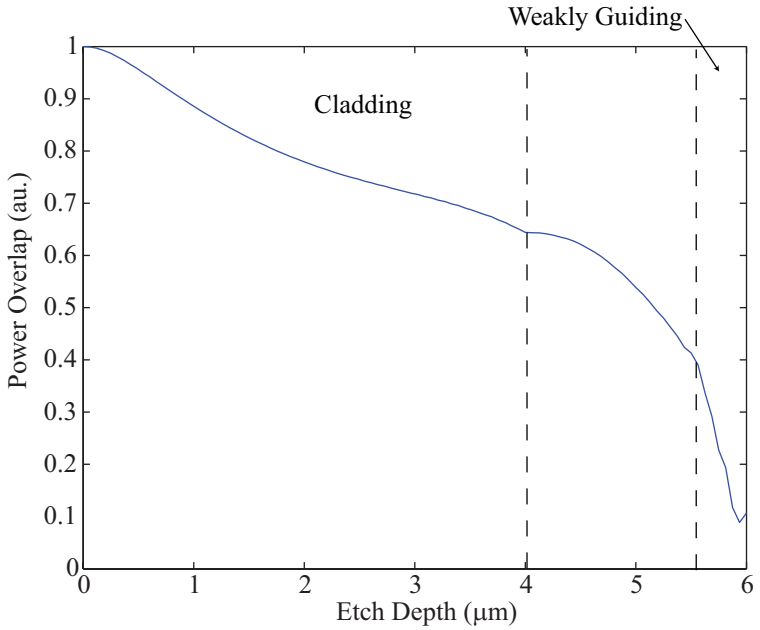

Figure 4.18: Plot of the overlap integral of the optical power in the "unetched" multi-slab waveguide with the optical power in the multi-layer slab at each phases of the "etching".

with the field at each increment from "unetched" to "etched." While this overlap is not an exact loss value, it can be used to estimate the loss. Empirically we have found that the overlap is a conservative estimate of the optical loss of a hybrid waveguide cross-section. For the purposes of these calculations the overlap can be taken as a minimum loss value. Figure 4.18 shows a plot of the overlap integral of the unetched vs. etched slabs. Note that the power drops with a varying slope through each phase of the "etching" process. The confinement decreases fairly linearly to 70% until all of the cladding is removed. As the core is removed, the overlap drops more rapidly, and finally was the weakly guiding region is reached, the overlap drops most rapidly down to about 10% overlap with the original optical power profile.

The design of the optimal hybrid waveguide requires that loss is minimized and confinement is maximized. Thus, it is useful to calculate the overlap-confinement product to determine the optimal etch point. The overlap and confinement values are multiplied and the values are plotted in Figure 4.19. The overlap-confinement product is plotted alongside the n_{eff} values for each etch depth to show how closely

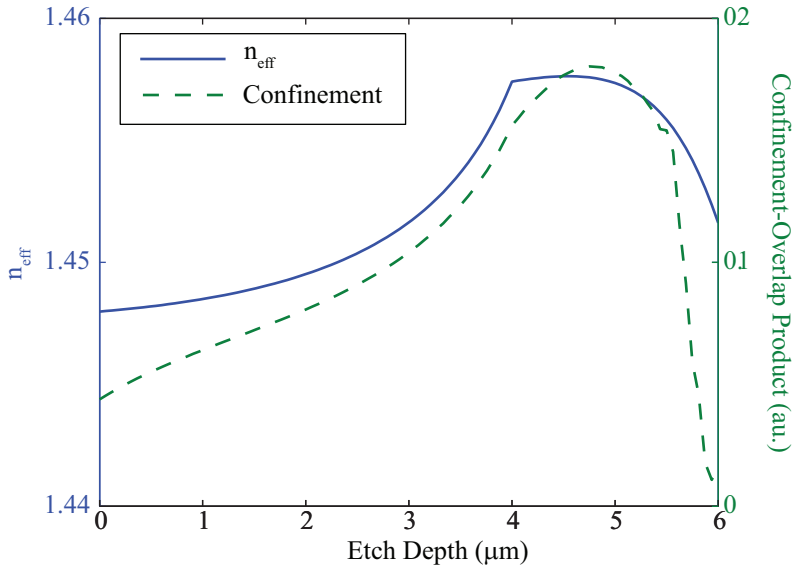

Figure 4.19: Double Y axis plot comparing the n_{eff} of the fundamental mode with the overlap-confinement product.

they match. If an overlap-confinement product is not known, the n_{eff} values can be used as an approximation.

Multiple-slab modeling can be used to gain intuition into the design of hybrid optical fiber waveguides, but actual hybrid fiber cross-sections must be used to accurately obtain an exact design. The etching of D-fiber waveguides is done with an in-situ etching process. The section of the fiber where the core is to be etched is immersed in a Hydrofluoric acid solution with a 25% concentration. A red laser is input into one end of the D-fiber and the other end is inserted into a photodetector. The transmitted power is monitored as a function of time, and when the transmitted power is reduced by a certain amount, usually measured in dB, the fiber is removed from the HF bath and immersed in water to terminate the etching process. An etch where only a small portion of the core is removed over a 1.5 to 2 cm length usually exhibits 4 dB difference between the initial optical power and the etched optical power. Thus, the etch depth is said to be a 4 dB etch depth.

The modeling of D-fiber hybrid waveguide cross-sections is done by obtaining SEM cross-sectional images of three fiber which are etched to various depths. Figure 4.20 shows the index profiles used for modeling three different etch depths of

Table 4.4: Modeling Results for Various Etch Depths

	4 dB	7 dB	15 dB
Overlap	80%	60%	30%
Confinement	7%	11%	34%
Overlap-Confinement Product	5.6	6.6	10.2

hybrid D-fiber waveguides. The polymer thickness for each waveguide is chosen so that the waveguide operates in single mode with maximum confinement. The fundamental mode is calculated for each fiber, and an overlap integral is performed with the fundamental mode of the etched fiber and the unetched fiber mode. The optical power confined to the polymer region for each profile is also calculated. Fibers such as these were fabricated experimentally and the data recorded. Table 4.4 records the data for the overlap, the confinement, and the overlap-confinement product. The maximum overlap was obtained by the core which was etched the least, as in the multi-slab modeling. The maximum confinement was obtained from the fiber core which was etched out completely, similar to the multi-slab modeling as well. The overlap-confinement product also indicates that the 15 dB etch depth would result in the best device sensitivity. However, the overlap does not accurately account for the total insertion loss of the device, and can only be used to get intuition concerning loss.

An experiment was done where three fibers were fabricated using the standard fabrication process and it was found that the 4 dB, 7 dB, and 15 dB etch depth fibers exhibited 1 dB, 10 dB and 30 dB insertion losses respectively. The loss-confinement product was calculated and it was determined that the least etched fiber would result in the greatest device sensitivity. Table 4.5 records the loss results and the loss-confinement product for the three etch depths. The 4 dB etched fiber resulted in a loss-confinement product of 5.56, the 7 dB etched fiber resulted in a loss-confinement product of 1.1, and the 15 dB etched fiber resulted in a loss-confinement product of 0.034. From this product it is clear that the improvement in confinement for the deeper etched fiber does not make up for the much higher losses associated with the deeper etches.

(a) (b) (c)

Figure 4.20: Index profiles of three fiber which were etched to (a) 4 dB, (b) 7 dB, and (c) 15 dB transmission loss. Each profile has a $\approx 0.5\ \mu m$ layer of polymer deposited in the core.

Table 4.5: Experimental Results for Various Etch Depths

	4 dB	7 dB	15 dB
Confinement	7%	11%	34%
Experimental Loss	1 dB	10 dB	30 dB
Experimental Loss %	0.794	0.1	0.001
Loss-Confinement Product	5.56	1.1	0.034

4.2.4 Transition Regions

Perhaps the most difficult aspect of modeling the guiding characteristics of a D-fiber is understanding the effect of the transition region between the unetched D-fiber and the region of the D-fiber which is etched and formed into a hybrid waveguide. This difficulty is one of the reasons why the overlap-confinement product and loss confinement-product based on experimental results show such a discrepancy. One reason it is difficult to understand, is because it is difficult to see what the core and cladding look like through the transition region. Figure 4.21 shows an SEM image of an etched D-fiber from a top down view. From the left to the right of the image the fiber goes from less etched to more etched. The fiber core is breached about two-thirds of the way in the image from left to right. The core appears white on the edges and a darker lines appears as the fiber is etched further. While a top down SEM image, as in Figure 4.21, can be used to determine the length of the transition region, it does not say anything about how and at what rate the core changes from unetched to etched through the transition region.

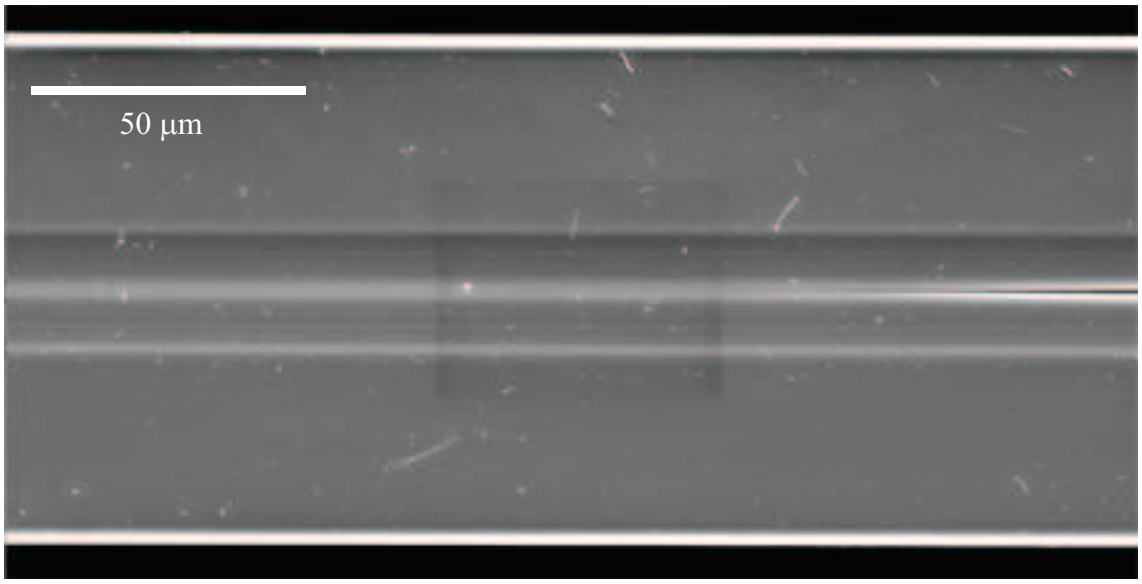

Figure 4.21: An SEM image of the top of an etched D-fiber. The core is breached and is visible on the right hand side of the image.

In order to obtain more information more images of the core in the transition region were necessary. To that end, a technique was developed to cleave a fiber into sections of less than 1 mm. Figure 4.22a shows the long working distance microscope and the cleaving assembly used to cleave these short fiber sections. Figure 4.22b shows a more closeup view of the cleaving assembly along with labels for several of the important parts. The process of cleaving the fiber involved mounting a fiber to a section of polyimide tape to hold it in place, scoring the fiber with the cleaving blade, applying slight pressure with a set of reverse action tweezer and then transferring the cleaved section to a stub for SEM imaging.

An SEM screenshot of a top down view of several of the slices which were cleaved with this assembly are pictured in Figure 4.23. The longest of these sections was 571 μm.

A cross-sectional back-scattered image of each of these cleaves was taken with an SEM. Figure 4.24a includes SEM cross-sectional images along with the top view of the D-fiber with the cross-section location indicated. It is interesting to note that the fiber transition region changes quickly from $z = 0$ μm to $z = 1.202$ μm but then stays about the same until the core is finally breached at $z = 2.140$ μm, where it again moves

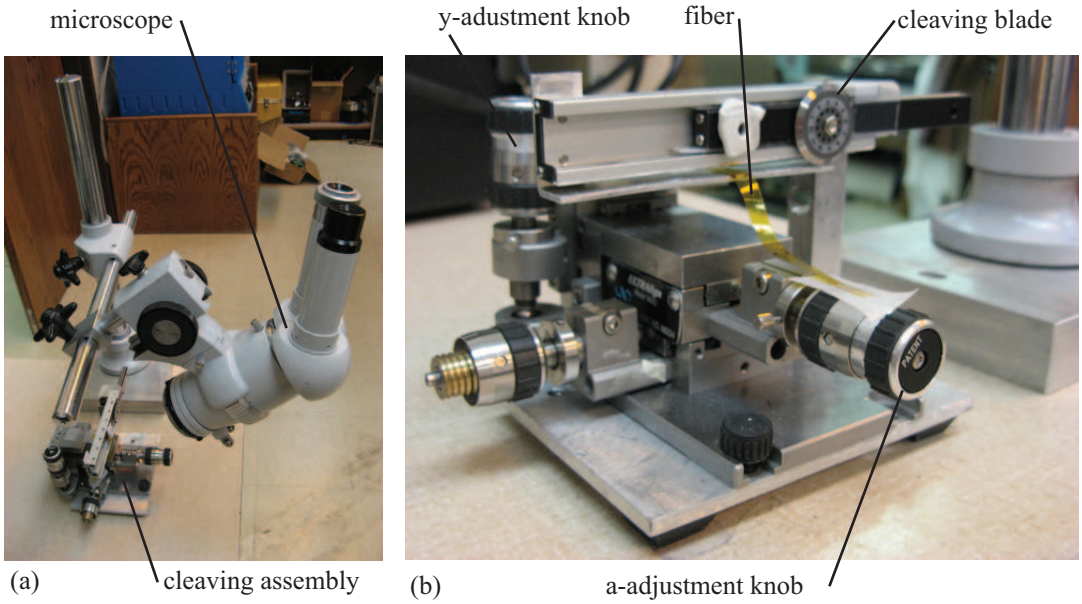

Figure 4.22: (a) The microscope and (b) the cleaving assembly used to cleave short sections of D-fiber to image the transition region

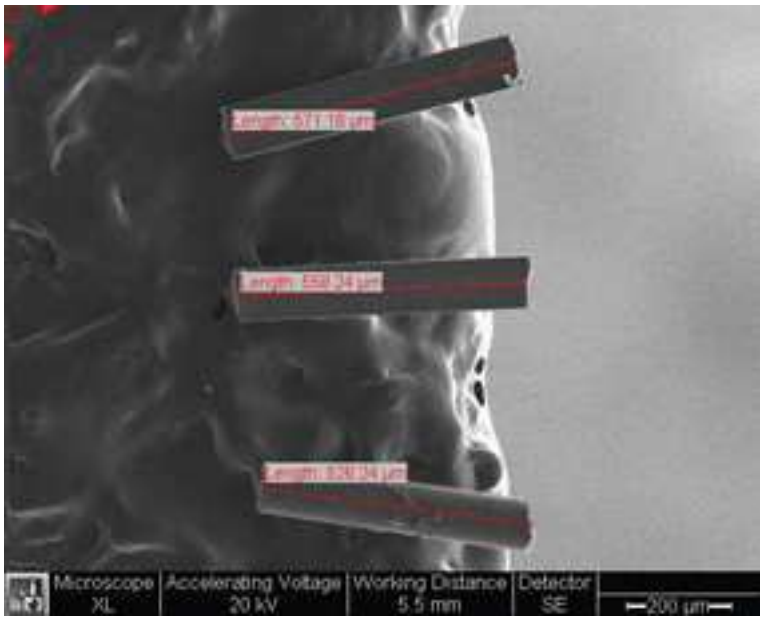

Figure 4.23: A top down SEM view of three cleaved sections of a fiber transition region

quickly, but then only increases slightly up until it is fully etched at $z = 7.123\ \mu m$. It was previously believed that the fiber transitioned fairly linearly from unetched to completely etched. These results diverge from that view, and provide the most accurate understanding of the transition region that has yet been obtained.

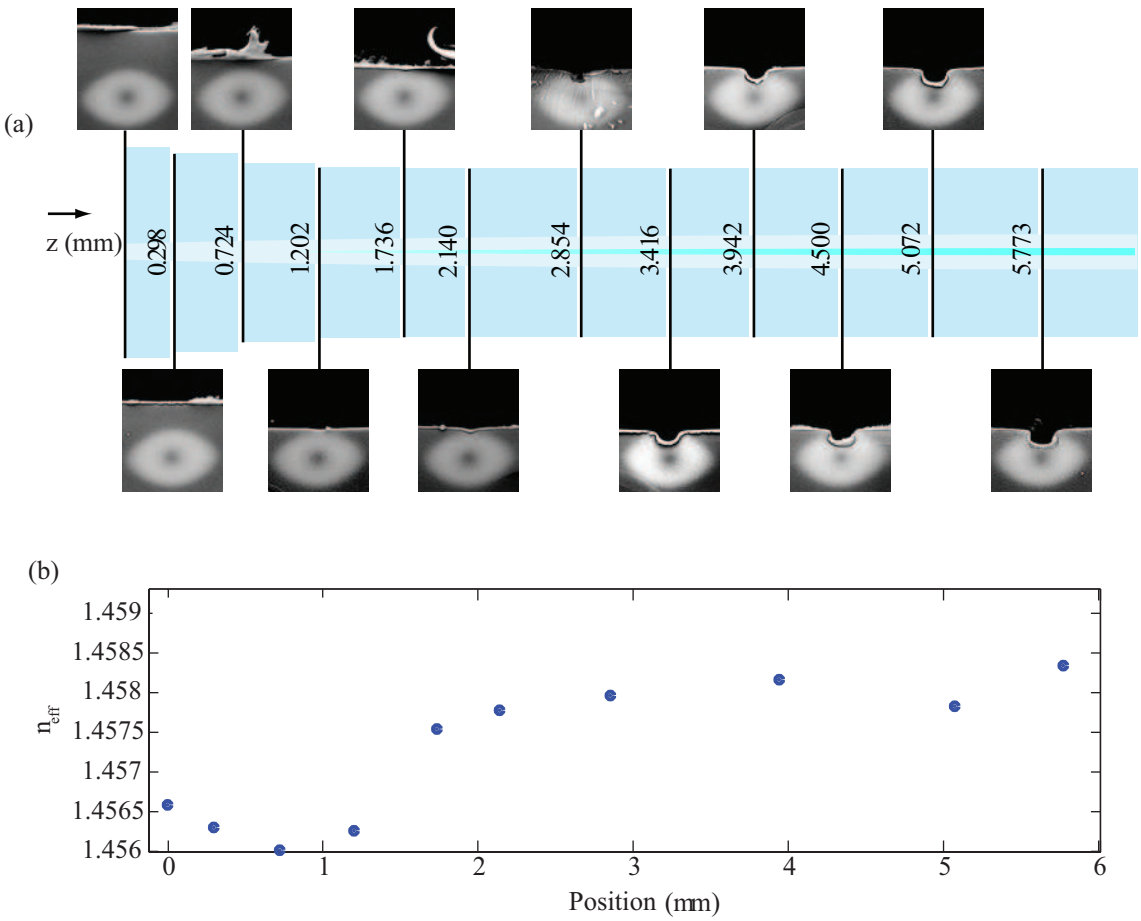

Figure 4.24: (a) SEM cross-sectional images with fiber transition illustration to show actual placement on the fiber. (b) Plot of n_{eff} calculated for each fiber cross-section in the transition region using Beamprop.

Once the images were taken, and index profile for each of the sections was generated using Adobe Illustrator and Matlab. These index profiles were input into BeamProp and their guiding characteristics obtained. Figure 4.24b plots the effective index of the fundamental TE mode for each of the cross-sections.

Table 4.6: Multiple-Slab Index of Refraction Modeling Parameters

Parameter	Value
Polymer Thickness	2 μm
Polymer Index of Refraction	1.5-1.7
Cladding Index of Refraction	1.441
Over Index	1.0

The plot of the effective index of an etched fiber transition matches very well with the effective index plot of the multiple-slab model plotted in Figure 4.16. Since this fiber is etched only to the 4 dB etching transmission loss point, it should be compared to the etch depth of up to 4.5 μm in the multi-slab etch model. Note how both plots decrease and then increase as the cladding is removed the the core barely breached.

If the transition region could be made long enough and the conversion from unetched to etched fiber made gradual enough, some of the losses could be eliminated and a more deeply etched fiber with higher polymer confinement used to maximize device sensitivity.

4.2.5 Polymer Index

Besides changing the etch depth of a fiber, another parameter which can be adjusted is the index of refraction of the electro-optic polymer. To get intuition as to what happens with the same materials and a varying index of refraction, a multiple layer slab was modeled according to the parameters in Table 4.6. The guiding region slab was assumed to be completely made from polymer, as if the core of the fiber were completely etched away. The thickness of the polymer was set to 2 μm, and the indices of refraction were increased from 1.5 to 1.7. Figure 4.25 plots the effective indices of the zero and first order modes in the multiple slab structure. Note that the first order mode is supported for indices of greater than about 1.56. As previously mentioned, the waveguide that supports more than one mode will be too lossy for good device sensitivity. Thus, with this design, the polymer index of refraction would need to be less than 1.56 so that the waveguide operates in single mode.

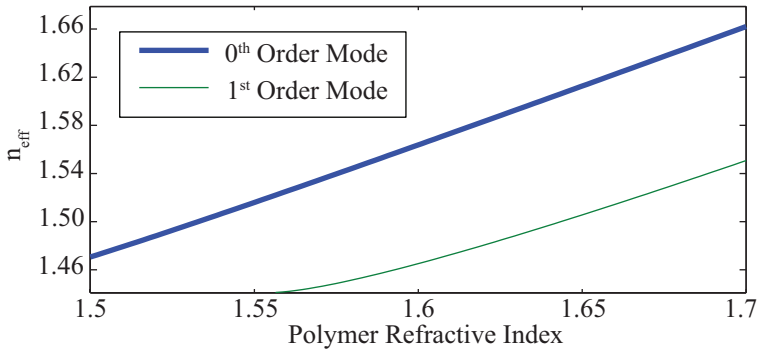

Figure 4.25: Plot of the effective index of refraction of a multiple slab structure as a function of polymer index of refraction. The index is varied from 1.5 to 1.7.

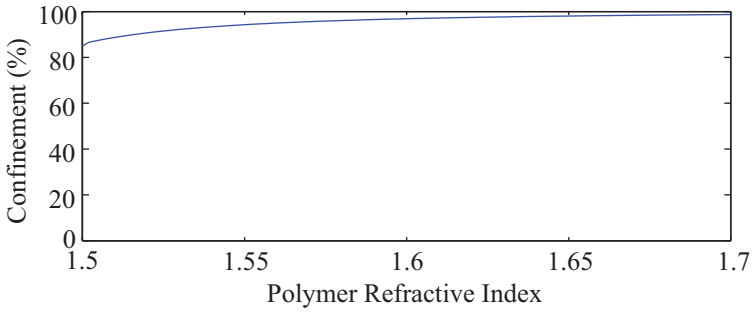

Figure 4.26: Plot of the percent of optical power confined to the polymer region in a multi-layer slab structure with a 2 μm thick layer of polymer and indices varying from 1.5 to 1.7.

The high effective index of the mode with a polymer index of refraction of 1.55 indicates that the confinement to the polymer is also high. Figure 4.25 plots the confinement of the optical power to the region of polymer for indices of refraction from 1.5 to 1.7. The highest single mode confinement would be somewhere around 95%.

The overlap integral of the fields for the 2 μm slab structure indicates that the overlap is still 69% at the highest single mode operating point. If overlap were the only indicator of loss, this waveguide should be fairly low loss. However, another consideration is that with a 2 μm thick slab of polymer, the effective index of refraction of the guided mode for a polymer index of 1.55 would be 1.524. The "unetched" slab mode would be 1.4476, and that difference would result in significant loss unless the the transition between the two were gradual enough.

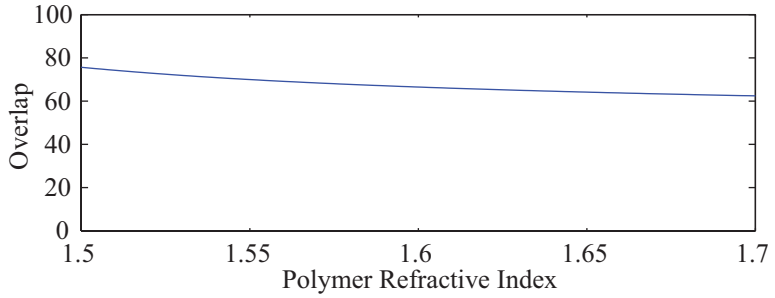

Figure 4.27: Plot of the overlap integral of the power in an "unetched" slab structure with the power in a multi-slab structure for indices of refraction from 1.5 to 1.7.

Based on these multiple slab calculations the intuition is that the higher the index of refraction, the higher the confinement to the polymer. It also has been noted that higher indices of refraction result in an increase in the number of supported modes even if the geometry of the waveguide stays the same. These facts hold true for the hybrid D-fiber waveguide as well.

Figure 4.28 plots the effective index of the zero order and first order modes of a hybrid D-fiber waveguide as the index of refraction is increased from 1.5 to 1.6. Note that the first order mode is cutoff at a polymer index of 1.52. For this type of hybrid waveguide the insertion losses were around 2 dB even with an index of up to about 1.55. However, the losses at 1.6 were as high as 15 dB due to the strongly supported first order mode at that point. Figure 4.29a is an index profile used in modeling the effective index as a function of polymer index. The field profiles of the zero and first order modes are shown in Figure 4.29b and c respectively.

One additional layer of complexity with the D-fiber as compared with the multiple slab model is that the polymer layers are deposited onto a structure with extreme topographical features, and their resulting shape is not that of a planar slab. The D-fiber hybrid waveguide mode is also confined laterally, which changes the field profile of the guided mode. These factors influence the effect of a higher index of refraction in such a way as to reduce the maximum optical power confinement possible in single mode operation. Figure 4.30 plots the confinement to the polymer and the power in the zeroth and first order modes for the previous waveguide structure. The power in the first order mode increases dramatically when it becomes fully supported

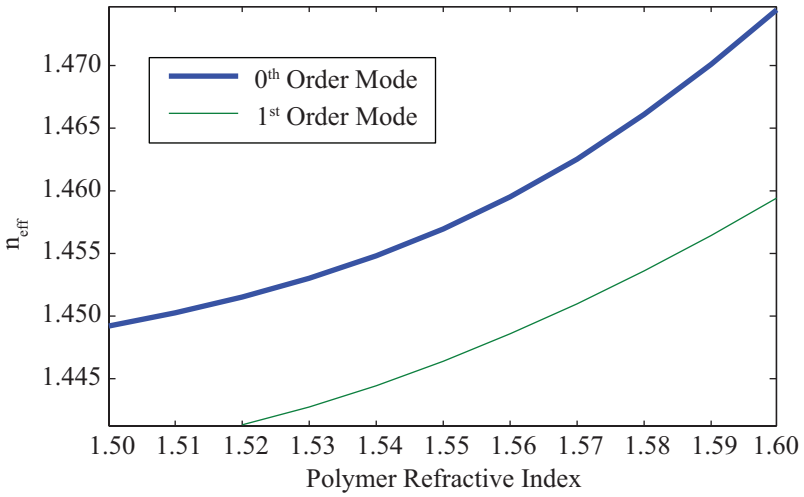

Figure 4.28: Plot of the effective index of the zeroth and first order modes of a hybrid D-fiber waveguide as the index of refraction is increased from 1.5 to 1.6.

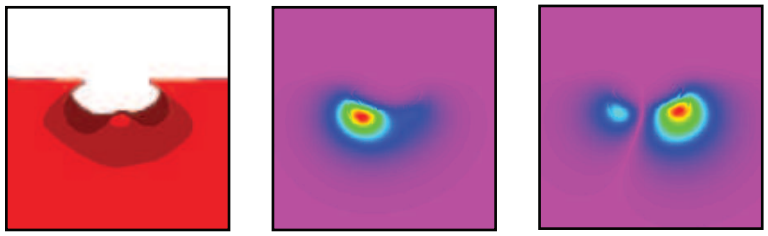

Figure 4.29: (a) Illustration of the index profile used for the D-fiber hybrid waveguide modeling in Figure 4.28, (b) The field profile for the zeroth order mode for the fiber in (a) with an index of 1.6 (c) The field profile for the first order mode for the fiber in (a) with an index of 1.6

in the waveguide structure and subsequently gradually increases until at an index of 1.6 is equal to the power in the zeroth order mode. The zeroth order overlap decreases until it matches the power in the first order mode at an index of 1.6. The maximum single mode confinement for this structure is about 13% for an index of 1.55 where the first order mode is still not maximized, and the effective index of the mode is still close to that of the unetched region.

In this work, there are only two options for index of refraction and they are based on the DR1/PMMA and AJL8/APC chemistry. DR1/PMMA has an index of

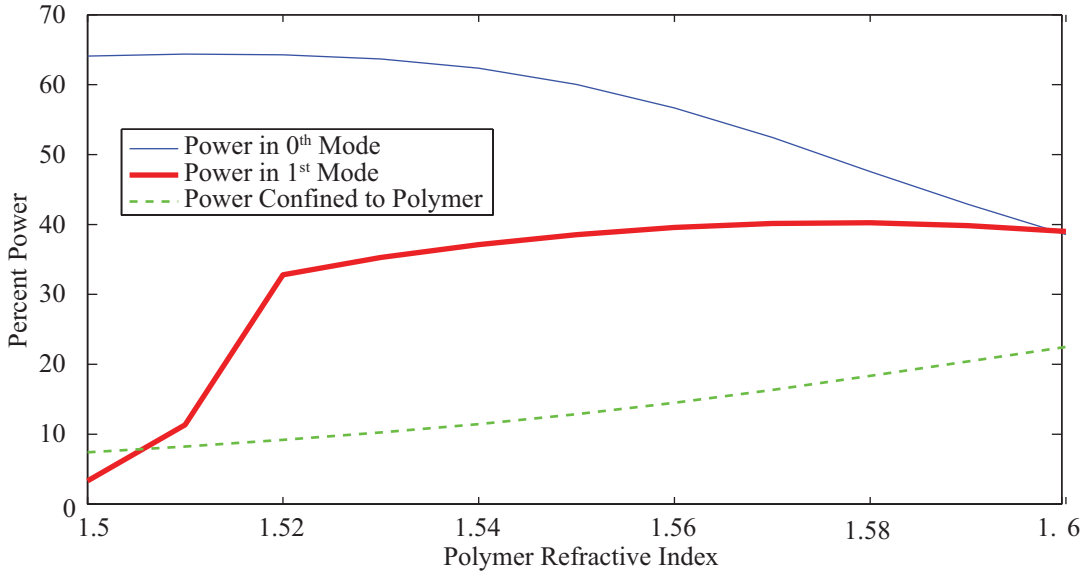

Figure 4.30: Plot of the percent power in the zeroth and first order modes as well as the percent confinement of optical power to the polymer region.

refraction of 1.55, as measured by a Metricon 2010/M Prism Coupler. The refractive index of the AJL8/APC is close to 1.6 as reported in [33].

Figure 4.31 illustrates the effect of the different indices of refraction for the SEM cross-sectional image shown in Figure 4.31b. This SEM image was converted into the index profile shown in Figure 4.31c. A wavelength vs. n_{eff} plot similar to those in the background section is used to show the guiding characteristics of this hybrid waveguide structure as a function of wavelength. The hybrid waveguide structure in this modeling was based on the low loss DR1/PMMA fiber which was published in [11]. Note that the first order mode of the DR1/PMMA structure is cutoff at exactly $\lambda = 1.55\mu m$, which is one reason for its low loss. On the other hand the AJL8/APC first order mode is cutoff at about $\lambda = 1.9\mu m$, and is strongly supported at $\lambda = 1.55\mu m$. In fact the effective index of the first order mode for AJL8/APC is just slightly lower that the fundamental mode for DR1/PMMA, indicating that the first order mode is likely to support a significant amount of optical power. The AJL8/APC waveguide with a slightly higher index of refraction modifies the guiding characteristics of the waveguide in such a way as to make it necessary to reduce the

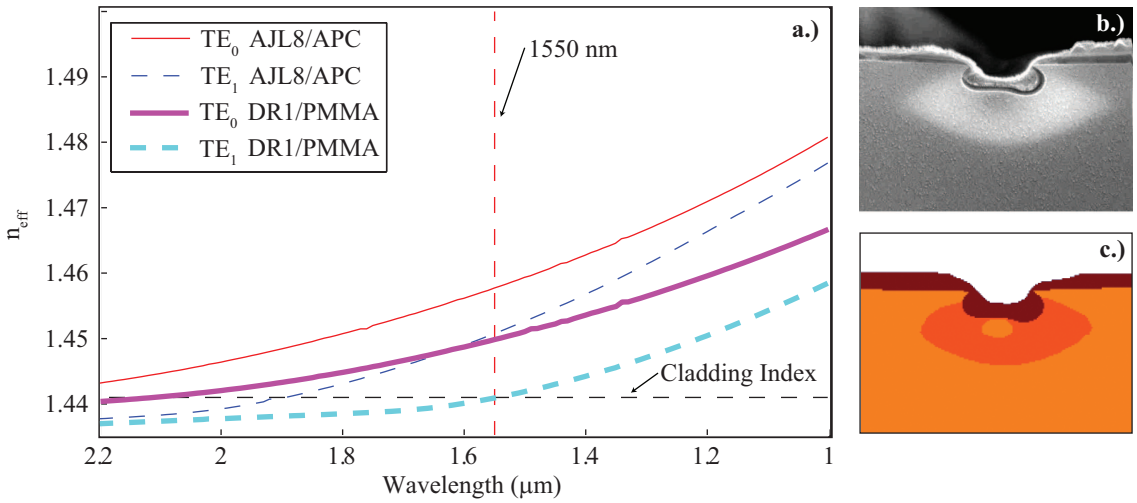

Figure 4.31: A comparison of AJL8/APC and DR1/PMMA for the same hybrid waveguide structure, including (a) a plot of the wavelength vs. effective index for the TE_0 and TE_1 modes for AJL8/APC and DR1/PMMA, (b) an SEM cross-sectional image of a low loss DR1/PMMA fiber cross-section, and (c) the index profile used for this modeling which was derived from (b).

thickness of the polymer in the core of the fiber in order to maintain single mode operation.

Figure 4.32a plots the effective index of the mode for a low loss DR1/PMMA hybrid waveguide structure and compares it to that low loss AJL8/APC waveguide structure. The profiles used in modeling are showin Figure 4.32b and c respectively. The polymer thickness in Figure 4.32b is much greater than that of the fiber in Figure 4.32c. While it is possible to slightly increase the polymer thickness in Figure 4.32c, while still operating in single mode, the thickness will still be significantly less. More detail about polymer thickness and confinement will be considered in the next section, but to illustrate the point it should be noted that the optical power confined to the polymer in Figure 4.32b is around 13%, while the optical power confined to the polymer in Figure 4.32c is only around 7%. So in this case the lower index of refraction results in a greater optical power confined to the polymer while operating in single mode.

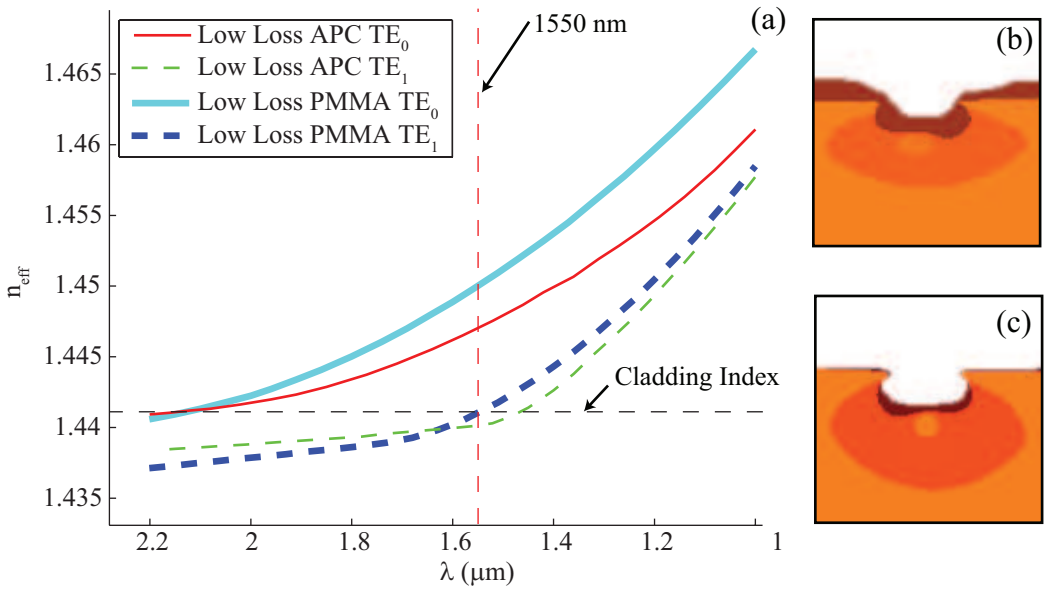

Figure 4.32: (a) A plot of the effective index of the zeroth and first order modes for the DR1/PMMA waveguide in (b) and the AJL8/APC waveguide in (c), (b) the index profile used to model the low loss DR1/PMMA waveguide structure, and (c) the index profile used to model the low loss AJL8/APC waveguide structure.

4.2.6 Polymer Thickness

The last variable that can be adjusted in designining a low loss high confinement hybrid D-fiber waveguide is the polymer thickness. Again, the multiple slab structure will be used to gain intuition and the principles will be applied to the understanding of a hybrid D-fiber waveguides. Table 4.7 records the physical parameters used in this modeling and Figure 4.33 plots the effective index of the zeroth and first order modes. As was the case for the other parameters, there is a thickness over which the slab waveguide no longer operates in the single mode regime. In this case the slab cannot be thicker than about 1.45 μm with a 1 μm core.

Again, the confinement of the optical power in the mode is plotted in Figure 4.34 and has a maximum single mode confinement of about 92%. The overlap integral of the zero and first order modes is plotted in Figure 4.35, and exhibits a local maximum at a polymer thickness of 0.48 μm. This local maximum in overlap occurs as the polymer thickness matches the 1 μm of core that was etched in this simulation.

Table 4.7: Multiple-Slab Index of Refraction Modeling Parameters

Parameter	Value
Polymer Thickness	.35 to 2 μm
Polymer Index of Refraction	1.6
Core Thickness	1 μm
Core Index of Refraction	1.4756
Cladding Index of Refraction	1.441
Over Index	1.0

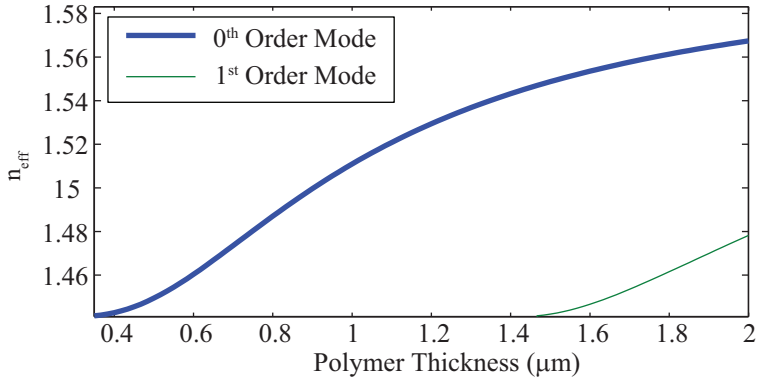

Figure 4.33: Plot of the effective index of the zeroth and first order modes of a multiple slab waveguide as the polymer layer thickness is increased from .35 to 2 μm.

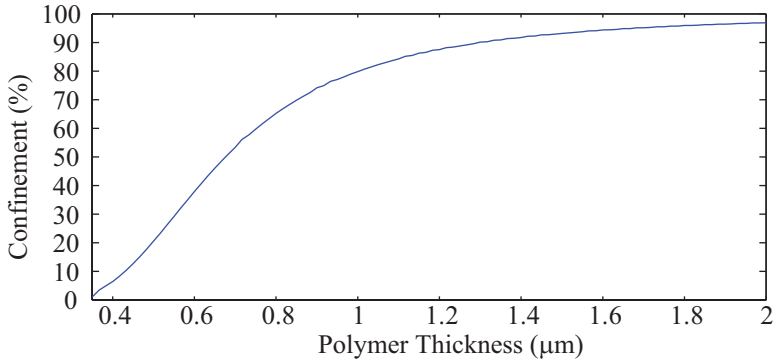

Figure 4.34: Plot of the percent of optical power confined to the polymer region in a multi-layer slab structure with a polymer index of 1.6 and a core thickness of 1 μm and a varying polymer thickness from .35 to 2 μm.

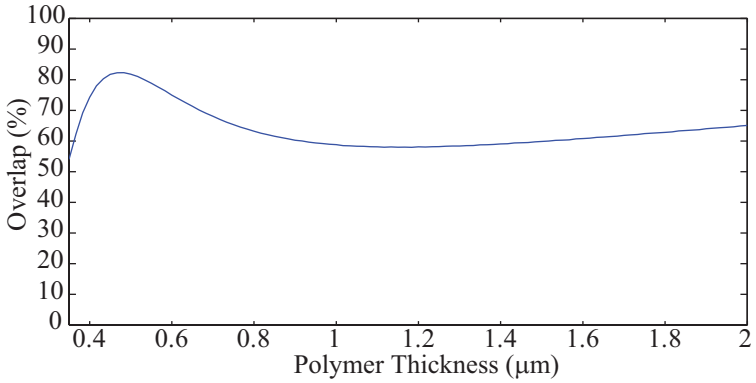

Figure 4.35: Plot of the overlap integral of the power in an "unetched" slab structure with the power in a multi-slab structure with a polymer index of 1.6 and a core thickness of 1 μm and a varying polymer thickness from .35 to 2 μm.

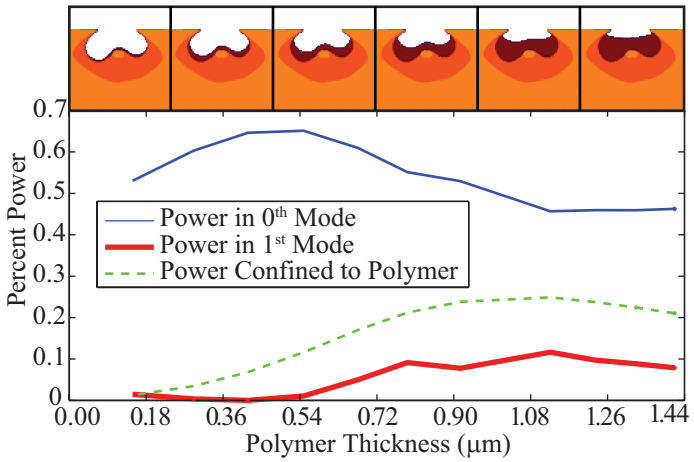

Figure 4.36: A plot of the power in the zero order and first order TE modes of a hybrid D-fiber waveguide. The overlap integral of the optical power with the polymer portion of the hybrid waveguide is also included. This fiber was etched to 4 dB transmission loss. A series of cross-sections for a range of polymer thicknesses used in this calculation is shown at the top of the plot.

From the multiple slab modeling it is found that the overlap increases as the polymer thickness increases until it fully replaces the etched portion of the core, at which point it begins to decrease again when more of the power is coupled to the first order mode and the mode become less and less similar to the unetched profile. The confinement increases as the polymer thickness increases. These trends also hold for the hybrid D-fiber waveguide. Figure 4.36 shows the same trends as polymer thickness

increases in a fiber which has been etched to about 7 dB etching transmission loss. At the top of the figure a sequence of index profiles show how the polymer thickness increases in the core. The plot below shows how the power in the first order mode begins increasing at about a 0.54 μm polymer thickness. That thickness represents the highest amount of polymer possible for single mode operation to occur. The maximum single mode confinement is therefore about 11%. Similar to the overlap for the multiple slab calculation, the overlap of the zeroth order mode power for the hybrid fiber waveguide also has a maximum at about 0.5 μm.

4.2.7 Balancing Etch Depth and Polymer Thickness

There are two major advantage of using the multiple slab code to get intuition into how a hybrid D-fiber waveguide works. First, it is very simple to adjust the physical parameters programatically. In the case of hybrid D-fiber waveguides the index profiles must be manually created for each etch depth and polymer thickness. Second, the multiple slab guided mode calculation is very fast. The two advantages make it possible to perform thousands of calculations in only a few hours, while it take a few hours to calculate only a few modes from index profiles in BeamProp. With the ability to calculate thousands of solutions in only a few hours, it is possible to perform two dimensional calculations which offer some insight into the how etch depth, polymer index, and polymer thickness are interrelated. This section discusses the interplay of etch depth and polymer thickness for the indices of refraction of a theoretical low index EO polymer ($n = 1.5$) DR1/PMMA ($n = 1.55$) and AJL8/APC ($n = 1.6$). The structure will be assumed to be a fiber whose cladding has been removed completely. Both the amount of core which is etched away (0 to 2 μm and the thickness of the polymer will be varied.

The only valid solutions for this array of variables are those solutions which are single mode. Figure 4.37 shows two dimensional plots where the x and y axes are polymer thickness and etch depth respectively. The shade on the plots indicates the number of modes which are supported for that combination of variables. Because this is an asymmetric slab, there is a region where there are no supported modes.

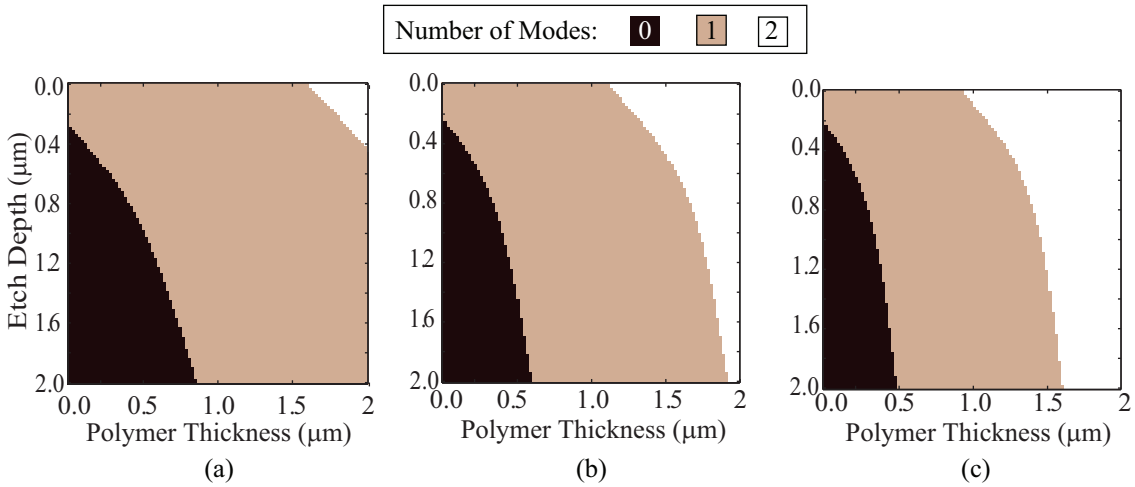

Figure 4.37: Two-dimensional plot indicating the areas where there are zero, one, and two supported modes for polymer indices of (a) $n = 1.5$, (b) $n = 1.55$, and (c) $n = 1.6$.

This region is where the etch depth is too high for the corresponding thickness of polymer. The width of this region increases as the etch depth increases. The middle region extending from the upper left corner of the plot down toward the lower right corner is the single mode region. The final region displayed on these spots is the lightest shaded region which represents the multimode region. As the polymer index increases from $n = 1.5$ to $n = 1.55$ and then on to $n = 1.6$ the area of the single mode region shrinks. The cut-off region also shrinks and the multimode region expands. The effect of the diminishing single mode region will be seen later on. In the following discussion the single mode region will be used to mask the confinement and overlap solutions so that only the valid single mode solution are plotted.

The confinement of optical power to the polymer region of a waveguide is calculated for each polymer index and for the same array of etch depths and polymer thicknesses which were used in the previous plots. Figure 4.38 plots the results of the simulation for each of the three polymer indices of refraction previously noted. A color bar is shown at the top of the plot to indicate the confinement value for each combination of variable. Not surprisingly, the plots show that as the polymer thickness increases, the confinement increases. The black regions are those that either do not support a mode or support more than one mode. For an indices of $n = 1.5$, $n =$

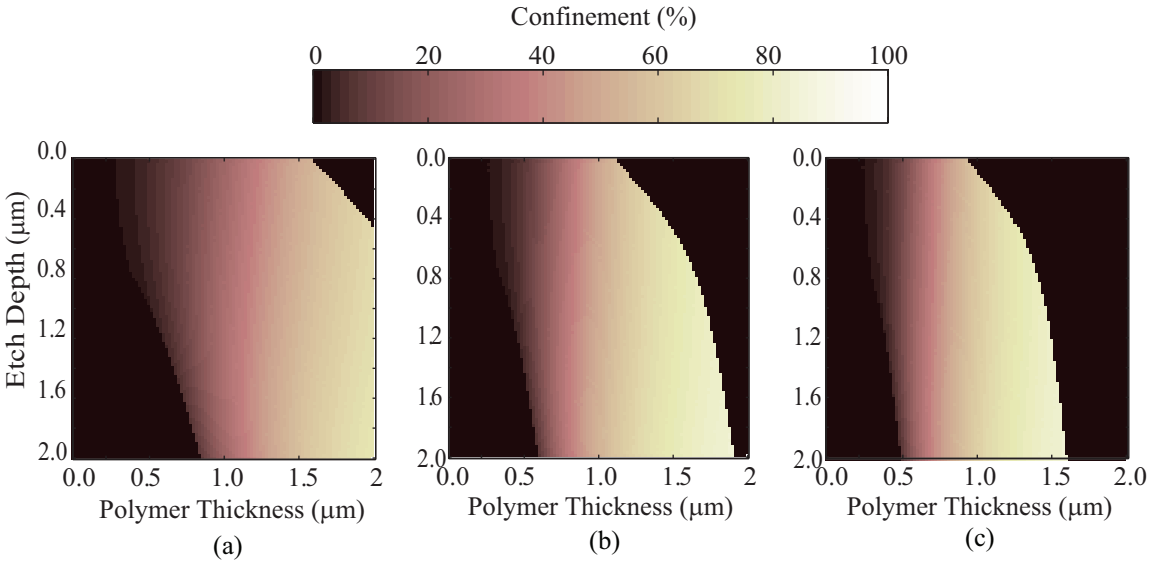

Figure 4.38: Two-dimensional plot indicating the confinement of optical power to the polymer region of the waveguide for a varying etch depth and polymer thickness and polymer refractive indices of (a) $n = 1.5$, (b) $n = 1.55$, and (c) $n = 1.6$

1.55, and $n = 1.6$, the maximum confinement values are 72.97%, 83.45%, and 83.41%. It is interesting to note that the maximum confinement drops slightly between the 1.55 and 1.6 index of refraction. This result is due to the smaller single mode region of the 1.6 polymer index. If the multimode regions were compared the 1.6 index would have a greater maximum confinement.

The next calculation to consider is the overlap of the fundamental unetched mode with the zero order mode of the waveguide for each combination of variable. Figure 4.39 plots the results of confinement. The lightest regions are the areas where the overlap integral was highest. The main difference between each polymer index of refraction here is the size of the high overlap area. The polymer index of 1.5 has a very large lightly shaded area which extends in a band from the top middle to the middle of the right hand side of the plot. The 1.6 index has the smallest region of maximum overlap and the 1.55 is somewhere in between the two.

Combining the two results the overlap-confinement product is used to determine the maximum device sensitivity if overlap and confinement were equally weighted. Figure 4.40 plots the results. The maximum possible overlap-confinement

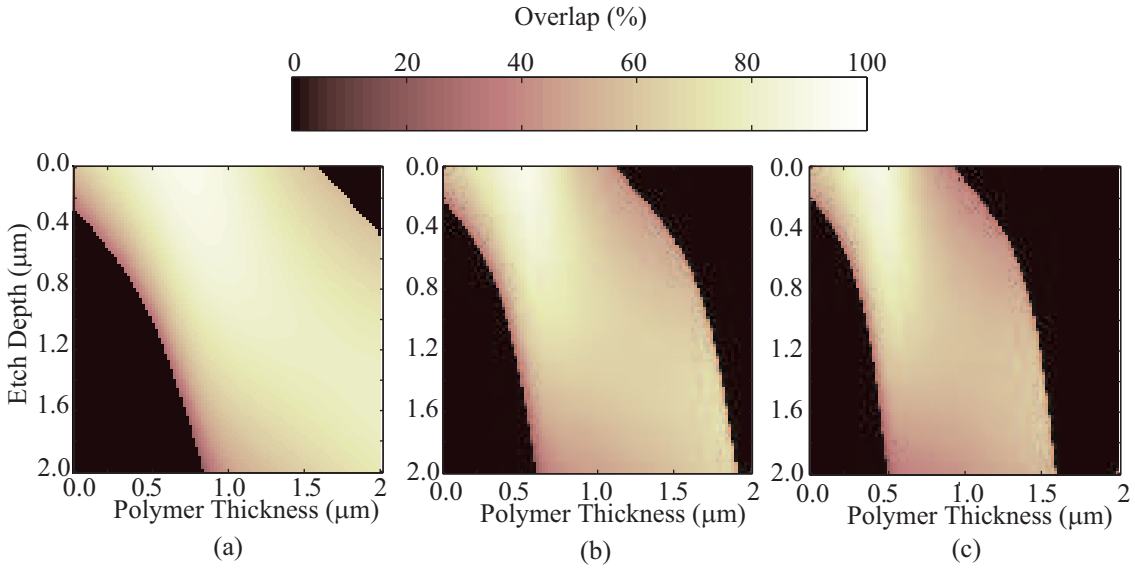

Figure 4.39: Two-dimensional plot indicating the overlap integral value of the calculated mode with the unetched mode for a varying etch depth and polymer thickness and polymer refractive indices of (a) $n = 1.5$, (b) $n = 1.55$, and (c) $n = 1.6$

product occurs in the $n = 1.5$ polymer at 56.9% due to its much larger single mode region. The $n = 1.55$ case is very slightly lower at 56.8%, and the $n = 1.6$ is just 6% lower at 50.2%. From the overlap-confinement product it appears that all three cases are almost equal in maximum sensitivity,but as previously noted the overlap is a conservative approximation for loss. Another method of determining loss is by comparing the effective index of the mode with the fundamental unetched mode. For the $n = 1.5$, $n = 1.55$, and $n = 1.6$ polymer indices the effective index as the maximum confinement positions were 1.4728, 1.5208, and 1.5520 respectively. Compare those values to the fundamental mode with an effective index of 1.4476, and it is clear that the lowest polymer index is much closer. This is not surprising since the core of the fiber has an index of 1.4756. Another interesting item to note is the amount of optical power that is confined to the polymer at the position where the mode most closely matches that of the unetched region. The differences are dramatic. For the $n = 1.5$, $n = 1.55$, and $n = 1.6$, the confinement at the maximum overlap position are 56.9%, 8.9% and 7%. Clearly, the lowest loss device would be possible with the lowest index of refraction polymer.

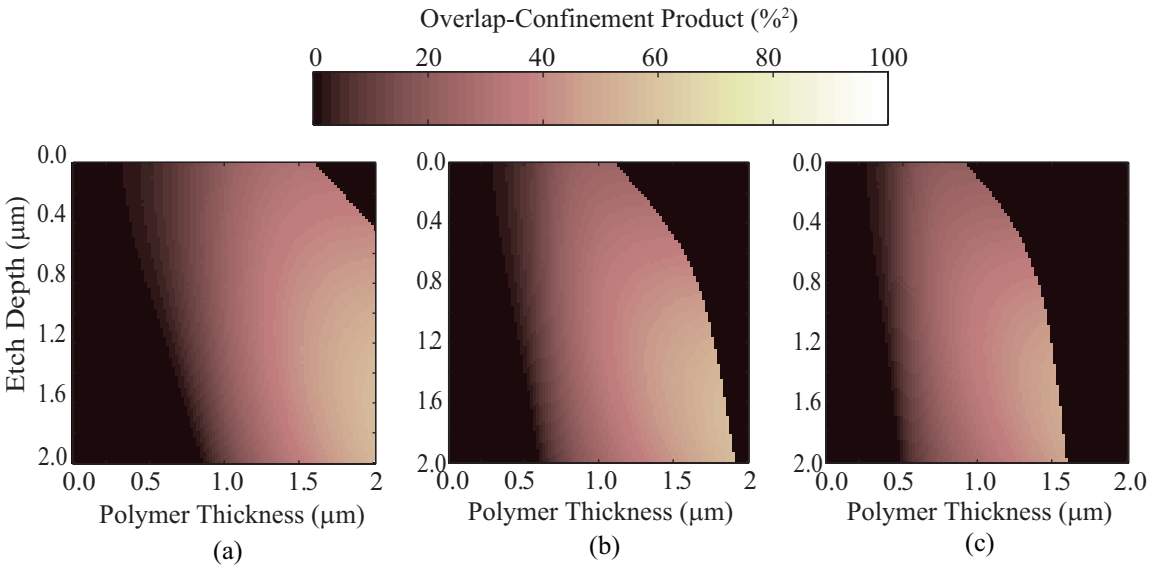

Figure 4.40: Two-dimensional plot indicating the overlap-confinement product for a varying etch depth and polymer thickness and polymer refractive indices of (a) $n = 1.5$, (b) $n = 1.55$, and (c) $n = 1.6$

These trends with index, etch depth, and polymer thickness for a multiple slab model are a good indicator of how a hybrid waveguide operate. It is impractical to consider such a large variable space with the hybrid waveguide. In the following treatment the variable space will be limited. First, the only practical polymer at BYU for in-fiber electric field sensing is AJL8/APC since the DR1/PMMA has a lower r_{33} and is not temporally stable, and BYU does not have a polymer with an index of $n = 1.5$. Second, rather than considering many different etch depths, three etch depths will be considered which are representative of the shallow, medium, and deep etch depths. Finally, several polymer thicknesses are considered for each etch depth as they were in Figure 4.36. By downselecting to the $n = 1.6$ polymer, choosing three different etch depths and a range of polymer thickness, the modeling of the hybrid waveguide becomes more manageable. Figure 4.41 shows the three etch depths and plots the overlap for the zeroth and first order modes for each. The optical power confined to the polymer region is also plotted. For the first etch depth, which corresponds to an etch depth of about 4 dB of transmitted power loss, the maximum polymer thickness for single mode operation is about 0.5 μm, and the confinement

at that point is 7%. For the second etch depth which corresponds to a transmitted optical power loss of 7 dB, the maximum polymer thickeness for single mode operation is about 0.54 μm, and the confinement at that point is 11%. For the deepest etch which corresponds to a transmitted power loss of greater than 15 dB, the maximum polymer thickness for single mode operation is about 0.62 μm, and the confinement at that point is 34%. One major difference with the hybrid waveguide compared to the multiple slab calculation is that the single mode region is even more limited in the hybrid waveguide. Thus the maximum confinement is limited. In practice the most shallow etched fiber is the only etch depth which produced low loss hybrid D-fiber waveguides, no matter what polymer thickness was used.

If a lower index polymer temporally stable, high r_{33} polymer were used, the single mode operating range would increase, as well as the maximum confinement.

4.3 Conclusions

In summary, the design of the hybrid electro-optic polymer D-fiber waveguide requires the understanding of the guiding characteristics of dielectrics and fiber waveguides. Because the guiding characteristics of the hybrid D-fiber waveguide are very complex, it is useful to use a multiple slab model to gain intuition into the effects of a change in various parameters. The principles observed can be used to gain greater insight into the operation of the hybrid D-fiber waveguide.

The situation, as it currently stands, is that the loss which results from deeper etches is too high to make a deeper etch practical. To increase confinement by a factor of five between the shallow etch and the deepest etch, the loss increases by a factor of over a thousand. This is not a good trade-off. The current hypothesis is that as long as the fiber is operating in single mode, the losses can be reduced by modifying the transition region length and slope, either by modifying the etch method, or modifying the index or presence of polymer on the transition region.

For low loss waveguides with a confinement of 7% a shallow 4 dB transmission loss etch should be used with an AJL8/APC layer which is about 0.5 μm thick. If it becomes possible to modify the transition region such that the completely etched

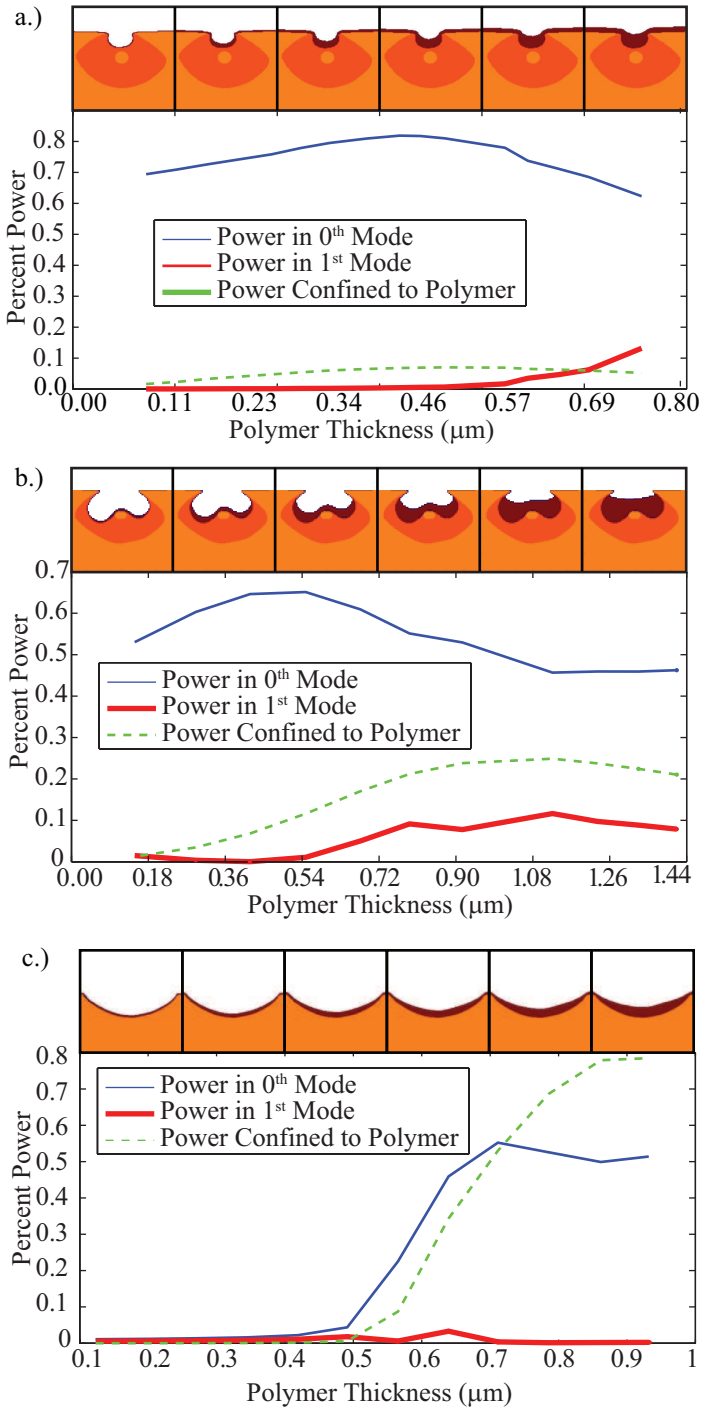

Figure 4.41: A plot of the power in the zero order and first order TE modes of a hybrid D-fiber waveguide as the polymer thickness is increased for three different etch depths. The overlap integral of the optical power with the polymer portion of the hybrid waveguide is also included. The fibers were etched to a (a) 4 dB, (b) 7 dB, and (c) 15 dB transmission loss. Series of cross-sections for a range of polymer thicknesses used in these calculations are shown at the top of each plot.

core can be used for a low loss hybrid waveguide configuration, a layer of 0.62 μm thick AJL8/APC should be used and a confinement of 34% obtained. If a temporally stable lower index polymer becomes available, that can be used without modifying the transition region for a lower loss, higher confinement single mode hybrid D-fiber waveguide.

Chapter 5

Ink-Jetting of AJL8/APC for D-fiber Electric Field Sensors

Some of the fabrication techniques common to integrated optics can be extended to in-fiber device fabrication, but the fiber substrate introduces unique challenges since it is flexible and has high contrast topographies. This chapter briefly discusses the aspects of the entire fabrication process, with a focus on on polymer deposition. One of the contributions of this work is a process for depositing electro-optic polymer using a commercial materials printer. The polymer was consistently and accurately deposited in small volumes into the partially removed core of a D-fiber. This method exhibits far superior control and much less material waste as compared to the spin casting method. The spin casting approach uses at least .1 ml of polymer for an adequate coating, and the ink-jetting method uses only .1 μl.

This chapter presents an overview of the hybrid D-fiber waveguide fabrication process, presents the background related to ink-jetting technology, and details the development of an ink-jetting process for in-fiber device fabrication.

5.1 Hybrid D-fiber Waveguide Fabrication Overview

5.1.1 Fiber Preparation

To begin the fabrication process, a section of 0.8 to 1 meter length of fiber is cut from the spool. Both ends are then stripped with the Fujikura HTS-12 high strength heat stripper. These ends are cleaved using the Fujikura precision cleaver to produce about a 2 degree cleave angle. This combination of stripper and cleaver have been found to produce the most consistently optimal cleave facets, which makes fusion splicing and optical alignment much easier. A 3 to 4 cm length of jacket is stripped from the center of the fiber, again using the HTS 12. It is important to

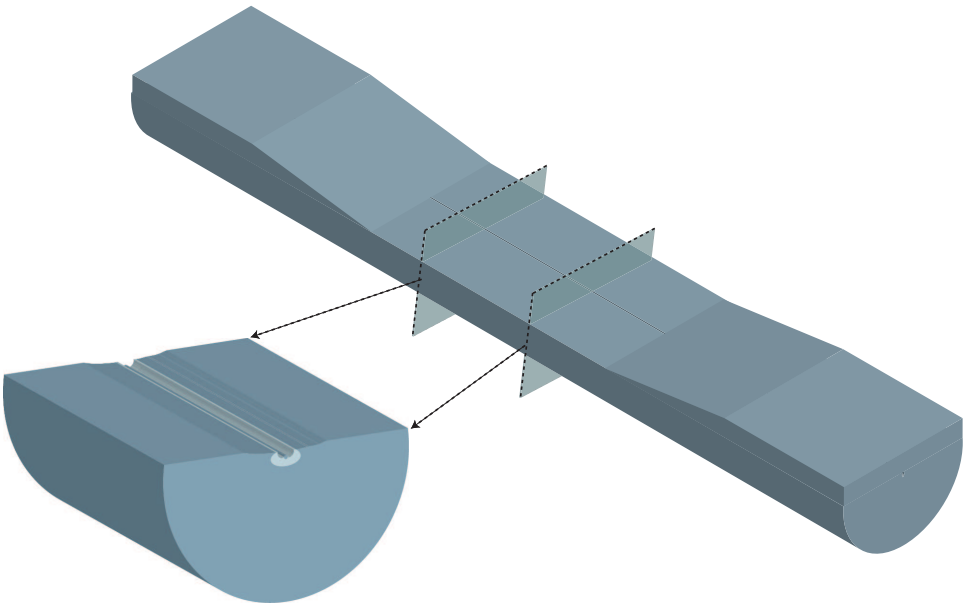

Figure 5.1: A section of the D-fiber core is exposed through selective chemical etching.

apply a good amount of force to close the blades shut during stripping to ensure that most of the fiber jacket is removed. The fiber is then positioned flat side up in the etch holder. The stripped section in the middle of the fiber is then lowered into an isopropanol bath which is agitated with a Branson 200 Ultrasonic Cleaner.

5.1.2 Selective Chemical Etching of D-fiber

Once the fiber is prepared, the partial core removal process is accomplished by etching the optical fiber using hydrofluoric (HF) acid. In HF acid the Germania-doped core etches approximately 8 times faster than the fluorine-doped cladding and about 11 times faster than the undoped cladding [55]. Since the Germania-doped core etches faster than the cladding materials, a groove is created in the optical fiber where the core material was removed while leaving most of the cladding intact as seen in Fig. 5.1. More information about the etching of D-fiber can be found in Chapter 2 of [56], and Chapter 3 of [57].

5.1.3 Polymer Deposition

With the core exposed, it is next necessary to create the hybrid waveguide. The etched fiber is attached to a substrate with the flat side of the fiber facing up. To ensure that the fiber maintains proper orientation, a thermal adhesive material is used to fasten the fiber to the substrate after taping. The fiber is then looped around the substrate to protect it during spin-casting. A solution of polymer is applied to the etched section of the fiber using a pipette and the fiber is spun using a standard commercial spinner. If the fiber maintains it flat side up orientation, the spinning process produces a uniform layer of polymer on the fiber. The fiber is then heated to remove the remaining solvent.

It is desirable to have as much of the light guided in the electro-optic polymer as possible to improve the sensitivity of the device. There are many factors that affect the amount of light being guided in the electro-optic portion of the waveguide such as the etch depth, polymer thickness, and the index of refraction of the polymer. The light guided in the polymer also needs to be coupled back into the fiber core after passing through the etched region to prevent high optical losses.

This chapter includes information about a new method presented in this work involving ink-jetting. It also compares ink-jetting and spin casting as a means of depositing EO polymer in hybrid D-fiber waveguides.

5.1.4 Poling

After polymer deposition, the chromophore molecules responsible for the EO effect are randomly oriented, so in order to make the polymer sensitive to electric field the EO polymer must be poled. Corona poling is used because of the high applied field that can be produced [22]. The basic corona poling process is shown in Fig. 5.2 and involves heating the sample to a temperature just below the glass transition temperature of the polymer, so that the molecules are free to reorient themselves, and applying a high electric field. The high electric field is applied by suspending a needle over the sample and applying a high voltage between the needle and a ground plane located on the other side of the sample. The high voltage on the needle tip

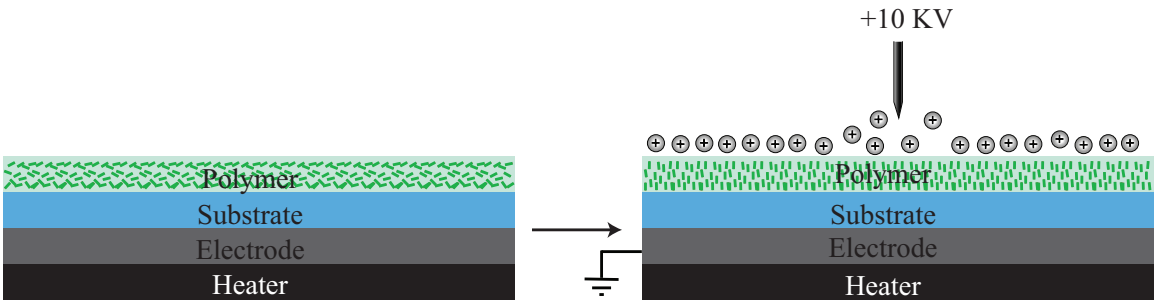

Figure 5.2: The polymer is poled to make it electro-optic by heating and cooling the polymer with an applied electric field.

ionizes the air and causes positive ions to build up on the surface of the sample with an equal amount of negative charges on the ground plane. The positive and negative charges produce a high electric field across the polymer and the polymer molecules orient themselves to this field. The sample is then cooled with the electric field still applied, thus fixing the aligned polymer molecules in place. Chapter 2 includes a more detailed treatment on the theoretical and experimental details of poling.

5.1.5 Packaging

The hybrid waveguide fabrication process leaves the fiber vulnerable to breaking. Therefore, the fiber must be packaged after the processing steps are complete in order to restore its mechanical robustness. Chapter 6 includes a more detailed description of the packaging design that has proven effective in increasing the robustness of the D-fiber hybrid waveguide sensor.

The remainder of this chapter focuses specifically on the polymer deposition step in the fabrication process.

5.2 Polymer Printing Background

Spin casting is the most common technique for the fabrication of polymer devices. The active device areas are then patterned and etched to form the device [32]. Some work has been done to optimize the spin casting process for the conservation of material, such as dipping the substrate into the material and then spinning, or spraying the material on the substrate resulting in transfer efficiencies of twenty percent

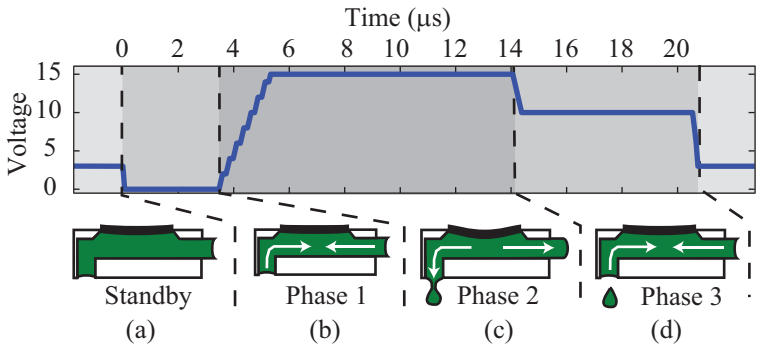

Figure 5.3: The phases of ink-jetting with a piezoelectric valve. (a) The valve is in the standby state. (b) The valve opens allowing more fluid into the reservoir. (c) The valve closes slightly to create a drop at the nozzle. (d) The valve returns to the standby state, causing the drop to eject cleanly.

[58]. Even with higher transfer efficiencies, most of the deposited material does not contribute to the actual device function.

Another recent development in coating technology is the direct writing of materials using a piezoelectric printhead. This technique uses a small volume of material to pattern fine features at high speed. Several types of materials printers have become commercially available, and have been found to be ideal for printing various functional polymers such as polythiophene [59], polyfluorene [60, 61], polyphenylenevinylene [62], and polypyrole [63]. Furthermore, research has been reported regarding various active polymer devices based on inkjet printing [64, 65, 66, 67].

There are two common methods for ink-jetting. The first is continuous jetting where a pattern is generated by blocking and unblocking the continuous stream. The second method is ink-jetting or drop on demand, where a pattern is formed by actuating a jetting valve. Drop on demand allows for smaller drop sizes as well as better drop placement, and is commonly realized by either heating the nozzle, or by using a piezoelectric membrane [64]. The work in this chapter is based on the piezoelectric ink-jetting method, where AJL8/APC is deposited for the first time in the core of a fiber, thus forming a hybrid waveguide.

The ejection of a drop from the nozzle is accomplished by creating an acoustic wave in the material solution. Figure 5.3 illustrates the four phases of the formation

of an acoustic wave that results in an optimal drop [68]. First the reservoir is in the rest or standby state where no pressures are acting on the material solution. Next the reservoir is filled by actuating the piezoelectric value to open the reservoir. The white arrows in Figure 5.3 illustrate the flow of material due to the pressure change. Then the piezoelectric value is actuated to make the reservoir smaller, increasing the pressure at the nozzle, and forming a drop. The piezoelectric valve returns to the standby state which creates a lower pressure region beneath the piezoelectric valve. The connecting thread is eliminated in the final step with a sharp backpressure.

5.3 Process Development

There is a variety of commercially available materials printers based on the ink-jetting technology. This work uses the DMP 2800 produced by Dimatix Inc. (Lebanon, NH). The electro-optic (EO) polymer solution used in this chapter is a guest-host polymer (AJL8/APC) mixed with cyclopentanone. This EO polymer has been shown to be a good candidate for fabricating electro-optic devices due to its high electro-optic coefficients, processibility, and temporal stability [32, 33]. One challenge with ink-jetting AJL8/APC is that a viscosity enhancer or surfactant cannot be added to the material to make it more compatible with ink-jetting, without dramatically affecting its chemistry. This section details the development of a successful process to obtain good drop formation of AJL8/APC. The technique is applied to the characterization of film deposition on a D-fiber. Finally, the ink-jetting method is compared with the spin casting method.

5.3.1 AJL8-APC Drop Formation

Before any jetting can be attempted, the material solution must be adjusted to satisfy the printing requirements while maintaining its desired chemistry. Once a good material solution is made, work must be done to characterize the optimal voltage waveform which controls the piezoelectric valve.

Since cyclopentanone is an aggressive solvent, the 10 pL liquid crystal polymer (LCP) cartridge is selected. Viscosity is the only material solution variable which can

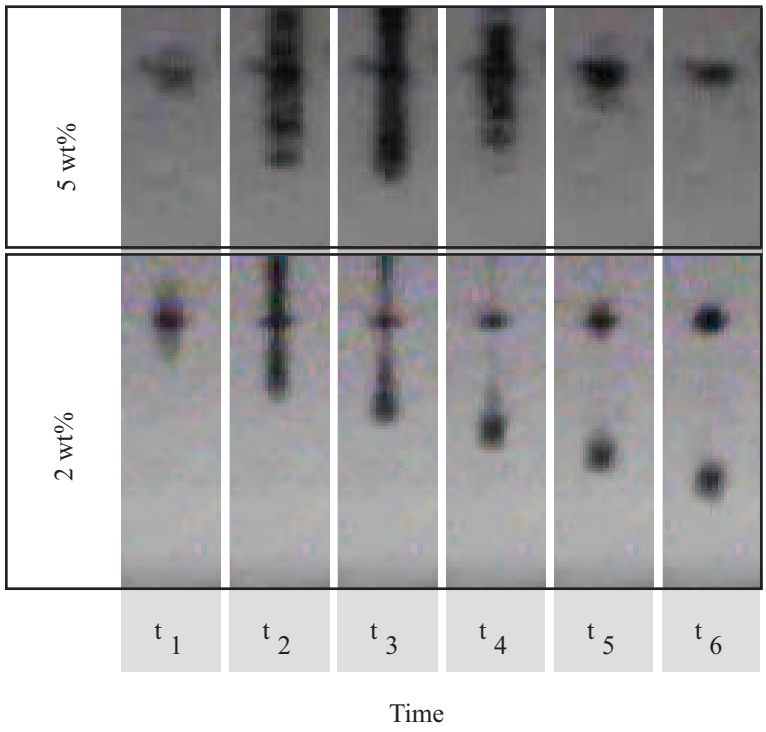

Figure 5.4: Sequence of side view images of the drop formation for 5 wt% and 2 wt% AJL8/APC solutions. As time progresses the 5 wt% solution drop begins to form, but at t4 begins to retract. The 2 wt% solution drop forms and at t4 the viscous thread is broken and the drop is fully formed.

be adjusted due to the sensitive electro-optic chemistry of AJL8/APC. Viscosity is adjusted by varying the solid concentration of AJL8/APC with respect to the amount of cyclopentanone. Figure 5.4 illustrates the pitfall of choosing an improper solid to solvent wt%. A sequence of lateral photographs taken by the DMP 2800, shows the drop formation of both a 5 wt% and a 2 wt% solution. The drop is the dark shape in each frame. The drop begins to form in the second and third frames. However, the viscous thread of the 5 wt% drop does not break and the drop is pulled back into the valve in the fourth frame. Using a 2 wt% solution, good drop formation was achieved. The kinematic viscosity of the solution with a polymer-to-solvent weight ratio of 5 wt% was measured to be 9.8 cP. Even though the kinematic viscosity of the solution should have been adequate for ink-jetting according to the fluid guidelines [69], it does not properly jet due to its higher elongational viscosity [64].

Table 5.1: Jetting Waveform

	Level (%)	Slew Rate (au.)	Slew Rate (V/ s)	Slew Rate (V/μs)
Phase 1	0	2.0	46.7	3.3
Phase 2	100	0.5	8.05	10.6
Phase 3	67	1.0	15.6	6.5
Phase 4	20	2.0	36.3	0.5

Once a compatible material solution was found, the voltage waveform was modified to optimize the speed, and shape of the drops, as well as eliminate satellite droplets. The shape and velocity of the drop is adjusted by varying the voltage waveform applied to the piezoelectric membrane which is the source of the acoustic wave. Parameters such as time, voltage, and slew rate are adjusted for each phase of jetting. Figure 5.3 illustrates the optimized waveform, and Table 5.1 shows the DMP 2800 specific parameters used to jet the 2 wt% solid concentration AJL8/APC solution.

5.3.2 AJL8/APC Hybrid Core Formation

Once optimal jetting is achieved, the film thickness of the AJL8/APC in the fiber core is optimized to maximize the electro-optic influence of the polymer, while maintaining single mode operation. This delicate balance can be realized using the DMP2800 by adjusting the drop spacing or applying multiple layers. Since each drop from the 10 pl cartridge covers about a 40 μm diameter, drop spacing of less than 40 μm results in material overlap.

Several D-fibers that were previously etched are mounted onto a glass slide, and placed on the printer stage. The built-in angular alignment feature of the DMP2800 is then used to align the fiber axis with the printing axis. The drop offset feature of the DMP2800 is then used to ensure accurate placement of drops to within a few micrometers. These fibers are printed with varying drop spacing and the transmitted power at 1550 nm is measured. The fibers are then cleaved and SEM cross-sectional images are taken. Figure 5.5 provides the cross-sections for three fibers where the

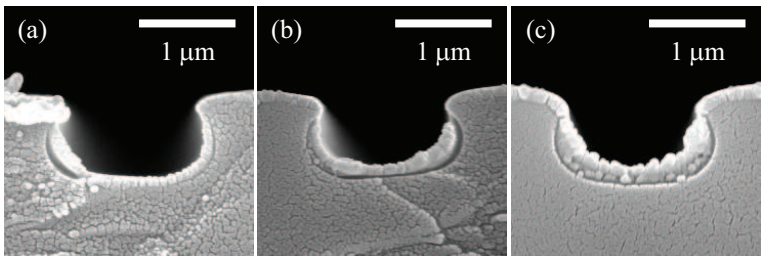

Figure 5.5: SEM cross-sectional images of the fibers with AJL8/APC polymer printed with drop spacings of (a) 30 μm, (b) 20 μm, and (c) 15 μm.

Table 5.2: Drop Spacing Results

Drop Spacing (μm)	Transmitted Power (mW)	Polymer Thickness in Core (nm)
15	0.55	186
20	1.25	152
30	1.3	114

polymer layer is the lighter colored layer. The roughness of the polymer and the fiber is an artifact of gold coating the fibers in preparation for SEM imaging. Table 5.2 provides the polymer thicknesses for these fibers. The transmitted power decreases as polymer thickness increases since the devices become more multimode with a thicker polymer layer. Rather than decreasing the drop spacing, a thicker polymer layer can also be attained by simply depositing multiple thin layers. Multiple layers can be effectively applied because the solvent volume of the drop is insufficient to dissolve any of the underlying EO polymer. Applying multiple layers is advantageous because power transmission through the fiber can be monitored during polymer deposition to attain an optimal film thickness. Figure 5.6 plots the transmitted power as a function of deposition layer for five layers with a drop spacing of 40 μm. The power begins to drop as the polymer thickness increases beyond the single-mode operation limit.

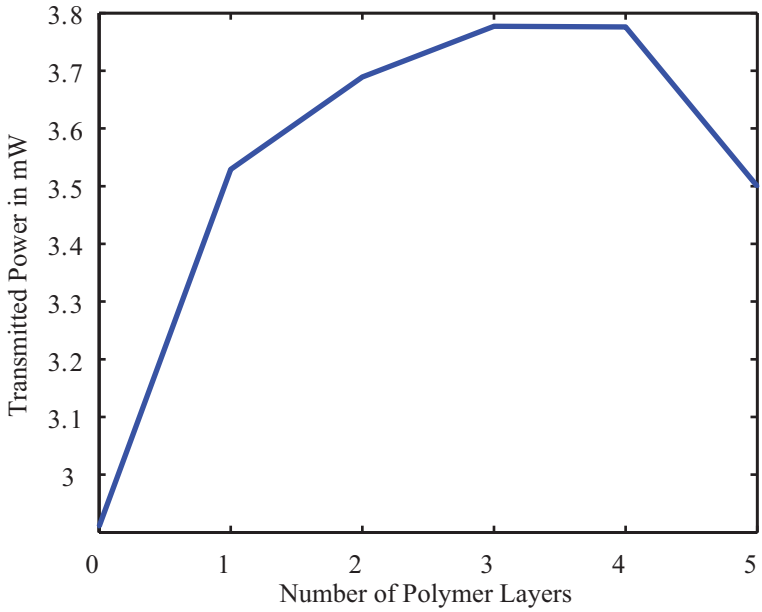

Figure 5.6: In-situ monitoring of power transmission for multiple layers with a drop size of 40 μm.

5.3.3 Spin Casting vs. Ink-Jetting

Since ink-jetting is relatively new as a means of waveguide deposition, a comparison with spin coating is necessary. Figure 5.7(a) is a cross-sectional SEM image of a spin coated fiber, and Figure 5.7(b) is an image of an ink-jetted fiber. The fiber core can be seen in these images as a lighter ellipse and the polymer is the slightly darker material in the etched portion of the fiber. The difference in softness between the polymer and fiber during cleaving causes the polymer to stretch slightly and separate from the glass, and is responsible for the dark area between the polymer and the fiber core.

The spin coated fiber is coated in a Laurel spinner with a 7 wt% solid concentration solution of AJL8/APC with a 500 rpm spread step and a 2000 rpm spin step, and accelerations of 100 rpm/s and 500 rpm/s respectively. The amount of polymer in contact with the light guiding region of the fiber is comparable. However, the ink jetted fiber pictured in Figure 5.7b was printed with less than one micro-liter of polymer, while in the case of the spin cast fiber more than 100 micro-liters were expended. The amount of AJL8/APC used to spin coat the fiber was approximately

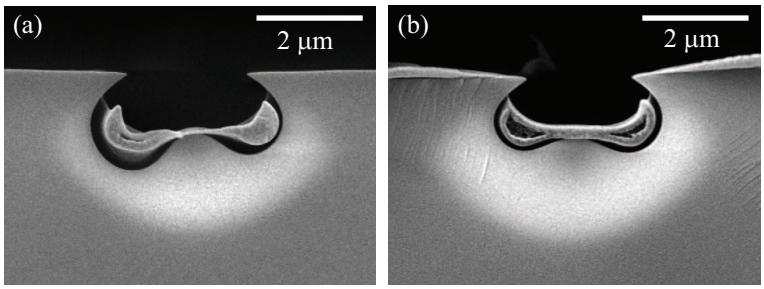

Figure 5.7: Cross-sectional SEM image of a (a) spin coated hybrid core fiber and (b) an ink-jetted hybrid core fiber.

2 mg while the amount of polymer used in the ink-jetted process was approximately 2 μg, indicating that the ink jetting process is more than 1000 times more efficient.

In addition to using much less polymer, as previously mentioned, ink jetting also has several other advantages over spin coating. (1) Spin coating requires that the fiber maintain its orientation during spin coating. The fiber must be bonded to the substrate with thermal adhesive which is not soluble in the polymer solvent, and the one meter section of fiber must be looped and fastened to the spinning substrate. Conversely, ink jetting requires a simple alignment of the fiber to the substrate, and it is only necessary to tape the fiber to the substrate to hold it in place. (2) Spin coating is dominated by both rheological and surface tension forces. It is thus difficult to reliably adjust polymer thickness with a simple change in spin speed. Ink jetting is more consistent since the only forces acting on the material are surface tension forces between the material and the fiber geometry. As previously mentioned the drop spacing or multiple layer deposition can be used to reliably adjust film thickness. (3) Ink-jetting is a very fast process taking less than 10 seconds. Table 5.3 provides a summary of the comparison between the two methods.

5.4 Device Fabrication and Testing

5.4.1 Device Fabrication

A solution of 21.9 mg of APC and 5.4 mg of AJL8 was mixed in solution with 1332.8 mg of cyclopentanone and agitated on a stir plate overnight. The material solution was then filtered and injected into an LCP 10 pL Dimatix print cartridge,

Table 5.3: Ink Jetting vs. Spin Casting

Comparison Category	Ink Jetting	Spin Casting
Polymer volume for one sensor	$\leq 1\ \mu l$	$\geq>$ 0.1 ml
Repeatability	Good	OK
Factors contributing to thickness	Drop Spacing	Material & Spin Parameters
Speed	10 seconds	1 minute +

Table 5.4: Cleaning Cycle Parameters

Step Type	Time (s)	Frequency (kHz)	Post Delay (s)
Spit	0.5	6.5	0.5
Purge	0.1	—	0.5
Spit	0.5	6.5	0.5
Blot	2.0	—	—

and left to sit for 30 minutes. The cartridge was primed by performing a 0.5 second purge until all 16 jets were functioning. A line was patterned and a drop placement calibration was performed. Before each printing step a cartridge cleaning cycle was performed to ensure good drop formation and repeatable results. For reference, Table 5.4 includes the DMP 2800 specific parameters used to clean the printhead.

The print cartridge was positioned to 1.5 mm above the fiber and each jet was set to a firing voltage of 14 volts. An angle calibration was performed to ensure the fiber length was parallel to the x-axis of the printer. The etched fiber was coated with a 15 μm drop spacing which resulted in a polymer thickness of about 200 nm, as in the fiber pictured in Figure 5.8. The slight surface roughness of the polymer is due to the gold coating method used to prepare the sample for microscopy. The fiber was removed from the printer and heated in an oven overnight at 70 °C to evaporate the residual solvent.

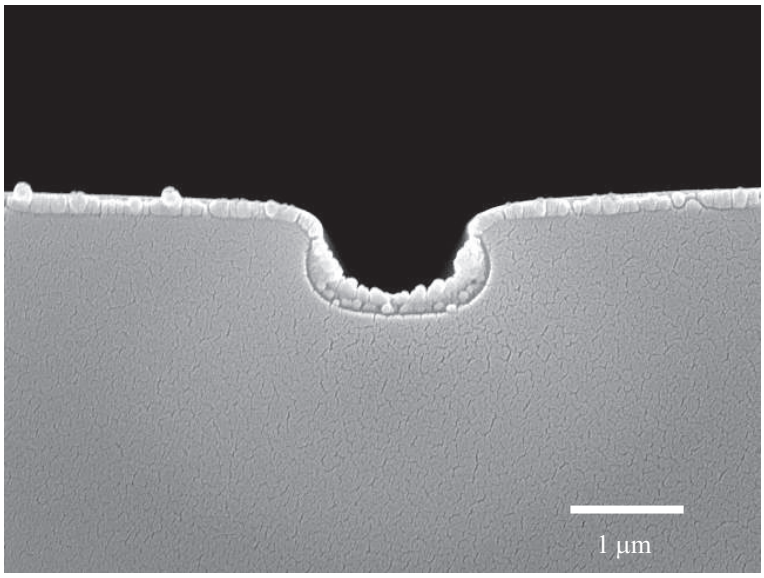

Figure 5.8: AJL8/APC polymer coating in etched D-fiber

5.5 Conclusion

This chapter outlines the development of a process whereby AJL8/APC is deposited onto an etched D-fiber using a commercially available materials printer. The ink-jetting method for depositing polymer for in-fiber device fabrication is superior to the spin casting method for several reasons. (1) Only one micro-litre of polymer is used in ink-jetting, while with spin casting more than 100 micro-liters were expended. (2) Due to the high velocities incident to spin coating, the fiber often twists and the polymer coating becomes non-uniform. Spin coating thus requires additional preparation and mounting of the fiber to a substrate to ensure proper orientation. Ink-jetting requires no special care in attaching the fiber to a substrate. (3) With both rheological and surface tension forces acting on the fiber during spin casting, it is difficult to reliably adjust polymer thickness. Both the spin recipe and the viscosity of the material must be changed and a significant amount of re-characterization must be done when adjustment is required. It is comparatively easy to adjust the film thickness with the ink-jetting method, requiring only a simple adjustment of the the drop to drop spacing and printhead angle. (4) The ink-jetting method is faster than the spin-casting method for depositing polymer on one or multiple fiber devices.

Using this ink-jetting method, polymer was deposited into the partially removed core of a D-fiber. The hybrid waveguide made up of the deposited polymer and the remaining portion of the fiber core is poled to make it electro-optic. A device fabricated using this method was tested and exhibited a sensitivity of 4 kV/m in the presence of a 100 kHz AC electric field as further detailed in (8.8.1).

Chapter 6

D-fiber Electric Field Sensor Packaging

The use of AJL8/APC as a the EO polymer in a hybrid waveguide was pursued due to its higher r_{33} and temporal stability of the polymer. The information presented in Chapter 4 was used to design a low loss AJL8/APC D-fiber waveguide. This chapter outlines the process which was used to package the sensor, and details various tests which prove its mechanical integrity and non-intrusive quality. The end product of a sensor packaged using the methods presented in this chapter withstands tensile stress up to 4 Newtons, torsional stress applied for 17 rotations, and bending stress down to a radius of .11 cm. The maximum outer diameter of sensor package is 1.5 mm.

6.1 AJL8/APC D-fiber Waveguide Fabrication

After a suitable waveguide design was determined, a fiber was fabricated to match those specifications. The following section details the waveguide fabrication process as well as the packaging of the fiber in preparation for testing.

6.1.1 Waveguide

First, a four centimeter section of jacket is stripped from a one meter section of D-fiber, and 1.5 cm length of stripped region is etched in 25% HF acid. The transmitted power is monitored to determine an etch stop at 4 dB. The fiber is then mounted to a substrate and a 5% (wt./wt.) solution of AJL8/APC with a 25% AJL8 loading level is spin cast onto the fiber. Figure 6.1 includes a cross-sectional SEM image of a fiber fabricated with this process. The core of the D-fiber is the lightly shaded elliptical shape. The darker shaded region in the center of the fiber core is

an undoped silica region which is an artifact of the fiber manufacturing process. The AJL8/APC polymer layer is located in the groove of the core as well as on the flat surface of the cladding and is the region of material which is slightly darker and higher contrast than the core.

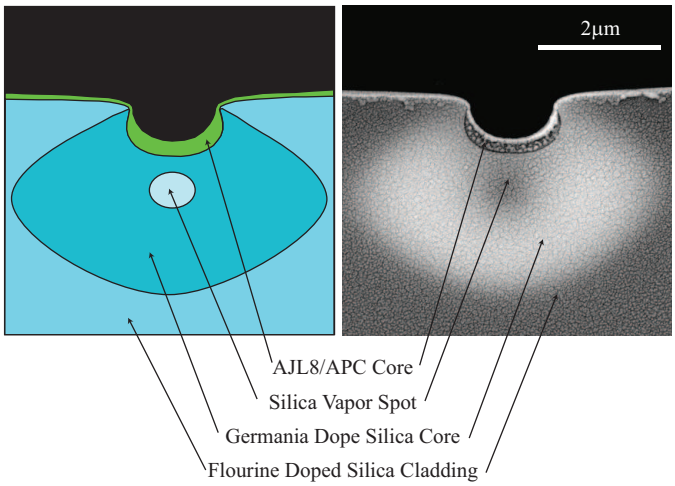

Figure 6.1: a.) SEM cross-sectional image of a D-fiber with AJL8/APC deposited in the core of the fiber. The light elliptically shaped region is the Germania doped core. The stretching of the polymer during the fiber cleaving process in preparation for SEM imaging is the cause of the partial separation of the polymer from the fiber core. The slightly darker region in the center of the core is the vapor spot, which is an artifact of fiber manufacturing b.) Illustration matching the SEM image indicating the various materials making up the hybrid core waveguide

After the polymer is deposited in the core of the fiber, the AJL8/APC layer must be poled. The shape of D-fiber makes standard poling techniques difficult, so a method is used whereby the fiber is embedded to form a planar substrate. The fiber is prepared for poling, by placing the fiber on an electrode, and then encapsulating it in a silicone-based epoxy (Nusil LS-6140, Carpinteria, California, USA). A glass cover slip is used to form a parallel planar surface with the bottom electrode while the epoxy cures. The embedded fiber is then heated to 140 °C and a corona poling field is applied. The corona poling field is maintained while the embedded fiber is cooled to room temperature. The AJL8 chromophore guest molecules are partially aligned in the APC host polymer during this poling process.

6.1.2 Packaging

After poling, the fiber is then packaged in order to make it robust enough for testing in harsh environments. First, the fiber is removed from the electrode, epoxy, and glass slide that were used during the poling process. Then the fiber is threaded through a 5 cm length of polyethelyne tubing. Next, a one centimeter length of EVA tubing is threaded over the fiber and inside the polyethelene tubing. Then a one centimeter length of polyolefin tubing is threaded over the fiber, EVA tubing, and polyethelene tubing. Finally, a point heat source is used to apply heat to the one centimeter EVA, polyolefin region. The EVA tubing melts during the heating, and the polyolefin tubing shrinks creating a strong bond around the outer polyethelene tubing and the fiber. Figure 6.2 illustrates the final package, indicating the various tubes used to protect the fiber. Figure 6.3 is a photograph of a packaged D-fiber electric field sensor placed next to a standard resistor to show scale. The maximum diameter of the outer tubing is 1.5 mm.

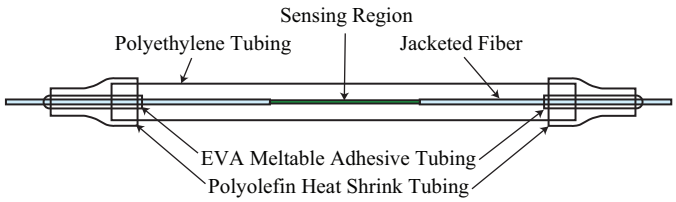

Figure 6.2: Illustration of the D-fiber packaging showing the various components.

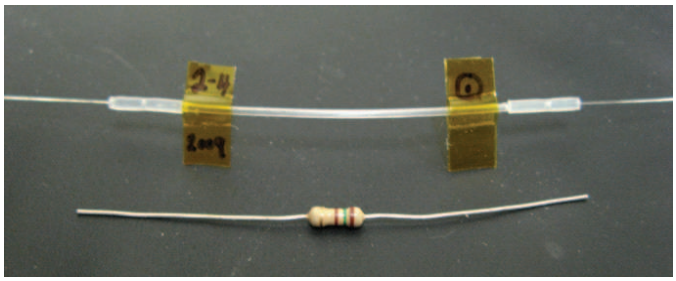

Figure 6.3: A photograph of a fully packaged AJL8/APC D-fiber sensor next to a standard resistor for scale comparison.

After the sensor is packaged, it is fusion spliced to make it compatible with standard optical sources and detectors. However, elliptical core D-fiber is difficult to fusion splice to other types of fiber due to its small core and D-shaped cladding. A method of splicing D-fiber to PANDA fiber, involving an elliptical core circular clad fiber (E-fiber) bridge splice was developed [70]. The E-fiber core is expanded to match the mode of the PANDA fiber. Then the D-fiber is connected to the E-fiber with a low temperature splice. The result is a low loss connection with standard PANDA fiber which can be connected to standard optical components. The final packaged sensor meets the requirement of having a small flexible cross-sectional area.

6.2 Testing

This section outlines several mechanical and electrical tests that show that this sensor also meets the desired requirements of mechanical strength, temporal stability, and minimal electrical perturbation. Another test is also performed to quantify the minimum detectable field strength of the low loss AJL8/APC D-fiber electric field sensor.

6.2.1 Mechanical Testing

During the fabrication of a D-fiber electric field sensor the region where the device is fabricated undergoes various processes which weaken the mechanical strength of that section compared to intrinsic D-fiber. First the protective jacket of the fiber is stripped away from the device region using a mechanical heat stripper. If the fiber comes in contact, even slightly, with the blades used to strip the jacket, small defects in the glass structure can be formed, which can act as cleaving points, thus weakening the mechanical integrity of the fiber. By chemically etching the fiber, and gaining access to the core of the fiber, the cladding diameter is also reduced from 80 μm to about 60 μm, or a 25% reduction in the cladding diameter. The reduced diameter results in a mechanically weaker fiber. Finally, during the handling or processing of the fiber device during fabrication some contamination can occur. The contamination

can act as a mechanical or chemical catalyst for a cleaving point, thus weakening the fiber.

In order to restore mechanical strength to the fiber, a compatible packaging technique is used. The final packaged sensor is 5 cm long with an outer diameter of 1.5 mm. The fiber geometry itself allows for even smaller package lengths and tubing cross-sections if desired.

The packaged fiber sensor was tested for tensile and torsional strength as well as bend radius. It is important that the fully packaged sensor retain most of the mechanical strength of a standard fiber so that it can be safely handled and placed in various testing setups. The mechanical tests that were chosen for this packaged sensor are representative of various types of forces that are applied when placing the sensor in a testing setup. For example, in some cases the sensor may need to be threaded through a small space, and bent in order to reach the desired sensing regions. Figure 6.4 illustrates the torsional, tensile, and bend radius mechanical strength tests. Table 6.2.1 records the results of each tests for a standard D-fiber which is unetched and fully jacketed, an etched fiber with a section of the plastic jacket removed, and a fully packaged etched fiber.

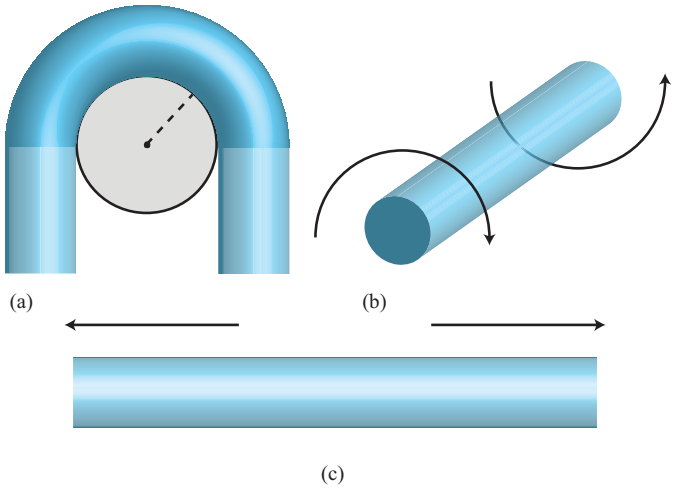

Figure 6.4: Illustration of the mechanical tests used to verify the physical integrity of the packaged sensor, a.) bend radius, b.) torsion, c.) tensile strength

Table 6.1: Mechanical Test Data

Test Type (units)	Sample Type	Value
Torsion (Rotations)	D-Fiber	5.5
	Etched D-fiber	2
	Packaged D-fiber	17
Tensile (Newtons)	D-Fiber	11.6
	Etched D-fiber	.94
	Packaged D-fiber	4.5
Bend Radius (cm)	D-Fiber	.08
	Etched D-fiber	2.12
	Packaged D-fiber	.11

The tests show that the packaged sensor shows improved mechanical strength over the etched fiber for each of the three types of mechanical stress. The tests also confirm that conditions common to the manual handling of these sensors are well within the tolerances of these sensors.

6.2.2 Electrical Testing

Electrical Perturbation

One of the principal advantages of optical fiber electric field sensors is that they do not significantly perturb the fields they measure. This allows them to give a more accurate reading of the field strength and distribution in compact spaces. The following section demonstrates that this is the case by showing a comparison of how the quality factor, Q, of a resonant cavity is affected by a fiber sensor and then by a series of small diameter conductive wires.

The resonator is formed in an X-band waveguide operating around 6 GHz. It consists of alternate sections of wax- and air-filled sections of waveguide to form a resonant tunneling structure. The operating frequency is below the X-band cutoff wavelength in air, but above cutoff in the wax region. This forms a moderate Q-resonator in the center wax-filled portion of the waveguide. Figure 6.5 shows how a fiber sensor is threaded through one millimeter holes in the opposing lateral walls of the resonator.

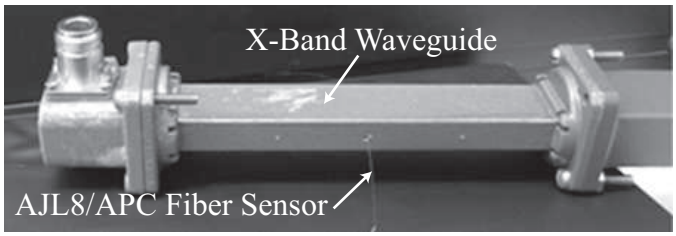

Figure 6.5: Photograph of an X-band waveguide formed into a resonant cavity. A fiber sensor is threaded through a hole which was made in the resonant cavity for the purpose of testing electric perturbation.

Excitation and measurement of the of the cavity Q using an Hewlett/Packard Model 8720C network analyzer produce a value of Q=1696 when the cylinder between the two opposing holes is filled with air only. The table shows how Q changes for the structure when that cylinder is filled with the fiber sensor and with conductive wires of different diameters. Note that the fiber sensor has a minimal effect on the Q and center frequency, even a small diameter wire perturbs the fields significantly as it decreases the Q and pulls the resonant frequency of the structure. The table also shows approximate values for the additional loss per pass caused by the perturbing medium. The additional loss for the fiber is insignificant while the loss per pass for even the smallest metal wire is greater than 7%.

Table 6.2: Electrical Perturbation Data

Material	Diameter (μm)	Q Factor	Loss Per Pass (GHz)	Frequency
Air	0	1696	6.2742	≈1 %
Fiber Sensor	125	1651	6.2743	≈1%
Metal Wire	10	297	6.2754	7%
Metal Wire	50	131	6.3015	15%
Metal Wire	70	75	6.2701	27%

6.3 Conclusion

This chapter reports the fabrication and testing of a packaged D-fiber electric field sensor using AJL8/APC as the sensing medium. This sensor withstands tensile stress up to 4 Newtons, torsional stress applied for 17 rotations, and bending stress down to a radius of .11 cm. The maximum outer diameter of sensor package is 1.5 mm. The total insertion loss of the sensor is 6 dB. The sensor has been shown to cause less than a 1% loss-per-pass in a resonant waveguide structure, proving that it is electrically non-intrusive. The sensor showed no temporal decay even 200 hours after poling. The sensor is capable of detecting fields of 50 V/m at and modulation frequency of 6 GHz with an E_π of 115 MV/m. Details of electrical tests which were packaged using this packaging technique are included in (8.8).

Chapter 7

Low Loss D-Fiber Fusion Splicing

Since the advent of optical fibers one of the principle challenges has been to find a means of creating low-loss splices. For large-core multimode fibers, mechanical alignment techniques were often sufficient to produce low-loss connections between fibers. Greater bandwidth requirements and the resulting intermodal dispersion at high frequencies motivated the use of single mode fiber. Techniques for microscopic alignment and methods such as electric arc fusion splicing thus became necessary. More recently the use of polarization maintaining (PM) fiber added the additional challenge of azimuthal core alignment, resulting in the development of new alignment methods [71, 72, 73].

In the passive azimuthal alignment method an automated algorithm determines alignment based on the imaged light intensity profile [71]. By observing the angular dependence of the light intensity profile, polarization axes may be determined, and the fiber can be set to a particular angular alignment. In contrast, the active alignment method directly aligns polarization states by using a polarizer to measure the maximum or minimum power transmission as a function of angular alignment. A combination of both passive and active schemes may be used together based on particular fiber requirements.

Each type of PM fiber has unique characteristics that determine the most appropriate splicing technique. PANDA fiber is one of the most common types of PM fiber and is designed so that the mode field diameter (MFD) and cladding diameter match well with other standard types of fiber. PANDA fiber uses stress to create an anisotropic refractive index in the core to make it polarization maintaining [74]. Figure 1 is a scanning electron microscope (SEM) image of the cleaved facet of a

PANDA fiber [75]. A back-scattered electron detector was used to increase the contrast between the various parts of the fiber. The core of the PANDA fiber is seen as a light circle in the center of the fiber in Figure 7.1(a). Note also in Figure 7.1(a) the stress rods that can be seen as two dark circles positioned on each side of the core.

These stress rods are the origin of the stress-induced birefringence. Figure 7.1(b) shows a more detailed view of the core of the PANDA fiber.

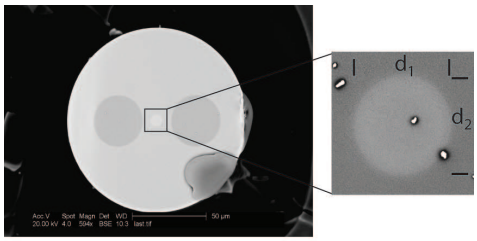

(a) (b)

Figure 7.1: SEM image of the cross-section of PANDA fiber (d1 = 7.805 μm, d2 =7.954 μm, NA = 0.12).

Figure 7.2 shows a cross sectional view of a polarization maintaining D-shaped optical fiber (D-fiber) [76]. The D-fiber core is positioned approximately 14 μm from the flat edge of the D-shape. Elliptical core D-fiber is PM due to the shape of the core. The size difference between the major and minor axes of the elliptical core shape affects modal confinement, yielding different effective indices of the modes [77]. The dark spot also seen in Figure 7.2(b) is an artifact of the fiber fabrication. Unfortunately, the core of the D-fiber has less than half of the cross-sectional area of the PANDA fiber core. A significant optical mode mismatch results from the cross-sectional core mismatch between the two fibers.

The non-standard core and cladding geometry of the D-fiber make it advantageous for infiber devices, due to the close proximity of the core to the edge of the cladding. However, in order to be more compatible with other devices it is important that the D-fiber be connected to a more standard type of fiber. A simple splice be-

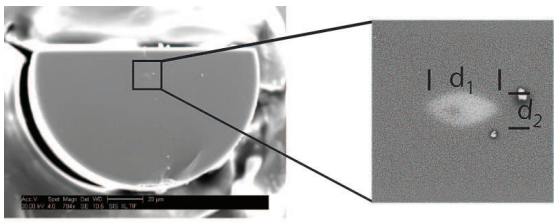

(a) (b)

Figure 7.2: SEM image of the cross-section of D-fiber (d1 = 4.689 μm, d2 = 2.181 μm).

tween D-fiber and PANDA fiber results in losses greater than 3 dB, because the small elliptical mode field of D-fiber is not well matched to the mode field of PANDA fiber.

We used a numerical modeling technique to determine the expected transmission loss due to the mode mismatch between PANDA fiber and D-fiber. In this analysis the refractive index profiles for each type of fiber are input into FimmWave (Photon Design, Oxford, UK) to determine the mode field. An overlap integral of the mode fields is then performed [52] resulting in 1.9 dB of loss for a direct connection between PANDA and D-fiber. In practice, the loss is greater than 3 dB due to factors such as core misalignment and the aforementioned deformation of the D-fiber cladding and core.

In order to reduce the splicing loss, the smaller fiber core needs to be gradually increased to match the size of the larger core. The core diameter can be gradually increased using local thermal diffusion [78]. However, the asymmetric shape of the D-fiber cladding complicates the core diffusion. Figure 7.3 shows an SEM cross-sectional image of a D-fiber before and after the application of an electric arc. Fluid dynamics and surface tension of the fiber at high temperature reduces the surface area to volume ratio and deforms the D-fiber into a more circular shape. In the process the fiber core is also distorted and shifted. The cladding and core deformation are problematic in any splice but are substantially worse following the long duration electric arc typically used for local core expansion.

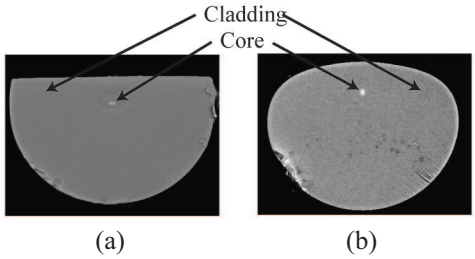

Figure 7.3: Cross-sectional SEM images of (a) standard D-fiber and (b) D-fiber after a high temperature arc.

7.1 PANDA to D-Fiber Splicing

This chapter presents a new method used to overcome the challenges of mode mismatch and fiber deformation during splicing between D-fiber and PANDA. Though the method described in this chapter deals exclusively with PANDA fiber the same approach can be taken to splice D-fiber to other types of stress induced PM fiber such as TIGER, Elliptical Clad, or Bowtie fiber. First, a PANDA fiber is spliced to an E-fiber, and then the E-fiber is spliced to a D-fiber. The technique whereby an additional fiber is used to splice two dissimilar fibers is called a bridge splice [79]. Using two separate splices the overall splice loss is reduced by creating a better match between the dissimilar fiber modes of PANDA and D-fiber.

E-fiber is chosen as the bridge fiber because its circular cladding matches with PANDA fiber, and its elliptical core matches with D-fiber. Figure 7.4 shows an SEM image of E-fiber (KVH Industries, Tinley Park, IL). Figure 7.4(b) shows a zoomed inset of the core of E-fiber which is taken at the same magnification as Figure 7.2(b).

A long duration high power electric arc expands the core of both fibers in the splice but has the greatest expanding effect upon the smaller core. The diffusion of dopants used to define the core results in a gradually larger MFD in the E-fiber and reduces the mismatch with the PANDA core. Since the cladding of the E-fiber is circular, the surface tension does not distort the shape of the cladding or cause any decentering of the core.

Figure 7.5 illustrates the resulting core expansion by showing a top view of the fibers in the splice along with cross-sectional SEM images of the core of the

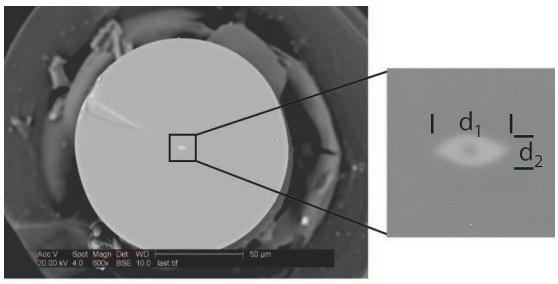

(a) (b)

Figure 7.4: SEM image of the cross-section of E-fiber (d1 = 4.885 μm, d2 = 2.152 μm, NA = 0.32)

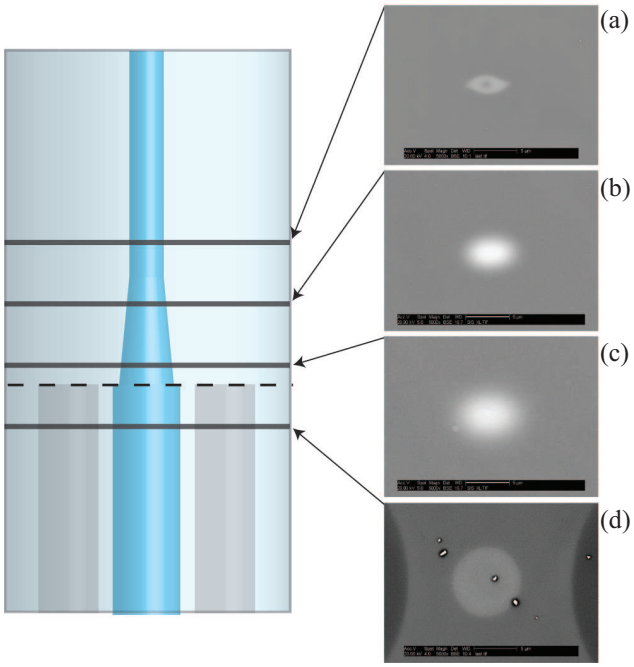

Figure 7.5: Illustration including cross-sectional SEM images of expanded elliptical core.

fiber at different points in the splice. Far away from the splice junction, Figure 7.5(a) shows that the core of the E-fiber is unchanged from its original cross-sectional shape. Approaching the splice junction, Figure 7.5(b) and Figure 7.5(c) show that the core expands to more closely match the PANDA core. Finally Figure 7.5(d) shows that the core of the PANDA fiber appears unaffected.

With the core of the E-fiber expanded a lower splice loss with PANDA fiber is possible, but the E-fiber still must be connected to the D-fiber. The E-fiber used in this method was chosen such that its core is the same as that of the D-fiber, making it possible to achieve a low loss splice between the two fibers. However, a low loss fusion splice is only possible if the splice can be accomplished without deforming the cladding and core of the D-fiber.

Figure 7.6 illustrates the dramatic cladding and core deformation of a D-fiber using a typical fiber splicing recipe, where the SEM images from which the illustration is based are shown in Figure 7.3. This figure shows how the surface tension forces act on the fiber when the fiber is molten during splicing. Since surface tension forces tend to reduce the surface area of the fiber, the corners on the D-fiber experience the most force. The shape of the core is distorted because of the asymmetric surface tension and the location of the core is also shifted relative to the curved surface of the D-fiber. Since the D-fiber and E-fiber have nearly identical core shapes, this distortion and displacement result in a significant increase in coupling loss. To eliminate the losses associated with the core distortion and displacement, a low-temperature and short-duration splice is used to attach the D-fiber to the E-fiber [80].

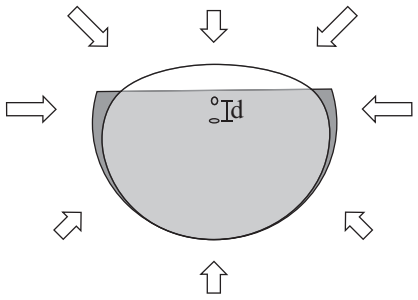

Figure 7.6: Illustration of the surface tension forces and an overlay of the two cross sections showing a core separation of d=10.6 μm.

7.2 Results

This section presents the results of applying the techniques described in the previous section. It describes how the PANDA to E-fiber splice is made, and then shows the technique used to create the E-fiber to D-fiber splice. Both splices are made using a Fujikura 40PM splicer.

A passive method is used to align the PANDA and E-fiber azimuthally. Next, an active alignment method is used to align the fibers laterally to maximize power transmission. Finally, the longitudinal alignment is set to 15 m for each splice. A prefuse arc is performed to soften the facets of the fibers. The PANDA fiber is then stuffed into the E-fiber while the splice arc is initiated. Figure 7.7 includes a plot of the transmitted power as measured during the splice as well as specific splice parameters. When the monitored transmission power is maximized the arc is terminated. Immediately after the splice arc, a lower power arc is initiated while the fibers are moved longitudinally in the direction of the E-fiber to further expand the E-fiber core. The cutback method is used to measure splice loss which was 0.41 dB on average for ten fibers. Further information regarding individual values is shown in Figure 7.8 (a).

Next, a D-fiber is spliced to the E-fiber. The length of the E-fiber used in the bridge is not important for the result and one meter was chosen for practical purposes. In order to prepare the D-fiber for splicing, it is necessary to create a smooth D-fiber facet. Unfortunately, the mechanical properties of the flat edge of D-fiber cladding make it susceptible to torsion. Undesirably large cleave angles result from torsion of the fiber during cleaving [79]. Applying longitudinal tension while scoring and cleaving the D-fiber in a Fujikura CT-04BS8 fiber cleaver produces adequate facet smoothness and cleave angles of less than 3 degrees.

A passive method is used again to align the E-fiber azimuthally. However, the light intensity profile used in the automatic passive alignment method is not easily recognizable for D-fiber. Therefore, the standard passive alignment system is unable to recognize the axes of the D-fiber core. Fortunately, D-fiber has angular diameter dependence. Since the flat of the D shape is parallel with the major axis

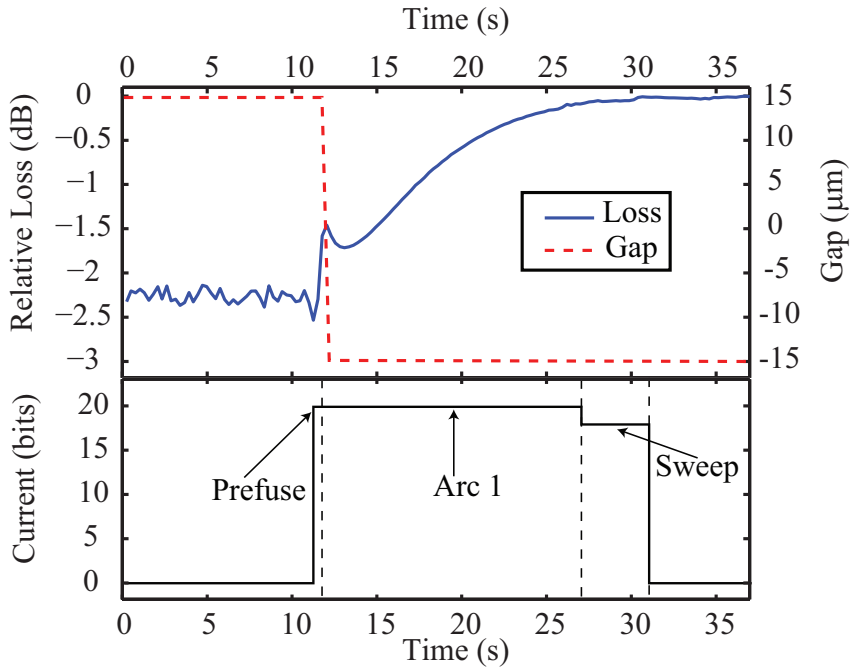

Figure 7.7: A plot of the relative loss as measured through the splice joint during the splice from PANDA to E-fiber. The gap was estimated from the splice parameters, the FSM-40 PM splicer manual, and the relative loss. The plot of the arc current shows the three phases of the splice, the prefuse, the arc, and the sweep.

of the elliptical core, the diameter dependence is aligned with the polarization axes. This dependence can be used to manually align the D-fiber azimuthally to the E-fiber. The D-fiber is then aligned laterally using manual power monitored feedback. Longitudinal alignment is again set to 15 μm for each splice.

A short pulsed low power prefuse arc is used to soften the ends of the fibers. After stuffing the E-fiber 12 m into the D-fiber, a short pulsed high power arc is applied to the fibers. Additional splicing parameters are included in Figure 7.7. While it should be noted that low temperature splices do not exhibit the same strength as a standard splice [79] the bond between the E-fiber and the D-fiber is more than sufficient to satisfy the 2.0 Newton pull test of the 40-PM as well as handling after the splice is completed. A protector sleeve is secured to the fibers when additional strength is needed.

Ten low temperature pulsed arc splices between E-fiber and D-fiber result in an average splice loss of 0.31 dB as illustrated in Figure 7.7(a). The cutback method

Table 7.1: The Relevant Splice Parameters for Both the PANDA to E-fiber and E-fiber to D-fiber Splices

Splice Parameters	PANDA to E-fiber	E-fiber to D-fiber
Cleaning Arc (ms)	150	150
Gap (μm)	15	15
Gapset Pos.	L-20 μm	Center
Overlap (μm)	15	12
Prefuse Power (bit)	20	20
Prefuse Time (ms)	450	320
Prefuse On (ms)	-	120
Prefuse Off (ms)	-	120
Arc1 Power (bit)	20	OFF
Arc1 Time (ms)	15000	-
Arc2 Power	OFF	15
Arc2 Time (s)	-	2
Arc2 On (ms)	-	200
Arc2 Off (ms)	-	200
Sweep Splice	R	OFF
Arc Power (bit)	18	-
Sweep Time (ms)	4000	-
Acceleration	OFF	-
Arc Start Position (μm)	0	-
Arc Stop Position (μm)	500	-

is used again to obtain the loss. The loss is higher than would be expected for the well matched MFDs of E-fiber and D-fiber. Though the MFDs are almost identical, losses have been reported due to the mismatch between the evanescent tails at the flat of the D-fiber [81]. Additional losses occur due to the manual alignment mode used.

The total transition between D-fiber and the PANDA fiber consists of both connections of the bridge splice. The total splice loss of the 10 splices had an average of 0.71 dB, which is substantially lower than the ideal splice loss of 1.9 dB that would be attained without any core expansion. The polarization crosstalk was measured for each splice and the results are show in Figure 7.8(b) to be less than 25 dB on average.

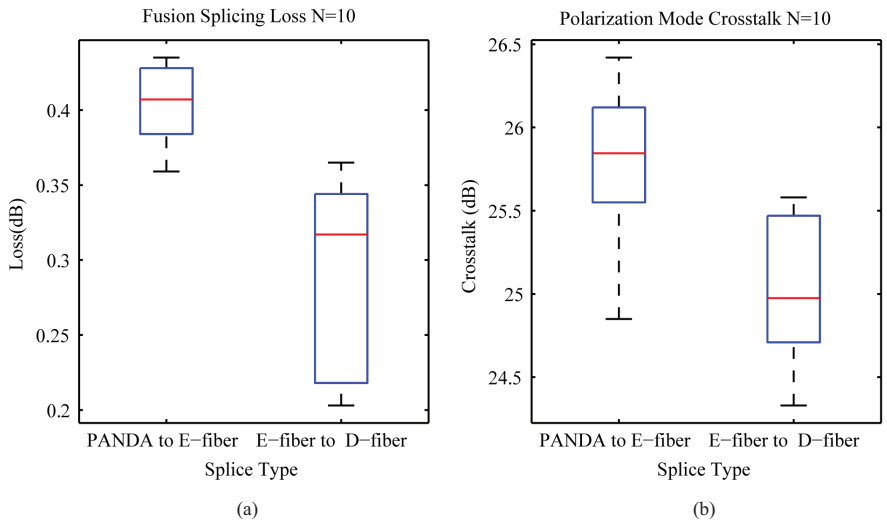

Figure 7.8: a) A boxplot of splice loss for PANDA to E-fiber and E-fiber to D-fiber splices. b) A boxplot of polarization crosstalk for PANDA to E-fiber and E-fiber to D-fiber splices.

7.3 Conclusion

The sensing of electric field with D-fiber is accomplished by converting electrical signals to an optical phase change. The optical signal must be input into the device and then retrieved from the device and measured. The challenge with this is that the core size and geometry of the core and cladding of D-fiber make it incompatible with standard equipment. The work in this chapter address the need for a low loss optical connection between standard equipment by developing a method of PM fusion splicing D-fiber to PANDA fiber with E-fiber as a bridge splice. The loss for the whole splice is less than 1 dB per D-fiber to PANDA fiber connection, making it a viable solution.

Chapter 8

Testing

The sensing of electric fields is accomplished by measuring the phase change of light in a hybrid D-fiber waveguide. This is accomplished by replacing the core of an etched D-fiber with an electro-optic polymer and then poling it. The device is then packaged and fusion spliced to make it compatible with standard test equipment. The ultimate proof of the effectiveness of this work is in the sensing of electric fields. This chapter describes testing methods that were used to characterize the sensitivity of these sensors. First, theory on how the phase change in the hybrid D-fiber waveguide is converted to and electrical signal is treated. Next, a detailed description of how the tests were performed for DR1/PMMA is included. Finally, the results for AJL8/APC hybrid D-fiber sensors are included. The sensors in this chapter showed electro-optic sensitivities of down to 50 V/m with a 6 GHz AC electric field.

8.1 Sensor Characterization Term

Since it is difficult to directly measure the effective indices of the modes, the sensor is characterized using

$$E_\pi = \frac{\lambda}{2n_0^3(r_{33} - r_{13})\Gamma L}, \tag{8.1}$$

where E_π is the electric field required to cause a change in birefringence that will result in a relative phase shift of π. The sensitivity of the sensor increases with decreased values of E_π which is decreased by increasing $(r_{33} - r_{13})$, Γ, or L. The E_π term is helpful because it quantifies the sensitivity by indicating the effects of all physical factors related to the device.

8.2 Stokes Parameters and the Poincaré Sphere

Substituting Eq. 8.1 into Eq. 4.62 and allowing the two modes to have different amplitudes the field becomes

$$\vec{E} = E_{0y}\hat{y} + E_{0z}\hat{z}\exp j\left(\phi_o + \pi\frac{E}{E_\pi}\right), \tag{8.2}$$

with

$$\epsilon = \phi_0 + \pi\frac{E}{E_\pi}, \tag{8.3}$$

the equation becomes

$$\vec{E} = E_{0y}\hat{y} + E_{0z}\hat{z}\exp j\epsilon. \tag{8.4}$$

The built in retardation ϕ_o, can be eliminated by measuring the change in ϵ.

$$\Delta\epsilon = \phi_0 + \pi\frac{E_2}{E_\pi} - \left(\phi_0 + \pi\frac{E_1}{E_\pi}\right) = \pi\frac{\Delta E}{E_\pi}. \tag{8.5}$$

A common way to represent E_{0y}, E_{0z}, and ϵ is with Stokes parameters

$$S_0 = I, \tag{8.6}$$

$$S_1 = E_{0y}^2 - E_{0z}^2, \tag{8.7}$$

$$S_2 = 2E_{0y}E_{0z}\cos(\epsilon), \tag{8.8}$$

and

$$S_3 = 2E_{0y}E_{0z}\sin(\epsilon). \tag{8.9}$$

The Stokes parameters are often normalized by dividing each parameter by S_0. This makes the intensity equal to unity. The normalized Stokes parameters for some polarization states of interest are listed in Table 8.1.

The Stokes parameters can be displayed visually on the Poincaré sphere as shown in Fig. 8.1. Points along the equator of the sphere correlate to linear polarization and the poles on the top and bottom of the sphere correlate to right-hand

Table 8.1: Normalized Stokes Parameters of Various Polarization States.

Polarization State	S_1	S_2	S_3
Linear Horizontal	1	0	0
Linear Vertical	-1	0	0
Linear +45	0	1	0
Linear -45	0	-1	0
Right-hand Circular	0	0	1
Left-hand Circular	0	0	-1

circular and left-hand circular polarizations respectively. Places between the equator and the poles correlate to elliptical polarizations.

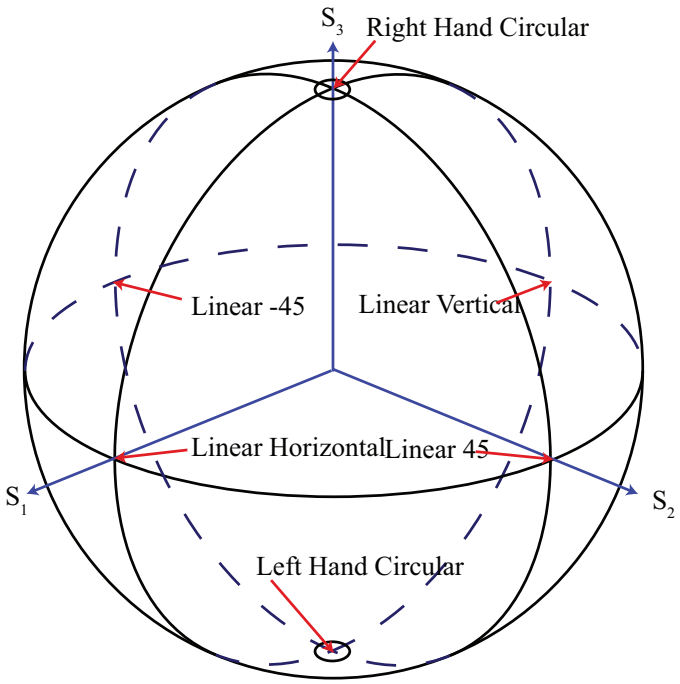

Figure 8.1: The Poincaré sphere is a way to visualize the Stokes parameters.

Changes in ϵ cause a change in the latitude on the sphere tracing out an arc around the sphere. If there is not equal intensity in the two modes, due to polarization dependent loss or unequally launched power, the arc will circle a smaller portion of the sphere. If more intensity is in the horizontal mode the arc will move closer to

the point on the sphere of horizontally polarized light and if there is more intensity in the vertical mode the arc will move closer to the point on the sphere of vertically polarized light as shown in Fig. 8.2.

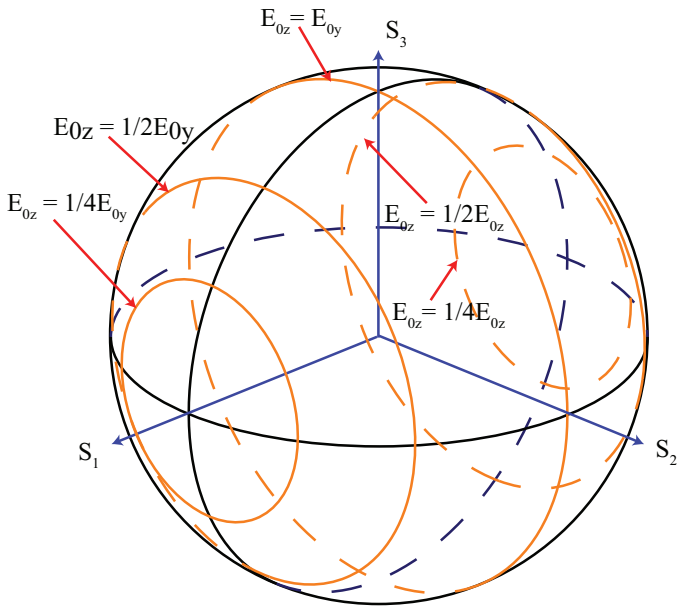

Figure 8.2: Unequal power in the two modes of the fiber will result in arcs on the Poincaré sphere with a reduced radius.

8.3 Transforming Polarization to Intensity

An electric field induced change in birefringence causes a phase change in the the polarization of the light at the sensor output. This change in polarization can be converted into an intensity change with a linear polarizer placed at the output of the sensor. A polarizer in this configuration is often called an analyzer. By taking the real part of Eq. 4.59 we have

$$\begin{aligned}\mathcal{E} = \Re\{\vec{E}\} =& \mathcal{E}_0\hat{y}\cos\left(wt - k_o N_{y,0} L_T - k_o \Delta N_y L_H + \Phi\right) + \\ & \mathcal{E}_0\hat{z}\cos\left(wt - k_o N_{z,0} L_T - k_o \Delta N_z L_H + \Phi\right). \end{aligned} \tag{8.10}$$

By placing a polarizer at an angle θ_p to the flat of the fiber in front of the sensor and an analyzer at an angle θ_a to the flat of the fiber at the end of the sensor, as shown in Fig. 8.3, Eq. 8.10 becomes

$$\begin{aligned}\mathcal{E} =&\mathcal{E}_0\hat{y}\cos\theta_p\cos\theta_a\cos\left(wt - k_oN_AL_T - k_o\Delta N_yL_H + \Phi\right) + \\ &\mathcal{E}_0\hat{z}\sin\theta_p\sin\theta_a\cos\left(wt - k_oN_zL_T - k_o\Delta N_zL_H + \Phi\right).\end{aligned} \tag{8.11}$$

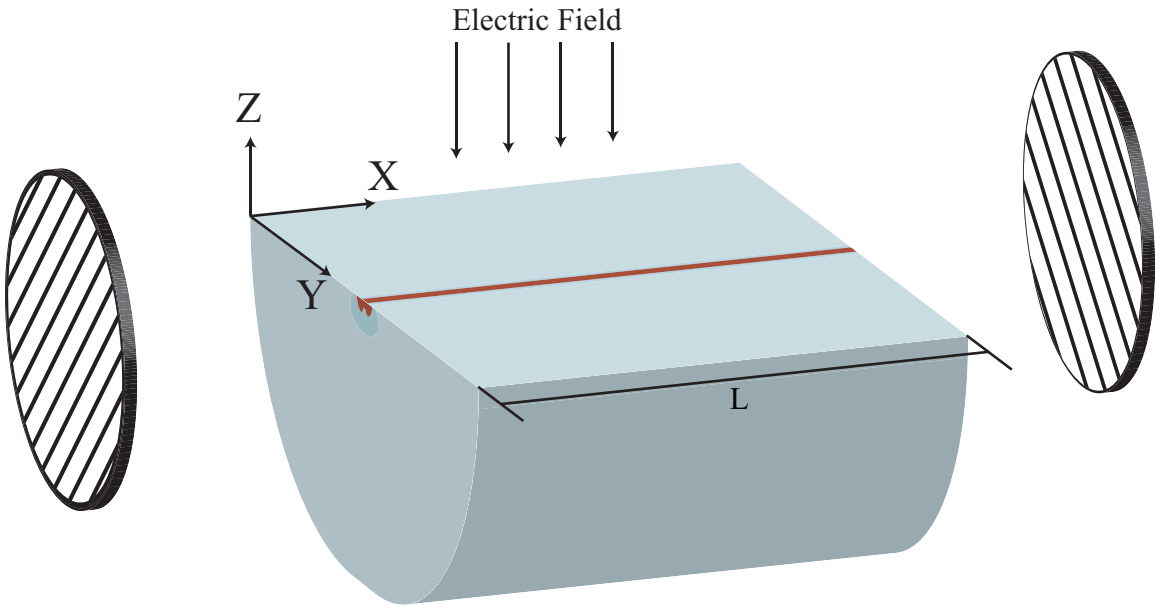

Figure 8.3: Linear polarizers in front and in back of the sensor are used to change the polarization into an intensity.

The irradiance received by an optical power detector is given by

$$I = \frac{1}{T}\int_o^T \mathcal{E}^2 dt \quad where \quad T = \frac{2\pi}{\omega}. \tag{8.12}$$

Substituting 8.11 into 8.12 and simplifying we have

$$\begin{aligned} I =& \mathcal{E}_0^2 \cos\theta_p \cos\theta_a \sin\theta_p \sin\theta_a \cos\left(k_0 L_H \left(\Delta N_y - \Delta N_z\right) + k_0 L_T \left(N_{y,0} - N_{z,0}\right)\right) \\ &+ \frac{1}{2}\mathcal{E}_0^2 \left(\cos^2\theta_p \cos^2\theta_a + \sin^2\theta_p \sin^2\theta_a\right). \end{aligned} \tag{8.13}$$

Substituting 4.58, and 4.61 into 8.13 the equation becomes

$$\begin{aligned} I =& \mathcal{E}_0^2 \cos\theta_p \cos\theta_a \sin\theta_p \sin\theta_a \cos\left(K_o \Delta B L_H + \phi_0\right) \\ &+ \frac{1}{2}\mathcal{E}_0^2 \left(\cos^2\theta_p \cos^2\theta_a + \sin^2\theta_p \sin^2\theta_a\right). \end{aligned} \tag{8.14}$$

Figure 8.4 shows the intensity as a function of applied electric field for different polarizer and analyzer angles. If both of the polarizers are at 45 or -45 degrees to the modes of the fiber the intensity sinusoid will have a maximum amplitude. If either of the polarizers is off of 45 or -45 degrees to the modes of the fiber the amplitude of the sinusoid will be decreased. If one of the polarizers is off of 45 or -45, the other polarizer can be adjusted to achieve maximum transmission or extinction but will also have the effect of reducing the sinusoidal amplitude. Although the diminishing amplitude caused by the polarizers being off of 45 and -45 makes the amplitude changes harder to detect, the E_π of the sensor is unaffected as long as the period of the sinusoid can be distinguished.

By setting θ_p and $\theta_a = \frac{\pi}{4} + n\pi$ and using Eq. 8.1 we have

$$I = \mathcal{E}_0^2 \left[\frac{1 + \cos\left(\pi \frac{E}{E_\pi} + \phi_0\right)}{4}\right]. \tag{8.15}$$

Using a power reduction identity

$$\cos^2(\theta) = \frac{1 + \cos(2\theta)}{2}, \tag{8.16}$$

the irradiance becomes

$$I = \mathcal{E}_0^2 \cos^2\left(\frac{\pi}{2}\frac{E}{E_\pi} + \frac{\phi_0}{2}\right). \tag{8.17}$$

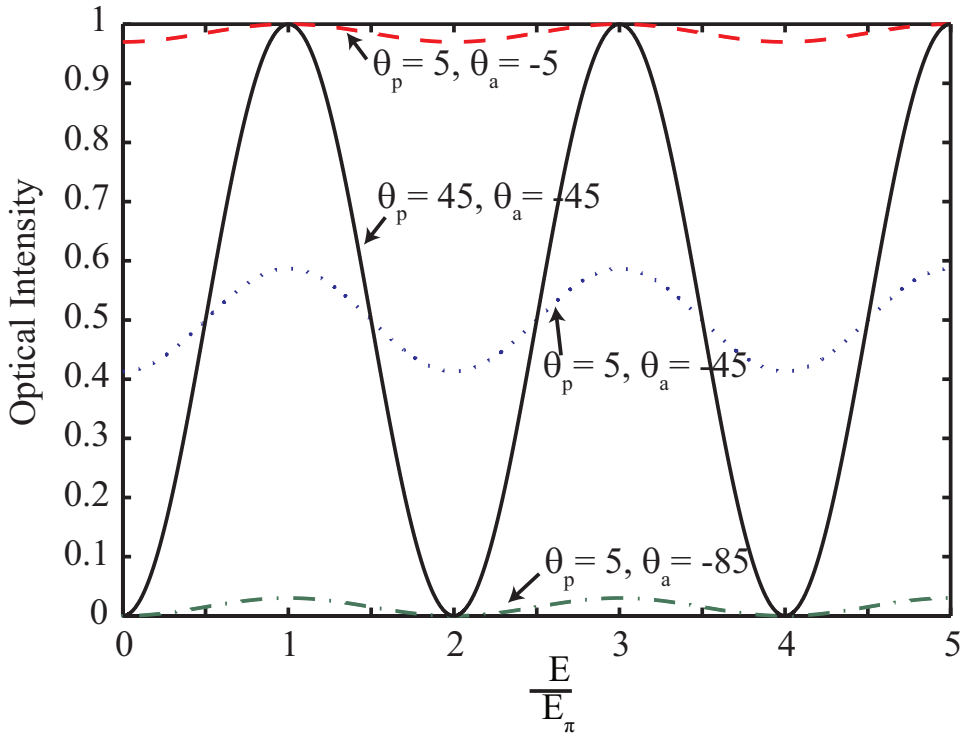

Figure 8.4: Plots of optical intensity with varying polarizer angles.

8.4 Use of FFT to Characterize E

If the applied electric field is a periodic alternating field, the E_π of the sensor can be characterized by applying a much smaller fraction of E_π with the use of a Fast Fourier Transform or FFT. The intensity of light after the linear polarizer, which is described by Eq. 8.17, can be turned into a voltage with the use of a optical power detector. An FFT can then be performed on the the voltage from the optical power detector with an electrical spectrum analyzer. The voltage corresponding to the optical power will be of the form

$$V = V_0 \cos^2\left(\pi \frac{E}{2E\pi} + \frac{\phi_0}{2}\right). \tag{8.18}$$

Where E is the applied electric field and E_π is the electric field required to cause a change in birefringence, ΔB, that will result in a relative phase shift of π. E is of the

form,

$$E = \Delta E \sin(wt). \tag{8.19}$$

If it is assumed that $E/E_\pi \ll 1$, and some trigonometric/algebraic manipulations are performed as in [82], the following relation is obtained,

$$\frac{V}{V_0} = \underbrace{\frac{1}{2} + \cos(\phi_0)\left[\frac{1}{2} - \frac{1}{8}\left(\frac{\pi\Delta E}{E_\pi}\right)^2\right]}_{DC\,value} + \underbrace{\frac{1}{8}\left(\frac{\pi\Delta E}{E_\pi}\right)^2 \cos(\phi_0)\cos(2wt)}_{Double\,frequency\,value} - \underbrace{\frac{\pi\Delta E}{2E_\pi}\sin(\phi_0)\sin(wt)}_{Single\,frequency\,value}. \tag{8.20}$$

If the bias point ϕ_0 is set to the quadrature point: $\phi_0 = \frac{\pi}{2} + n\pi$, Eq. 8.20 simplifies to

$$V = \underbrace{V_0\frac{1}{2}}_{DC\,value} - \underbrace{V_0\frac{\pi\Delta E}{2E_\pi}\sin(wt)}_{Single\,frequency\,value}. \tag{8.21}$$

Figure 8.5 shows the voltage output from the optical power detector verses the applied field. As the applied field is swept through multiple E_π voltages the resulting curve is a sinusoid with a period of $2E_\pi$ as modeled by Eq. 8.18.

With the requirements for Eq. 8.21 to be satisfied, the signal coming out of the optical power detector will be equal to E scaled by a factor that depends on the slope of the sinusoid modeled by Eq. 8.18. This signal is too small to detect with an oscilloscope, but because of its periodic nature it can be measured with the use of an FFT. If the FFT of this signal is taken and the DC bias is filtered out, the peak value at the frequency of E will correlate to the amplitude, ΔE_{out}, of the signal from the optical power detector. The E_π of the sensor can then be calculated with

$$E_\pi = \frac{V_0\pi\Delta E}{2E_p A_{FFT}}, \tag{8.22}$$

where E_p is the peak height of the FFT at the frequency of E and A_{FFT} is a scaling factor that relates the amplitude of the periodic signal to its FFT peak height.

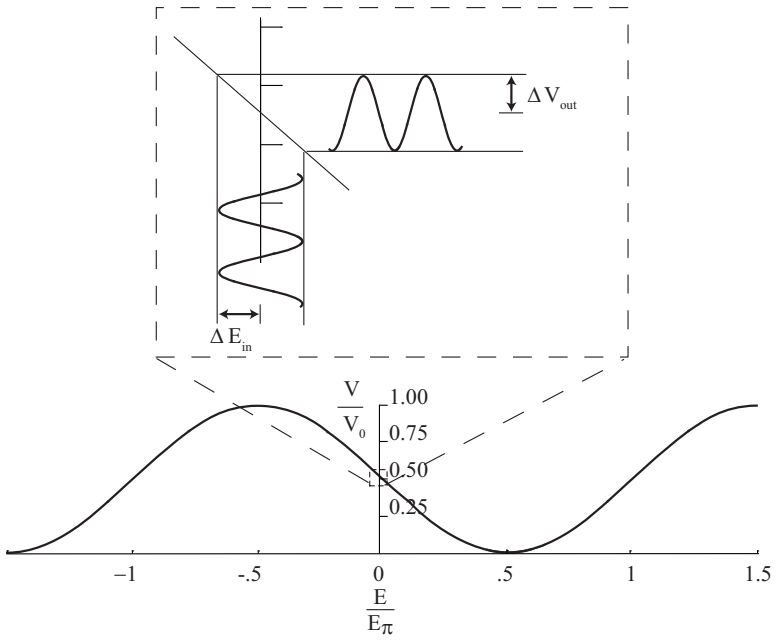

Figure 8.5: Optical power detector voltage output verses the applied voltage.

Figure 8.6 shows the percent error of the calculated E_π verses the number of degrees off of the quadrature point and the value of $\frac{\pi\Delta E}{E_\pi}$. This figure shows that even if $\frac{\pi\Delta E}{E_\pi} = 1$ and the bias point is off by plus or minus 36 degrees, the calculated E_π would only be off by a factor of two. This range of bias points of plus or minus 36 degrees is very practical to achieve being forty percent of all the bias points possible.

Because $\frac{\pi\Delta E}{E_\pi}$ is usually three or more orders of magnitude smaller than 1, the requirement of $\frac{\pi\Delta E}{E_\pi} \ll 1$ is almost always met leaving the accuracy of the calculated E_π dependent on the number of degrees the bias point is off of the quadrature point. Figure 8.7 shows that the bias point can be off of the quadrature point as much as plus or minus 24 degrees and still have a percent error of calculated E_π less than ten percent.

8.5 Polarimetric Sensing

The relative phase change between the two modes in the hybrid waveguide caused by an electric field creates a change in the polarization of the light at the end of the sensor. This change in polarization can either be measured directly using a

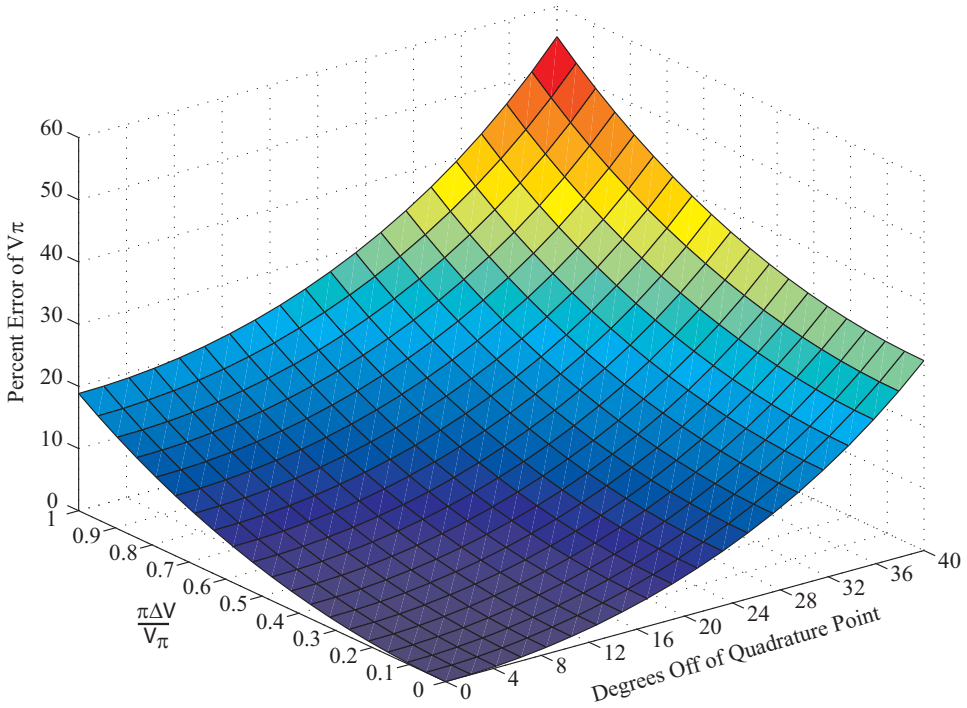

Figure 8.6: Percent error of the calculated E_π verses the number of degrees off of the quadrature point and the value of $\frac{\pi \Delta E}{E_\pi}$.

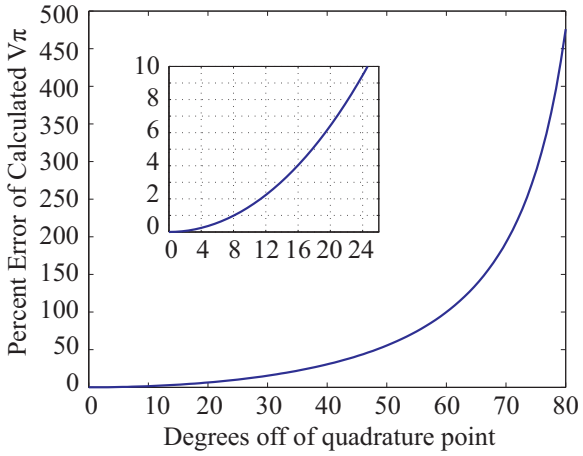

Figure 8.7: Percent error of the calculated E_π verses the number of degrees off of the quadrature point.

polarization analyzer or by changing the polarization into an intensity with a linear polarizer and measuring the change in intensity. Fig. 8.8 shows how the relative phase

changes correspond to polarization and intensity after the light is passed through a linear polarizer oriented at -45 degrees to the flat of the D-fiber.

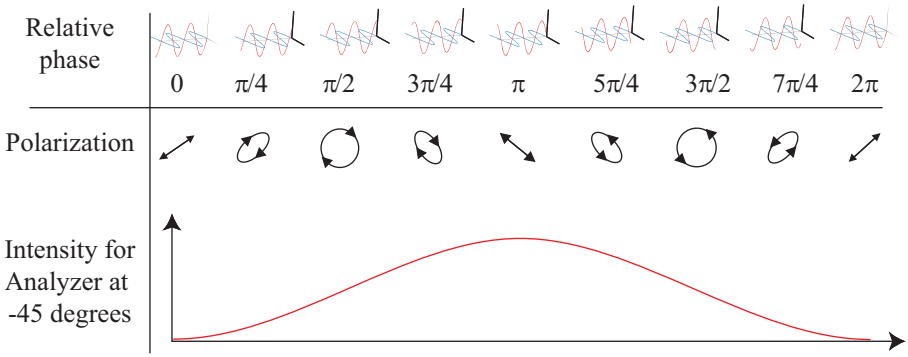

Figure 8.8: Relative phase changes between the light in the two modes of the sensor can be measured by measuring the polarization or by changing the polarization into an intensity.

If the applied electric field is created from a voltage across two electrodes, the voltage required to cause a relative phase change of π, or V_π, is first determined. The sensor is then SEM imaged to determine the spacing between the electrodes to be able to calculate E_π by dividing V_π by the electrode spacing.

8.6 Testing Set Up

8.6.1 Testing Sensors by Measuring Polarization

Figure 8.9 shows how the sensor is characterized based on polarization change. This is done by connecting one end of the sensor to a laser source and the other end to a polarization analyzer. An electrode is attached to the top of the cover glass and a voltage is applied between the two electrodes thus producing a specific electric field through the sensor.

The laser is focused into the optical fiber by the use of a three dimensional alignment stage. Before the laser light enters the fiber it passes through a linear polarizer and then a quarter waveplate that has its fast axis at 45 degrees to the linear polarizer to produce circular light. This is done to launch into both modes of

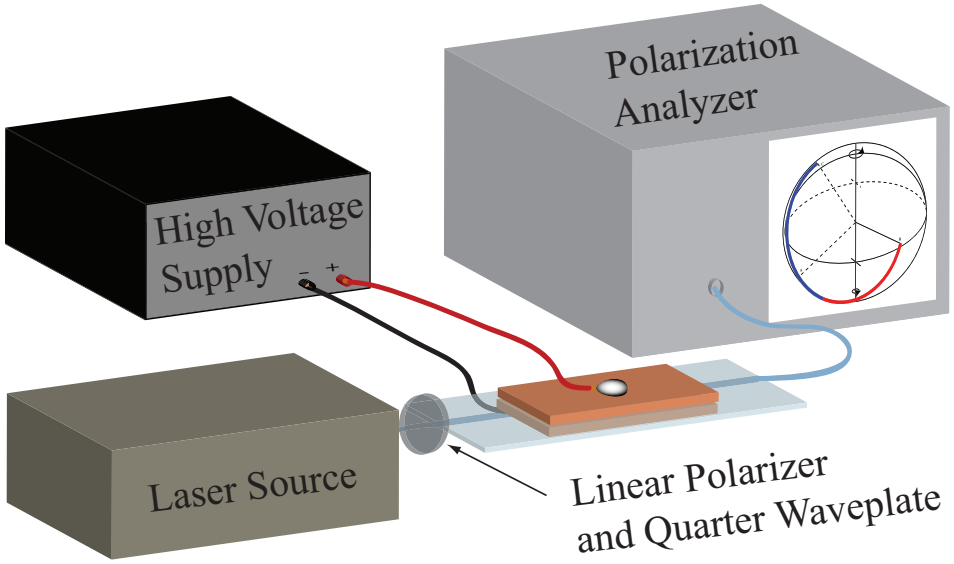

Figure 8.9: The sensors can be tested by measuring the polarization of the light guided in the sensor with a polarization analyzer.

the fiber regardless of the orientation of the elliptical core of the fiber. If polarization loss or unequal light coupling into the fiber is causing unequal amounts of light in the two modes, the unequal power can be compensated with the use of another polarizer after the quarter waveplate.

One advantage of using the polarization analyzer is that no biasing is necessary since the actual polarization states are obtained. The polarization analyzer displays the polarization state of the light coming out of the fiber on the Poincaré sphere. The polarization analyzer also gives the Stokes vectors and consequently the polarization state of the light.

For the exact polarization states to be measured it is essential that the modes of the fiber match up to the key on the polarization analyzer. If a relative polarization change is all that is needed the orientation of the fiber is insignificant. To better understand how the electric field is changing the polarization of the light it may be helpful to eliminate the birefringence of the system by applying a reference frame to the polarization analyzer (see the polarization analyzer manual for details on applying a reference frame).

The polarization analyzer is also able to measure the angle between selected points on the Poincaré sphere. An angle shift of 180 degrees correlates to a π phase shift if there is equal power in both of the modes. If there is unequal power in the modes the arc traced out on the Poincaré sphere will be smaller as shown in Fig. 8.2 and will result in the angle measurement being smaller.

The Stokes vectors for selected points on the Poincaré sphere can also be recorded and used to calculate V_π using Eq. 8.6-8.9 and Eq. 8.5. However, it is very important that the modes of the fiber are aligned correctly with respect to the polarization analyzer so that the angle change corresponds to a change in polarization and not a change in the intensity in the modes. If aligned properly, a change of polarization will create a change only in the latitude on the Poincaré sphere and changes in relative power between the modes will cause changes only in longitude on the Poincaré sphere.

8.6.2 Optical Intensity with a DC E-field Applied

Figure 8.10 shows how the sensor is tested by turning the polarization into an intensity. Equations 8.15 and 8.17 show that the measured power should fit a cosine function with a varying built in retardation ϕ_o. The built in retardation depends on a variety of parameters such as the temperature and stress on the optical fiber, and thus varies between measurement. V_π is calculated by plotting the optical power versus the applied voltage and fitting it to Eq. 8.17. The voltage required to go from a minima to a maxima is V_π.

8.6.3 Optical Intensity with an AC E-field Applied

AC testing can be used to measure the E_π of the sensors. This is done by applying a periodic signal to the sensor with electrodes or a horn antenna. The change in the polarization of light in the sensor is turned into an intensity with a

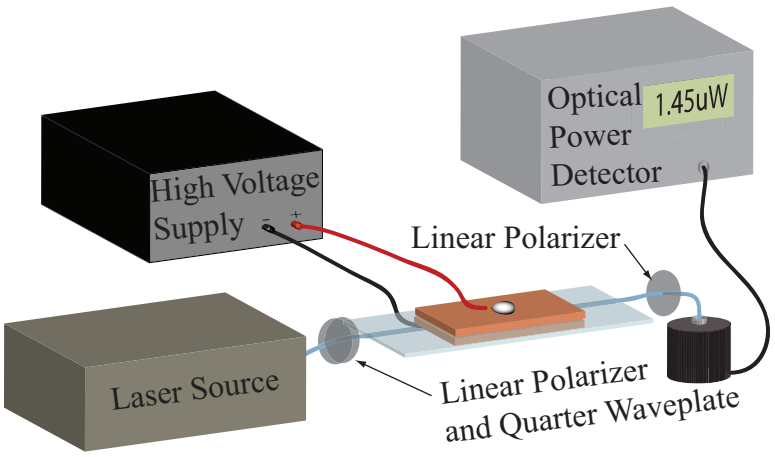

Figure 8.10: The sensor can be tested by converting the polarization state into intensity using a linear polarizer oriented at 45° with respect to the flat surface of the D-fiber.

linear polarizer. The signal is then detected by converting the optical intensity into a voltage with an optical power detector and then taking the FFT of the voltage signal as shown in Fig. 8.11. Testing the sensors in this manner can also be done at high frequencies to insure that the observed effect is an electro-optic effect.

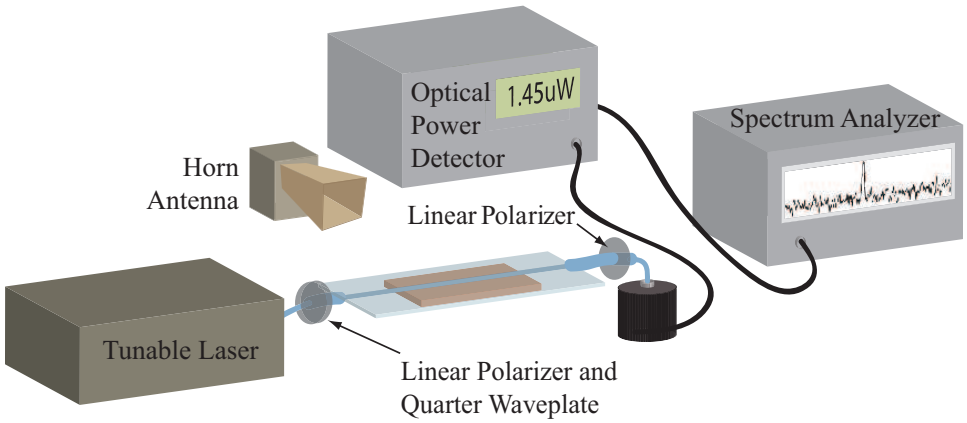

Figure 8.11: The E_π of the sensors can be calculated by biasing the sensor to the quadrature point and converting the intensity change into a voltage change and taking the FFT.

For the E_π to be measured in this configuration the sensor needs to be biased to a quadrature point. This can be done by adjusting the wavelength of the laser source which changes the bias ϕ_0 in Eq. 8.18. The voltage from the output of the optical power detector can be measured as a function of the laser source wavelength to determine V_0 and the wavelength needed to set ϕ_0 to a quadrature point as shown in Fig. 8.12. The quadrature point is set by finding the wavelength that causes the voltage minima and maxima and calculating the wavelength in the center of these two points. V_0 is the maximum voltage from the optical power detector.

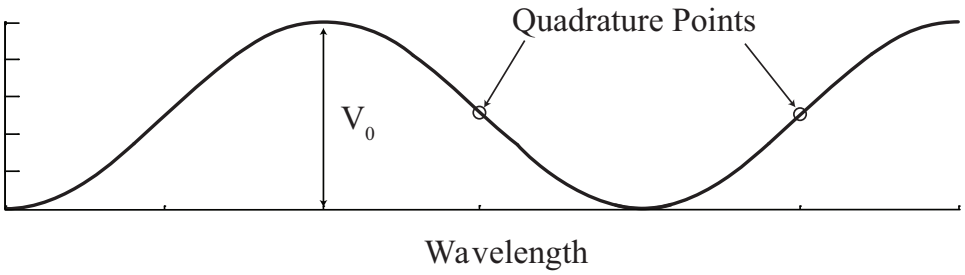

Figure 8.12: Adjusting the laser source wavelength can bias the optical intensity and therefore the corresponding voltage output from the optical power detector at the quadrature point.

With the wavelength of the laser source held constant at the quadrature point, a sinusoidal E-field is applied and the FFT voltage is measured at the applied signals frequency. The E_π and the $V_\pi$of the sensor can then be calculated with Eq. 8.22.

To Ensure that the AC testing set up can accurately measure the V_π of the sensors, a commercially available modulator was tested with the AC testing set up. The V_π of the modulator was measured with the AC setup with a varying bias point. Fig. 8.13 shows the percent error of the theoretical (solid line) and measured (points) V_π of the modulator verses the degrees the bias point was off of the quadrature point. As can be seen from the figure, the measured percent error follows the theoretical limit well.

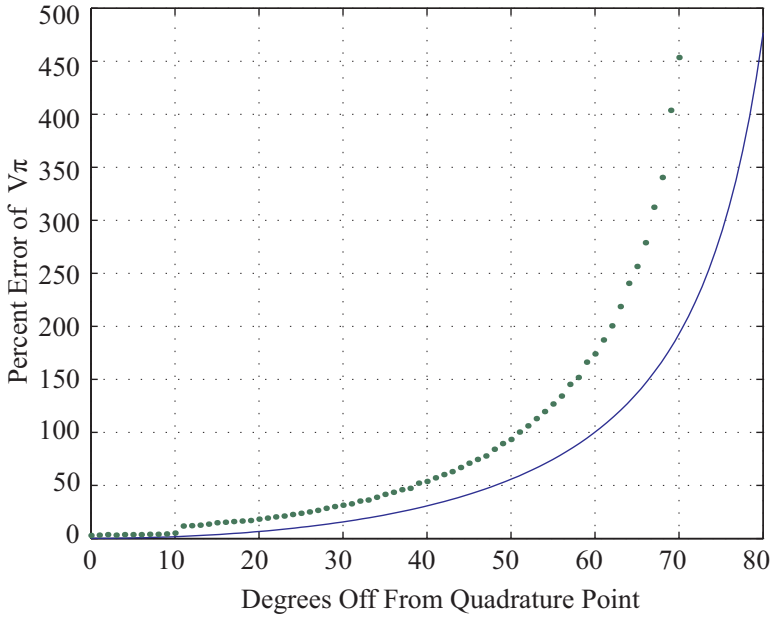

Figure 8.13: Percent error of the theoretical (solid line) and measured (points) V_π of the modulator verses the number of degrees the bias point was off of the quadrature point.

8.7 Results

This section demonstrates the operation of various sensors in different testing configurations. Testing of a thin and a thick polymer sensor by measuring the Stokes parameters with a polarization analyzer is demonstrated to show that the sensitivity of the device can be increased by increasing the thickness of the polymer. A sensor made with the optimized fabrication parameters is then demonstrated to have the increased sensitivity of a thicker polymer while maintaining the low optical loss of a thin polymer sensor by measuring the relative phase change of the sensor with the polarization analyzer. To validate the results measured with the polarization analyzer, the unoptimized thick polymer sensor that was tested with the polarization analyzer is also tested using an intensity based measurement. Finally, a sensor is shown to operate at high frequencies to ensure the observed effect is an electro-optic effect.

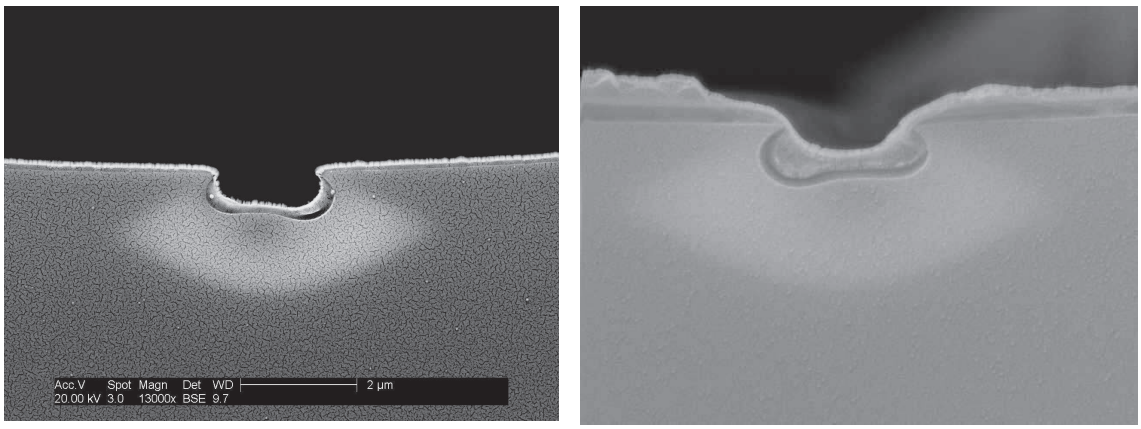

(a) (b)

Figure 8.14: Cross-sectional SEM image of D-fiber with the core partially replaced with (a) a thin layer of polymer and (b) a thicker layer of polymer

8.7.1 Measuring the Electrode Spacing

For the E_π of the sensors to be calculated the spacing between the electrodes needs to be known to be able to calculate the applied electric field. Figure 8.15 shows SEM images and illustrations of a sensor with a thin layer of polymer in the fiber core and a sensor with a thicker layer of polymer in the fiber core. From these images the spacing of the electrodes can be determined. The polymer thicknesses in the core of the fiber are shown in Fig. 8.14. Fig 8.16 shows an SEM image of the epoxy from the sensor made with the optimized recipe. The polymer thickness in the core of the fiber for this sensor is shown in Fig. 8.17. The applied electrical field is estimated by dividing the applied voltage by the measured electrode separation of $296\mu m$ for the sensor in Fig. 8.15a, $227\mu m$ for the sensor in Fig. 8.15b and $366\mu m$ for the sensor in Fig. 8.16.

8.7.2 Results of Testing Sensors by Measuring Polarization

With 9.5 kV applied to the sensors, the applied electric field is estimated to be $E = 32.1MV/m$ for the sensor in Fig. 8.15a and $E = 41.9MV/m$ for the sensor in Fig. 8.15b. The Stokes parameters are measured for no voltage applied, 9.5 kV

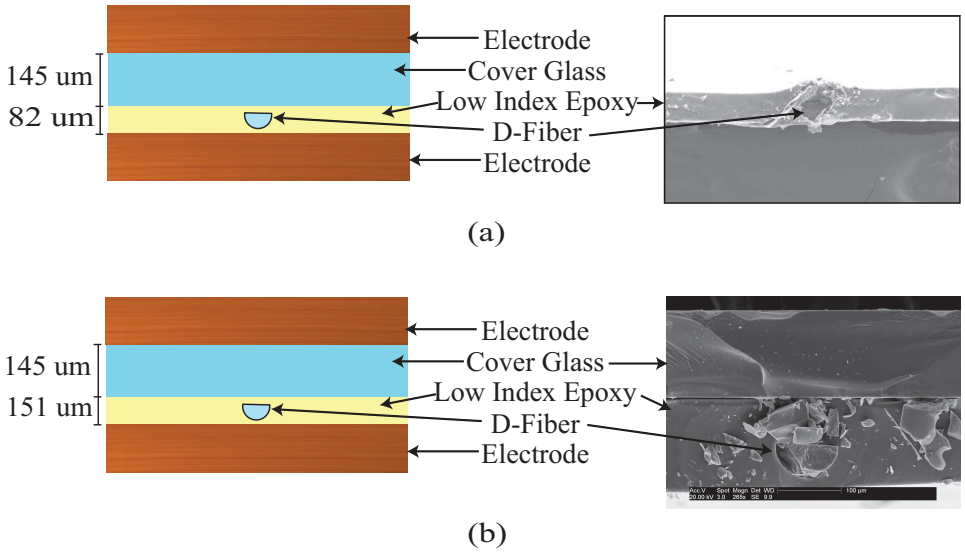

Figure 8.15: SEM images of planarized D-fiber sensors and a corresponding illustration for (a) sensor with thin EO polymer and (b) sensor with thicker EO polymer.

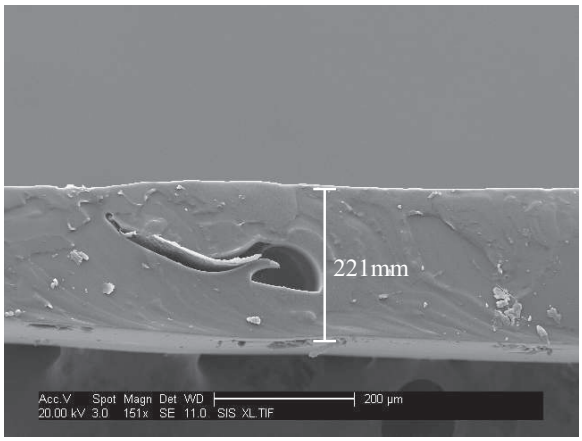

Figure 8.16: SEM image of the low index epoxy that encapsulated the sensor made with the optimized recipe.

applied, and -9.5 kV applied with the polarization analyzer. ϵ is then calculated from the Stokes parameters using Eq. 8.6-8.9.

With the applied electric field and ϵ known, E_π is calculated using Eq. 8.5. Tables 8.2 and 8.3 list the applied field, the normalized Stokes vectors, the polarization state parameters calculated from the Stokes vectors, and the resulting E_π for the

low loss (E_π=222 MV/m, loss≈1dB) and the higher sensitivity (E_π=60.2 MV/m, loss=14.4dB) E-field sensors respectively.

Table 8.2: Testing Results of Low Loss E-field Sensor.

Applied Field (MV/m)	**S1**	**S2**	**S3**	$\mathbf{E}_{0y}$	$\mathbf{E}_{0z}$	ϵ	$\Delta\epsilon$	$\mathbf{E}_\pi$ **(MV/m)**
32.1	0.73	-0.59	-0.37	0.675	0.738	0.3806	0.3775	267
0	0.80	-0.62	0.00	0.675	0.738	0.0031	0	—
-32.1	0.72	-0.55	0.44	0.675	0.738	-0.4509	-0.454	-222

Table 8.3: Testing Results of Higher Sensitivity E-field Sensor.

Applied Field (MV/m)	**S1**	**S2**	**S3**	$\mathbf{E}_{0y}$	$\mathbf{E}_{0z}$	ϵ	$\Delta\epsilon$	$\mathbf{E}_\pi$ **(MV/m)**
41.9	0.270	-0.398	0.877	0.797	0.604	1.997	2.186	60.2
0	0.270	0.946	-0.181	0.797	0.604	-0.189	0	—
-41.9	0.270	-0.444	-0.854	0.797	0.604	-2.050	-1.861	-70.7

A sensor that was made with the optimized recipe was also tested by measuring the relative phase change as a function of applied voltage (see Fig. 8.17 and 8.16 for SEM images of this sensor). Figure 8.18 shows the measured relative phase change and the calculated V_π versus the applied voltage. The calculated V_π is fairly constant once the applied voltage is high enough to overcome the noise caused by temperature and stress changes on the optical fiber. By taking the average calculated V_π over the range from 3 kV to 8 kV (30.4 kV) and dividing by the electrode spacing of 366μm, the E_π is calculated to be 83.1 MV/m. The optical loss of this sensor is measured to be only 1.4 dB.

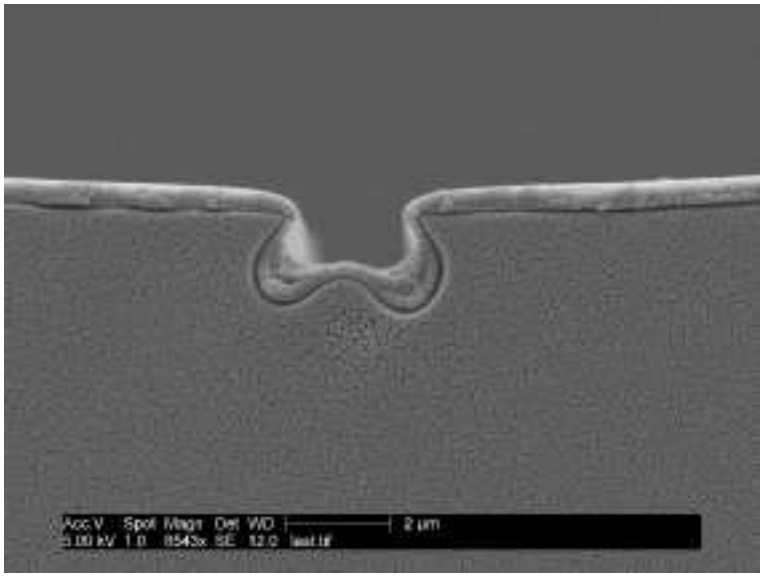

Figure 8.17: SEM image of a sensor made with the optimized hybrid waveguide parameters

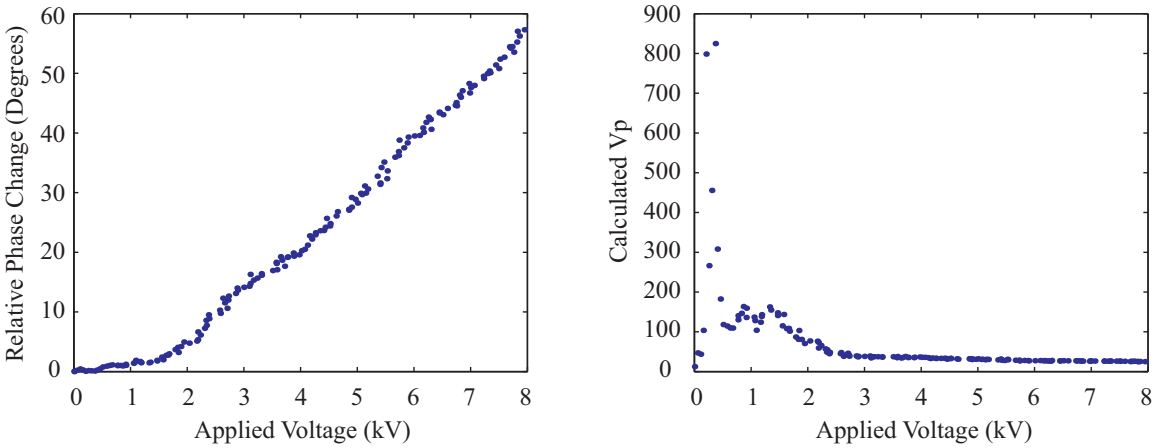

Figure 8.18: Measured relative phase change and the calculated V_π versus the applied voltage of a sensor made with the optimized recipe.

8.7.3 Measuring Optical Intensity with a DC E-field Applied

The sensor shown in Fig. 8.14b and 8.15b was also tested using the testing configuration shown in Fig. 8.10. Figure 8.19 shows the intensity of transmitted light as a function of applied voltage. By fitting this data to a cosine wave, the voltage required to change the power between adjacent minima and maxima (V_π) is

calculated to be 13.5 kV. By dividing this voltage by the electrode spacing of 227 μm the E_π is estimated to be 59.5 MV/m, which correlates well with the E_π of 60.2 MV/m obtained from the polarization analyzer data.

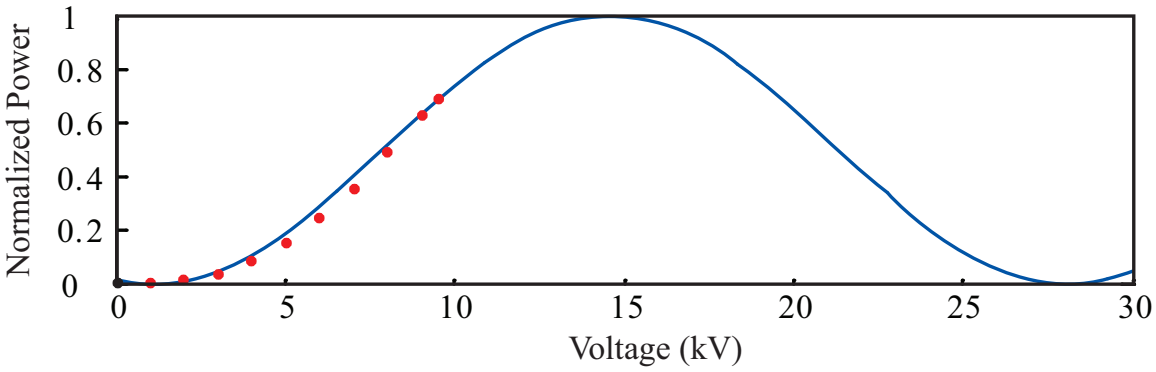

Figure 8.19: The measured power (dots) as a function of applied voltage and the corresponding fit (solid line).

8.7.4 Measuring Optical Intensity with an AC E-field Applied

To verify that the effect observed is in fact an EO effect, a sensor was tested at high frequency using an antenna horn to create an E-field around E=100 V/m as shown in Fig. 8.11. The optical signal created by the sensor is transported into an electrically isolated room by the use of optical fiber. The change in birefringence is converted into an intensity change using a polarizer as previously described. Figure 8.20 shows the resulting electrical signal that was generated using an electrical spectrum analyzer. A 2.9 GHz AC signal is detected by this sensor, demonstrating high frequency operation. The exact amplitude of the signal varied between measurements because of the arbitrary retardation ϕ_o.

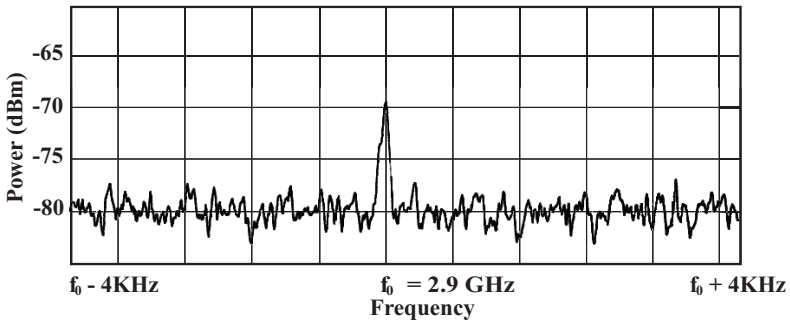

Figure 8.20: The measured power when an electric field is applied across the sensor with a frequency of approximately f=2.9 GHz and an amplitude of $E \sim 100V/m$.

8.8 AJL8/APC Device Testing

All of the testing method described previously in this chapter were developed for use with initial DR1/PMMA testing, and were subsequently used to test AJL8/APC waveguides as well. Figure 8.21 plots the angle change verses voltage for an AJL8/APC sensor. The maximum angle change was about 100 degrees, which corresponds to an E_π of 80 MV/m. This is comparable to the PMMA/DR1 because of the less than optimal poling field which was applied to AJL8/APC due to its conductivity. More information about why the r_{33} of the AJL8/APC and the resulting EO sensitivity was not as high can be found in Chapter 2.

The Stoke's parameters are extracted in order to calculate the angle change verses voltage, but they can also be plotted on the Poincaré sphere to get an idea of how much the polarization changed with a particular voltage. Figure 8.22 plots this data on a sphere.

8.8.1 Polymer Printed Hybrid Core Device Testing

It was necessary to test the AJL8/APC sensors which were fabricated using the polymer printing process in Chapter 5. Figure 8.23 illustrates the experimental setup used for testing. The test was performed using a polarizer analyzer configuration. A 1550 nm laser source with a 3 nm tuning range was input into the D-fiber sensor, input

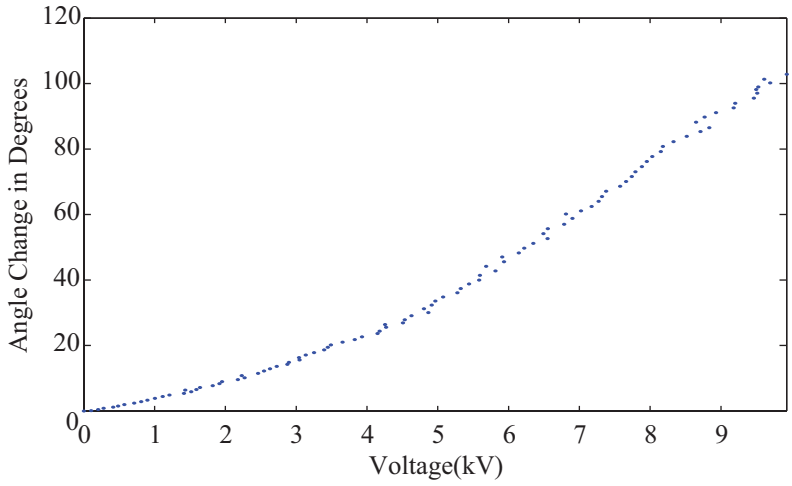

Figure 8.21: A plot of the angle change verses applied voltage for a AJL8/APC sensor. This sensor exhibited an $E_\pi = 80$ MV/m.

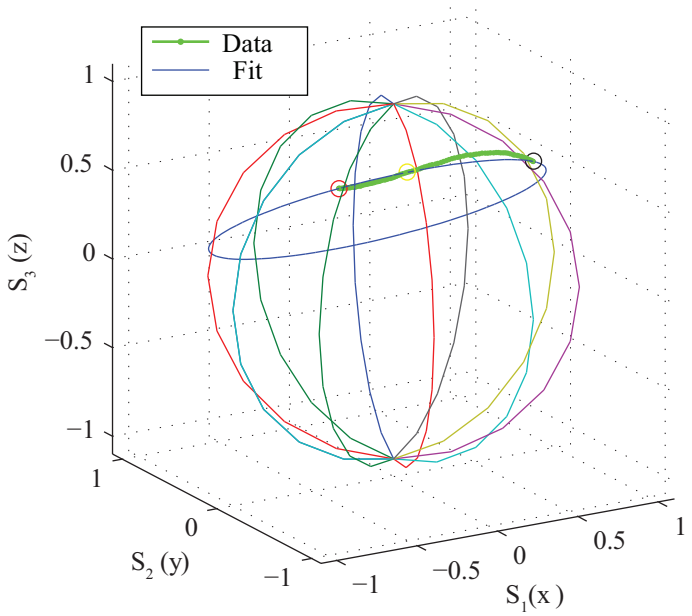

Figure 8.22: Three dimensional plot of the Stoke's parameters for an AJL8/APC sensor that was tested with a DC highvoltage source. The record data traces out part of a circle of and a circle is drawn to fit the data.

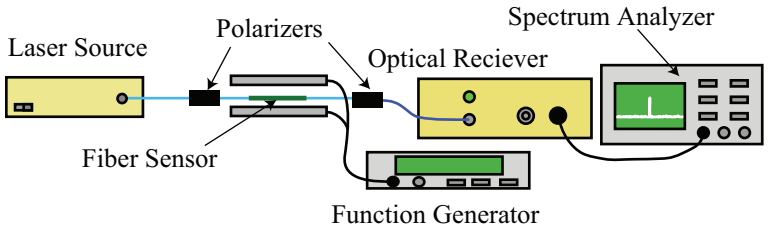

Figure 8.23: AC testing setup for in-fiber electric field sensors

and output polarizers were set at 45 degrees, and the optical power from the sensor was input into an optical receiver. The electrical signal from the optical receiver was measured with a spectrum analyzer.

The fiber sensor was place between two electrodes with a 0.5 mm gap, where the normal to the electrode was in the same direction as the poled axis of the fiber sensor. A 10 V peak-to-peak sinusoidal waveform with a frequency of 100 kHz was applied to the electrode resulting in an applied voltage of 20 kV/m.

The sensor's quadrature point was determined by tuning the wavelength of the laser source so that the FFT signal was maximized. The spectrum analyzer was set to a 24.4 HZ bandwidth, and the signal was recorded with Labview. Figure 8.24 plots the resulting FFT spectrum for the AC signal obtained at a field of 20 kV/m. The minimum detectable field above the noise floor was around 4 kV/m. With more careful alignment of the fiber to the polarizers and by amplifying the signal, the sensitivity of the device would scale with increased optical power.

8.8.2 Temporal Stability

Not all EO polymers retain their EO response for a sufficient amount of time to be viable in electric field sensing devices [11]. Thus, it is important to verify that the response of these AJL8/APC D-fiber sensors are temporally stable. To that end, a sensor was tested for temporal EO response by applying a DC electric field and measuring the change in the output polarization state with an Agilent 8509B

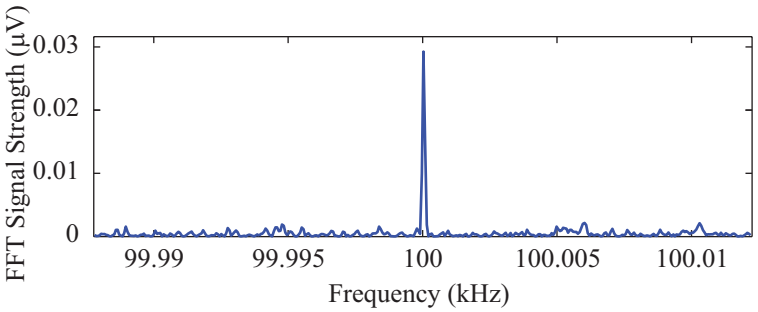

Figure 8.24: FFT response of an ink-jetted D-fiber electric field sensor with a 100 kHz signal applied that had and amplitude of 20 kV/m

Polarization Analyzer. Figure 8.25 illustrates the experimental setup used in this test. A 1550nm source is transmitted through a polarizer, converted to circularly polarized light, and then input into the D-fiber electric field sensor. The sensor output is fed into the polarization analyzer. A LabView interface is used to control a high voltage source and record the the angle change during testing. The LabView program tests the fiber once per hour and records the results. Figure 8.26 plots the change in polarization state for a given reference voltage each hour for over fifty hours. The sensor was tested again after 175 hours had elapsed from the time of poling. Again, the sensor was tested 50 hours, and the results recorded. The final angle change of the sensor after 220 hours was within 10% of the initial angle change. The variations in angle change are due to variations in biasing during the testing.

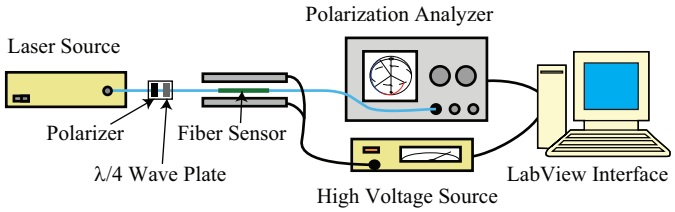

Figure 8.25: Experimental setup used to test the D-fiber sensor for its electro-optic temporal stability

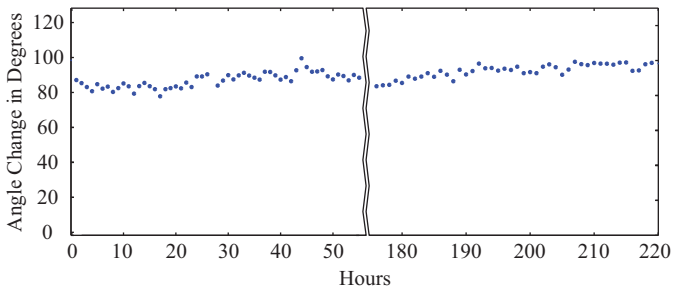

Figure 8.26: Plot of the amount of phase change in a AJL8/APC D-fiber sensor each hour for a period of 220 hours.

This test confirms that the AJL8/APC D-fiber electric field sensor meets the temporal stability requirement. A similar test performed with an AJL8/APC slab was used to show that this material maintains over 80% of its EO response when heated to 85 °C for more than 500 hours [33].

8.8.3 Electrical Sensitivity of a Fully Packaged AJL8/APC D-fiber Sensor

In order to ensure that the packaging method was compatible with poled hybrid D-fiber sensors a fully packaged, fusion spliced AJL8/APC D-fiber electric field sensor was shipped off-site for high frequency testing in an extended Mach-Zehnder interferometer configuration. The total fiber length of this sensor is 3 meters, as measured by an optical reflectometer. The total insertion loss, including polarization maintaining fusion splices was 6 dB. The sensor was inserted into a waveguide and was exposed to a 50 V/m electric field at a modulation frequency of 6 GHz. The resulting optical signal was transmitted to a photo-detector. The electrical signal from the photo detector was fed into a spectrum analyzer. Figure 8.27 shows the data obtained from the spectrum analyzer showing that there is a detectable signal at about 6 GHz. The device sensitivity, E_π of this sensor was calculated to be 115 MV/m.

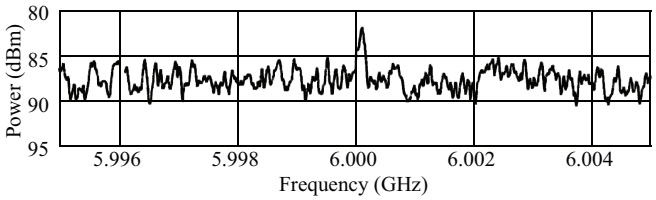

Figure 8.27: Spectrum analyzer plot showing the received optical signal for a 50 V/m electric field with a modulation frequency of 6 GHz.

8.9 Conclusion

We have reported the design, fabrication, and testing of a packaged D-fiber electric field sensor using DR1/PMMA and AJL8/APC as the sensing medium. The packaged AJL8/APC sensor as showed no temporal decay even 200 hours after poling. The sensor is capable of detecting fields of 50 V/m at and modulation frequency of 6 GHz with an E_π of 115 MV/m.

Future work aims to increase device sensitivity by using alternative poling techniques, and using an EO polymer with a lower index of refraction allowing for greater single-mode optical power confinement to the EO polymer.

Chapter 9

Fiber Patterning for In-Fiber Device Fabrication

9.1 Motivation

Optical fiber systems are currently made up of discrete components which require alignment between fibers, lasers, detectors, multiplexers, etc. While the connection between fibers has been made to be very efficient and simple, other components are more difficult to interface with fibers. One method of making these systems simpler, more efficient, and more cost effective is to make active fiber devices. This would mean that the whole system is contained within the fiber making it easy to connect devices together. Fiber devices such as these are often referred to as in-fiber devices.

In the electronics industry a similar integration from discrete to integrated components has taken place over the past few decades. This integration has driven circuit prices down and performance up. There is hope that the same may be done with optics; research on in-fiber devices is indicative of this hope. Two devices that show the successful implementation of in-fiber devices in commercial products are: the erbium doped fiber amplifier [83] and fiber Bragg gratings [84].

In order to fabricate in-fiber devices several things are needed.

1. The core of the fiber must be partially removed, and exposed for the strongest interaction with the optical material.

2. There must be an efficient transition between the core and the optical material.

3. An electrical connection to the optical fiber must be made. This is usually done by using electrodes, which are spaced metal strips.

In-fiber devices are produced using a variety of processes which include etching, polymer deposition, patterning, and electrode deposition, to name a few. Making complex devices usually requires some type of patterning. Two novel approaches for the successful patterning of in-fiber devices are (1) to encapsulate the fiber so that fabrication challenges are reduced to a planar fabrication process, and (2) to use a self-aligning patterning method.

9.2 Fiber Device Fabrication Challenges

The first major challenge in working with fibers is the fact that the core of the fiber, the area through which light is transmitted, is surrounded by a protective cladding layer. Figure 9.1 illustrates the cladding and core structures for the industry standard fiber (SMF28), and for D-fiber. All the significant interactions of fiber devices take place in the core of the fiber. In standard fiber, the core is surrounded equally on all sides by a cladding layer, making it difficult to reach the core. KVH Industries has developed a D-shaped fiber that allows for easier access to the core, allowing for direct interaction with the light traveling through the core. A HF acid etch, immersing the fiber in a bath of HF acid, can then be used to remove the surface of the fiber, exposing the core for direct interaction with the desired device.

Other challenges of fiber device fabrication include the following.

1. The orientation of D-fiber needs to be maintained such that the flat of the surface of the fiber is parallel with the mounting surface. The fibers tend to twist and bend and even slight bending and twisting could result in inconsistent device fabrication.

2. One major method of applying thin films used in making in-fiber devices is to spin the material on the fiber at speeds at or exceeding 2000 rpm. These high spin speeds mixed with the chemistry of the material being spun, and the geometry of the fiber produce undesirable spin effects.

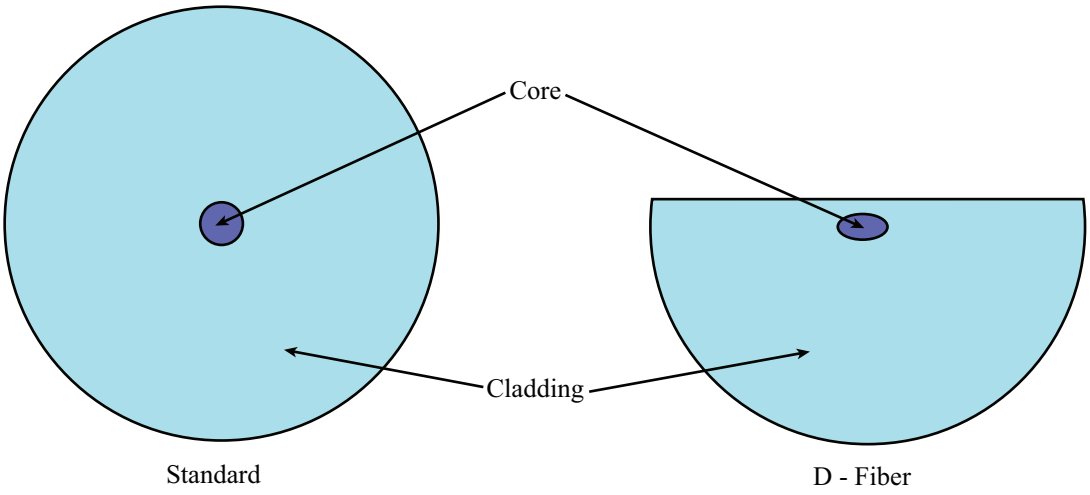

Figure 9.1: Illustration of the optical fiber geometry for standard fiber and D-fiber

3. Fibers are fragile; hence a plastic jacket surrounds the optical fiber to increase its strength. When fabricating In-fiber devices, the plastic jacket around the device area is removed making it extremely fragile.

4. The core diameter of fibers is in the micron range, making it difficult to selectively pattern anything just over the core, or not over the core.

A method was developed that eliminates all these problems and reduces the fiber device fabrication to a planar substrate fabrication problem. The process is called fiber encapsulation.

9.3 Encapsulated Fiber Patterning

The first step to encapsulating a fiber is to ensure that the fiber is mounted completely straight and flat side up. This fiber orientation is crucial so that subsequent alignment to the core is possible. Figure 9.2 shows how a silicon V-groove is used as a means of keeping the fiber in place in such a configuration.

Figure 9.3 shows how the flat side of the fiber is covered to prevent any material from contaminating the sensitive core region of the fiber. A simple method using tape

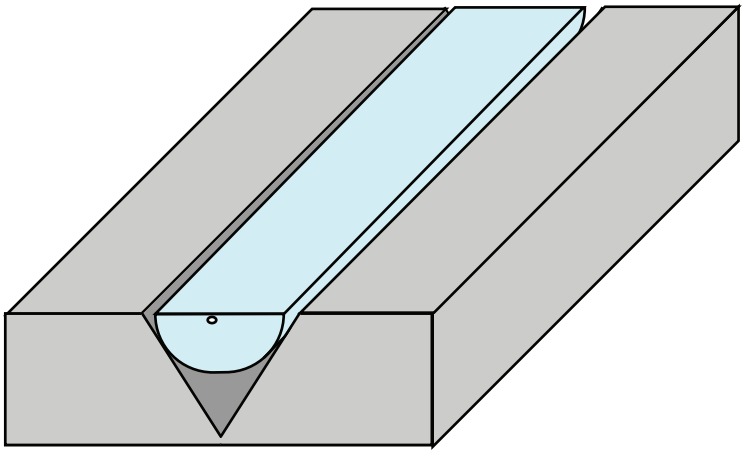

Figure 9.2: Illustration of the Silicon v-groove with the D-fiber positioned flat side up

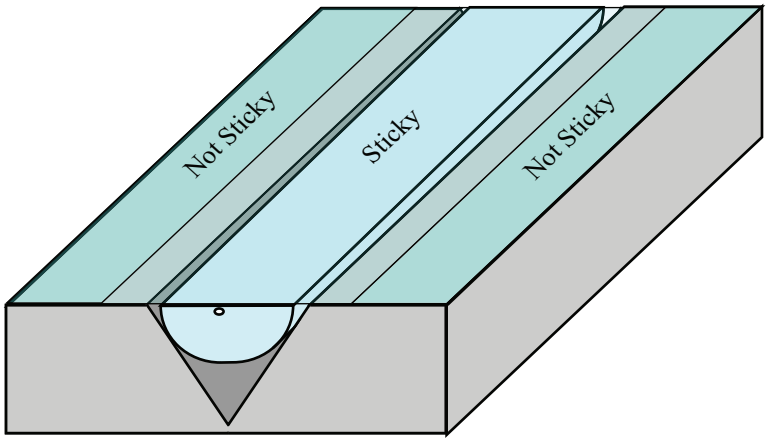

Figure 9.3: Illustration of the application of tape to protect the fiber surface from being covered with epoxy or other contamination

to make contact with the flat side of the fiber is one possible solution. The tape must be made to stick only to the fiber, and not to the silicon, so that the fiber may be removed from the v-groove while maintaining its straightness.

An epoxy is then applied to the back side of the fiber. It should then be cured until the epoxy is hardened enough to remove the tape. Figure 9.4 shows how the epoxy is applied and how the tape is then removed. The result is a straight fiber, which is encapsulated in a protective material that forms a planar surface. This planar surface is conducive to the fabrication of devices.

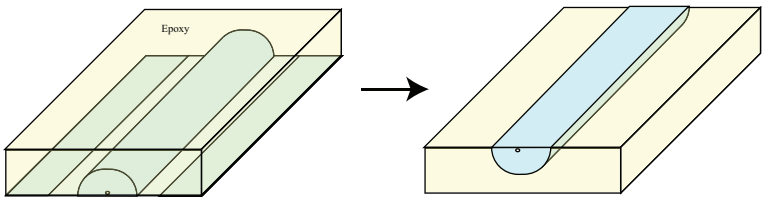

Figure 9.4: Illustration of the epoxy deposition and the final encapsulated fiber

9.4 Solutions to Fiber Device Fabrication Challenges

1. The fiber cannot bend or twist when encapsulated in epoxy
2. The planar surface that the epoxy and fiber create, allow for standard spinning techniques, which are the most common for applying thin materials to a surface.
3. The fragile area of the fiber is encased in epoxy making it more robust.
4. A pattern can be made on the surface of the embedded fiber using standard photolithography, the method that integrated circuits now use.

Certainly with any solution, new problems arise, and such is the case with fiber encapsulation. Using the embedding technique which is presented here offers many advantages, but some challenges still need to be overcome. For example, it is possible that during the embedding process that the epoxy will have some wedge problems between the top and bottom surface. Also the fiber flat itself may not be completely parallel to the epoxy plane. There are also some challenges with patterning fibers lithographically. One challenge is that it can be difficult to align a pattern to the core of a fiber. The microscopic features, even if only slightly off would make the device unusable. While not offering some of the same benefits of fiber encapsulation another method promises to eliminate the need for difficult alignment. It is called self-aligned patterning.

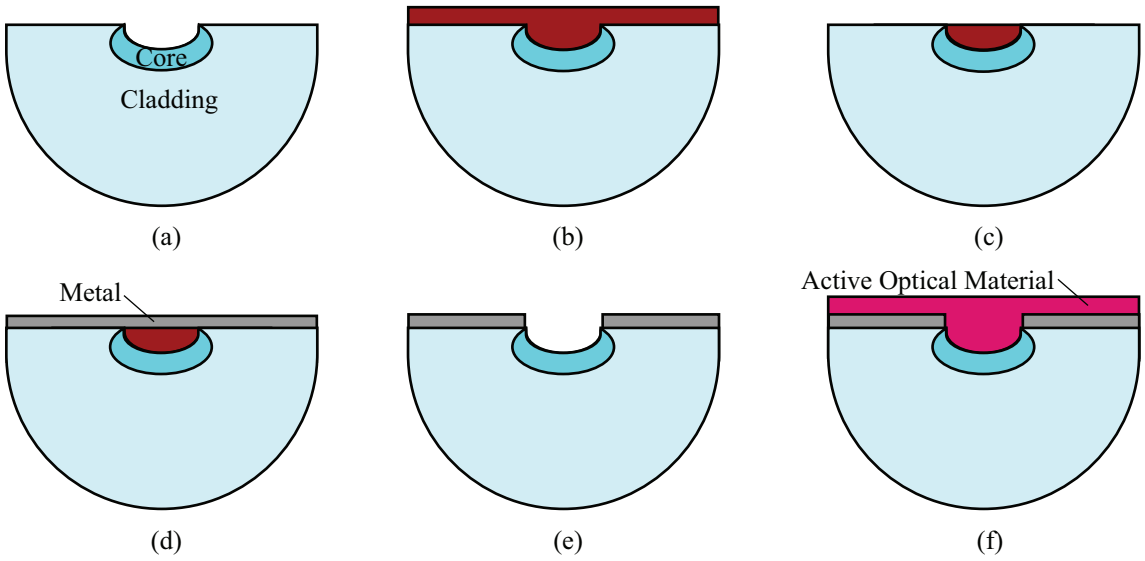

Figure 9.5: Illustration of the self-aligned patterning process flow

9.5 Self-aligned Patterning

In order to reach the core of an optical fiber Hydrofluoric (HF) acid is used to etch away the glass. The rate of the etch is dependent upon the characteristics of the material being etched and the chemical etchant. The core of an optical fiber is made up of a slightly different material than the cladding. This difference makes the etch rate of the core much faster than the etch rate of the cladding, so once the core is reached, it etches quickly away. This process of etching only a portion of the core is well characterized by monitoring the transmitted power during the etch. Figure 9.5(a) shows the etched out fiber core as the start of the self-aligned patterning process. The end product is a

A polymer material is then applied to the fiber, filling the groove and creating a flat surface (Figure 9.5(b)). A plasma etch is then used to remove the polymer, which then leaves polymer only in the groove (Figure 9.5(c)). Metal is then deposited on the fiber (Figure 9.5(d)). The polymer is then removed using a chemical, leaving the metal that rested on top of it unsupported. That metal is washed away with the polymer (Figure 9.5(e)). That process of removing the metal over the groove is

called Lift-off. An active optical material can then be deposited on the structure for interaction with light (Figure 9.5(f)).

Some of the challenges with either of these methods involve variability that must be eliminated in order to make working devices. The first challenge for fiber encapsulation is aligning a straight line, ten microns wide, to the fiber core, 2-4 microns wide, over a length of two centimeters through an ultra accurate process. Some progress was made in achieving this alignment, but some further work is required in order to get consistently perfect alignment. The depth of the etch into the core and the removal of the lift-off material everywhere except in the core is highly sensitive, and process variability must be reduced in order to make self-alignment possible.

9.6 Experimental Results

Some research has been done in testing the validity of these methods. The optimal embedding solution has been to use UV cure epoxy and polyimide tape. These materials offer an very clean surface for device fabrication. The following figures show some of the results. Success has been obtained in lithographically patterning over the core of a small section of an encapsulated fiber as in Figure 9.6. Photoresist was spin cast onto an embedded fiber and a lithography mask was aligned to a fiber using the Karl Suss MA 150 aligner. The photo-resist was exposed using hard contact lithography. The embedded fiber was then developed and an optical microscope image was taken of the resulting pattern. A center line like this could be used to pattern a polymer on the surface of a fiber, or could be used in metal lift-off process to create isolated electrodes on either side of the fiber.

Another method of patterning electrodes, other than lift-off, is to directly pattern them. One type of pattern that would be compatible with generating electrodes was attempted, and the results are shown in Figure 9.7. The pattern was aligned, exposed and developed as in the previous example, and an optical microscope image

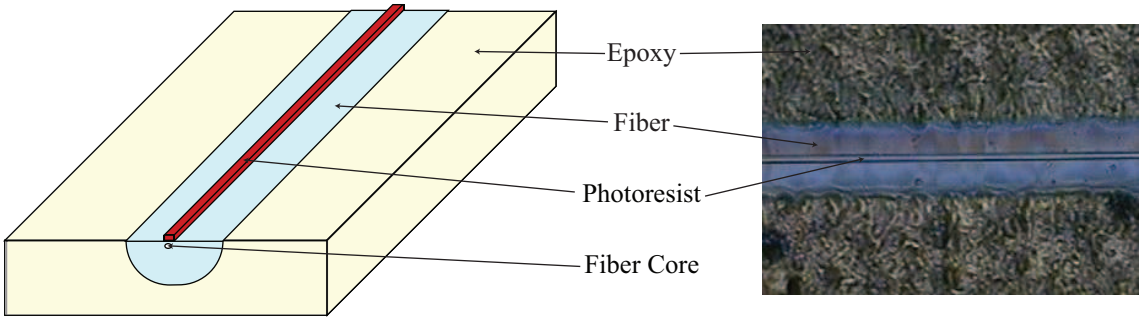

Figure 9.6: An illustration and optical microscope image of an encapsulated fiber with photo-resist over the core

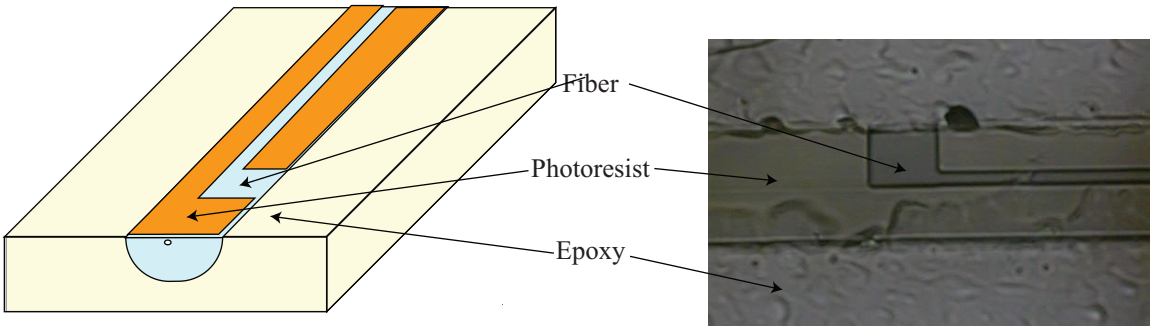

Figure 9.7: An illustration and optical microscope image of an encapsulated fiber with an electrode photo-resist pattern on the fiber surface

was taken showing how the electrodes are aligned to the core and are separated by a small gap on either end to isolate them from one another.

The lift-off process was successfully implemented to remove deposited metal from the surface of the core of a fiber using the self-aligned patterning process as in Figure 9.8. Photoresist was spin cast onto a fiber, and then RIE etched so that photoresist only remained in the core of the fiber. Then Aluminum was deposited on the whole surface of the embedded fibers. Finally, the photoresist was removed which lifted off the metal in the core of the fiber, and an optical microscope image was taken showing the resulting electrodes. The dark line in the center is the core of the fiber which has no metal in it, and the lighter more reflective area in the image is the Aluminum layer.

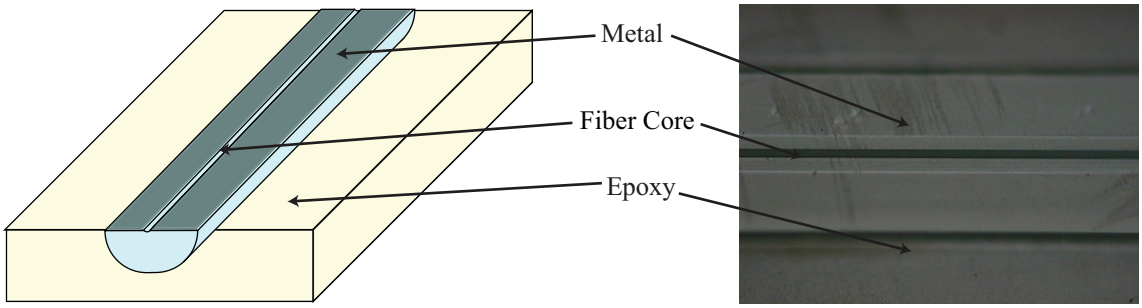

Figure 9.8: An illustration and optical microscope image of a self-aligned metal electrode pattern on a fiber

9.7 Conclusion

Two novel methods are presented for patterning components of integrated devices. Preliminary work has been done, and shows the feasibility of these solutions. Using these methods, work toward making active devices such as electric field sensors, and elector optic modulators is possible.

Chapter 10

E-Beam Written SR-FBG's For Electric Field Sensing

10.1 Introduction

The primary technique used for electric field sensing in this dissertation is to modify the phase of transmitted light through the device region of a fiber. The phase is then translated into an intensity change and the intensity change is used to determine the electric field. Another technique that can be used to detect a change in electric field is fiber Bragg grating (FBG) sensing. FBG's are a periodic structure which affects the forward traveling wave in such as a way as to reflect those wavelengths which satisfy the Bragg condition. FBG's can be fabricated by modulating the volume index of the fiber core as in [85]. Alternatively FBG's can be fabricated by creating a periodic modulation in the geometry of the fiber itself, resulting in a surface relief fiber Bragg grating (SR-FBG) [56, 57]. Much work has been done to apply SR-FBG's to the sensing of various physical phenomenon such as temperature [8], strain [9], and the presence of volatile organic compounds [10]. This chapter focuses on the idea of using SR-FBG's as a method of sensing electric fields.

10.2 Electric Field Sensing with SR-FBG's

The relationship between the reflected wavelength, λ_b, and the grating parameters is

$$\lambda_b = 2n_{eff}\Lambda, \tag{10.1}$$

where n_{eff} is the effective index of the guided mode, and Λ is the grating period. By changing either the effective index or the grating period, the reflected wavelength changes.

Electric field sensing can be accomplished by means of the linear electro-optic effect. An electric field acting on an electro-optic polymer causes a bulk refractive index change. This change in index can be used to shift the reflected wavelength of a SR-FBG by influencing the effective index of the guided mode.

There are various methods whereby the effective index of a guided D-fiber mode can be influenced. The main point is that an electro-optic polymer must form a portion of the index contrast region which makes the gratings. Specifics of the various methods and their advantages and disadvantages will be discussed in the next section.

10.3 SRFBG's with E-Beam Lithography

10.3.1 Introduction to EBL Written SR-FBG's

E-beam lithography (EBL) is a versatile method of generating high resolution patterns. The purpose of EBL, as with any other type of lithography, is the transferring of a pattern to a substrate. EBL differs from other types of lithography in that its patterns are written serially. Unlike in the optical lithography process, the pattern is directly translated from an electrical signal. Because it is directly transferred it is simple to change the pattern without making a new photomask. The EBL process is much more versatile in terms of changing the period, length, chirp, and apodization of SRFBG's. For research in SRFBG's this versatility opens many avenues of research which are not practical with interference or standard photolithography. Additionally, even outdated EBL systems can produce patterns with much greater resolution than their optical lithography counterparts. The system at BYU, which is not a state of the art EBL system, is capable of producing gold lines with resolutions of 20-30 nm,

while the best optical aligner in the BYU cleanroom struggles to produce lines of .5 μm.

Figure 10.1 shows a photograph of the Philips XL30 ESEM FEG scanning electron microscope (SEM) with a nanometer pattern generation system (NPGS) (JC Nabity Lithography Systems) which is housed in the Cluff building at BYU for EBL. Each SEM which is converted into an EBL system requires two things [86]. First, the SEM needs an analog input in order for the external software to control the beam positions. Second, The SEM requires an output for measuring the beam current. At BYU, a DAC is controlled by NPGS and input into the SEM to control the beam lenses. A coaxial cable is taken from the output on the front of the chamber door and connected with a picoammeter in order to measure the beam current in a Faraday cup on the SEM sample holder. In addition to these required items BYU also has: a high speed beam blanker, which is used to turn on and off the beam during patterning; an image signal connection, which is used to align to existing mark on the sample; and an automated stage, which is used to move the stage during the patterning of multiple fields. Chapter 5 in [86] was written by the designer of NPGS, and includes some very good information about all aspects of EBL.

There are various resist materials which can be used to generate EBL patterns. PMMA is the most common positive resist, due to its low cost and high molecular weight. ZEP is another type of e-beam resist which allows for higher contrast patterns and improved etch resistance over PMMA. At the molecular level, EBL is generally accomplished by simply the breaking of high molecular weight polymer bonds into lower molecular weight regions. The portion that has been exposed to the electron beam then becomes more soluble in the developer than the unexposed region. The beam must dwell on a area for a certain amount of time in order to sufficiently expose that area. The time for which the beam dwell's on a particular area is called the "dwell time." A different amount of exposure is required for each type of material.

Figure 10.1: Photograph of Phillips XL30 ESEM FEG SEM with NPGS

The substrate and other device layers or features upon which the pattern is written can also influence the amount of dose necessary.

10.3.2 NPGS

The NPGS system is a software package that interfaces with an SEM and allows the user to control all the necessary subsystems required for EBL. The user manual included with NPGS is an excellent resource in understanding the specifics of patterning with the NPGS system [87]. The software package includes two main interfaces the NPGS system itself, and a CAD program used for drafting the EBL patterns. The NPGS system includes a file manager environment, and a runfile editor. The runfile is used to adjust parameters such as where the pattern will be made, the magnification of the microscope, the beam current of the microscope, the desired dose or doses, as well as a variety of parameters used for automatic or semiautomatic alignment. In the CAD interface the user is able to manually draw the desired patterns with some extra macro-like options added from the NPGS system. The CAD program also allows for scripting.

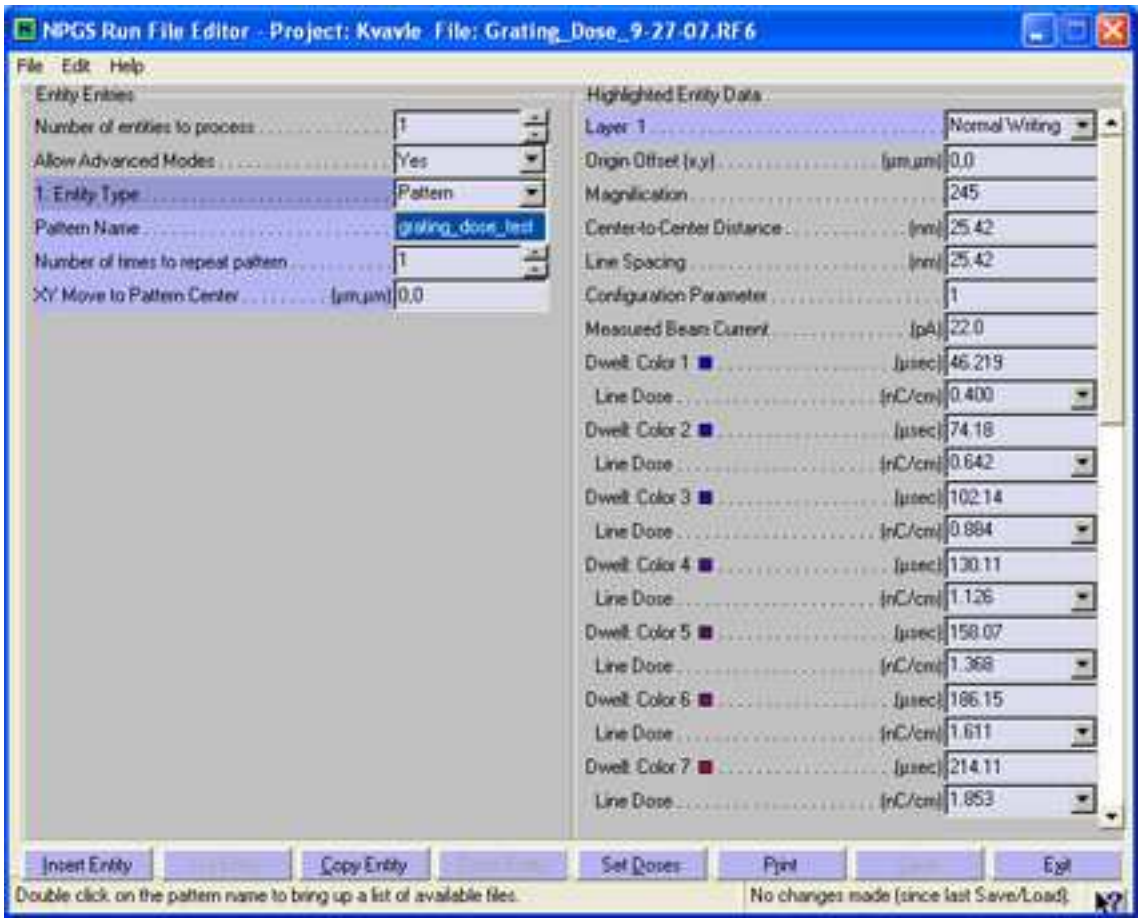

Figure 10.2: Screenshot of an NPGS runfile editor window with an array of doses in the left hand column

10.3.3 EBL Dose Tests

The first thing that must be done when characterizing EBL with a new substrate, pattern, or resist is to perform a dose test. This test is done by exposing an array of patterns with varying doses, and then choosing the dose with the best pattern. Figure 10.2 is a screenshot of the NPGS runfile window which is used to setup the dose test. The left half of the window is the area used for selecting the type of pattern that will be made. More than one pattern, or entity, can be made. Each pattern can have a different position, and a different set of patterning parameters.

In the right half of the screen are the parameters that are used in the selected entity. The parameters of note and their corresponding values or this dose test are

included in Table 10.1. The magnification is generally determining by the maximum magnification possible for the size of the field of view that is to be patterned. In this dissertation the center-to-center distance and line spacing are always set to 20 nm, but the NPGS software rounds it to the nearest possible value depending on the magnification. This parameter often varies between 15 nm and 25 nm. The measured beam current is determined by measuring the beam current in the Faraday cup on the sample holder with the Keithley picoammeter. The parameter entitled Dwell: Color is actually the dwell time. Each dwell time is calculated by using the beam current and line dose parameters. Different doses can be used for each different color drawn in the CAD program.

Table 10.1: Dose Test Parameters

Parameter	Value
Magnification	245
Center-to-Center Distance	25.42 nm
Line Spacing	25.42 nm
Measured Beam Current	22.0 pA
Dwell Time	46.219 μs
Line Dose	0.400 nC/cm

There are two different types of doses that can be used: a line dose and an area dose. The standard at BYU is to always use the line dose, even when patterning area structures. Work has been done to determine the differences between line dose and area dose, but no significant difference in pattern quality was found. A line dose increasing from 0.400 nC/cm to 5.000 nC/cm was done with 20 dose regions on the surface of an etched D-fiber.

Figure 10.3 shows a screenshot of the layout of DesignCad, the CAD program included with NPGS. The screenshot also shows the standard structural layout of a

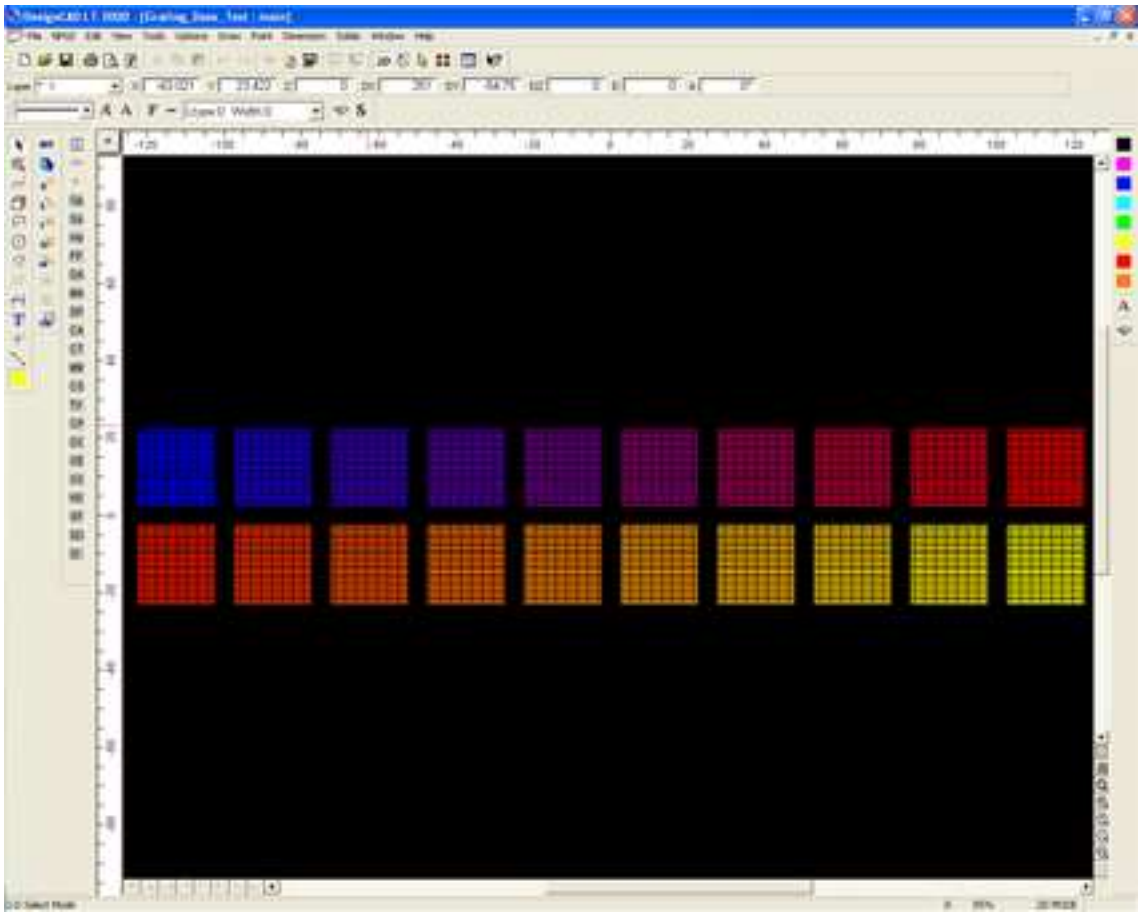

Figure 10.3: Screenshot of the array of structures used for a standard dose test. Each squares is a different color which will be set as a different dose in NPGS

dose test that was typically used to determine the proper dose for fabricating SRFBG's on the surface of a fiber.

Figure 10.4 shows an optical microscope image that was taken of the surface of a fiber after this pattern was transfered onto the surface of a fiber with EBL. The doses used are written next to each structure. The smallest dose (0.40 nC/cm) did not expose the PMMA at all, so no structure is visible. In the 0.64 dose a pattern begins to be visible. The doses from about 0.88 nC/cm to 1.61 nC/cm all look about the same. Then as the dose increases from 1.85 nC/cm to 5.00 nC/cm, the grating lines begin to be overexposed, leaving only a square where gratings should have been.

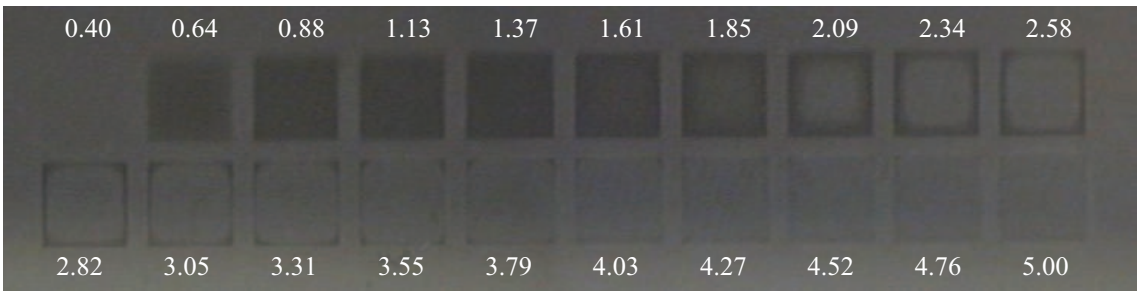

Figure 10.4: Optical microscope image of the dose structure which were patterned on the surface of a fiber. The dose in nC/cm is written either above or below.

This optical image indicates that a somewhere between 0.88 nC/cm and 1.61 nC/cm the optimal dose can be found. However, intuition indicates that the resulting grating structure can vary greatly over that range of doses. Therefore, another means of determining grating strength must be used. One method to determine the grating strength is to use an Atomic Force Microscope (AFM) to image the surface of the gratings. AFM's use the deflection of a microscopic cantilever to obtain information about a sample surface.

The fiber which was shown in Figure 10.4 was taken to the AFM lab in the physics department where the gratings for the doses from 0.64 nC/cm to 2.09 nC/cm were imaged. The measurements which were desired to be obtained were the period, shape, and grating height. The period affects the wavelength that the grating reflects, and the shape and height affect the efficiency of the grating. These gratings are necessarily short due to the nature of EBL, therefore the grating dose which results in the highest contrast gratings is the optimal dose. Figure 10.5a is a plot of the grating height, or peak to trough distance in nanometers. Notice how the grating height increases with dose until 1.13 nC/cm and then begins to drop as the dose is increased further. This result matches well with expectation.

Figure 10.5b includes slices of the AFM image for each of the grating doses which were tested. Note how the fill factor changes as well as the grating height for each dose. The dose of 1.13 nC/cm had an approximately 50% fill factor.

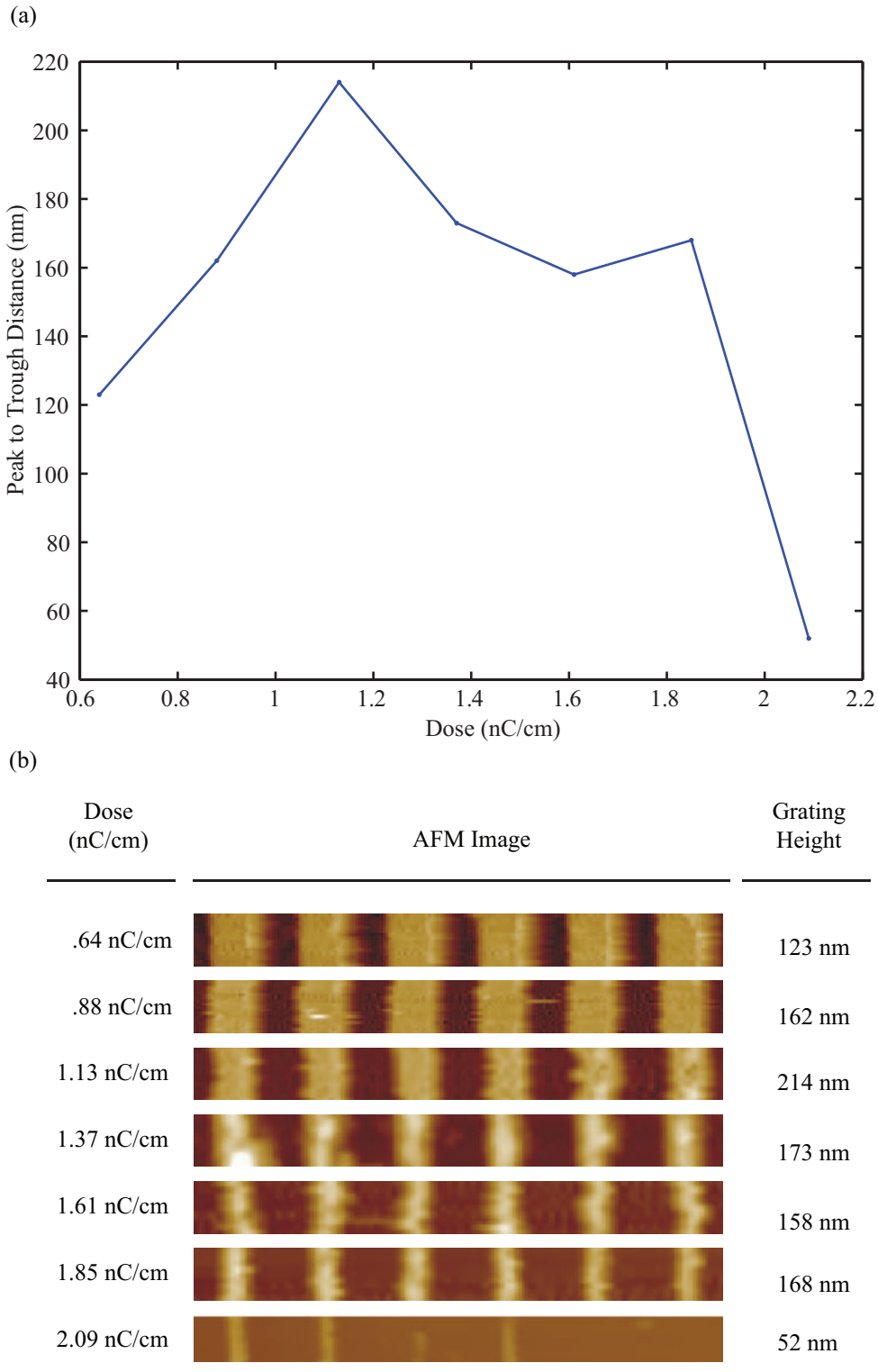

Figure 10.5: (a) Plot of grating height as obtained through AFM imaging. (b) AFM image slices for several different doses indicating shape and fill factor

Periodic dose tests are essential in keeping the fabrication process repeatable. It is also essential to make sure that the beam current parameter, which is input into the run file is as accurate as possible, otherwise the dose test data could be spurious.

10.3.4 Scripting with NPGS and DesignCad

Due to the repetitive nature of grating structure, generating the grating patterns by hand can be extremely tedious, even with the NPGS built-in "MakeArray" command. Whenever a period needs to be adjusted slightly it would require about 5-10 minutes to redo the EBL pattern.

To avoid this mindless repetition, the option to generate scripts is available. A script can be adjusted and run and the desired patterns obtained in only seconds. DesignCad supports a simple scripting language which enables the generation of grating patterns quickly and efficiently.

The following code allows the user to define each of the important grating parameters:

```
************************************************************
'Selects 2D mode in DesignCad
>2DSelectMode
{
  }
'Set the grating Length
Length = 1000
'Set the Grating Height
Height = 20
'Set the grating period
Period = .500
'Set the grating Fill-Factor
```

```
Fill = .50
'Determine the number of periods
N = Length/Period
'Instantiate the starting position at (x,y) = (0,0)
LLx=0
LLy=0
'Creates a rectangle for each grating period
for i = 1 to N step 1
>Line
{
  <Color 255,255,0
  <Layer 1
  <LineStyle 1,2.0000,0.0000
  <PointXYZ [LLx+Offset,LLy,0.0000]
  <PointXYZ [LLx+Offset,LLy+Height,0.0000]
  <PointXYZ [LLx+Width+Offset,LLy+Height,0.0000]
  <PointXYZ LLx+Width+Offset,LLy,0.0000]
  <PointXYZ \[LLx+Offset,LLy,0.0000]
  }
Offset = Offset + Period
next i
************************************************************
```

The scripts can be edited in notepad. Script files should have a ".DC3" file type. Running the script is simply done by selecting Tools Run Executable from the top command bar, and then selecting the desired script from the pop-up menu. If one desires to determine a scripting command he can refer to the documentation or record a macro and examine its contents afterwards.

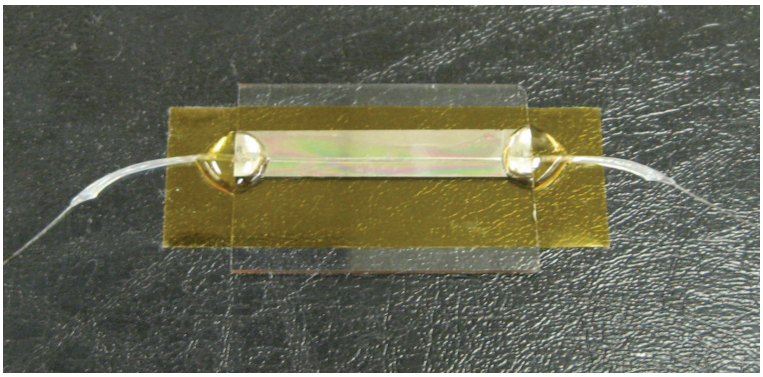

Figure 10.6: Photograph of a fiber mounted to a conductive substrate for EBL

10.3.5 Fabrication of EBL Written SRFBG's

With the dose test complete SRFBG's can be fabricated on the surface or in the core of a D-fiber. The preparation of a fiber for EBL requires first that the fiber be etched to expose the core for interaction with the SRFBG's. Then the fiber must be mounted to a conductive substrate so that the sample does not charge during EBL patterning. Figure 10.6 is a photograph of a fiber which was mounted to a conductive substrate and fixed to it with UV cure epoxy. The fiber also has tubing on the side to protect it from breaking during processing.

The E-beam resist, either PMMA or ZEP, must then be deposited on the sample. Then a layer of conductive polymer must be deposited. Finally, if the fiber is not is contact with the conductive substrate, a layer of gold must be sputtered on to the sample to eliminate charging. If the fiber is in good contact with the substrate, the gold sputtering step is not necessary. Figure 10.7 illustrates the final product that is used for EBL processing.

Once the fiber is ready for patterning it is brought to the SEM microscopy lab. The microscope is then hooked up to all the necessary equipment, the sample is loaded into the chamber, the beam current is measured, the run file is adjusted if necessary, the location for patterning is chosen, the working distance and magnification are set, the X-Y axis is set in NPGS, and finally the sample is patterned.

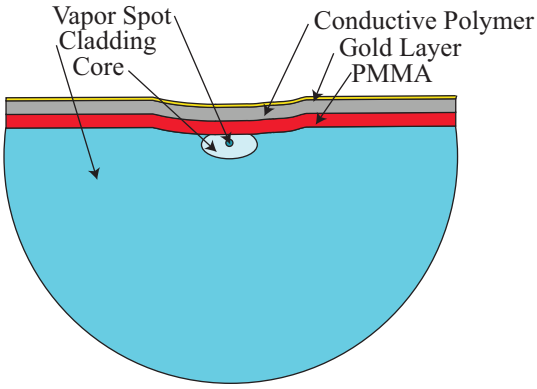

Figure 10.7: Illustration of materials which are deposited on the fiber surface for EBL processing

After patterning, the sample is removed from the SEM and is taken to the cleanroom, where it is developed. After development the grating patterns can be seen in an optical microscope, or for more detail, in an SEM.

When a good grating is fabricated on the surface of a fiber, the fiber is then fusion spliced to a PANDA fiber E-fiber cord and tested for reflectance. Often the Micron interrogator is used for this testing, but a tunable laser and photodetector can also be used.

After a time of making gratings without obtaining a successful reflection spectrum, it was determined that the grating period in the DesignCad file will translate into a period which is about 106% greater than the intended period. Therefore, a grating with a period of between 480-500 nm actually reflects light at about 1550 nm. The actual period for this grating would be around 532 nm. One theory is that the Mag Scale parameter on the SEM is slighly off, but since the increased period is consistent, it can be worked around.

10.4 EBL Written SRFBG's

Successful gratings have been fabricated in the core of a D-fiber with both PMMA and ZEP. This section outlines some of the gratings that were fabricated as well as their reflection spectra.

10.4.1 PMMA Gratings

The recipe for making PMMA gratings in the core of a fiber is as follows:

1. Etch Fiber
   (a) between 4.5 and 6 oscillations - 6 oscillations is when the core is breached.
2. Deposit PMMA/DR1
   (a) 2 grams of PMMA
   (b) 0.4 grams of DR1
   (c) 37.5 ml of Cyclohexanone
   (d) 6.33
   (e) The polymer was then spun on a fiber at 3000rpms for 30 seconds with maximum acceleration.
   (f) Heat at 180 C for 5 minutes
3. Deposit Conductive Polymer
   (a) heat at 90 C for 1 Minute
4. Deposit Gold (optional)
5. EBL
   (a) Line Dose: 1.200 nC/cm

(b) 23.36 nm Line Spacing

(c) 23.36 nm Center-to-Center Distance

(d) Magnification: 400 X

6. DI water Rinse

7. Develop

   (a) M/I 1:3 (1:3 MIBK to IPA from Microchem) for 30 seconds.

8. Heat to 90 $^{\circ}C$ for 30 seconds to remove the water that the PMMA absorbed

9. Rinse in IPA

10. Examine and Test

    (a) Microscope

    (b) Interrogator

    (c) Tunable Laser Transmission Scan

    (d) AFM

    (e) SEM

Figure 10.8 is an SEM image of a D-fiber which has a SRFBG written in the partially etched out core with EBL. Figure 10.9 shows a close view of the same fiber. There is some slight surface irregularity, but overall the gratings were very smooth in the core.

Before cleaving this fiber it was tested with the Micron Interrogator to determine the reflection spectrum. Figure 10.10 plots the results. The length of the grating region was 1 mm. The overall strength of the reflection was a little over 10 dB and the 3 dB width of the reflection spectrum was about 4 nm.

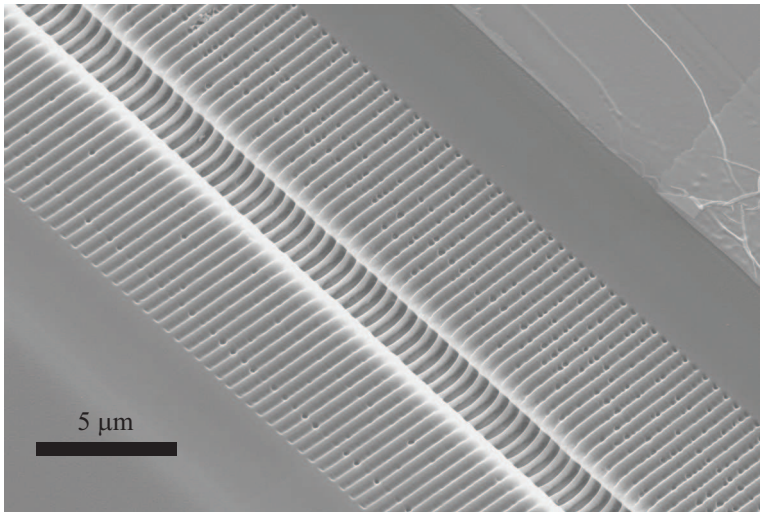

Figure 10.8: SEM image of a PMMA/DR1 grating in the core of a D-fiber. The view is coming in at a 45 ° angle from the top and side of the length of the fiber.

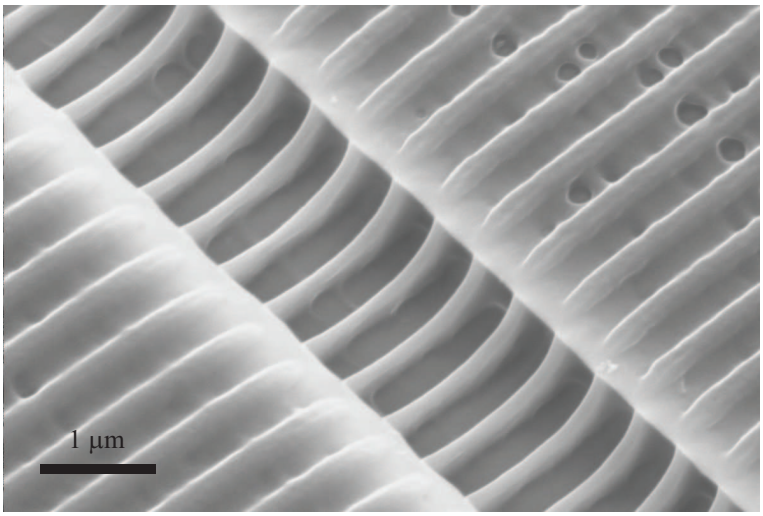

Figure 10.9: Close up view of EBL written DR1/PMMA gratings in the core of a D-fiber

Another grating was fabricated and heated from 25 °C to 80 °C to observe the spectral response. The peak of the grating shifted from a maximum height of -21 dB at 1523 nm to a maximum height of -21.35 dB at 1523.5 nm, for a shift of 0.5 nm total. Figure 10.11 plots the spectrum before and after heating.

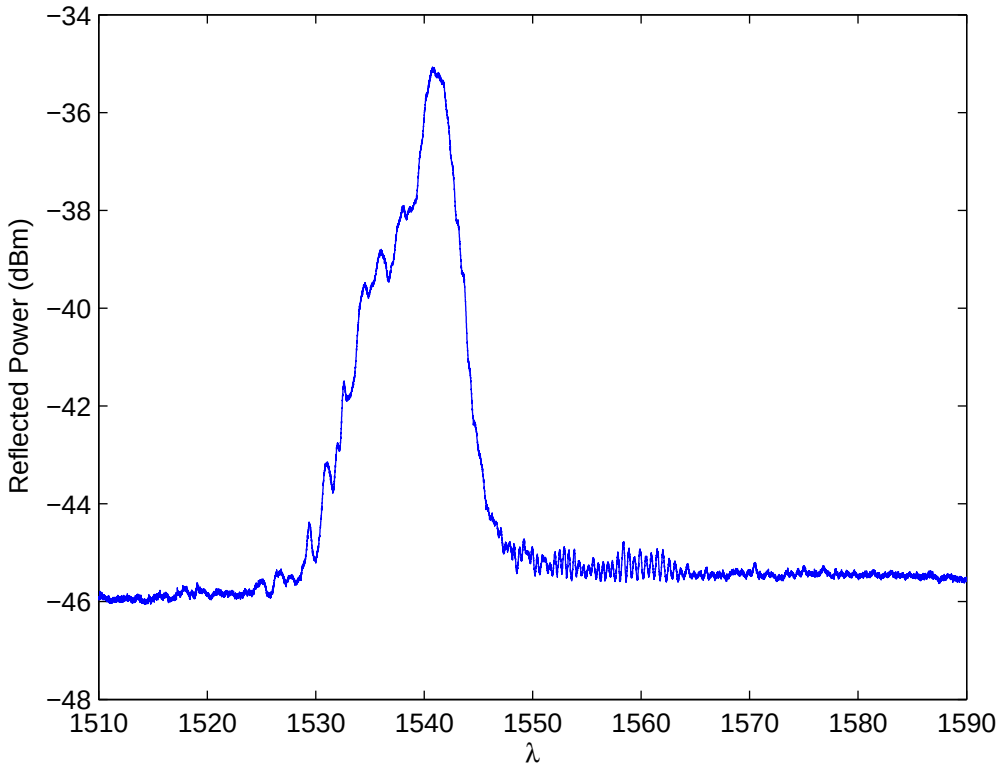

Figure 10.10: Reflection spectrum of the EBL written DR1/PMMA gratings shown in Figure 10.9

10.4.2 Electro-Optic Response of a DR1/PMMA SR-FBG

It was with electro-optic sensing that the DR1/PMMA EBL resist was chosen. The poling process used for electric field sensors was used to pole a DR1/PMMA grating, but no AC electro-optic response was measurable. The equations the govern the spectral shift of a DR1/PMMA were analyzed and an analysis is included below. If,

$$n_{w/field} = n_0 + n_e^3 r_{33} E, \tag{10.2}$$

where, $n_0 = 1.555$, $n_eff = 1.451474203$, $r_33 = 3pm/v$, $V = 10kV$, and $d = 250\mu m$. Then,

$$n_{w/field} = 1.5552. \tag{10.3}$$

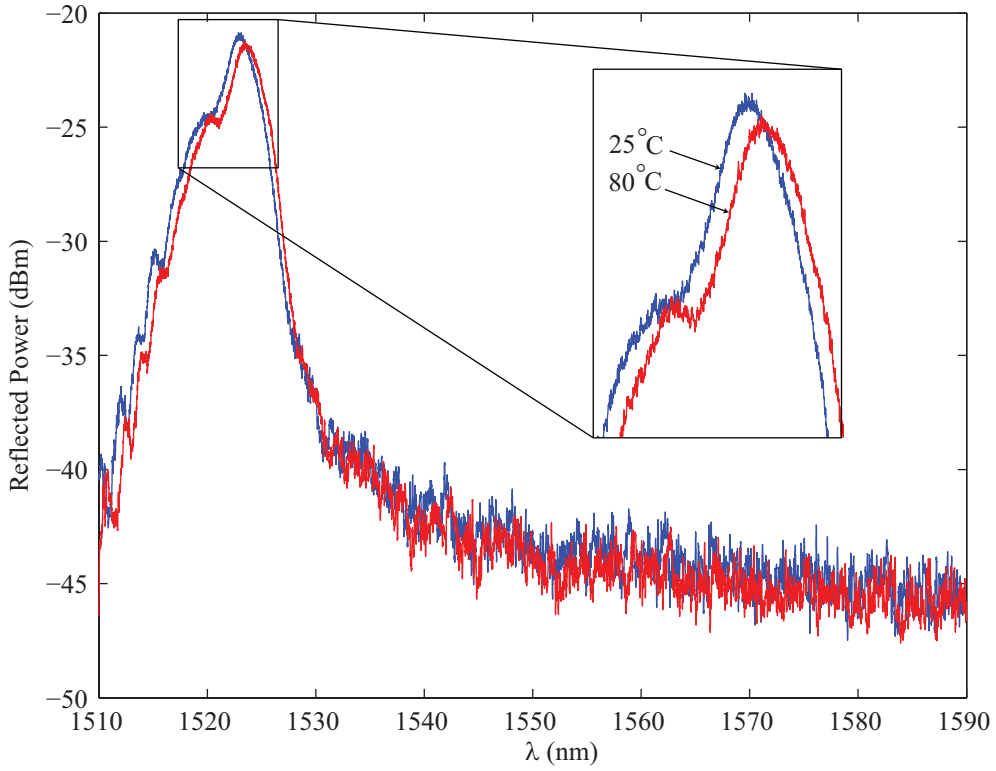

Figure 10.11: Spectral response of a heated EBL written DR1/PMMA grating

If this bulk index is used for the index profile of the fiber cross-section in BeamProp then we find that the effective of the mode with an electric field applied is $n_{eff\ with\ field} = 1.452502$, which results in a $\Delta n_{eff} = 2.81E-5$. Using this as the change in n_{eff}, we find that the wavelength shift follows the following relationship,

$$\Delta\lambda_{Bragg} = 2\Delta n_e f f \Lambda = 2(2.81E-5)(532E-9) = 30pm. \tag{10.4}$$

Based on other experimental AC tests done in the lab, this 30 pm shift would not be sufficient to pick up with our electronics. It was thus determined that the DR1/PMMA EO sensing was not the best sensing solution.

However, there are a variety of ways in which the gratings can be fabricated with EBL. With electric field sensing in mind let us consider four method of patterning an electro-optic polymer into an SRFBG. Figure 10.12 illustrates these four methods

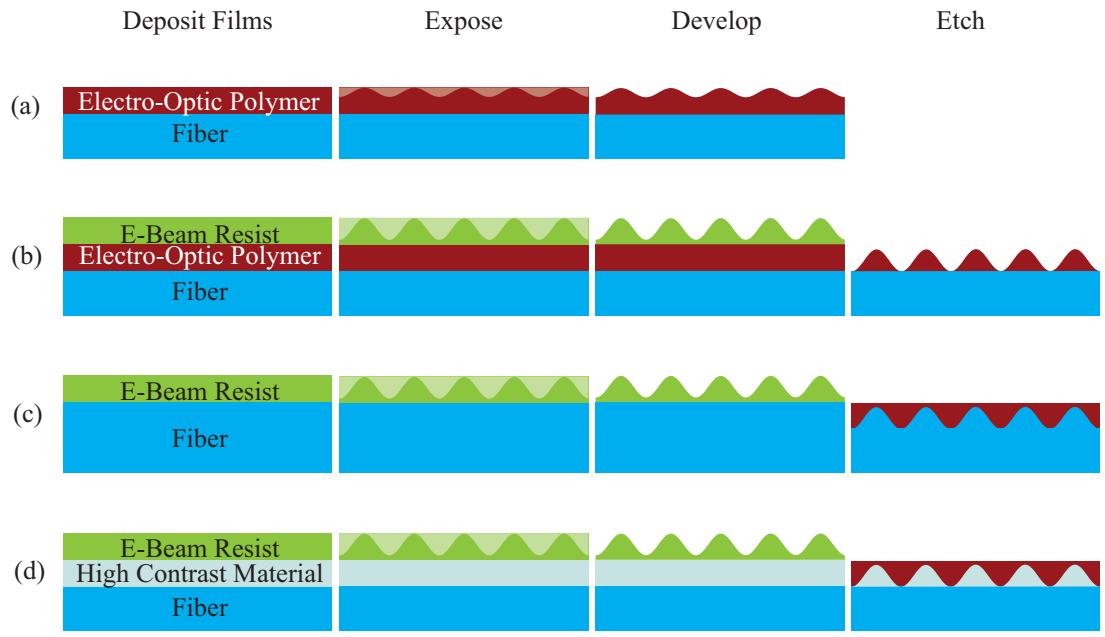

Figure 10.12: Illustration of various methods which can be used to fabricate EO polymer Gratings on a fiber

including (a.) patterning the electro-optic polymer itself, (b.) an electron-beam resist is used to pattern the electro-optic polymer, (c.) an electron-beam resist is used to pattern the glass of an optical fiber, and then the polymer is deposited on top of the fiber gratings, (d.) an electron-beam resist is used to pattern a high contrast material and the polymer is deposited on that.

The DR1/PMMA gratings were fabricated with method a.), but what if instead of using an EO polymer as the EBL resist, ZEP were used and then an EO polymer were deposited on the surface of the fiber after the fiber was etched. This method of patterning, etching and then depositing material is method c.) in Figure 10.12

10.4.3 ZEP Gratings

As previously mentioned, ZEP is a high contrast EBL resist with good etch resistance. The basic process for using ZEP instead of PMMA is the same. The only significant difference is that ZEP requires a dose of only 0.260 nC/cm, which make

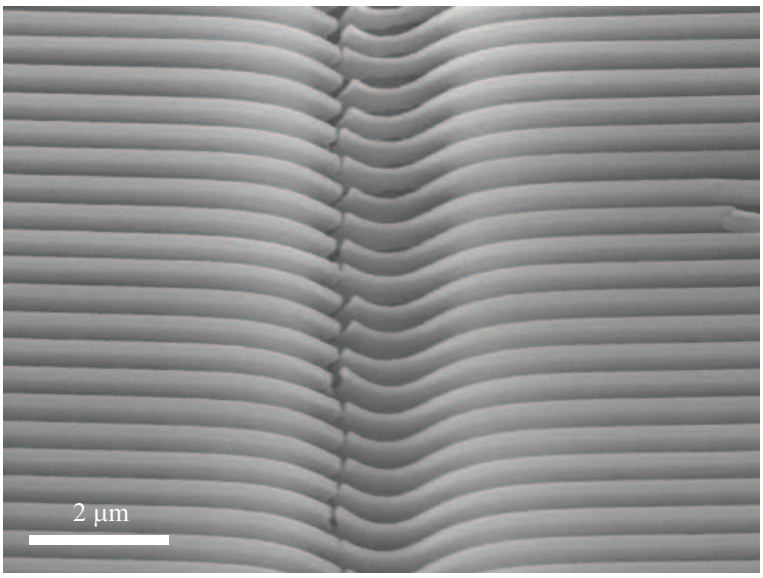

Figure 10.13: SEM image of ZEP gratings written in the core of an optical fiber. Note that the grating contrast is so high that the bottom of the grating is not visible from this view.

the patterning much faster. The gratings fabricated with ZEP have much sharper edges. The grating shape with ZEP is much close to the binary grating structure than PMMA grating, which are closer to a sinusoidal shape. These ZEP gratings are very promising for future research because of their high contrast and fast writing speed.

10.5 Short Grating Array EBL SR-FBG's

The versatility of EBL written gratings allows for research in a variety of area. One area which shows some promise is the fabrication of a short array of grating on the surface of a fiber. A D-fiber with DR1/PMMA resist was patterned with an array of three gratings, each 500 μm long, and spaced about 500 μm apart. Periods of 480 nm, 490 nm, and 500 nm, were chosen so that the reflection spectrum of all three gratings would be within the Micron Interrogator's detectable spectrum. Figure 10.15 shows an SEM image of a D-fiber with the grating array visible on the surface of the fiber. The first grating is located at the edge of the D-fiber, where it was cleaved. The second grating is visible as one follows the fiber surface up in the image window.

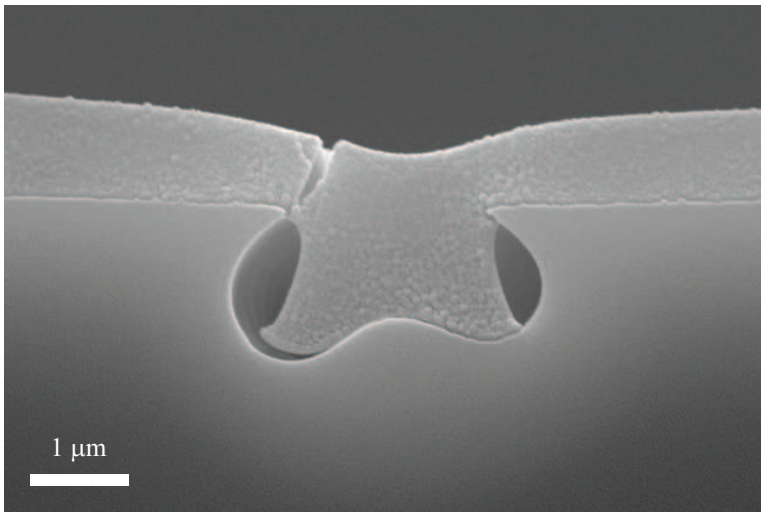

Figure 10.14: SEM cross-sectional image of the partially etched out core of the fiber shown in Figure 10.13. Notice the crack in the ZEP resist on the left side of the image. This crack was likely caused by the dramatic difference between the thermal expansion of the ZEP and the glass of the fiber core. When heated to the curing temperature, the topographical irregularities of the partially etched fiber core resulted in stress on the ZEP film.

The third grating is located in the top of the image, and is out of focus due to the working distance of the SEM at this magnification.

A closer view of the end of the fiber indicates the the gratings were exposed all the way down to the surface of the core, which was partially etched away. Figure 10.16 shows a very shallow angle view of the gratings on the surface of the fiber, while also showing a portion of the etched out core of the fiber on which this array was written. The index profile of this fiber was modeled in BeamProp with and without gratings to determine the Δn_{eff}. Table 10.2 records the results for each polarization state and the total change in n_eff for each polarization state. The maximum change in n_{eff} was 6E-3 which is much higher than standard UV written FBG's and higher than any of the SRFBG's reported in [57].

The reflection spectrum of this array fiber was taken and Figure 10.17 plots the results. There are three distinctly visible peaks. A few things to note are that the very noisy and the peaks increase in strength as a function of wavelength. The

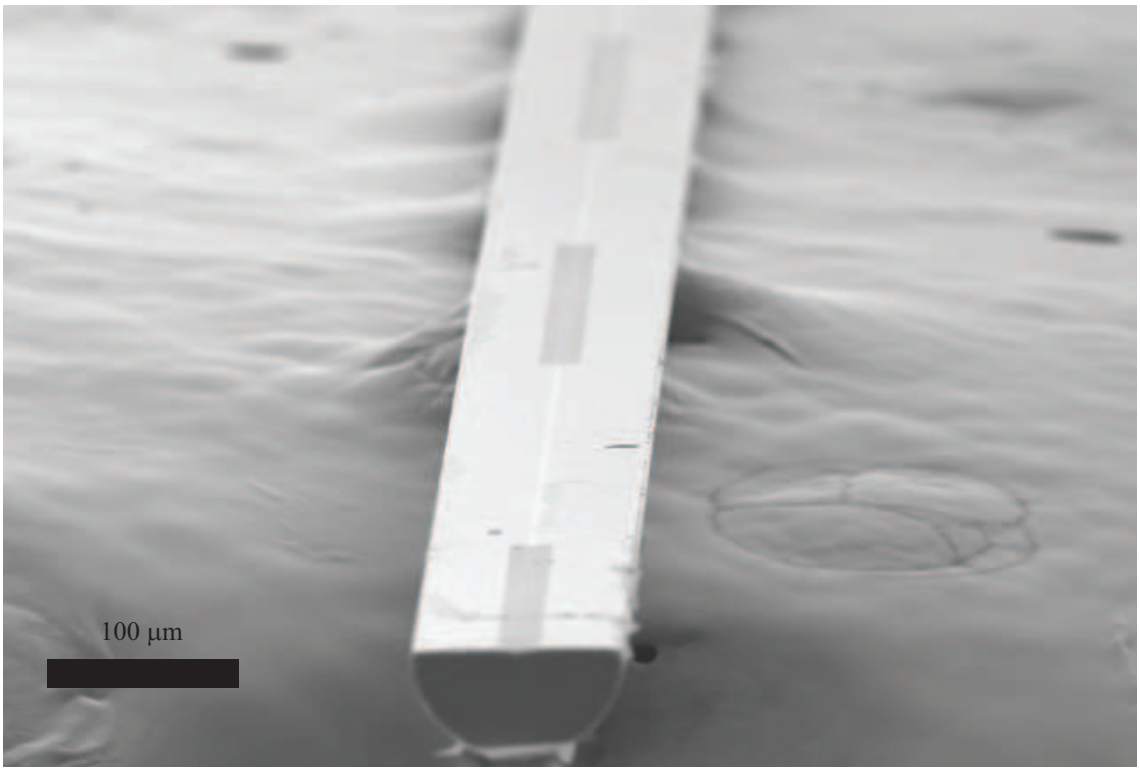

Figure 10.15: A view of three EBL written gratings each with a different periods as seen from a shallow angle

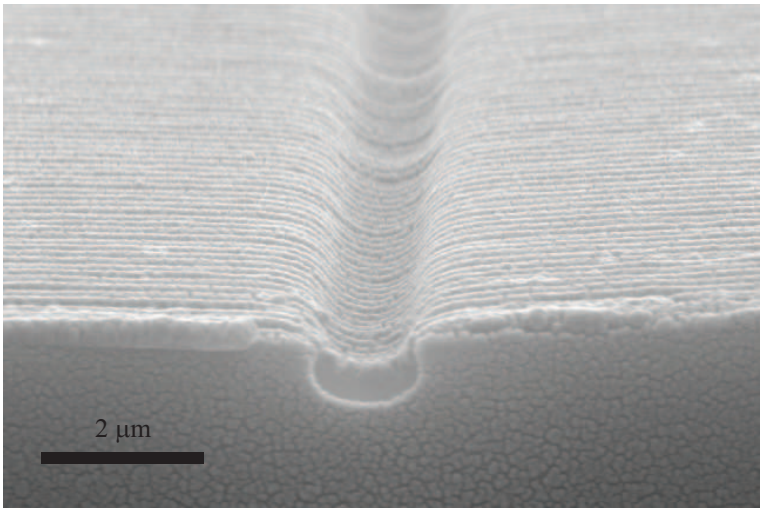

Figure 10.16: A closeup view of the EBL written gratings showing how the polymer in the core was completely exposed in between each line making these gratings very high contrast. The image also shows how the uniformity of the gratings is pretty

Table 10.2: Δn_{eff} for TE and TM Modes

TE_{ridge}	1.4484	TM_{ridge}	1.4476
TE_{valley}	1.4545	TM_{valley}	1.4528
ΔTE	0.0061	ΔTM	0.0052

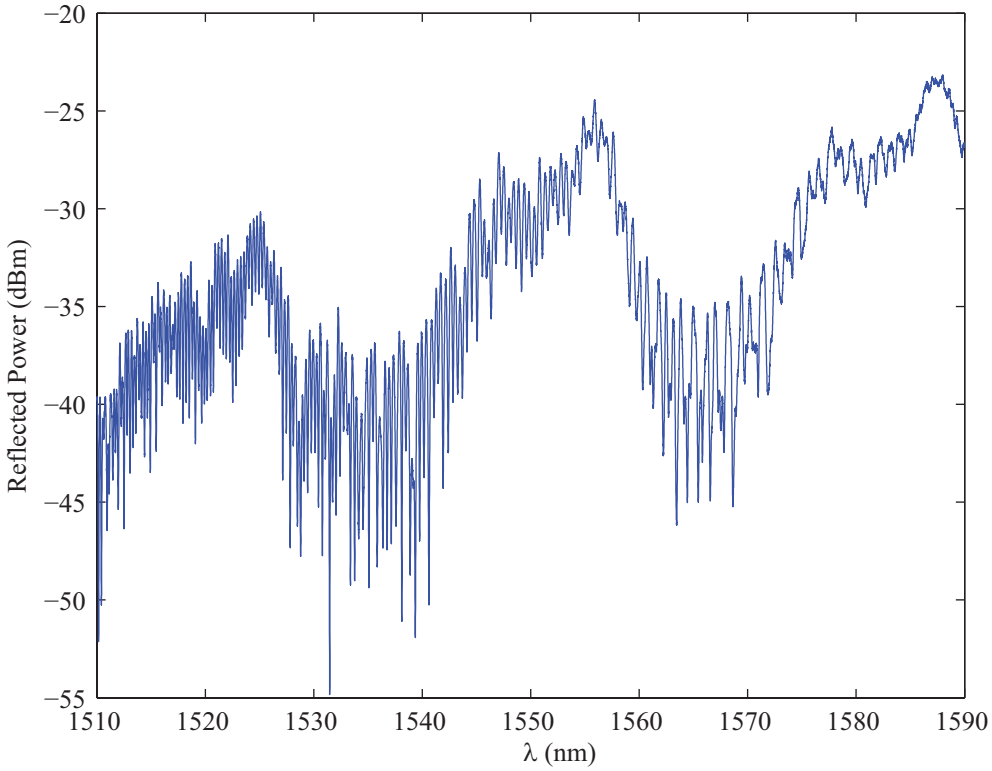

Figure 10.17: Reflection spectrum for the EBL written grating array shown in Figure 10.16

increase is close to linear in this dB scale plot which indicates that the losses are probably α decay type losses. The total insertion loss of these gratings was on the order of 7 dB.

10.6 A Note on Grating Strength

These gratings should have a much stronger reflection spectrum based on their Δn_{eff}. One possible reason for this is the aforementioned loss. Another possible reason is that with strong gratings, the reflection strength is no longer proportional

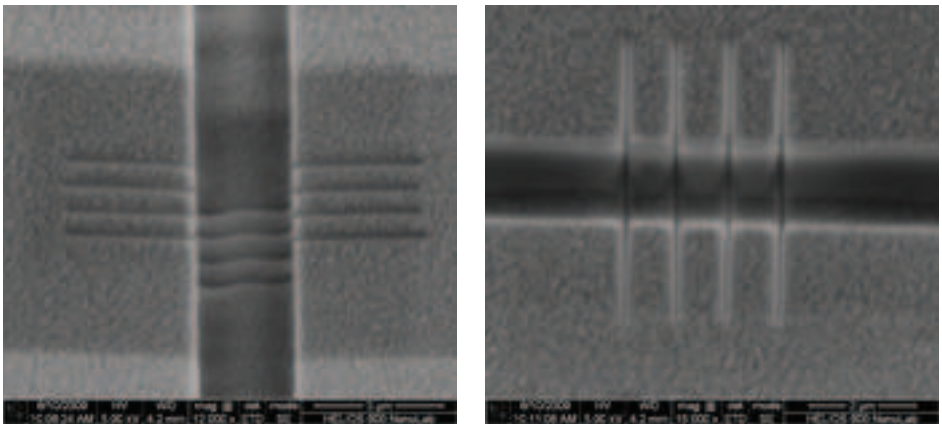

(a) (b)

Figure 10.18: SEM images of the (a) tilted image view and (b) top view of a hybrid waveguide structure into which four grating lines were written in the core of a fiber.

to length as indicated in [88]. Further experimental work should be done to fabricate gratings with varying lengths. Also, it is important to look more closely into the theory behind strong gratings.

10.7 SR-FBG's with Ion Beam Milling

Another promising method of fabricating SR-FBG's is with the Helios dual beam microscope. The Helios microscope is a new cutting edge dual beam microscope tool which was recently acquired by BYU that can be used to mill structures into a D-fiber. Some preliminary work was done showing that it is a promising new area for a variety of in-fiber devices. Figure 10.18 shows an SEM image of some test gratings that were milled with this microscope.

10.8 Conclusion

This chapter presented research with regard to the fabrication of SR-FBG's which were written in the core of a D-fiber. These gratings exhibited reflection strengths of over 10 dB above their side lobes, and a three grating array was fabricated on a short section of D-fiber.

While it was found that the standard electro-optic SR-FBG was not sensitive enough to detect electric fields, the next chapter presents a method of using SR-FBG's to obtain greater electro-optic sensitivity.

Chapter 11

Vernier Gratings for D-fiber Electric Field Sensing

11.1 Structured Gratings

Extending on the ideas presented in Chapter 10, this chapter focuses using FBG's to sense electric fields. Rather than simply using the standard SR-FBG, this chapter adds an additional level of complexity to the sensing method by introducing superstructured (SS) and Fabry Pérot (FP) gratings in which sections of gratings are separated by gaps to manipulate the reflection and transmission spectra. Figure 11.1 illustrates both of these grating structures, which result in multiple reflected or transmitted peaks.

In the case of a SS FBG a periodic section with and without grating, a subgrating, is repeated a certain number of times. This periodic repetition results in a transmission spectrum which is dependent upon the subgrating period. An SS-FBG spectrum which was modeled numerically using transfer matrix code is shown in Figure 11.2. Note how there are multiple reflection peaks contained within a sinc-like envelope. The subgrating dependent envelope determines the reflection strength of each peak.

The FP-FBG is just like any other FP cavity. There are two section of reflective gratings separated by a gap. A FP-FBG spectrum, also modeled with the transfer matrix method is plotted in Figure 11.3. The FP structure results in a band in which narrow peaks are transmitted. The FP structure has much narrower peaks than the SS grating.

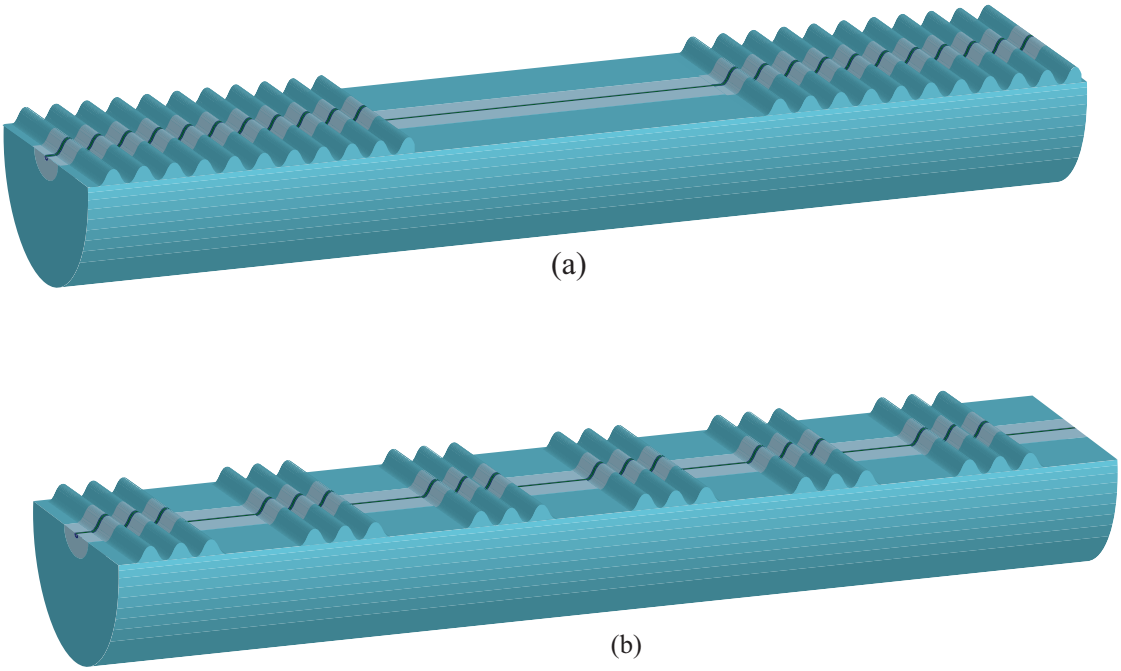

Figure 11.1: Illustrations of (a) the Fabry Pérot grating and (b) the sampled grating structures with labels for the dimension that define the free spectral range of the grating spectum

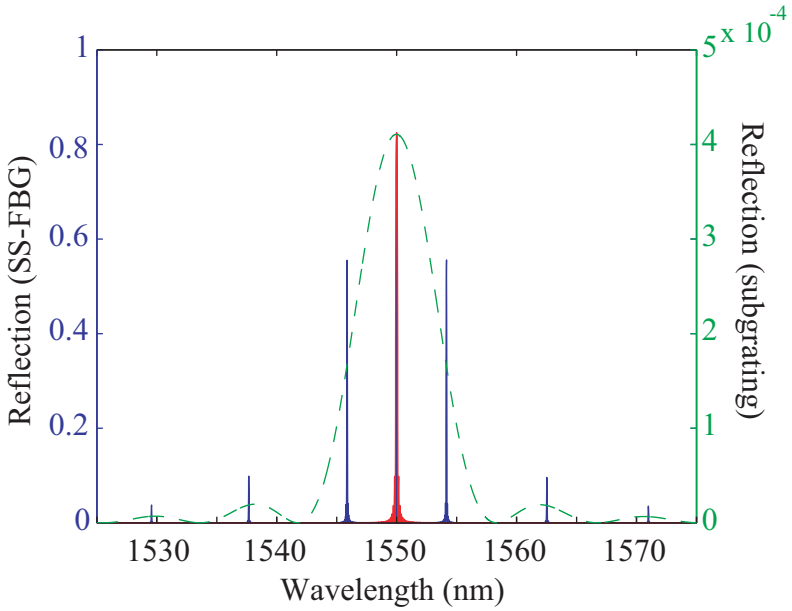

Figure 11.2: Graph showing that the SS-FBG relection spectrum corresponds to an envelope from a single subgrating(dash line) and that the maximum reflectivity corresponds to the reflectivity of all the subgratings concatenated together.

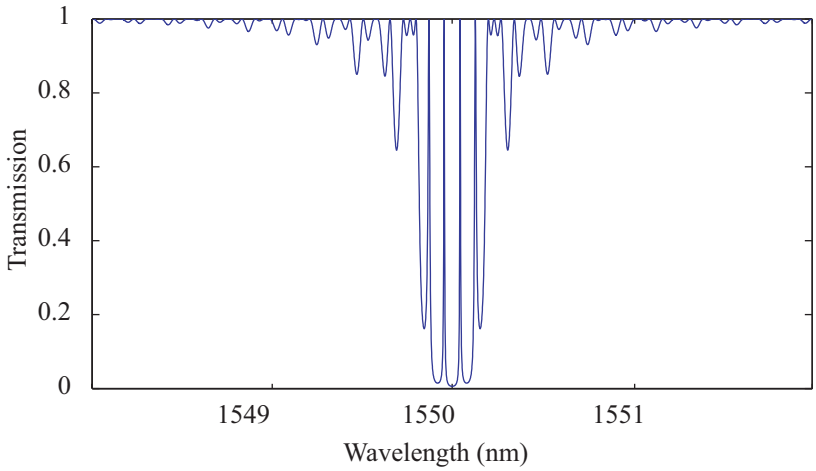

Figure 11.3: Simulated transmission spectrum of FP-FBG

A more detailed treatment of why and how these structures result in periodic reflection or transmission peaks can be found in [57]. For the purposes of this dissertation, the FP FBG grating structure will be evaluated as a means of sensing electric fields.

11.2 The Vernier Interrogation Scheme

One of the useful characteristics of FP-FBG's is that the effective index of the mode of the fiber in the gap between the two grating sections influences the position of the peaks of the FP-FBG spectrum. Similar to the case for SR-FBG's in Chapter 10, the FP-FBG peaks can be shifted by applying an electric field which changes the index of the polymer material in the core. A device based upon FP-FBG's would be more sensitive than a standard SR-FBG because the peaks are more narrow. Beyond the narrowness of the peaks though, FP-FBG's lend themselves to a Vernier sensing scheme.

The Vernier concept can be found in a variety of areas such as in rifle sights [89], slide rules[90], vernier calipers and micrometers [91], and tunable optical filters [92]. The ubiquitousness of the vernier scale in such a variety of areas is proof that

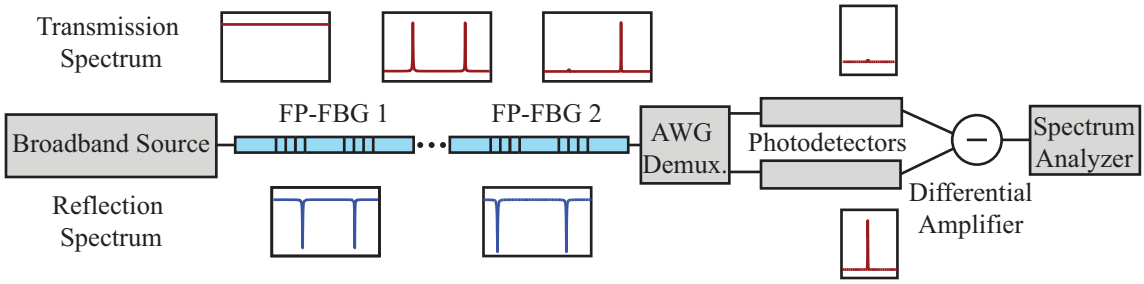

Figure 11.4: Illustration of Vernier sensing scheme with two FP-FBG's

this simple idea is effective at what it does. Essentially the purpose of the vernier scale is to translate a small change more easily determined. It can also be used to translate a small change into a much larger one.

By combining two FP-FBG's with slightly different gaps between the grating sections, one can use the change in the effective index inside the cavity to produce a change in the total transmitted spectrum. With the proper setup, this change in transmission spectrum can be used to transduce electrical signals into optical ones. The setup that Figure 11.4 shows how two FP-FBG's can be interrogated to obtain information about an electric field. A set of two FP-FBG's with a hybrid waveguide making up the area in between grating sections are connected together. The first FP FBG is fixed, and the second FP FBG is made electro-optic and used as the sensing device. A broadband source is transmitted into the first FP FBG. Only the wavelengths that the FP cavity allows to transmit through are passed on to the next FP-FBG. After the second FP-FBG the spectrum is demultiplexed with an AWG. The two signals are subtracted from one another in a differential amplifier. The electrical output from the differential amplifier is input into a spectrum analyzer to measure the signal.

There are two major advantages to this kind of setup. First, it uses the Vernier scheme, so a small shift results in a large optical power change. Second, the differential

takes the difference between two adjacent peaks thereby decreasing the noise from the broadband source.

In order to understand the vernier effect a theoretical device was designed with fabrication tolerances in mind. Figure 11.5 takes a closer look at what happens to the peaks as the effective index of the sensing grating is changed slightly. Notice how in Figure 11.5a the peak at 1550.6 nm is partially transmitting. Then, as the effective index is increased (Figure 11.5b), the peak reaches almost maximum transmission. When the index is increased further (Figure 11.5c), the peak at 1549.8 nm becomes larger than the other. When the effective index is increased further (Figure 11.5d), the peak at 1549.8 nm reaches almost maximum transmission and the peak at 1550.6 nm has all but disappeared.

This phenomenon is a lot like a teeter-totter where one side goes up and the other goes down. This up and down motion results in a differential signal which Figure 11.6 plots. This differential appears like one period of a *sin* function. The region we are most interested in is where the slope is linear. This linear region corresponds to where the second peaks is dropping down while the first peak is rising up. The $\frac{\Delta I}{\Delta n_{eff}}$ slope of the differential signal will be important when considering device sensitivity.

11.3 Comparison between Polarimetric and Vernier Sensing

To be able to compare the Vernier and the polarimetric testing schemes the for a sensor which has about a 100 MV/m E_π

The polarimetric sensing scheme and the Vernier sensing scheme are much different, to motivate the use of the more complicated Vernier scheme it is important to reduce both schemes to a quantity that can be compared. Both schemes produce a change in optical power for a given electric field. The term we are looking for is

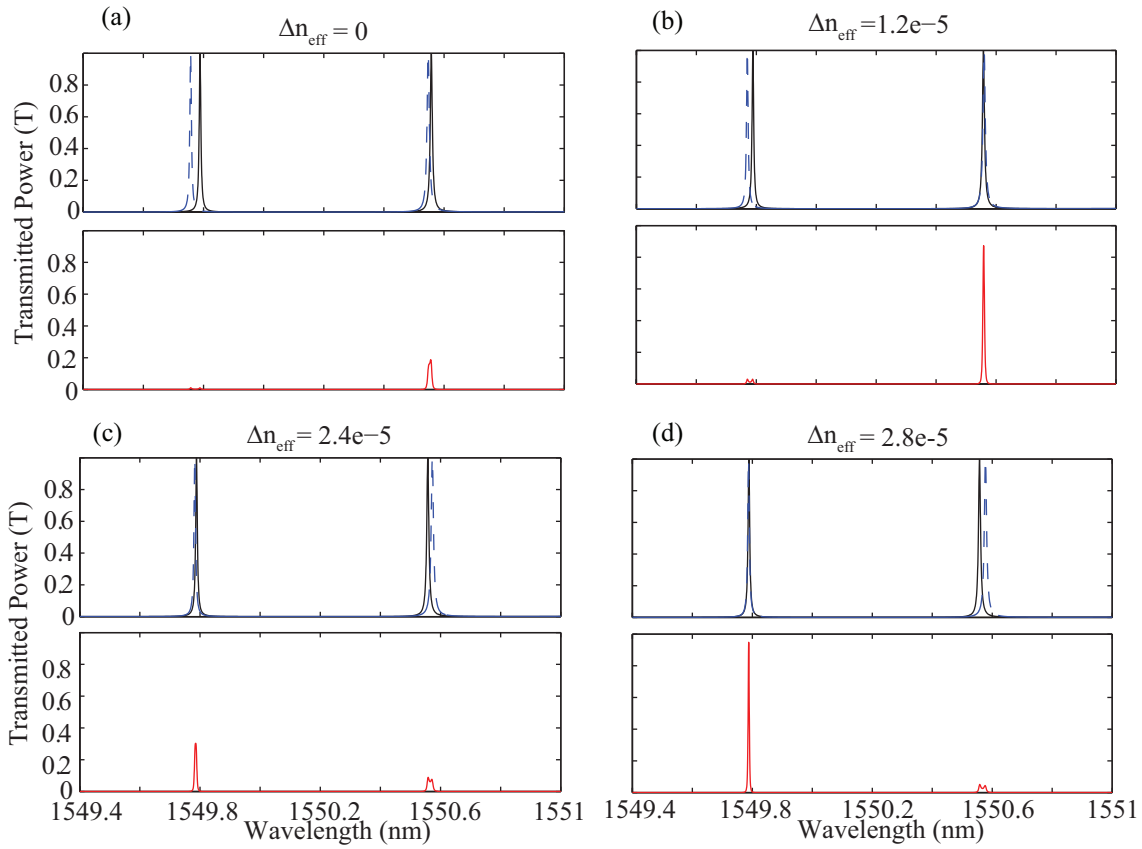

Figure 11.5: Simulated transmission spectrum of a system of two FP FBG connected in series. Each of the sets of two plots contains the transmission spectrum of the two FP FBG's (the solid and dashed line in the top plot), and the total spectrum transmitted after the second FP FBG. The effective index of the mode was varied and is labeled for each plot plot (a) $\Delta n_{eff} = 0$, (b) $\Delta n_{eff} = 1.2e-5$, (c) $\Delta n_{eff} = 2.4e-5$, and (d) $\Delta n_{eff} = 2.8e-5$

the change in irradience over the change in electric field ($\frac{\Delta I}{\Delta E}$), or how much does the optical power change when a field of 1 V/m is applied to the sensor.

The maximum value of $\frac{\Delta I}{\Delta E}$ for the polarimetric sensing scheme in the linear range can be obtained from Equation 8.15, and is $\frac{\pi}{E_{pi}}$. For a sensor with an E_π of 100 MV/m this would it would be $\frac{\Delta I}{\Delta E} = 6.28e-8$.

The $\frac{\Delta I}{\Delta E}$ for the Vernier sensing scheme cannot be analytically obtained, but the ratio can be obtained by multiplying other ratios that are numerically calculable.

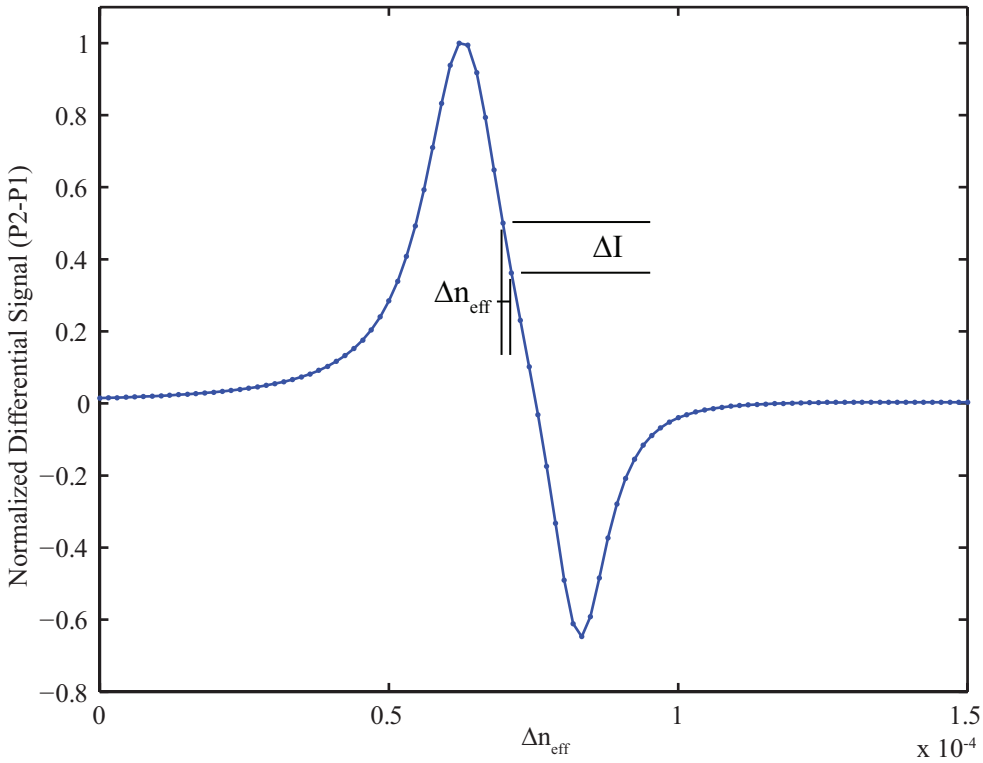

Figure 11.6: The differential signal plotted from the simulation

Table 11.1: Physical Parameters for Vernier Modeling

Parameter	Value
Grating Length	500 μm
Gap 1	3.97 mm
Gap 2	3.93 mm
Δn_{eff}	3e-3

The relation of ratios is as follows,

$$\frac{\Delta I}{\Delta E} = \underbrace{\left(\frac{\Delta I}{\Delta n_{eff}}\right)}_{\text{Vernier Differential}} \underbrace{\left(\frac{\Delta n_{eff}}{\Delta n_{polymer}}\right)}_{\text{Waveguide}} \underbrace{\left(\frac{\Delta n_{polymer}}{\Delta E}\right)}_{\text{Electro-Optic}}. \tag{11.1}$$

We determine the first term by modeling the Vernier scheme, again using the transfer matrix code. The physical parameters of the gratings used for this simulation are included in Table 11.1 found that the $\frac{\Delta I}{\Delta n_{eff}} = 1.15e + 6$.

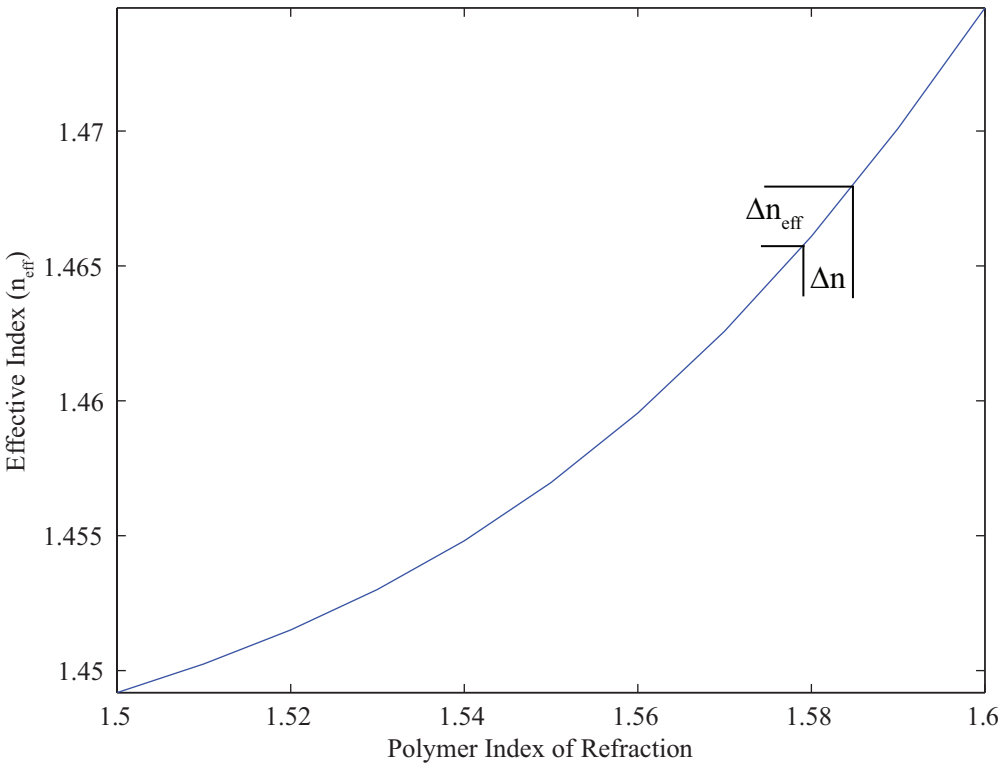

Figure 11.7: Plot of change in effective index of an AJL8/APC waveguide as a function of change in polymer index of refraction as calculated from BeamProp

The second term can be obtained by using BeamProp to calculate the slope of the change in effective index for a given change in polymer bulk index. This result is plotted in Figure 11.7 for indices varying from 1.5 to 1.6. Since AJL8/APC has an index of about 1.6, we take the slope at that point, which is $\frac{\Delta n_{eff}}{\Delta n_{polymer}} = 0.4459$.

Finally the last term is simply calculated from Equation 2.9,

$$\Delta n_{polymer} = 1.6 - \frac{1}{2}1.6^3 * (7E - 12) = 1.43e - 11. \tag{11.2}$$

Multiplying the three ratios together, we find that

$$\frac{\Delta I}{\Delta E} = (1.15e + 6) * (0.4459) * (1.43e - 11) = 7.32e - 6. \tag{11.3}$$

This change in optical power for a given electric field change would represent a 233 times improvement over the same sensor which was tested polarimetrically. However, this gain in sensitivity would come with a cost. For example, the Vernier setup would require a greater equipment cost in order to obtain the signal. Additionally, the process of fabricating Vernier gratings is not trivial. It would require doing all of the processing which is required for polarimetric sensing, plus the fabrication of gratings. One area of fabrication which would be challenging is to be able to fabricate two sets of FP gratings with gaps which only have a difference of 40 μm. Also, due to the narrowness of the transmission peaks, much of the power is lost, so amplification would be necessary. Biasing could also be a challenge since the fixed grating would need to be tuned so that the peaks are offset just slightly during sensing. Each of these physical constraints can be relaxed, but a decrease in sensitivity accompanies the greater fabrication tolerances.

11.4 Fabrication of Vernier Gratings

Some preliminary work has been done to verify the viability of the Vernier grating fabrication process.

Two SS-FBGs were fabricated using a pre-exposure mask and holographic grating patterning. The first SS-FBG is designed to have 100 μm long subgratings with a 50% duty cycle. The total grating length is 1.5 cm. The second SS-FBG is designed to have 150 μm long subgratings with 500 μm long gaps representing a duty cycle of $\sim$23%. Again the total grating length is 1.5 cm. Figure 11.8(a) shows an optical image from the first SS-FBG. Red light is coupled into the fiber to better show the regions where grating exists on the surface of the D-fiber. Figure 11.8(b) shows the measured reflection spectrum from this grating. The measured channel spacing from the reflection spectrum was found to be 4.13 nm.

Figure 11.9(a) shows an optical image from the second SS-FBG. Red light is again coupled into the fiber to better show the regions where grating exists on the surface of the D-fiber. Figure 11.9(b) shows the measured reflection spectrum from this grating. The measured channel spacing from the reflection spectrum was found to be 1.2 nm.

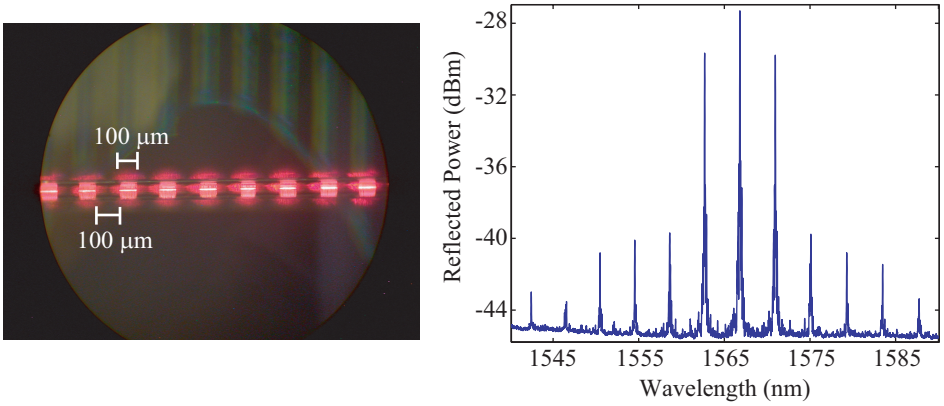

Figure 11.8: (a) Optical photograph of a SS-FBG on the flat surface of a D-Fiber. (b) The measured reflection spectrum from the SS-FBG.

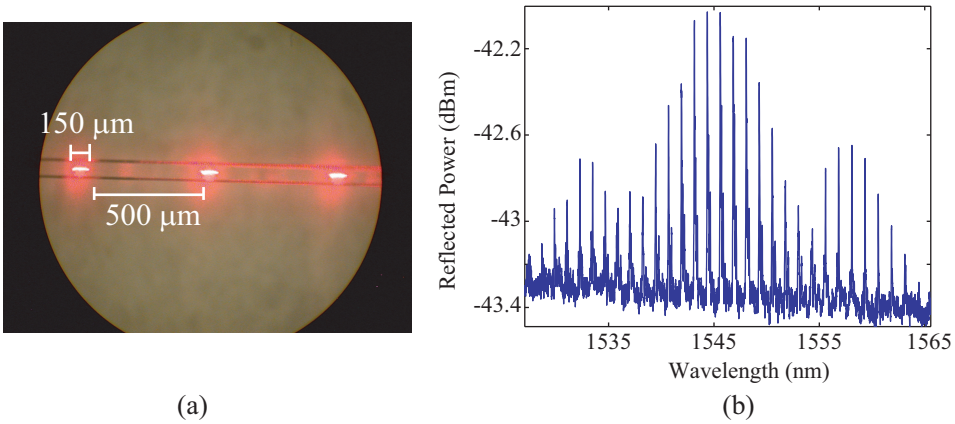

Figure 11.9: (a) Optical photograph of a SS-FBG on the flat surface of a D-Fiber. (b) The measured reflection spectrum from the SS-FBG.

FP-FBGs are also successfully fabricated using the masking technique. Figure 11.10 shows the measured and modeled transmission spectra for a FP-FBG created from two 1 mm long gratings with a 3.5 mm long gap. The measured spectrum is captured while launching vertically polarized light into the the fiber. It is expected that the measured Fabry-Pérot peaks extend to the top of the spectrum but are not visible due to the limited resolution of the OSA.

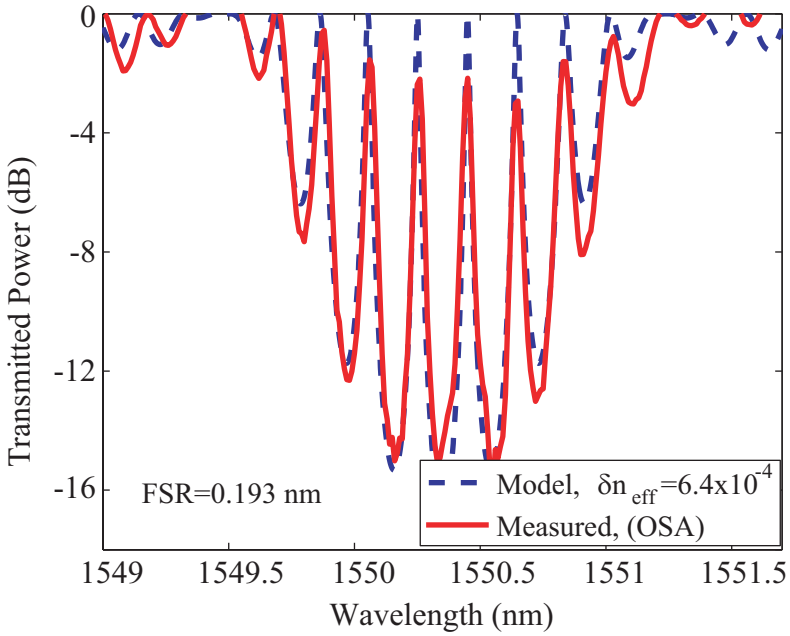

Figure 11.10: Measured and modeled transmission spectra from a FP-FBG.

11.5 Temperature Testing Results

Two FP-FBG's were fabricated and the transmission spectrum of the gratings was recorded with the Micron interrogator at a frequency of 1 Hz as the temperature of the sensing grating was increased. Figure 11.11 plots the spectrum as filmstrip where the temperature increases from Figure 11.11a to the right and down to 11.11l. At first the rightmost peak is transmits the most power. Then as the temperature is

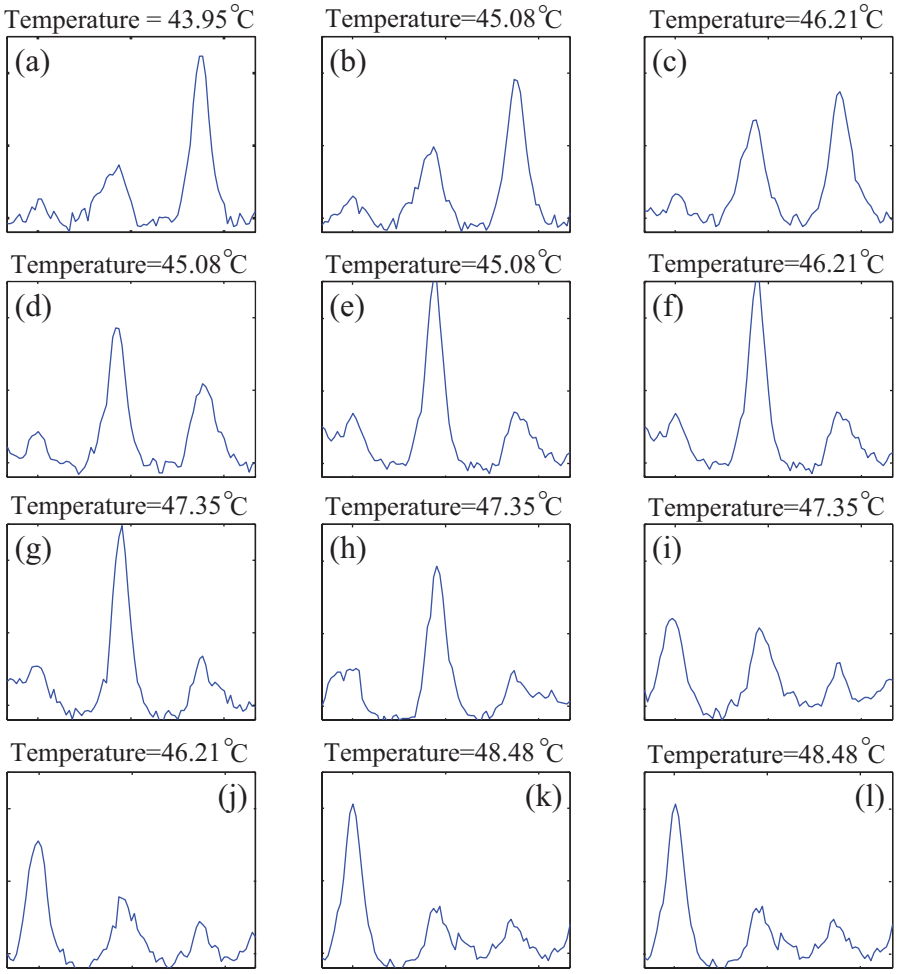

Figure 11.11: Filmstrip a FP-FBG Vernier scheme where the sensing grating was heated and the transmission spectrum observed. The temperature is increased from frame (a) to frame (l) and recorded above each frame. The y-axis tick marks from top to bottom correspond to -41, -42, and -43 dBm, and the x-axis tick marks from left to right correspond to 1551.85, 1552, and -1552.15.

increased the middle peak and then the leftmost peak become most prominent. This shifting of the peaks is proof of concept for how an electro-optic sensor would work, though the shift would be much smaller.

11.6 Future Work

Much work still needs to be done before the Vernier scheme could be used for electric field sensing. First, a much higher finesse with the vernier gratings would

have to be obtained. Second, the ability to fabricate two FP-FBG's with only a slightly different channel spacing would be needed. Next, a compatible process of make hybrid waveguide and gratings would need to be developed. One method that might be promising is to fabricate the gratings with photoresist using holography, and then afterwards to use the ink-jetting deposition method to deposit polymer in the Fabry-Pérot cavity

Chapter 12

Conclusion

Engineering often requires detailed knowledge about a system or situation in order to make design decisions. As a more accurate picture is obtained, greater clarity in making good engineering decisions is possible. One area where there is currently a lack of satisfactory information is in the testing of high power microwave weapons. The currently available sensors do not have all of the qualities of mechanical strength, temporal stability, minimal perturbation of the electric field by the sensor, and a small and flexible cross-sectional that would make for the optimal solution.

The optical transduction of high speed electric fields is promising solution. The D-fiber hybrid electro-optic polymer waveguide that has been developed and described in this dissertation. This dissertation is a compilation of the foundational research and the roadmap toward greater sensitivity of the D-fiber hybrid waveguide structure.

12.1 Contributions

Research toward making D-fiber devices and sensors using polymer material has been ongoing for over ten years at BYU. The research in this dissertation improves and extends upon the results reported in [93, 94, 95, 96, 46, 56, 82]. The previous work provides a technique for removing a portion of the core of the fiber and replacing it with a polymer material. The work in this dissertation represents the first successful hybrid D-fiber electric field sensor that BYU has produced. This work provides the theoretical foundation for each subsystem. Also, information about a

new method of modeling the guiding properties of the fiber core and transition regions is also presented and used to design a low loss AJL8/APC waveguide structure. Experimental results for the several subsystems are included such as the fabrication involved in making a hybrid waveguide, the packaging of the sensor, its connection with standard optical equipment, and electric-field sensing results. Additionally, a new method of photolithographically patterning feature on or in the core of a D-fiber is presented. Surface relief fiber Bragg gratings are written in the core of a hybrid D-fiber waveguide using E-beam lithography. Further work is done to improve the sensitivity of the sensors by working toward a Vernier sensing scheme. The MATLAB code which was used for some of the modeling is also included for completeness. My contributions to this work are summarized below.

Research from this work has resulted in the submission or publication of four peer reviewed journal articles, and two conference publications. A summary of the major contributions of this work is included below.

- Materials
  - Demonstration of an effective hybrid waveguide poling process.
  - Implementation of an in-situ second harmonic generation testing setup to characterize poling efficiency.
- Waveguide
  - Achievement of a greater understanding of the guiding characteristics of the D-fiber hybrid waveguide.
  - Development of D-fiber compatible polymer deposition methods.
- System
  - Development of a technique for low loss D-fiber fusion splicing.

  - Design of a compatible packaging technique for a D-fiber optical sensor and the testing of its mechanical strength.
  - Demonstration of the electrically non-intrusive nature of the D-fiber sensor by comparing it to the perturbation of thin metal wires inserted into a resonant waveguide.
  - Demonstration of effective E-field sensor testing and evaluation for both DR1/PMMA and AJL8/APC hybrid D-fiber waveguides,

- Supporting Technology
  - Development of an embedding technique for making a planar substrate from a D-shaped fiber, and the fabrication of various photolithographically patterned structures on the surface of an embdedded D-fiber.
  - Fabrication of SR-FBG's with E-Beam lithography and Ion Beam Milling.
  - Theoretical demonstration of Vernier scheme for Electric field sensing.

A more specific description of each contribution, as organized into the four main areas of (1) Material, (2) Waveguide, (3) System, and (4) Supporting Technologies follows.

12.1.1 Materials

Demonstration of an Effective Hybrid Waveguide Poling Process

Even with an optimal poling recipe for planar polymer layers on slides, as obtained through in-situ SHG, it was necessary to work towards extending these result to the poling of electro-optic polymer in the core of a D-fiber. The basic corona poling process is not amenable to poling a polymer located in the fiber core. The primary reason for this incompatibility is that the positive charges used to pole the polymer build up on the substrate rather than just on the flat surface of the fiber

resulting in the high electric field not being across the hybrid waveguide. In order to overcome this deficiency, the hybrid waveguide is encapsulated in low index epoxy and a protective layer of cover glass. This keeps the high electric field created through corona poling across the polymer. Additionally, the orientation of the fiber to the direction of the poling field is also critical for the device to work as an E-field sensor. Because of the geometry of the D-fiber, the fiber rotates when bent causing frequent unwanted fiber rotations. Some work was done to minimize the rotation of the fiber, and decrease the thickness of the low index epoxy to maximize the poling field.

Though this method worked well with DR1/PMMA, it was determined that AJL8/APC's higher conductivity results in a non-optimal poling with with the standard corona poling technique. Work toward in-line poling of electro-optic polymers in the core of a fiber was done using the embedding and patterning techniques presented in Chapter 9. It was found that using a barrier layer of PAA over the electrodes, and electro-optic polymer that a field of over 100 MV/m was possible at room temperature. Future work would aim to find compatible embedding materials that would allow for heating the embedded fiber to 150 $^{\circ}C$ during poling.

More details about the poling of electro-optic polymer can be found in Chapter 2.

Implementation of an In-Situ Second Harmonic Generation Testing Setup to Characterize Poling Efficiency

The poling of polymer is a sensitive process which aligns the microscopic chromophore molecules inside the polymer matrix to form a non-centro-symmetric material whose electron distribution is influenced by an applied electric field. Because this phenomenon occurs at such a small level, a measure of the effectiveness must be obtained indirectly. One method that this dissertation used to optimize the poling recipe was to use an in-situ second harmonic generation technique to indirectly measure the non-centro-symmetry of a polymer during the poling process. Various EO

polymers were poled and recipes obtained for their optimal poling conditions. Also, collaboration with the Tetramer from the University of Clemson was done to examine the potential of some of their materials as electro-optic polymers. More information about this effort is included in Chapter 3

12.1.2 Waveguide

Achievement of a Greater Understanding of the Guiding Characteristics of the D-fiber Hybrid Waveguide

At the beginning of the research efforts presented in this dissertation the greatest source of loss in a D-fiber hybrid waveguide was unknown. First, the hypothesis was that particle contamination was the major cause. Then, when particle contamination was almost eliminated and the losses still occurred, it was theorized that transition regions, or the lack of lateral confinement was the source. Depending on the latest experimental evidence the working theory varied between these two hypotheses.

Some of the work in this dissertation contributed to accurately placing the importance of various factors in waveguide loss. It was determined through numerical modeling and confirmed through experiment that the single mode guiding condition of the waveguide is of the greatest importance. V vs. b plots were used to determine the single mode guiding conditions for the hybrid waveguide structure, and were used to determine the optimal fabrication structure. The importance of the index of refraction of the polymer was realized, and it was determined that a lower index of refraction of EO polymer would provide optimal single-mode optical power polymer confinement.

It was also found that a fiber from which more of the fiber core is removed exhibits greater loss even with the same polymer layer thickness. A new hypothesis has been presented which ties the transition region to this loss. It is that the effective

index of the mode must be gradually increased from the unetched portion of the waveguide to the etched portion. A more accurate method of determining the profile of the fiber throughout the entire transition region was developed and carried out. This new model of the transition of the fiber indicates that the transitions are not linear, and therefore it is likely that the deepest etched fibers have an abrupt shift in effective index which results in greater loss.

Some preliminary experiments were performed to test this hypothesis. In one experiment the polymer was etched completely off the transitions. In another experiment the polymer was photobleached to form a tapered volume index from the unetched portion to the etched portion of the fiber using a UV laser and a LabView interfaced linear stage. Future work in this area would need to be done to determine if the hypothesis is true, but preliminary results showed improved power transmission in both of these experiments.

Development of D-fiber Compatible Polymer Deposition Methods

Prior to this work the deposition of the polymer layer was the most inconsistent step in the fabrication process. It was not uncommon for the polymer thickness to vary even on the same fiber. This inconsistency made it very difficult to determine an optimal polymer deposition recipe since the same recipe would often result in low and high loss sensors. It was determine that a more tightly controlled spin-cast process was required in order to get any sort of consistent results. First, a thermal was used to hold the fiber flat side up and tight during the spin-casting step. The twisting of the fiber flat during spin-casting was thus eliminated. Next, a spin casting recipe was developed using the Laurel spinner instead of the Solitec spinner. The Laurel spinner offered a more consistent spin casting program option. A maximum acceleration three second spin was found to be the best recipe to planarize the polymer layer on the D-fiber flat. It was also found that for consistent results it was imperative to use at least 0.5 ml of polymer.

With much more consistent results, low loss hybrid waveguide were finally obtained. Unfortunately, the amount of polymer required for consistent result made that technique prohibitive once a more expensive chromophore was used. The Dimatix DMP 2800 was used to ink-jet a very small volume of polymer into the core of the fiber. The ink-jetting method of polymer deposition is described further in Chapter 5.

12.1.3 System

Development of a Technique for Low Loss D-fiber Fusion Splicing

Due to D-fiber's non-standard core and cladding geometry, a technique using a commercially available fusion splicer was developed to obtain low loss connection from D-fiber to standard PM fiber. Chapter 7 includes more details of how this was done, and records the results.

Design of a Compatible Packaging Technique for a D-fiber Optical Sensor and the Testing of its Mechanical Strength

After all of the processing which is necessary for the fabrication of hybrid waveguide electric field sensors, the device section becomes fragile. Therefore, it becomes necessary to package the sensor in such a way as to maintain its flexibility and small cross-section while restoring its mechanical strength. A packaging design is developed and implemented in this dissertation and is shown to make the sensor section robust enough for normal handling. Chapter 6 includes more details of this research effort.

Demonstration of the Electrically Non-Intrusive Nature of the D-fiber Sensor by Comparing it to the Perturbation of Thin Metal Wires Inserted into a Resonant Waveguide

It has been assumed based on boundary conditions that an electric field would be minimally perturbed by using an all dielectric sensors. This dissertation reports a test which was done to prove this non-perturbing quality of the all dielectric D-fiber

E-field sensor as compared with the perturbation of small metal wires in a resonant waveguide structure.

Demonstration of Effective E-field Sensor Testing and Evaluation for both DR1/PMMA and AJL8/APC Hybrid D-fiber Waveguides

The DR1/PMMA E-field sensor demonstrated here is formed as part of a contiguous fiber resulting in a flexible and small cross-section device that can be embedded into electronic circuitry. This device is made by replacing part of the core of a D-fiber with DR1/PMMA that is electro-optic. The DR1/PMMA was used as proof of concept for the EO sensitivity of these devices.

Once the concept was proven with DR1/PMMA, a collaborative effort was commenced with Dr. Jen's group at the University of Washington to implement AJL8/APC as the hybrid core material. The lessons learned in the fabrication of DR1/PMMA hybrid waveguides were implemented. New obstacles were encountered in using the AJL8/APC material, such as its higher index of refraction, and it higher electrical conductivity. Successful electric field sensors were fabricated and found to show minimal electro-optic temporal decay, and the electro-optic coefficient were estimated to be twice as high as in DR1/PMMA.

Various sensor testing methods were developed throughout the course of this research. These testing setups included a high applied field DC testing setup with the polarization analyzer as well as a polarizer/analyzer configuration. Another testing setup was a MHz frequency testing setup that was used to measure the spectrum of a modulated electrical signal. Another setup was implemented to automatically measure the EO response of a sensor over a period of two-hundred hours to measure the temporal stability of its EO response. Other work was done manipulate and analyze the data from these various tests. Finally, successful collaboration with Ipitek in the testing of both DR1/PMMA, and AJL8/APC sensors at their site in Carlsbad,

California was accomplished. Chapter 8 describes these tests and their results in more detail.

12.1.4 Supporting Technology

Development of an Embedding Technique for Making a Planar Substrate from a D-shaped Fiber, and the Fabrication of Various Photolithographically Patterned Structures on the Surface of an Embdedded D-fiber.

D-fiber's geometry makes it difficult to apply standard integrated circuit fabrication techniques, so a method whereby the flat of a D-fiber is made to form a planar substrate is developed in this dissertation. This embedding technique reduces the fabrication challenges and makes possible the implementation of standard fabrication techniques. Chapter 9 includes a description of how this embedding technique was done.

Using the planar substrate formed with a D-fiber with the embedding technique, several structures were patterned on the surface of a fiber. First, a 10 micron line of photoresist is patterned over the core of a fiber. Second, an electrode structure is patterned, and then transfered into aluminum to form electrodes on the flat of the fiber that can be used for in-line contact polymer of the polymer in the core of the fiber. Finally, a self aligned electrode structure is made using the topography inherent to an etched D-fiber. These methods, and results are all described in Chapter 9.

Fabrication of SR-FBG's with E-Beam Lithography and Ion Beam Milling.

Work toward integrating the E-field sensor and fiber Bragg grating expertise of the optics lab was performed in this dissertation by fabricating DR1/PMMA surface relief grating in the core of an etched D-fiber with E-beam lithography. Also a grating array was written to show the versatility of the EBL SR-FBG fabrication process. The gratings fabricated in this dissertation had the highest SR-FBG contrast yet

obtained in the optics lab. More specific information about this effort can be found in Chapter 10.

Theoretical Demonstration of Vernier Scheme for Electric Field Sensing and Preliminary Experimental Results Toward Vernier Sensing.

A theoretical analysis of the increased sensitivity obtained from a differential Vernier sensing scheme is considered in this dissertation. Also, preliminary SR-FBG grating structures were also fabricated which match well with modeling results. The research efforts in this dissertation began the effort towards eventually using the Vernier scheme to sense electric fields. Chapter 11 discusses the analysis and results with respect to the Vernier sensing scheme.

12.2 Future Work

The results presented in this dissertation represent efforts which began by building the foundational expertise, and extended toward the successful fabrication of electric field sensors with hybrid EO polymer D-fiber waveguides. The ultimate sensitivity of these devices is not high enough for the current needs in the detection of high power microwave weapon testing, and future work should aim toward improving the overall device sensitivity. Three major areas of research would provide for the most sensitivity gain. First, the poling of higher conductivity EO polymer must be done with in-plane poling electrodes, which would result in a sensitivity improvement of 5x. Second, a more highly confined low loss waveguide should be fabricated. This can be done by using a lower refractive index EO polymer used to form single mode hybrid waveguide. The other way this can be done is by modifying the transition region more gradually from unetched to etched fiber. The increased confinement could result in an improvement of 5x-10x assuming minimal losses. Finally, using a vernier sensing scheme can also improve the ultimate devices sensitivity by as much as 200x. These three efforts combined would likely result in a three to four order of

magnitude improvement in sensitivity. Therefore the sensors would likely be able to measure electric fields as low as 0.5 to 0.05 V/m.

Additionally, the expertise gained by the optics lab in the fabrication of SR-FBG's with E-beam lithography and Ion-Beam milling as well as the ability to deposit small volumes of material in the core of a fiber with ink-jetting open up a variety of new possible research paths.

Bibliography

[1] "William Gilbert," July 2009. [Online]. Available: http://en.wikipedia.org/wiki/William_Gilbert 1

[2] R. Forber, W. C. Wang, D.-Y. Zang, S. Schultz, , and R. Selfridge, "Dielectric em field probes for hpm test & evaluation," *presented at the Annual ITEA Technology Review, Cambridge, United Kingdom*, pp. 7–10, 2007. 2

[3] H. Sun, A. Pyajt, J. Luo, Z. Shi, S. Hau, A. K.-Y. Jen, L. R. Dalton, and A. Chen, "All-dielectric electrooptic sensor based on a polymer microresonator coupled side-polished optical fiber," *IEEE Sensors*, vol. 7, pp. 515–524, 2007. 2

[4] T. S. Priest, G. B. Scelsi, and G. A. Woolsey, "Optical fiber sensor for electric field and electric charge using low-coherence, fabry-perot interferometry," *Appl. Opt.*, vol. 36, pp. 4505–4508, 1997. 2

[5] S. T. Vohra, F. Bucholtz, and A. D. Kersey, "Fiber-optic dc and low-frequency electric-field sensor," *Opt. Lett.*, vol. 16, pp. 1445–1447, 1991. 2

[6] K. Yang, P. Katehi, and J. Whitaker, "Electric field mapping system using an optical-fiber-based electrooptic probe," *IEEE Microwave and Wireless Components Letters*, vol. 11, no. 4, pp. 164–166, 2001. 2

[7] Y. J. Rao, H. Gnewuch, C. Pannell, and D. Jackson, "Electro-optic electric field sensor based on periodically poled linbo3," *Electronics Letters*, vol. 35, no. 7, pp. 596–597, 1999. 2

[8] T. L. Lowder, K. H. Smith, B. L. Ipson, A. R. Hawkins, R. H. Selfridge, and S. M. Schultz, "High-temperature sensing using surface relief fiber bragg gratings," *IEEE Photon. Tech. Lett.*, vol. 17, pp. 1926–1928, 2005. 3, 181

[9] R. H. Selfridge, S. M. Schultz, T. L. Lowder, V. P. Wnuk, A. Mendez, S. Ferguson, and T. Graver, "Packaging of surface relief fiber bragg gratings for use as strain sensors at high temperature," *Proc. SPIE*, vol. 6167, pp. 616 702.1–616 702.7, 2006. 3, 181

[10] T. L. Lowder, J. D. Gordon, S. M. Schultz, and R. H. Selfridge, "Volatile organic compound sensing using a surface relief d-shaped fiber bragg grating and a polydimethylsiloxane layer," *Opt. Lett.*, vol. 32, no. 17, pp. 2523–2525, 2007. 3, 181

[11] E. K. Johnson, J. M. Kvavle, R. H. Selfridge, S. M. Schultz, R. Forber, W. Wang, and D. Y. Zang, "Electric field sensing with a hybrid polymer/glass fiber," *Appl. Opt.*, vol. 46, no. 28, pp. 6953–6958, 2007. [Online]. Available: http://ao.osa.org/abstract.cfm?URI=ao-46-28-6953 3, 98, 166

[12] R. Gibson, R. Selfridge, S. Schultz, W. Wang, , and R. Forber, "Electro-optic sensor from high q resonance between optical d-fiber and slab waveguide," *Appl. Opt.*, vol. 47, pp. 2234–2240, 2008. 3

[13] X. C. Long, R. A. Myers, and S. R. J. Brueck, "A poled electrooptic fiber." *IEEE Photonics Technology Letters*, vol. 8, pp. 227–+, Feb. 1996. 4

[14] F. Kajzar, K.-S. Lee, and A. K. Y. Jen, *Polymers for Photonics Applications II.* Berlin Heidelberg: Springer-Verlag, 2003, ch. Polymeric Materials and their Orientation Techniques for Second-Order Nonlinear Optics, pp. 1–85. 11, 15

[15] H. Ma, A.-Y. Jen, and L. Dalton, "Polymer-based optical waveguides: Materials, processing, and devices," *Advanced Materials*, vol. 14, no. 19, pp. 1339–1365, 2002. 11

[16] L. Dalton, *Polymers for Photonics Applications I.* Berlin Heidelberg: Springer-Verlag, 2001, ch. Nonlinear Optical Polymeric Materials: From Chromophore Design to Commercial Applications, pp. 1–86. 11

[17] M. Lee, H. E. Katz, C. Erben, D. M. Gill, P. G. J. D. Heber, and D. J. McGee, "Broadband modulation of light by using an electro-optic polymer," *Science*, vol. 298, no. 5597, pp. 1401–1403, 2002. 11

[18] V. Tomme, V. Deale, R. Baets, and P. Lagasse, "Integrated optic devices based on nonlinear optical polymers," *IEEE Journal of Quantum Electronics*, vol. 27, pp. 778–787, March 1991. 12

[19] L. R. Dalton, A. K. Jen, W. H. Steier, B. H. Robinson, S.-H. Jang, O. Clot, H. C. Song, Y.-H. Kuo, C. Zhang, P. Rabiei, S.-W. Ahn, and M. C. Oh, "Organic electro-optic materials: some unique opportunities," *Organic Photonic Materials and Devices VI*, vol. 5351, no. 1, pp. 1–15, 2004. 14

[20] K. SINGER, W. HOLLAND, M. G. KUZYK, G. L. WOLK, and P. A. CAHILL, "Guest-host polymers for nonlinear optics," *Molecular crystals and liquid crystals*, vol. 189, pp. 123–136, 1990. 15

[21] D. Healy, G. Cross, and D. Bloor, "Guest-host polymeric systems as non-linear optical materials," *Electrets, 1994. (ISE 8), 8th International Symposium on*, pp. 787–793, Sep 1994. 15

[22] M. A. Mortazavi, A. Knoesen, and V. Kowel, "Second-harmonic generation and absorption studies of polymer-dye films oriented by corona-onset poling at elevated temperatures," *J. Opt. Soc. Am. B.*, vol. 6, pp. 1733–741, Apr 1989. 15, 16, 35, 39, 113

[23] H. L. Hampsch, J. M. Torkelson, S. J. Bethke, and S. G. Grubb, "Second harmonic generation in corona poled, doped polymer films as a function of corona processing," *Journal of Applied Physics*, vol. 67, no. 2, pp. 1037–1041, 1990. [Online]. Available: http://link.aip.org/link/?JAP/67/1037/1 16, 35, 40, 49

[24] R. Inaba, M. Sagawa, M. Isogai, and A. Kakuta, "In situ observation of the orientational motion of chromophores during corona poling of electro-optic polyimides," *Macromolecules*, vol. 29, no. 8, pp. 2954–2959, 1996. [Online]. Available: http://pubs.acs.org/doi/abs/10.1021/ma950748f 16, 35

[25] K. D. Singer, M. G. Kuzyk, W. R. Holland, J. E. Sohn, S. J. Lalama, R. B. Comizzoli, H. E. Katz, and M. L. Schilling, "Electro-optic phase modulation and optical second-harmonic generation in corona-poled polymer films," *Applied Physics Letters*, vol. 53, no. 19, pp. 1800–1802, 1988. [Online]. Available: http://link.aip.org/link/?APL/53/1800/1 16

[26] P. Ribeiro, M. Raposo, J. Marat-Mendes, and J. Giacometti, "Constant-current corona charging of biaxially stretched pvdf films in humidity-controlled atmospheres," *Electrical Insulation, IEEE Transactions on*, vol. 27, no. 4, pp. 744–750, Aug 1992. 16, 40

[27] B. Gross, J. A. Giacometti, and G. F. L. Ferreira, "Charge storage and transport in electron-irradiated and corona-charged dielectrics," *Nuclear Science, IEEE Transactions on*, vol. 28, no. 6, pp. 4513–4522, Dec. 1981. 16

[28] J. Giacometti, S. Fedosov, and M. Costa, "Corona charging of polymers: Recent advances on constant current charging," *Brazilian Journal of Physics*, vol. 29, no. 2, pp. 269 – 279, 1999. 16, 40, 44

[29] R. A. Hill, A. Knoesen, and M. A. Mortazavi, "Corona poling of nonlinear polymer thin films for electro-optic modulators," *Applied Physics Letters*, vol. 65, no. 14, pp. 1733–1735, 1994. [Online]. Available: http://link.aip.org/link/?APL/65/1733/1 17, 49

[30] "Email correspondence from josh kvavle to dr. jingdong luo," July 2008. 19

[31] H. Tazawa, Y.-H. Kuo, I. Dunayevskiy, J. Luo, A. K.-Y. Jen, H. R. Fetterman, and W. H. Steier, "Ring resonator-based electrooptic polymer traveling-wave modulator," *J. Lightwave Technol.*, vol. 24, no. 9, p. 3514, 2006. [Online]. Available: http://jlt.osa.org/abstract.cfm?URI=JLT-24-9-3514 24

[32] R. Michalak, Y.-H. Kuo, F. Nash, A. Szep, J. Caffey, P. Payson, F. Haas, B. McKeon, P. Cook, G. Brost, J. Luo, A.-Y. Jen, L. Dalton, and W. Steier, "High-speed ajl8/apc polymer modulator," *Photonics Technology Letters, IEEE*, vol. 18, no. 11, pp. 1207–1209, June 2006. 24, 114, 116

[33] J. Luo, S. Liu, M. A. Haller, J.-W. Kang, T.-D. Kim, S.-H. Jang, B. Chen, N. Tucker, H. Li, H.-Z. Tang, L. R. Dalton, Y. Liao, B. H. Robinson, and A. K. Jen, "Recent progress in developing highly efficient and thermally stable nonlinear optical polymers for electro-optics," *Organic Photonic Materials and Devices VI*, vol. 5351, no. 1, pp. 36–43, 2004. [Online]. Available: http://link.aip.org/link/?PSI/5351/36/1 24, 53, 98, 116, 168

[34] R. Song, A. Yick, and W. H. Steier, "Conductivity-dependency-free in-plane poling for mach-zehnder modulator with highly conductive electro-optic polymer," *Applied Physics Letters*, vol. 90, no. 19, p. 191103, 2007. 27

[35] "Glass," May 2009. [Online]. Available: http://en.wikipedia.org/wiki/Glass 27

[36] P. A. Franken, A. E. Hill, C. W. Peters, and G. Weinreich, "Generation of optical harmonics," *Phys. Rev. Lett.*, vol. 7, no. 4, pp. 118–119, Aug 1961. 31

[37] "Encyclopedia of laser physics and technology - frequency doubling," Jan 2009. [Online]. Available: http://www.rp-photonics.com/frequency_doubling.html 32

[38] R. W. Boyd, *Nonlinear Optics: Third Edition.* Burlington, MA: Academic Press, 2008. 33

[39] D. J. Williams, "Organic polymeric and non-polymeric materials with large optical nonlinearities," *Angewandte Chemie International Edition in English*, vol. 23, no. 9, pp. 690–703, 1984. 35

[40] K. D. Singer, J. E. Sohn, and S. J. Lalama, "Second harmonic generation in poled polymer films," *Applied Physics Letters*, vol. 49, no. 5, pp. 248–250, 1986. [Online]. Available: http://link.aip.org/link/?APL/49/248/1 35

[41] Z. Hou, L. Liu, L. Xu, J. Chen, Z. Xu, W. Wang, F. Li, and M. Ye, "In situ second-harmonic generation measurement study of poled phenylhydrazone doped polymer films," *Thin Solid Films*, vol. 354, no. 1-2, pp. 232 – 236, 1999. [Online]. Available: http://www.sciencedirect.com/science/article/B6TW0-3XVG894-1B/2/49ba5a64377b9ed65c344481e59496f6 35

[42] R. Hagen, O. Zobel, O. Sahr, M. Biber, M. Eckl, P. Strohriegl, C.-D. Eisenbach, and D. Haarer, "Poling and orientational relaxation: Comparison of nonlinear optical main-chain and side-chain polymers," *Journal of Applied Physics*, vol. 80, no. 6, pp. 3162–3166, 1996. [Online]. Available: http://link.aip.org/link/?JAP/80/3162/1 35, 40

[43] W. Shi, "Investigation of the polyetherketone guest host DR1/PEK-c polymer films by real-time monitoring of the second-harmonic generation," *Optics and Lasers in Engineering*, vol. 32, pp. 139–145, Aug. 1999. 35, 40

[44] Z. Hou, L. Liu, J. Chen, L. Xu, Z. Xu, W. Wang, F. Li, and M. Ye, "Improved optical nonlinearity of poled stilbene doped polymer films,"

Physics Letters A, vol. 252, no. 1-2, pp. 87 – 91, 1999. [Online]. Available: http://www.sciencedirect.com/science/article/B6TVM-3W6M037-K/2/d7e3597237be8da1f74c4a4e34e94f4e 35, 40

[45] S. E. Creager, D. D. DesMarteau, and D. W. Smith, "New proton-conducting fluoropolymer electrolytes for pem fuel cells," Oct 2007. [Online]. Available: www.hydrogen.energy.gov/pdfs/review07/besp_18_creager.pdf 50

[46] B. L. Ipson, "Polarimetric temperature sensing using core-replaced fiber," Master's thesis, Brigham Young University, Provo, UT, December 2004. 57, 221

[47] J. A. Kong, *Electromagnetic Wave Theory*. New York: John Wiley & Sons, 1986. 59

[48] G. P. Agrawal, *Fiber-Optic Communication Systems*. New York: John Wiley & Sons, 2002. 59, 73, 74

[49] D. H. Staelin, A. W. Morgenthaler, and J. A. Kong, *Electromagnetic Waves*. New Jersey: Prentice Hall, 1994. 59

[50] F. T. Ulaby, *Applied Electromagnetics*. New Jersey: Prentice Hall, 2004. 59

[51] B. E. A. Saleh and M. C. Teich, *Fundamentals of Photonics*. New York: John Wiley & Sons, 1991. 59

[52] R. Syms and J. Cozens, *Optical Guided Waves and Devices*. London: McGraw-Hill, 1992. 59, 135

[53] J. Chilwell and I. Hodgkinson, "Thin-films filed-transfer matrix theory of planar multilayer waveguides and reflection from prism-loaded waveguides," *J. Opt. Soc. Am. A*, vol. 1, pp. 742–753, Jun. 1984. 69

[54] M. Abramowitz and I. A. Stegun, *Handbook of Mathematical Functions With Formulas, Graphs, and Mathematical Tables*. Washington, D.C.: U.S. Government Printing Office, 1964. 73

[55] S. Mononobe and M. Ohtsu, "Fabrication of a pencil-shaped fiber probe for near-field optics by selective chemical etching," *J. Light. Techn.*, vol. 14, pp. 2231–2235, Oct 1996. 112

[56] K. H. Smith, "In-fiber optical devices based on d-fiber," Ph.D. dissertation, Brigham Young Univ., Provo, UT, Apr. 2005. 112, 181, 221

[57] T. L. Lowder, "Surface relief d-fiber bragg gratings for sensing applications," Ph.D. dissertation, Brigham Young Univ., Provo, UT, October 2008. 112, 181, 201, 209, 279

[58] N. P. Pham, J. N. Burghartz, and P. M. Sarro, "Spray coating of photoresist for pattern transfer on high topography surfaces," *Journal of Micromechanics and Microengineering*, vol. 15, pp. 691–697, 2005. 115

[59] M. F. Mabrook, C. Pearson, , and M. C. Petty, "An inkjet-printed chemical fuse," *Appl. Phys. Lett.*, vol. 86, p. 013507, 2005. 115

[60] Y. Xia and R. H. Friend, "Controlled phase separation of polyfluorene blends via inkjet printing," *Macromolecules*, vol. 38, pp. 6466–6471, 2005. 115

[61] Y. X. and R. H. Friend, "Polymer bilayer structure via inkjet printing," *Appl. Phys. Lett.*, vol. 88, p. 163508, 2006. 115

[62] Y. Liu, K. Varahramyan, and T.Cui, "Low-voltage all-polymer field-effect transistor fabricated using an inkjet printing technique," *Macromolecular Rapid Communications*, vol. 26, no. 24, pp. 1955–1959, 2005. 115

[63] M. Mabrook, C. Pearson, and M. Petty, "Inkjet-printed polypyrrole thin films for vapour sensing," *Sensors and Actuators B: Chemical*, vol. 115, no. 1, pp. 547–551, 2006. 115

[64] B.-J. de Gans, P. C. Duineveld, and U. S. Schubert, "Inkjet printing of polymers: State of the art and future developments," *Advanced Materials*, vol. 16, pp. 203–213, 2004. 115, 117

[65] P. Calvert, "Inkjet printing for materials and devices," *Chemistry of Materials*, vol. 13, pp. 3299–3305, 2001. 115

[66] Y. Yoshioka and G. E. Jabbour, "Desktop inkjet printer as a tool to print conducting polymers," *Synthetic Metals*, vol. 156, pp. 779–783, 2006. 115

[67] G. H. Shim, M. G. Han, J. C. Sharp-Norton, S. E. Creager, and S. H. Foulger, "Inkjet-printed electrochromic devices utilizing polyaniline-silica and poly (3,4-ethylenedioxythiophene) -silica colloidal composite particles," *J. Mater. Chem.*, vol. 18, pp. 594–601, 2008. 115

[68] E. Tekin-Kazancioglu, "Thin film libraries of functional polymers and materials prepared by inkjet printing," Ph.D. dissertation, Eindhoven University of Technology, Eindhoven, Netherlands, 2007. 116

[69] "Jettable fluid formulation guidelines," June 2009. [Online]. Available: http://www.dimatix.com/ 117

[70] J. M. Kvavle, S. M. Schultz, and R. H. Selfridge, "Low loss elliptical core d-fiber to panda fiber fusion splicing," *Optics Express*, vol. 16, no. 18, pp. 13 552–13 559, 2008. 128

[71] W. Zheng, "Automated fusion-splicing of polarization maintaining fibers," *Journal of Lightwave Technology*, vol. 15, pp. 125–134, Jan. 1997. 133

[72] Y. Kato, "Fusion splicing of polarization preserving fibers," *Appl. Opt.*, vol. 24, pp. 2346–2350, Aug. 1985. 133

[73] J. Noda, N. Shibata, T. Edahiro, and Y. Sasaki, "Splicing of single polarization-maintaining fibers," *Lightwave Technology, Journal of*, vol. 1, no. 1, pp. 61–66, Mar 1983. 133

[74] J. Noda, K. Okamoto, and Y. Sasaki, "Polarization-maintaining fibers and their applications," *Lightwave Technology, Journal of*, vol. 4, no. 8, pp. 1071–1089, Aug 1986. 133

[75] "Optical fibre: Panda fibre," Jan 2009. [Online]. Available: www.fujikura.co.uk/fibre_optics/products/speciality_fibre/panda_fibre.html 134

[76] "KVH e-core polarization maintaining optical fiber," Jan 2009. [Online]. Available: www.kvh.com/pdf/EcorePMFiber_6.04.pdf 134

[77] H. Tsuchiya and N. Imoto, "Dispersion-free single-mode fibre in 1.5 m wavelength region," *Electronics Letters*, vol. 15, no. 15, pp. 476–478, 19 1979. 134

[78] Y. Ando and H. Hanafusa, "Low-loss optical connector between dissimilar single-mode fibers using local core expansion technique by thermal diffusion," *Photonics Technology Letters, IEEE*, vol. 4, no. 9, pp. 1028–1031, Sep 1992. 135

[79] A. D. Yablon, *Optical Fiber Fusion Splicing.* New York: Springer, 2005. 136, 139, 140

[80] e. a. L. Ohzawa, G. Barbarossa, "Development of a new optical fusion splicer for factory use," *Proc. of the 48th IWCS at Atlantic City*, pp. 644–649, 1999. 138

[81] T. Conese, G. Barbarossa, and M. N. Armenise, "Accurate loss analysis of single-mode fiber/d-fiber splice by vectorial finite-element method," *IEEE Photonics Technology Letters*, vol. 7, pp. 523–525, May 1995. 141

[82] E. K. Johnson, "Low loss hybrid waveguide electric field sensor based on optical d-fiber," Master's thesis, Brigham Young University, Provo, UT, December 2007. 150, 221

[83] R. Mears, L. Reekie, I. Jauncey, , and D. Payne, "Low noise erbium-doped fiber amplifier operating at 1.54μm," *Electron Lett.*, vol. 23, pp. 1026–1028, 1987. 171

[84] K. Hill and G. Meltz, "Fiber bragg grating technology fundamentals and overview," *IEEE J. Lightwave Technol.*, vol. 15, pp. 1263–1276, 1997. 171

[85] A. Othonos and K. Kalli, *Fiber Bragg Gratings: Fundamentals and Applications in Telecommunications and Sensing.* Boston: Artech House, 1999. 181

[86] W. Zhou and Z. Wang, *Scanning Microscopy for Nanotechnology Techniques and Applications.* New York, NY: Springer Science, 2006. 183

[87] J. C. Nabity, *Nanometer Pattern Generation System-User's Manual for NPGS v8 & v9.* Bozeman, MT: Lithography Systems, 2002. 184

[88] L. Pierno, M. Dispenza, A. Secchi, A. Fiorello, and V. Foglietti, "A lithium niobate electro-optic tunable bragg filter fabricated by electron beam lithography," *Journal of Optics A: Pure and Applied Optics*, vol. 10, no. 6, p. 064017 (6pp), 2008. [Online]. Available: http://stacks.iop.org/1464-4258/10/064017 204

[89] "Rifle sights," June 2009. [Online]. Available: http://www.riflesmith.com/sights.html 209

[90] M. J. Everitt, "A vernier method of using a slide-rule," *Journal of Scientific Instruments*, vol. 27, no. 11, pp. 316–317, 1950. [Online]. Available: http://stacks.iop.org/0950-7671/27/316 209

[91] "Vernier scale," June 2009. [Online]. Available: http://en.wikipedia.org/wiki/Vernier_scale 209

[92] S. Choi, Z. Peng, Q. Yang, S. J. Choi, and P. Dapkus, "Tunable narrow linewidth all-buried heterostructure ring resonator filters using vernier effects," *Photonics Technology Letters, IEEE*, vol. 17, no. 1, pp. 106–108, Jan. 2005. 209

[93] I. A. E. Bakri, "Elliptical-core d-fiber temperature sensitivity measurement for temperature sensor applications," Master's thesis, Brigham Young University, Provo, UT, April 1997. 221

[94] G. M. Kraus, "Polymer waveguide formation in a d-shaped fiber," Master's thesis, Brigham Young University, Provo, UT, August 2001. 221

[95] M. V. Pack, "Numerical analysis of an electro-optic polymer core waveguide for high-speed optical modulation," Master's thesis, Brigham Young University, Provo, UT, December 2007. 221

[96] M. S. Smith, "Centrifugal casting to create an integrated active waveguide," Master's thesis, Brigham Young University, Provo, UT, December 2001. 221

[97] A. S. Sudbo, "Film mode matching: a versatile numerical method for vector mode field calculations in dielectric waveguides," *Pure and Applied Optics*, no. 11, pp. 211–233, 1993. 296

Appendix A

Detailed Processes

A.1 Fiber Preparation and Power Monitored Etching

1. Brake off a section of D-fiber 80 cm in length.

2. Use the Luminos jacket striper or mechanical heat stripper to strip off the jacket on both ends of the fiber and a section 5 cm in length in the middle of the fiber.

3. Place the fiber in the etch boat with the reflective flat side facing up and the stripped middle region in the center of the etch boat.

4. Cleave both ends of the fiber by placing the fiber flat side up in the Fujikura precision cleaver.

5. Slide the two fiber holders of the etch boat close together.

6. If the fiber does not bend straight up or down or the bend is not in the center of the stripped region adjust the placement of the fiber.

7. Place the stripped center region in the isopropanol alcohol of the ultra sonic cleaner and turn the ultra sonic cleaner on for ten minuets.

8. Take the fiber out of the ultra sonic cleaner and slide the fiber holders away from each other to make the fiber taut.

9. Dry the fiber off with compressed air.

10. If the spool of fiber being used tends to become brittle under the jacket after etching in HF, glide a drop of AZ3330 photo resist along both sides of stripped region of the fiber covering most of the jacket that is between the fiber holders and dry with the heat gun.

11. Clean out the water container in the fume hood, fill it up with de-ionized water, and place it in the metal pan in the fume hood.

12. Place the etch boat on the water container and place the ends of the fiber in the xyz stage and optical power detector.

13. Connect the 660 nm laser to the xyz stage and turn on the laser and temperature controller.

14. Align the fiber to the laser source by adjusting the xyz stage until maximum power is achieved.

15. Put on personal protection equipment appropriate for HF handling (two pairs of gloves, apron, goggles, and face shield).

16. Make sure there is sufficient air flow through the fume hood.

17. Slightly open the lid of the HF to loosen the seal and place the container of HF in the metal pan in the fume hood.

18. Finish taking the lid off of the HF, being careful to watch out for droplets of HF that may have condensated on the top of the lid, and place the lid upside down inside of the fume hood.

19. Place the etch boat on the container of HF and slide the fiber holders together so that about 2 cm of the stripped fiber is immersed in the HF.

20. Close the fume hood door.

21. Start the Labview etching program.

22. Select the desired etch depth in the program and click on the calculate extraction power button.

23. Once the power drops to the desired level, place the fiber in the container of water.

24. Put the lid on the HF container and put it back in its storage place.

25. Click on the save and record button in the Labview program.

26. Turn off the laser and the temperature controller and take the fiber out of the xyz stage and power detector.

27. Place the fiber in the ultra sonic cleaner filled with isopropanol alcohol and turn it on for five minutes.

28. Slide the fiber holders away from each other to make the fiber taught and dry off the fiber with compressed air.

A.2 Fiber Preparation and Polarimetric Etching for SR-FBG's

1. Brake off section of D-fiber ∼80 cm in length.

2. Use the Luminos jacket striper or mechanical heat stripper to strip of the jacket on both ends of the fiber and a section ∼2 cm in length in the middle of the fiber.

3. Place the fiber in the etch boat with the shiny side flat side up and the stripped middle region in the center of the etch boat.

4. Cleave both ends of the fiber by placing the fiber flat side up in the Fujikura precision cleaver or using the "Battle-ax".

5. Slide the two fiber holders of the etch boat close together.

6. If the fiber does not bend straight up or down or the bend is not in the center of the stripped region adjust the placement of the fiber.

7. Place the stripped center region in the isopropanol alcohol (IPA) of the ultra sonic cleaner and turn the ultra sonic cleaner. The ultra sonic cleaner automatically turns off when the cleaning cycle is done.

8. Take the fiber out of the ultra sonic cleaner and slide the fiber holders away from each other to make the fiber taught.

9. Dry the fiber off with compressed air. It is important to blow the IPA off of the fiber or else a residue is left behind.

10. Place the fiber in a bath of DeContam and think good thoughts. Leave the fiber in the bath for at least a few minutes and then wash off the DeContam with DI water.

11. Clean out the water container in the fume hood, fill it up with DI water, and place it in the metal pan in the fume hood.

12. Place the etch boat on the water container and place the ends of the fiber in the xyz stage and optical power detector.

13. Connect the 1550 nm laser to the xyz stage and turn on the laser. Make sure that the polarizers are placed both at the source (on the xyz stage) and in front of the detector. The polarizers should be placed at 45° angles with respect to the flat surface of the D-fiber.

14. Align the fiber to the laser source by adjusting the xyz stage until maximum power is achieved.

15. The wavelength adjust knob can be used to check to see if the fiber is correctly aligned with respect to the polarizers. As the wavelength is tuned the power should fluctuate. It is best to try to get at least a 3 dB swing.

16. Put on personal protection equipment appropriate for HF handling (two pairs of gloves, apron, goggles, and face shield).

17. Make sure there is sufficient air flow through the fume hood.

18. Slightly open the lid of the HF to loosen the seal and place the container of HF in the metal pan in the fume hood.

19. Finish taking the lid off of the HF, being careful to watch out for droplets of HF that may be on the top of the lid, and place the lid upside down inside of the fume hood.

20. Place the etch boat on the container of HF and slide the fiber holders together so that $\sim$2 cm of the stripped fiber is immersed in the HF.

21. Close the fume hood door.

22. Start the Labview etching program.

23. Etch the fiber until the desired etch depth has been achieved by watching the complete oscillations in the output power. Usually the fiber is taken out at 3 oscillations which corresponds to $\sim$0.4 μm of cladding left above the core. Remove the fiber and put it directly into the DI water.

24. Put the lid on the HF container and put it back in its storage place.

25. Stop the Labview etching program.

26. Turn off the laser.

27. Slide the fiber holders away from each other to make the fiber taught and rinse clean using the bottle of DI water.

28. It is usually best to take the fiber into the clean room as quickly as possible to avoid any further contamination.

A.3 Polymer/Chromophore and Solvent Mixing

1. Notes about EO polymer Mixing

   (a) Each part in the polymer, chromophore and solvent mixture should be weighed with an accurate scale to ensure proper chemistry.

   (b) Dr. Mazzeo has a Cole-Parmer Symmetry PA Analytical Balances 120g x 0.0001g scale in room CB 417 that can be used with his permission for the mixing of EO polymer.

   (c) Only plan on mixing about .5 ml of polymer at a time, since after about a week of sitting in solution the chances of the chromophore reacting with the solvent increase significantly. It is not wise to use an EO polymer solution that is more than one week old.

2. Place a sheet of 4" by 4" sheet of FisherBrand weighing paper on the scale

3. Put a micro stir bar into a .5 dram FisherBrand shell vial (sold with a tite-seal cap) and place it on the scale.

4. Carefully add polymer to the vial until the desired amount of polymer is added.

5. Calculate the weight of polymer necessary for a certain doping percent using this ratio: Doping % = (Chromophore Weight)/(Chromophore Weight + Polymer Weight)

6. Add the calculated amount of chromophore to the vial with the small metal spoon.

7. Calculate the amount of solvent required for the correct viscosity. The solution is usually described in terms of wt% from the following relationship: wt% = (Weight of Solids)/(Weight of Solids + Weight of Solvent).

8. Add solvent to the vial using a FisherBrand 5 3/4" Pasteur Pipette. Plastic pipettes are likely to react with the solvent and potentially detrimentally affect the chemistry of the EO polymer solution.

9. Put a tite-seal cap on the vial.

10. Place the vial on the stir plate until the polymer is completely dissolved.

    (a) For High Molecular Weight PMMA it may take several days with a heated (60 ° stir-plate before the polymer completely dissolves

    (b) For APC it should only require stirring at room temperature for several hours due to its lower molecular weight

11. Attach a .2 μm pore size 13 mm diameter PTFE filter to a 1 ml syringe. PTFE will not react with the solvents. The 13 mm diameter filter will also waste less material.

12. Using a Pasteur Pipette, transfer the polymer solution to the syringe. Use the syringe plunger to force the polymer solution through the filter, and into another clean shell vial.

13. Place a cap on the vial and label it with the date, and solution parameters for later identification.

A.4 Spin Casting for Polymer Deposition

1. Place a silicon wafer under the etched region of the fiber and tape the fiber down to the wafer at both ends of the stripped region.

2. Place a drop of hot glue on both ends of the stripped region as close to the jacket of the fiber as possible.

3. Coil the remaining fiber onto the silicon wafer and tape it down.

4. Take the etched fiber into the clean room or cover with a clean room paper towel to prevent contaminants from getting into the etched core.

5. Once in the cleanroom, use the nitrogen gun to blow off any particles that may have landed on the fiber.

6. Place the wafer on the Laurel spinner and set the desired spin speed, ramp rate, and spin time.

7. Turn on the spinner vacuum, place the desired amount of polymer in solution to the etched region, close the lid and start the spinning program.

8. Once the wafer has stopped spinning, turn off the vacuum and place the wafer on a hot plate at the desired temperature for the desired time to dry the polymer.

9. Remove the tape holding the fiber onto the wafer and uncoil the fiber.

10. Place the wafer on a hot plate set at 95° C Celsius to melt the hot glue.

11. Remove as much of the hot glue as possible once it is melted and then carefully pull the fiber off of the wafer.

A.5 Polymer Printing

1. Mount the fiber to a glass slide with Polyimide tape

2. Insert Materials cartridge into the printer

3. Turn on the DMP2800 Printer

4. Turn on the Jetting Software

5. Place sample on the printing stage when prompted
6. Open the correct cartridge jet settings
7. Select the right pattern
8. If the cartridge has never been used, run two purge steps to prime the valves
9. Open the Drop Watcher menu, and examine the drops for consistency
10. Close the drop watcher and open the fiducial camera view.
11. Align the fiber longitudinal axis with the "calibrated theta" option in menu
12. Set the origin to somewhere under the fiber, and print a test line
13. If the line is good, proceed by setting the origin to the center of the fiber where the jacket is stripped
14. If the line is not good, clean the cartridge, and repeat the test line somewhere else on the sample
15. After printing, remove the sample from the printing and place it in an oven overnight for dehydration baking.

A.6 Fiber Encapsulation for Poling

1. Slide a section of tubing onto each side of the fiber next to the etched region.
2. Slide each end of the fiber into the tool used for making the fiber flat side up.
3. Keep the fiber taught by placing the mounted magnets about a half a centimeter apart.
4. Rotate the ends of the fiber until the flat side of the fiber is facing up.

5. Use a microscope to get the fiber exactly flat side up and to determine the exact location of the etched region.

6. Put a piece of polyimide tape sticky side up in between the spacers of the electrode holder.

7. Place the bottom electrode on top of the polyimide tape and secure it in place by taping the wire down.

8. Slide the electrode holder under the etched region and onto the magnets that hold it in place.

9. Mix up a few drops of the low index epoxy and allow all of the bubbles to come out (placing it on top of the ultrasonic cleaner helps the bubbles to come out).

10. Place the low index epoxy on the etched region making sure to completely cover the electrode and fiber up to the protective tubing.

11. Place a cover glass slide on top of the fiber.

12. Put small magnets on top of the cover glass to hold it in place.

13. Place the fiber in the oven set at 50° C until the low index epoxy is cured (about 4 hrs).

14. Remove the sensor from the oven and tool being careful not to crack the cover glass.

15. Tape the protective tubing to the ends of the cover glass.

A.7 Corona Poling

1. Place the sensor in the poling setup.

2. Slide the Teflon bar holding the poling needles on top of the sensor so that the sensor is pressed against silicon wafer in the poling set up so that there is good heat transfer to the sensor.

3. Connect the electrode to the ground wire of the high voltage supply.

4. Set the temperature controller to the desired poling temperature and ramp rate.

5. Once the desired temperature is reached, apply 10 kV to the three needles from the high voltage supply.

6. Pole for the desired amount of time then ramp the temperature down with the voltage applied.

7. Once the sensor is cooled down sufficiently, turn off the high voltage supply and remove the sensor from the poling set up.

A.8 DC Testing

1. Place another electrode on top of the cover glass and tape down.

2. Place one fiber end into an xyz stage and place the other end of the fiber into an optical power detector.

3. Place the linear polarizer and quarter wave plate that are fixed together in a rotatable holder in the path of the collimated laser before it is focused into the fiber.

4. Rotate the linear polarizer and quarter wave plate to maximize optical power going through the sensor.

5. Adjust the xyz stage to achieve maximum optical power through the sensor.

6. Follow steps in the sections testing with a polarization analyzer or testing with a polarizer.

A.8.1 Testing with a Polarization Analyzer

1. Turn on the polarization analyzer and turn on the marker angles.
2. Take the end of the sensor that is in the optical power detector and put it in a bare fiber adapter.
3. Connect the bare fiber adapter to the polarization analyzer.
4. Connect the high voltage supply to the two electrodes.
5. Clear the Poincaré sphere on the computer screen and mark the current point with one of the markers by clicking on A, B, or C.
6. Turn on the voltage and mark the second point.
7. Switch the positive and negative connections from the high voltage source.
8. Turn on the voltage and mark the third point.
9. The Stokes parameters and angles between the points will then be displayed.
10. Calculate the V_π of the sensor by multiplying the applied voltage by 180 and dividing by the angle change measured.

A.8.2 Testing with a Polarizer

1. Take the fiber out of the optical power detector and place it in a bare fiber adapter.
2. Place a linear polarizer in the optical power detector.
3. Connect the bare fiber adapter to the optical power detector using a connectorized fiber to detector adapter (using this setup over the bare fiber adapter allows for less error due to changes in power when rotating the fiber).

4. Rotate the fiber in the detector to find the orientation that gives the minimum amount of optical power (if there is not much change in optical power when rotating the fiber adjust the laser wavelength and rotate again).

5. Set the bias point of the sensor to the desired position by adjusting the wavelength of the laser.

6. Measure and plot the optical power verses the applied voltage.

7. Fit the data to a sine curve.

8. Calculate V_π by finding the voltage required to go from adjacent minima and maxima on the sine curve.

A.9 AC Testing

1. Place another electrode on top of the cover glass and tape down.

2. Place one fiber end into an xyz stage and place the other end of the fiber into an optical power detector.

3. Place the linear polarizer and quarter wave plate that are fixed together in a rotatable holder in the path of the collimated laser before it is focused into the fiber.

4. Connect an adjustable wavelength laser to the xyz stage.

5. Rotate the linear polarizer and quarter wave plate to maximize optical power going through the sensor.

6. Adjust the xyz stage to achieve maximum optical power through the sensor.

7. Take the fiber out of the optical power detector and place it in a bare fiber adapter.

8. Place a linear polarizer in the optical power detector.

9. Connect the bare fiber adapter to the optical power detector using a connectorized fiber to detector adapter. (using this setup over the bare fiber adapter allows for less error due to changes in power when rotating the fiber).

10. Rotate the fiber in the detector to find the orientation that gives the minimum amount of optical power (if there is not much change in optical power when rotating the fiber adjust the wavelength of the laser and rotate again).

11. Adjust the wavelength of the laser to find the maximum voltage from the optical power detector and record the optical power and voltage from the optical power detector.

12. Turn off the auto scaling function on the optical power detector.

13. Adjust the wavelength of the laser to find the minimum voltage from the optical power detector and record the optical power and voltage from the optical power detector.

14. Record the difference between the maximum and minimum voltage from the optical power detector; this is V_0 and will be needed to calculate V_π.

15. Adjust the laser wavelength to the middle of the wavelengths that correspond to the maximum and minimum voltages to set the bias point of the sensor to the quadrature point.

16. Because the bias point changes with temperature and stress on the fiber it may be necessary to adjust the wavelength during testing to make sure the optical power stays in the middle of the maximum and minimum optical powers previously recorded.

17. Connect the voltage output of the optical power detector to a spectrum analyzer.

18. Connect a function generator to the electrodes on the sensor and apply a sinusoidal voltage; the peak amplitude is ΔV (make sure that the output is set to high Z or the calculations may be off by a factor of two).

19. Measure the FFT peak height at the applied voltage frequency; this is V_P.

20. If not already known, measure the value of A_{FFT} by hooking the function generator to the spectrum analyzer and applying a sinusoidal signal and comparing the FFT peak height to the amplitude of the sinusoid.

21. Calculate V_π.

A.10 Embedding for Fiber Photolithography

1. Preparing Fiber

   (a) Cut a length of fiber from the spool.

   (b) Strip the middle of the fiber with the Heat stripper

   (c) Clean the fiber in the ultra sonic cleaner (in Isopropanol)

   (d) Strip the ends of the fiber

   (e) Cleave the ends of the fiber

   (f) Align the fiber in the stage

   (g) Etch the Fiber

   (h) Re-clean the fiber in the ultra sonic cleaner

2. Preparing Taped Slide

   (a) Stretch tape sticky side up across slide

   (b) Apply tape to both sides of the stretched tape, leaving a sticky strip in the middle

(c) Cut the stretched tape on the top and bottom, making it so the tap on the sides is the only thing holding it to the slide.

(d) Put a tape tab on the top and bottom of the stretched tape, sticking it to the back of the slide.

(e) Cut the tape on the sides of the stretched tape freeing the stretched tape from the front of the slide. Now the stretched tape is only being held on to the slide by the tabs on the back of the slide.

(f) Optional: if the stretched tape isn't flat enough, use tape tabs to pull it taught on the sides.

3. Taping fiber to Slide

(a) Clean V-Groove Plate with Acetone and Isopropyl Alchohol

(b) Put V-Groove plate under the fiber.

(c) Line up the fiber in the smallest V-groove

(d) Fix V-groove plate to the etch boat with tape so that it doesn't shift when taping the fiber.

(e) Carefully lower the taped slide onto the fiber, gently applying pressure so that the fiber will make contact with the sticky part of the tape.

(f) Undo the magnetic clamps on the etch boat

(g) Carefully raise the slide from the v-groove plate. (It might stick to the plate, so this is why care is especially important. The fiber should come off the grooves.

(h) Using the blue tape backing or a q-tip end, apply pressure to the back of the fiber, making it seal with the tape adhesive. This is important so that no epoxy can come in contact with the etched fiber core.

4. Epoxy Application

   (a) Apply a thin bead (2-3mm wide) of UV cure epoxy (60-7170 UV) starting at the plastic jacket, through the stripped region, and ending at the next plastic jacket.

   (b) Place a clean glass slide on the epoxy. Care should be taken to lower it slowly so as not to induce the forming of bubbles in the epoxy.

5. Curing

   (a) Place the slides with the epoxy and fiber under the black lamp.

      i. It seems that 45 minutes is sufficient to cure a thick layer of uv cure epoxy.

   (b) The yellow polyimide tape acts as a UV blocker, so make sure that the lamp is shining through the slide with no tape on it.

6. Removing the Slide and Tape

   (a) After curing, carefully remove the slide from under the lamp, making sure that the stray ends of the fiber don't get caught on anything.

   (b) Flip the slides over, so that the one with tape on it is up. The tabs used to hold the tape it place should now be accessible

   (c) Carefully undo the tape tabs, releasing the slide from the tape.

      i. Sometime if too much glue was applied, the glue will come in contact with the slide, if this is true, use a razor blade to carefully apply leverage between the slides so that the glue will come undone.

   (d) Remove the slide from the tape.

(e) Peel the tape carefully from the fiber, any sudden jerk of the tape, while the fiber is stuck to it could cause the fiber to cleave, even within the jacket.

A.11 EBL Process Steps

Steps for Electron Beam Lithography (EBL) with a Nanometer Pattern Generation System (JC Nabity NPGS) by a Field Emission Environmental Scanning Electron Microscope (FEI/Phillips XL30 ESEM-FEG)

1. Switch monitor control to Litho
2. Turn two knobs on the left side of the desk to B-LITHO
3. Turn on the Scanservice Corp. box. Make sure the reading on the display is about 132.
4. Vent.
5. Home the stage (Optional, as long as rotation is 0 degree)
6. Switch the ground connection on the microscope door to up direction.
7. Change the beam blanker and connect the black cable.
8. Set up the picoammeter:
   (a) Connect the BNC cable to the microscope and attach the ground wire.
   (b) Reset the picoammeter to factory defaults.(Menu -¿ defaults is Factory)
   (c) Turn on the Zero check.(Menu -¿ Zero check)
   (d) Adjust the range to display pA(0.0xx nA)
9. Load the sample.

10. Pump.
11. Adjust Tilt to 0 degree
12. Mag- ¿Device- ¿Display, spot size 1.
13. Turn on the beam, EHT 5kv, locate on the triangle structure, roughly focus at WD=10mm.
14. Change to EHT 30KV, focus, stigmate.
15. Find the Faraday cup, zoom in to 20KX.
16. Measure the beam current:
    (a) Note the reading on the picoammeter with the beam on.
    (b) Blank the beam by turning the knob on the Scanservice Corp. box to OFF.
    (c) Again note the reading on the picoammeterthe beam current is the absolute value of the difference between the two readings.
    (d) Turn the beam back ON.
17. Move to the sample, focus only, no stigmate.
18. Keep 0 degree stage rotation and tilt. Level the sample by scanning rotation.
19. Set up NPGS file
    (a) Beam current
    (b) Magnification
    (c) Desired doses
20. Change the magnification on the microscope to the same magnification in the run file.

21. Process NPGS run file.

22. Define the X axis.

23. Locate the starting field in the center of the screen.

24. Turn the knob on the Scanservice Corp. box to EXTERNAL.

25. On the microscope computer, set the scan to External XY.

26. After finished, make the settings back to the original.

A.12 PANDA to D-fiber Fusion Splicing

A.12.1 PANDA to E-fiber Splicing

1. Perform an Arc Calibration before doing any splicing that matter

2. Strip, Clean and Cleave a PANDA fiber in a 400 μm fiber holder

3. Insert the PANDA fiber holder into the left side of the Fujikura 40PM splicer

4. Strip, Clean and Cleave a E-fiber in a 250 μm fiber holder.

5. Insert the E-fiber holder into the right side of the Fujikura 40PM splicer

6. Close the clamps and Fusion Splicer Lid

7. Go to the splice mode menu and select the PANDA to E-fiber recipe

8. Press the "set" key to initiate the splicing recipe

9. When the splicing recipe has completed, remove the spliced fiber from the holder, and use the built-in heater to fasten a protection sleeve to the splice

A.12.2 E-fiber to D-fiber Splicing

1. Perform an Arc Calibration before doing any splicing that matter
2. Connect one of of the E-fiber to a 1550nm Laser, and one end of the D-fiber to a photodector
3. Strip, Clean and Cleave an E-fiber in a 250 μm fiber holder
4. Insert the E-fiber holder into the left side of the Fujikura 40PM splicer
5. Strip, Clean and Cleave a D-fiber in a 250 μm fiber holder.
   (a) Strip the fiber with the Fujikura HTS-12 High Strength Fiber Stripper
   (b) Clean the fiber with IPA
   (c) Ensure that the D-fiber is flat side up and perpendicular to the cleaver blade, and use the Fujikura Precision Cleaver to score and cleave the D-fiber.
6. Rotate the D-fiber to a 45 ° angle in the fiber holder
7. Insert the D-fiber holder into the right side of the Fujikura 40PM splicer
8. Close the clamps and Fusion Splicer Lid
9. Go to the splice mode menu and select the E-fiber to D-fiber splicing recipe
10. Press the “set” key to initiate the splicing recipe
11. When prompted align the D-fiber by rotating and adjusting the x and y motors so that maximum power is transmitted through the E-fiber into the power meter.
12. When the splicing recipe has completed, remove the spliced fiber from the holder, and use the built-in heater to fasten a protection sleeve to the splice

Appendix B

Matlab Code

B.1 Dielectric Slab Mode Solver

This function calls the slab mode solver function and plots the effective index index of the mode for the slab over a range of V parameters and wavelengths

```
clear all
close all

% Physical Parameters
lambda=linspace(.8e-6,2.2e-6,100);  %Wavelength
n1 = 1.454; %Core
n2 = 1.441; %Overindex material
n3 = 1.441; %Substrate
h = 4e-6;   %Height of Waveguide

%Instantiates length count to zero
l0 = 0;

%Determines the number of supported modes for each wavelength
for ii = 1:length(lambda)

    l1=length(mode_slab_calc(lambda(ii),n1,n2,n3,h));
```

```
    if l1>l0
    l0=l1;
    end
    l_index(ii) = l1;

end

%Instantiates an array that will fit all the supported modes
neff_mat = zeros(l0,length(lambda));

%Fills the array with the modal solutions to the slab waveguide
for ii = 1:length(lambda)

   neff_mat(1:l_index(ii),ii)=mode_slab_calc(lambda(ii),n1,n2,n3,h);

end

%plots the effective index vs wavelength
figure(1)
plot(lambda,neff_mat,'.-',[1.55e-6 1.55e-6],[n3 n1],'--r')
axis([lambda(1) lambda(end) n3 n1])
legend('Zero Order','First Order','Second Order','1550 nm')
xlabel('\lambda (\mum)')
ylabel('n_{eff}')
set(gca,'XDir','reverse')

%creates the V-Parameter
V = (2*pi)./lambda*h*sqrt((n1.^2-n2.^2));
V_1550=V(match(1.55e-6,lambda,1e-8));
```

```
%plots the effective index vs the V parameter
figure(2)
plot(V,neff_mat,'.-',[V_1550 V_1550],[n3 n1],'--r')
axis([V(end) V(1) n3 n1])
legend('Zero Order','First Order','Second Order','1550 nm')
xlabel('normalized frequency V')
ylabel('n_{eff}')
```

This function calculates the effective index solutions of a slab waveguide.

```
function [neff_sol]=mode_slab_calc(lambda,n1,n2,n3,h)

% Physical Constants
k0 = 2*pi/lambda; % Wavenumber
neff = linspace(n2,n1,10000); % Effective Index Range
Beta = 2.*pi.*neff./lambda; %
kappa = sqrt(n1^2*k0^2-Beta.^2);
gamma = sqrt(Beta.^2-n2^2*k0^2);
delta = sqrt(Beta.^2-n3^2*k0^2);

% Right and LHS soluctions to the equations
LHS = tan(kappa.*h);
RHS = kappa.*(gamma+delta)./(kappa.^2-gamma.*delta);

% find the absolute difference between the RHS and LHS. This results in a
% function where the minima represent a place where the solutions crossed
% paths
```

```
f=abs(LHS-RHS);
% Finds the local minima of a function
[lmval indd]=lmin(f);

%% Optional code used to plot solutions
%  hold on
%  plot(neff,LHS,'b',neff,RHS,'-r',neff,f,'g')
%  plot(neff(indd),lmval, 'ok')
%  axis([neff(1) neff(end) -10 10])
%  hold off

neff_sol = sort(neff(indd),'descend');
```

B.2 Fiber Mode Solver

This function runs the fiber mode solver function and calculates the effective index solutions over a range of V parameters for the Bessel function orders from zero to three, and then plots the values.

```
clear all
close all
n1 = 1.4509; %Core
n1 = 1.455
n2 = 1.444; %Cladding
a = 4.11e-6; % Core Diameter
lambda_min = .5e-6; %minimum wavelength for solution window
lambda_max = 20e-6; %maximum wavelength for solution window
NN = 100; %number of wavelength divisions
```

```
lambda=linspace(lambda_min,lambda_max,NN); %wavelength vector
% Normalized Frequency -> the V parameter
V_min = (2*pi)./lambda_max*a*sqrt((n1.^2-n2.^2));
V_max = (2*pi)./lambda_min*a*sqrt((n1.^2-n2.^2));
V = linspace(V_min,V_max,NN)
V_1550=(2*pi)./1550e-9*a*sqrt((n1.^2-n2.^2));
lambda = (2*pi)./V*a*sqrt((n1.^2-n2.^2));
% Bessel function order used to determine for which modes to solve.
m = 0
for ii = 1:length(lambda)
    % Calculates fiber mode solutions at a particular wavelength for a
    % particular Bessel function order
    mode_solutions=fiber_mode_calc(lambda(ii),n1,n2,a,m);

    % Stores the number of valid solutions
    length_mode_solutions = length(mode_solutions);

    % Instantiates neff_mat to contains the maximum number of solutions
    % corresponding to the smallest wavelength.
    if ii == 1
        neff_mat0 = NaN(length_mode_solutions,NN);
    end

    % Stores the solutions into the neff_mat variable
    neff_mat0(1:length_mode_solutions,ii)=mode_solutions;
end
%Repeats for the first order Bessel function
m = 1
for ii = 1:length(lambda)
```

```
    mode_solutions=fiber_mode_calc(lambda(ii),n1,n2,a,m);
    length_mode_solutions = length(mode_solutions);
    if ii == 1
        neff_mat1 = NaN(length_mode_solutions,NN);
    end
    neff_mat1(1:length_mode_solutions,ii)=mode_solutions;
end
%Repeats for the second order Bessel function
m = 2
for ii = 1:length(lambda)
    mode_solutions=fiber_mode_calc(lambda(ii),n1,n2,a,m);
    length_mode_solutions = length(mode_solutions);
    if ii == 1
        neff_mat2 = NaN(length_mode_solutions,NN);
    end
    neff_mat2(1:length_mode_solutions,ii)=mode_solutions;
end
% Repeats for the third order Bessel function
m = 3
for ii = 1:length(lambda)
    mode_solutions=fiber_mode_calc(lambda(ii),n1,n2,a,m);
    length_mode_solutions = length(mode_solutions);
    if ii == 1
        neff_mat3 = NaN(length_mode_solutions,NN);
    end
    neff_mat3(1:length_mode_solutions,ii)=mode_solutions;
end

b0= (neff_mat0-n2)/(n1-n2);
```

```
b1= (neff_mat1-n2)/(n1-n2);

b2= (neff_mat2-n2)/(n1-n2);

b3= (neff_mat3-n2)/(n1-n2);


figure(1)

plot(V,b0,'-',V,b1,'-',V,b2,'-',V,b3,'-')

axis([V(end) V(1) 0 1])

xlabel('normalized frequency (V)')

ylabel('Normalized Propagation Constant (b)')
```

This function is used to solve for all of the valid solutions for a fiber waveguide for a particular Bessel function order.

```
\%\-\-\-\-\-\-\-\-\-\-\-\-\-\-\-\-\-\-\-\-\-\-\-\-\-\-\-\-\-\-\-\-\-\-\-\-
\% Function used to find the local minima of the difference between the RHS
\% and LHS of the transcendental fiber mode equation
\% Inputs Variables:
\%   lambda - the free space wavelength
\%   n1 - the index of the fiber core
\%   n2 - the index of the fiber cladding
\%   a  - the diameter of the core of the fiber (the cladding is infinite)
\%   m  - the Bessel function order to be solved
\%\-\-\-\-\-\-\-\-\-\-\-\-\-\-\-\-\-\-\-\-\-\-\-\-\-\-\-\-\-\-\-\-\-\-\-\-
function [neff_sol]=fiber_mode_calc(lambda,n1,n2,a,m)
\% wavenumber
k0 = 2*pi/lambda;
\% effective index
neff = linspace(n2,n1,10000);
\% The propagation constant
```

```
Beta = 2.*pi.*neff./lambda;
\% Variables used to simplify Bessel function equations
p=((n1*k0)^2-Beta.^2).^.5;
q=(Beta.^2-(n2*k0)^2).^.5;
\% Bessel function of the first kind
J= besselj(m,a.*p);
\% modified Bessel function of the second kind
K=besselk(m,a.*q);
\% Derivative of Bessel function of the first kind
Jp = -besselj(m+1,a.*p) + m./(a.*p).*besselj(m,a.*p);
\% Jp = besselj(m-1,a.*p) - m./(a.*p).*besselj(m,a.*p);
\% Derivative of modified Bessel function of the second kind
Kp = -besselk(m+1,a.*q) + m./(a.*q).*besselk(m,a.*q);
\% Kp = besselk(m-1,a.*q) - m./(a.*q).*besselk(m,a.*q);
\% Right and LHS soluctions to The equations
LHS=(Jp./p./J+Kp./q./K).*(Jp./p./J+n2^2/n1^2.*Kp./q./K);
RHS=m^2/a^2*((1./p.^2+1./q.^2).*(1./p.^2+n2^2/n1^2*1./q.^2));
\% find the absolute difference between the RHS and LHS. This results in a
\% function where the minima represent a place where the solutions crossed
\% paths
f=abs(LHS-RHS);
\% Function that finds the local minima of a function
[lmval indd]=lmin(f);
\% Sorting and taking care of the case where no solutions are found
if length(indd) == 0
 neff_sol = NaN;
else
 neff_sol = sort(neff(indd),'descend');
end
```

```
\% Code to remove spurious solutions to the equations that occur after the
\% mode is close to cutoff.
if min(lmval) > 1e-13
   neff_sol = NaN;
end
```

B.3 Calculating the E-pi of a Sensor

This function is used to input the data into the Mode Finder Function and manipulate the data to determine the E_π of the modeled sensor.

```
tic
%Constants
E_field = 40E6;
lambda = 1550e-9;
Length = .02;

% Calculate the Electric Field and Effective Indicies of
% each mode with and without field applied
% function [Efield,neff] = mode_finder_function(name_in,epsname,TETM)
% TETM: 0 for TE polarization, 1 for TM polarization

[Efield_TE_0, neff_TE_0] = mode_finder_function(nameTE1,epsTE1,0,lambda);
[Efield_TM_0, neff_TM_0] = mode_finder_function(nameTM1,epsTM1,1,lambda);
[Efield_TE_F, neff_TE_F] = mode_finder_function(nameTEF,epsTEF,0,lambda);
[Efield_TM_F, neff_TM_F] = mode_finder_function(nameTMF,epsTMF,1,lambda);

% For the Horizontal Elliptical core fiber the TE polarization is in the y
% direction and the TM polarization is in the z direction.
```

```
delta_Ny = neff_TE_0 - neff_TE_F;
delta_Nz = neff_TM_0 - neff_TM_F;
delta_Beta = abs(delta_Ny-delta_Nz);

% Rearranging: (2*pi/lambda)*delta_Beta = pi * E_field/E_pi

L_Pi = (lambda)/(2*delta_Beta);
L_Pi_cm = L_Pi*100

E_Pi = E_field/(Length/L_Pi);
E_Pi_MV_m = E_Pi*1e-6

toc
```

B.4 Mode Finder Function

This is the function that generates the circuit file for BeamProp, runs the circuit file, and manipulates the BeamProp output to generate usable information.

```
function [Efield,neff] = mode_finder_function(name_in,epsname,TETM,lambda)

clear eps

lambda

mainpath=pwd; %sets the location of this m-file

    cd(mainpath)

    clear eps
```

```
%lambda=1.55; % Free space wavelength in microns

%setup polarization stuff for naming file
if TETM==0
    pol='TE';
else
    pol='TM';
end

% Name the files to be used
 name=[strcat(name_in,'_',pol)];



% Make a directory for the name
if exist(['Edata/' name])~=7
   mkdir(['Edata/' name]);
end
%%%%%%%%%%%%%%%%%%%%%%%%%%%%%%%%%%%%%%%%%%%%%%%%%%%%%%%%%%%%%%%%%%%%
%% Create or load the index profile to be used by BeamProp
%%%%%%%%%%%%%%%%%%%%%%%%%%%%%%%%%%%%%%%%%%%%%%%%%%%%%%%%%%%%%%%%%%%%

%This file loads an index profile and defines the
%dimensions of x and y in microns

cd Edata\eps_files\

N=400; %Number of cells in each direction
l=16; %length of simulation region (in microns)
```

```
x = ([0:N])/N*l - l/2; %x-cordinates in microns
y = ([0:N])/N*l - l/2; %y-cordinates in microns
dx=x(2)-x(1); %grid size in the x-direction
dy=y(2)-y(1); %grid size in the y-direction
[xx,yy]=meshgrid(x,y);

%load the eps file
eps=load(epsname);

n0=min(min(eps)) %n0 is the lowest index
n3=max(max(eps)) %n3 is the highest index
del=num2str(n3-n0); %Index difference

% This code writes the file Fiber.ind to the Edata folder.
% It contains the 2-D profile in a form that BeamPROP
% can interpret.

cd ../../
cd(['Edata/' name '/']);

w_ind=strcat(name,'.ind');
fid=fopen(w_ind,'w');  % Open the file to write

% These first three lines are junk that BeamPROP
% needs at the beginning
fprintf(fid,'/rn,a,b/nx0/ls1 \n');
fprintf(fid,'%g %g %g %g %s \n', N+1, -1, 1, 0, 'OUTPUT_REAL_3D');
fprintf(fid,'%g %g %g \n', N+1, -1, 1);
```

```
    % Normalize the index matrix according to BeampProp standards
    eps1=(eps-n0)/(max(max(eps))-min(min(eps)));

    % Write the matrix
    fprintf(fid, '%6.6f  ', eps1);

    fclose(fid);

    cd ../../

    % Outputs a figure of the index profile
    if 0
        figure(1);pcolor(x,y,eps); shading interp;colorbar;
    end
%%%%%%%%%%%%%%%%%%%%%%%%%%%%%%%%%%%%%%%%%%%%%%%%%%%%%%%%%%%%%%%%%%%%%%%
%%  This file creates the circuit that will be used by BeamPROP
%%%%%%%%%%%%%%%%%%%%%%%%%%%%%%%%%%%%%%%%%%%%%%%%%%%%%%%%%%%%%%%%%%%%%%%
    circuit=[mainpath '\Edata\' name '\' name '_circuit.ind'];

    fid=fopen(circuit,'w');

    % Input data into circuit file

    fprintf(fid,['\nalpha = 0 \n' ...
            'background_index = 1' '\n' ...
            'boundary_max = ' num2str(l/2) '\n' ...
            'boundary_max_y = ' num2str(l/2) '\n' ...
            'boundary_min = ' num2str(-l/2) '\n' ...
            'boundary_min_y = ' num2str(-l/2) '\n' ...
```

```
        'background_index = ' num2str(n0)  '\n'...
        'delta = ' num2str(del) '\n' ...
        'dimension = 3 \n' ...
        'eim = 0 \n' ...
        'field_output_format = OUTPUT_REAL_3D \n' ...
        'free_space_wavelength = ' num2str(lambda) '\n' ...
        'grid_size = ' num2str(dx) '\n' ...
        'grid_size_y = ' num2str(dy) '\n' ...
        'height = ' num2str(l) ' \n' ...
        'idbpm_convergence_warning = 0'...
        'index_display_mode = DISPLAY_CONTOURMAPXY \n' ...
        'k0 = (2*pi)/free_space_wavelength \n' ...
        'launch_height = 2 \n' ...
        'launch_type = LAUNCH_GAUSSIAN \n' ...
        'launch_width = 4 \n' ...
        'mode_output_format = OUTPUT_REAL_3D \n' ...
        'mode_set = 0 \n' ...
        'prefix = ' name '\n' ...
        'profile_type = PROF_USER_1 \n' ...
        'slice_display_mode = DISPLAY_CONTOURMAPXY \n' ...
        'structure = STRUCT_FIBER \n' ...
        'vector = 1 \n' ...
        'wait = 0 \n' ...
        'width = ' num2str(l) ' \n' ...
        'step_size_idbpm = .1 \n' ...
        '\n']);


%define user profile
```

```
    fprintf(fid,['user_profile 1' '\n' ...
            'type = UF_DATAFILE\n' ...
            'filename = ' '' name '.ind' '\n' ...
            'end user_profile\n' ...
            '\n']);

    %make circuit structure

    fprintf(fid,['segment 1 \n' ...
            'profile_type = PROF_USER_1 \n' ...
            'begin.x = 0 \n' ...
            'begin.z = 0 \n' ...
            'end.x = 0 rel begin segment 1 \n' ...
            'end.z = 1000 rel begin segment 1 \n' ...
            'end segment \n' ...
            '\n']);

    fclose(fid);
%%%%%%%%%%%%%%%%%%%%%%%%%%%%%%%%%%%%%%%%%%%%%%%%%%%%%%%%%%%%%%%%%%%%%%%%%%%%
%% Find and save the fundamental mode of the waveguide by Calling Beamprop
%%%%%%%%%%%%%%%%%%%%%%%%%%%%%%%%%%%%%%%%%%%%%%%%%%%%%%%%%%%%%%%%%%%%%%%%%%%%
    cd(['Edata/' name '/']);
    str1=['c:\BeamProp\bsimw32...
    ' name '_circuit.ind ' 'polarization=' num2str(TETM)];

    % if exist([name '.m00'])~=2  %Generate E-field if it doesn't exist
         dos(str1);
    % end
```

```
%%%%%%%%%%%%%%%%%%%%%%%%%%%%%%%%%%%%%%%%%%%%%%%%%%%%%%%%%%%%%%%%%%%%%%%%%%%%
%% Load the Efield back into matlab
%%%%%%%%%%%%%%%%%%%%%%%%%%%%%%%%%%%%%%%%%%%%%%%%%%%%%%%%%%%%%%%%%%%%%%%%%%%%
    cd ../../
    filename=[name '.m00']; % .m00 is the fund. mode,
    % use .mxx for higher modes

    % This section takes the electric field of a mode found by BeamPROP
    % and loads it into Matlab.  The filename needs to be a string and is
    % usually a .mxx or .nxx file where the xx corresponds to the mode
    % number (00, 01, 02, etc.)

    cd(['Edata/' name '/']);
    % Open the file and junk the first two lines.
    % Save the third line and unpack it to get useful values.
    fid=fopen(filename);
    fgetl(fid);
    fgetl(fid);
    a=fgetl(fid);

    % Extract BeamPROP's n_effective, as well as the number of rows,
    % and the maximum and minimum points in the domain
    [r, lmin, lmax, junk1, junk2, neff, junk3]= ...
    strread(a,'%f%f%f%f%s%f%f');

    % Unpack the fourth row to get the number of columns
    a=fgetl(fid);
    [c, lmin, lmax]=strread(a,'%f%f%f');
```

```
    % Initialize the field to zeros
    y1=zeros(r,c);

    % Load the field one line at a time
    for j=1:r,
        y1(j,:)=str2num(fgetl(fid));
    end

    % Close the file
    st=fclose(fid);

    % Rotate the field to get it into the right form
    Efield=fliplr(rot90(y1,-1));

%%%%%%%%%%%%%%%%%%%%%%%%%%%%%%%%%%%%%%%%%%%%%%%%%%%%%%%%%%%%%%%%%%%%%%%%%%%%
cd ../../
epsname
neff
```

B.5 Vernier Grating Code

The following code was modified from Tyson Lowder's transfer matrix code [57] and shows how a Vernier grating scheme is simulated in matlab. There are two separate ".m" files. The transfer matrix code is used to calculate the reflection spectrum for a set of grating parameters. The main function calls the transfer matrix code, and manipulates and plots the data for a given set of grating parameters. The code also generates a movie that can be used to observe the Vernier scheme in action. Differential signals are calculated and plotted as well.

B.5.1 Transfer Matrix Code

```
function [R Tran] = ...
Transfer_Matrix_Func(lambda, dz_temp, dneff_temp, neff_temp, Lam)

%%%%%%%%%%%%%%%%%%%%%%%%%%%%%%%%%%%%%%%%%%%%%%%%%%%%%%%%%%%%%%%%%%%%%%%%
%Code for calculating the reflection spectrum of a fiber Bragg grating
%using the piecewise-uniform aproach as described by Othonos and Kali
%
% Required inputs:
%   lambda          wavlength
%   dz_temp         segment lengths
%   dneff_temp      index modulation of segments
%   neff_temp       effective indices of segments
%   Lam             grating period
%
% Main outputs:
%   R
%   Tran

clear a b r R Tran P_r P_t P
%Fringe visliblity; set to 1 for strong gratings,
%set to 0.5 for weak gratings
s=1;
%initial conditions 'a0' is the forward propagating
%wave and 'b0' is the backward one
a0b0=[1;0];

for n=1:length(lambda)
```

```
%    n
for m=1:length(dz_temp)
dneff=dneff_temp(m);
dz=dz_temp(m);
neff=neff_temp(m);
zeta=2*pi/lambda(n)*dneff;
%deld=2*pi*neff*(1/lambda(n)-1/lambda_d);
deld=2*pi*neff/lambda(n)-pi/Lam;
%'dc' self-coupling coefficient
zetap=deld+zeta;
%'ac' coupling coeffiecient
kappa=pi/lambda(n)*s*dneff;
kap(n)=kappa;
omega=sqrt(kappa.^2-zetap.^2);

%transfer matrix kernal
T_temp(1,1)=cosh(omega*dz)+i*zetap/omega*sinh(omega*dz);
T_temp(1,2)=kappa/omega*sinh(omega*dz);
T_temp(2,1)=kappa/omega*sinh(omega*dz);
T_temp(2,2)=cosh(omega*dz)-i*zetap/omega*sinh(omega*dz)];

if m==1
T=T_temp*eye(2);
else
  T=T_temp*T;
end
end
    %fields after propagating through the grating
    ambm=T*a0b0;
```

```
    a(n)=ambm(1);
    b(n)=ambm(2);
    %complex reflextion coefficent
    r(n)=ambm(2)/ambm(1);
    %reflectance
    R(n)=abs(ambm(2))^2/abs(ambm(1))^2;
    %transmittance
    Tran(n)=1/abs(ambm(1))^2;
    %Power reflected
    P_r(n)=R(n).*a0b0(1);
    %Power transmitted
    P_t(n)=(1-R(n)).*a0b0(1);
    %Power transmitted in dB
    P(n)=abs(10*log10(1-R(n)));

end
```

B.5.2 Vernier Scheme Code

```
%Code for calculating the reflection spectrum of a fiber Bragg grating
%using the piecewise-uniform aproach as described by Othonos and Kali

clear all
close all;

% Number of frames for the scanning of the vernier scheme
QQ = 100;

% Initial offset adjustment between spectra
```

```
offset =4e-5;

% Total Effective index change
delta_neff = 2e-5;

% Boolean which determines if movie is made or not;
% 0 - No Move, 1 - Movie is Output
movie_output = 1;

%Total number of data points
MM = 5000;

%Wavelength range for simulation
lambda=linspace(1544e-9,1556e-9,MM);

% Set range for which peaks will be found
start_lam = 1550.1e-9;
end_lam = 1550.5e-9;

% The difference between the neff of the unetched and the
% etched grating regions.
dneff0 = 0.003;

%Effective Index of the Mode -
%the quantity that changes for Refractive index sensing.
neff0=1.47455544900000;

%Grating Period
Lam=1550e-9/(2*(neff0+dneff0));
```

```
% Dimensions of the Fabry Perot Cavity
% Length of the First grating Section
l1 = 500e-6;
% Length of the Gap
gap = 3.97e-3;

gap2 = 3.93e-3;
% Length of the Second Grating Section
l2 = l1;

% Sets up Matrices for Transfer Matrix Code
dz_temp=[l1, gap, l2];
dneff_temp=[dneff0, 0, dneff0];
neff_temp=[neff0,neff0, neff0];
% Calls the Transfer Matrix Code Function which returns Reflected and
% Transmitted spectra
[R Tran1] = Transfer_Matrix_Func(lambda, dz_temp, dneff_temp, ...
neff_temp, Lam);

figure(1);
subplot(2,1,1)
plot(lambda*1e9,Tran1,'b')
xlabel('Wavelength, \lambda (nm)')
ylabel('Transmitted Power')

%Zoomed in View of Previous Spectrum
lambda=linspace(start_lam,end_lam,MM);
[R2 Tran2] = Transfer_Matrix_Func(lambda, dz_temp, dneff_temp, ...
```

```
neff_temp, Lam);


peaks = find_peaks(lambda,Tran2,start_lam,end_lam);
subplot(2,1,2)
plot(lambda*1e9,Tran2,'b')
xlabel('Wavelength, \lambda (nm)')
ylabel('Transmitted Power')
axis([start_lam*1e9 end_lam*1e9 0 1])

% Stores the Fixed Grating Transmitted Spectrum
Tran_Fixed = Tran2;

[fixed_peaks, fixed_troughs] = ...
find_peaks_troughs(lambda,Tran_Fixed,start_lam,end_lam)

% Resized the gap for the sensing grating free spectral range adjustment
dz_temp=[l1, gap2, l1];

% Code to open a figure to a predetermined size and screen placement
bdwidth = 5;
topbdwidth = 70;
set(0,'Units','pixels')
scnsize = get(0,'ScreenSize');
pos1  = [50,...
50,...
scnsize(3)*4/5 - 2*bdwidth,...
scnsize(4)*4/5 - (topbdwidth + bdwidth)];
figure('Position',pos1)
```

```
% Matrix where the change in effective index is define for each frame
neff_mat=linspace(neff0,neff0 + delta_neff,QQ)-offset;

% Begins the movie output
if movie_output == 1
    MakeQTMovie start 'AJL8 Shifted gratings.mov'
end



for qq=1:QQ

    % Selects the neff for the current frame
    neff = neff_mat(qq);

    % Populates neff matrix for transfer matrix code
    neff_temp=[neff, neff, neff];

    % Transfer Matrix Code Function Called
    [R Tran] = Transfer_Matrix_Func(lambda, dz_temp, dneff_temp, ...
    neff_temp, Lam);

    % Stores transmitted power for each frame
    Tran_mat(qq,:) = Tran;

    subplot(3,1,1)
    plot(lambda*1e9,Tran_Fixed,'b',lambda*1e9,Tran,'g')
    axis([lambda(1)*1e9 lambda(end)*1e9 0 1]);

    % The transmitted power throught both the fixed
```

```
% and sensing fabry perot gratings
total_Tran = Tran_Fixed.*Tran;
total_Tran_mat(qq,:) = total_Tran;

% Find peaks for the total transmitted power through gratings
trans_peaks = find_peaks(lambda,total_Tran,start_lam,end_lam);


subplot(3,1,2)


for ss = 1:length(fixed_peaks)

    if ss ~= length(fixed_peaks)
        begin_ind = fixed_troughs(ss);
        end_ind = fixed_troughs(ss+1);
        total_power_WDM(ss) = sum(total_Tran(begin_ind:end_ind));
    else
        begin_ind = fixed_troughs(ss);
        total_power_WDM(ss) = sum(total_Tran(begin_ind:end));
    end

end

% This is the maximum integrated power in one peak.
% It was solved for by integrating one peak;
Max_Power_Trans = 70.8086;
norm_power_WDM = total_power_WDM ./ ...
(Max_Power_Trans.*ones(1,length(total_power_WDM)));
```

```
    plot(lambda*1e9,total_Tran,'b',[lambda(fixed_troughs)*1e9; ...
    lambda(fixed_troughs)*1e9],[total_Tran(fixed_troughs); ...
    ones(size(total_Tran(fixed_troughs)))],'-r', ...
    lambda(fixed_peaks)*1e9, norm_power_WDM ,'*g')

    axis([lambda(1)*1e9 lambda(end)*1e9 0 1]);

    differentials = [total_power_WDM 0] - [0 total_power_WDM];
    differentials_mat(:,qq) = differentials(2:end-1)';
    neff_mat2(:,qq) = neff_mat(qq).*ones(size(differentials_mat(:,qq)));

    subplot(3,1,3)
    plot(neff_mat(1:qq),differentials_mat(1,:))
    axis tight
    if movie_output == 1
       MakeQTMovie addfigure
    end

end



% Ends the movie output
if movie_output == 1
    MakeQTMovie finish
    MakeQTMovie cleanup
end
```

Appendix C

Calculating the mode of an SEM Cross-Sectional Image

To obtain and accurate understanding of the guiding characteristics of a hybrid polymer/glass fiber waveguide, it is necessary to construct an accurate model of the fiber waveguide. Scanning Electron Microscope (SEM) imaging provides a means of obtaining an accurate idea of the composition of a hybrid waveguide structure. That hybrid waveguide is composed of a combination complex shapes with different indices of refraction. This complexity precludes the use of mathematical equations to describe the various areas. The following treatment outlines a method whereby an SEM cross-sectional image is converted into various layer using Adobe Illustrator. Each index region is exported to a GIF image which is then imported into matlab, and an index profile is generated. Numerical solutions of the waveguiding characteristics for these index profiles can then be obtained using either BeamProp or FimmWave.

C.1 SEM imaging of D-fiber

First, it is necessary to obtain a clear SEM image of the hybrid waveguide. This is accomplished by using a vice to hold a 45 ^{circ} stub, and applying conductive carbon tape to the stub. The fiber is attached to the ahesive portion of the tape, and a score is made with the "battle axe" on the flat of the fiber about 1 mm from the sharp edge of the stub. This process is repeated until the area of interest has been cleaved into multiple section mounted on the stub.

The sample is then taken to the microscopy lab, and gold coated in the gold sputtering machine for between 45 and 90 seconds. The sample is then imaged using

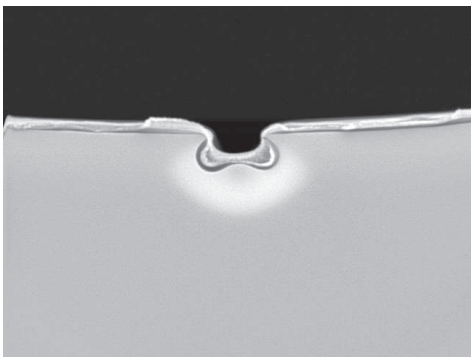

Figure C.1: Cross-sectional SEM image of a hybrid polymer D-fiber waveguide

one of the SEM's. Both the SFEG and the ESEM produce good images. Figure C.1 shows an SEM image of a hyper waveguide structure that was imaged using the ESEM.

C.2 Construction of a Cross-Sectional Index Profile

Once an SEM image is obtained, it is imported into Adobe Illustrator. At that point the scale of the SEM image should be used to draw a square whose dimensions can then be input into the modeling program. For example, if the SEM image has a scale of 25 pixel/μm, then the square would be sized to 400 pixels for an 16 μm modeling window. Normally the square is centered on the center of the hybrid waveguide region. In

Using the SEM image, closed paths are then generated for each of the following shapes using the pen tool: the core, the vapor spot, the polymer, and the cladding. Fill each shape with solid black, and then save them individually using the "Save for Web" option in the file menu. A popup window will appear, and export options are available for selection. The GIF image output should be selected and the "Black and White" and "No Dither" options chosen in the preset menu.

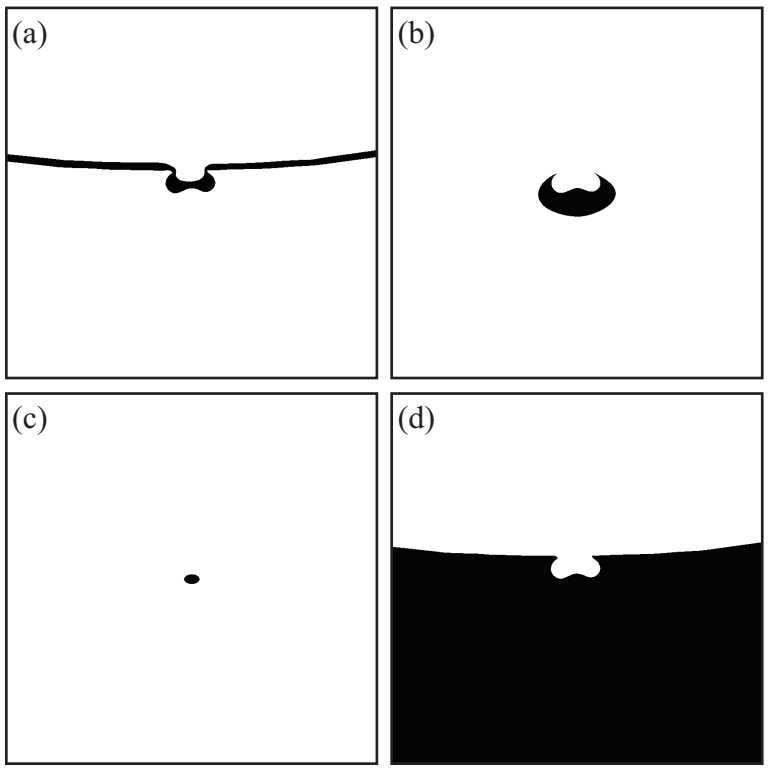

Figure C.2: Black and white GIF images generated from the SEM image in Figure C.1, and exported from Adobe Illustrator for hybrid waveguide modeling,(a) the polymer, (b) the core, (c) the vapor spot, (d) the cladding.

C.3 Code to Generate Index Profile for BeamProp

Each of these GIF images is place in the same directory as the matlab function. The function that follows is used to import them, assign each layer a priority, and set each shapes' index of refraction in the index profile. The index profile can then exported to an ascii text file in preparation for importing the profile into the numerical modeling program.

The function which follows is used to generate files which can then be used for numerical modeling:

```
clear all

close all
```

```
L=16; %Length in Microns
NN=401; %Number of Pixels

%setting up x axis
dx = L/(NN-1);
x = -L/2:dx:(L/2);
y=x;

%To Plot Images: P == 1
P = 0;

%Read in images from Gif Files and
Core = 1-double(imresize(imread('Core', 'gif'),[NN NN],'nearest'));
Clad = 1-double(imresize(imread('Cladding', 'gif'),[NN NN],'nearest'));
Poly = 1-double(imresize(imread('Polymer', 'gif'),[NN NN],'nearest'));
Vapo = 1-double(imresize(imread('VaporSpot', 'gif'),[NN NN],'nearest'));

%Set Priority for Common Bits at Interfaces
Core = Core-bitand(Core,Poly)-bitand(Core,Vapo) + bitand(Vapo,Poly);
Clad = Clad - bitand(Clad,Core) - bitand(Clad,Poly) - bitand(Clad,Vapo);
Vapo = Vapo - bitand(Vapo,Poly);
Core = Core-bitand(Core,Poly);

%Adjust Polymer Index Based on Applied Electric Field
n_polymer = 1.555;
n_e = 1.445;
r33 = 30e-12;
r13 = r33/3;
```

```
%Determines the bulk index of refraction of the polymer in the
%z and y direction for EO polymers
E_Field = 40e6;
n_r33 = n_polymer + (n_polymer)^3/2*r33*E_Field;
n_r13 = n_polymer + (n_polymer)^3/2*r13*E_Field;

%Indices of Materials
n_air = 1;
n_clad=1.441;           %Flourine-doped cladding index
n_core=1.4756;           %Germania-doped core index
n_vapo=1.444;          %S-core index

%Populates eps matrices with index data for each index profile
eps = n_clad.*(Clad) + n_poly.*Poly + n_vapo.*Vapo + n_core.*(Core);
eps33 = n_clad.*Clad + n_r33.*Poly + n_vapo.*Vapo + n_core.*(Core);
eps13 = n_clad.*Clad + n_r13.*Poly + n_vapo.*Vapo + n_core.*(Core);

%sets any transparent index values to that of air
eps(find(eps==0))=1;
eps33(find(eps33==0))=1;
eps13(find(eps13==0))=1;

%rotates index profiles for proper orientation in the modeling programs
eps = flipud(eps);
eps13 = flipud(eps13);
eps33 = flipud(eps33);

%plots the eps file
```

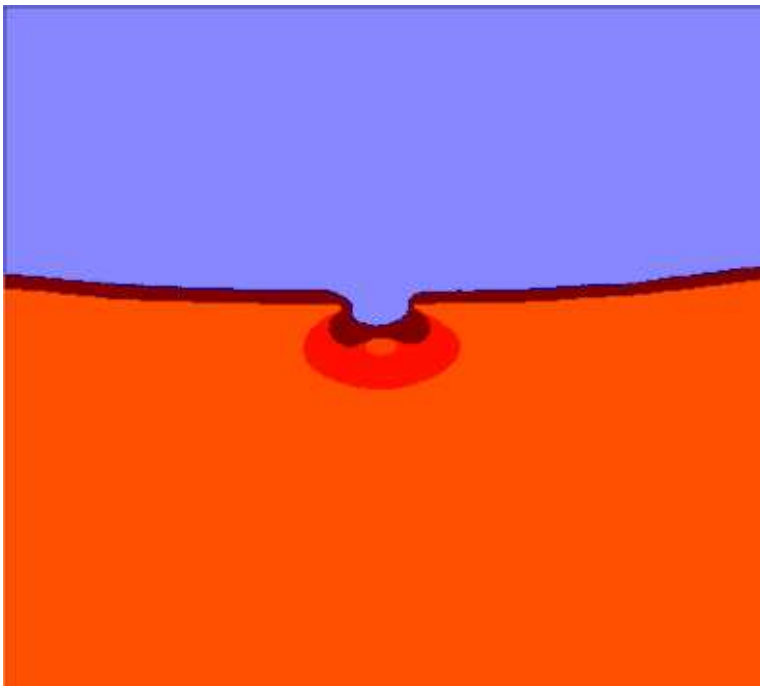

Figure C.3: Figure generated by the index profile generation function with each index area a different color

```
figure

pcolor(x,y,eps)

shading interp

axis equal


%outputs the eps files into the ASCII text format

save('eps_no_field','eps','-ASCII')

save('eps_r33','eps33','-ASCII')

save('eps_r13','eps13','-ASCII')
```

Figure C.3 shows the plot generated by this function. The use can verify that it correctly portrays the SEM image.

C.4 Solving for Modes with BeamProp

The index profile is ready for numerical modeling in BeamProp. To solve for a mode in BeamProp a Matlab batch file is written which calls the Mode Finder Function as described in B.4.

One simple example of a function to use that used the mode finder function is included below:

```
clear all
close all

%Constants
lambda = 1550e-9;
lambda = linspace(1515,1595,16)

% Calculate the Electric Field and Effective Indicies of each mode
% for multiple wavelengths

for ii=1:length(lambda)

[E(:,:,ii), neff(ii)] = mode_finder_function(name,epsname,0,lambda);

end
```

C.5 Solving for Modes with Fimmwave

Fimmwave is another type of modeling program which uses the film mode matching method [97] to solve for the waveguiding characteristic of various optical structures.

The only thing that needs to be changed with the index profile is to add these two lines to the beginning of the file that was created for BeamProp

```
<fmwx-rix-profile(1,0)>
401 401 16 16 1 0
```

FimmWave can also be controlled using batch processing with Python. The following function creates a neff vs. wavelength plot.

```
from numpy import *
from pdPythonLib import *
fimm = pdApp()
fimm.ConnectToApp()
#fimm.Exec("app.openproject(Z:\Kvavle\FimmWave\11-17-08\test3.mwg,)")

filename = "Complete_Etch-1.6_"

for sub_n in range(4,13,1):

for l in arange(1.0,2.2,.01):

print str(sub_n)
print str(l)

fimm.Exec("app.subnodes[{sub_n}].evlist.svp.lambda={l}")
fimm.Exec("app.subnodes[{sub_n}].evlist.update")
```

```
fimm.Exec("app.subnodes[{sub_n}].evlist.svp.lambda")
neff_1 = fimm.Exec("app.subnodes[{sub_n}].evlist.list[1].neff")
neff_2 = fimm.Exec("app.subnodes[{sub_n}].evlist.list[2].neff")
neff_3 = fimm.Exec("app.subnodes[{sub_n}].evlist.list[3].neff")
neff_4 = fimm.Exec("app.subnodes[{sub_n}].evlist.list[4].neff")

print str(neff_1)
print str(neff_2)
print str(neff_3)
print str(neff_4)

filename2 = filename + str(sub_n) + "_" + str(l)

fimm.Exec("app.subnodes[{sub_n}].evlist.list[1].
profile.data.writeamf({filename2}-1.amf,%10.6f)")

fimm.Exec("app.subnodes[{sub_n}].evlist.list[2].
profile.data.writeamf({filename2}-2.amf,%10.6f)")

fimm.Exec("app.subnodes[{sub_n}].evlist.list[3].
profile.data.writeamf({filename2}-3.amf,%10.6f)")

fimm.Exec("app.subnodes[{sub_n}].evlist.list[4].
profile.data.writeamf({filename2}-4.amf,%10.6f)")

del fimm
```

Appendix D

Factors Contributing to Electric Field Sensitivity

D.1 Testing Equipment

- The noise floor, and speed of the testing equipment affects the lower limit on sensitivity of these devices. AC testing is inherently more sensitive since it filters out DC noise.
  - Polarizer/Analyzer with Power Meter (DC)
    - Independent Variables: Angle of polarizer/quarter wave plate, Angle of input Polarizer with respect to fiber axes, Angle of Output Polarizer with respect to fiber axes, Electrode Configuration (does it arc)
    - Dependent Variables: max to min power levels in decibels - curve trace the rest of the field response to determine E_π
  - Polarization Analyzer (DC)
    - Independent Variables: Angle of polarizer/quarter wave plate with respect to input light, Angle of input Polarizer with respect to fiber axes, Electrode Configuration (does it arc)
    - Dependent Variables: Angle Change for a given field (E_π)
  - Polarizer/Analyzer with Power Meter (AC)
    - Independent Variables: Angle of polarizers, Electrode Configuration
    - Dependent Variables: Detectable E-field in V/m

    Ipitek's Setup (AC)

* Independent Variables: Optical Length of Sensor, Polarization Extinction
* Dependent Variables: minimum detectable field (V/m)

D.2 Electro-Optic Coefficient - r33

- The r33 value indicates the change in the anisotropic index of a polymer axis for a given electric field. It is influenced by the strength of change in the electron distribution in the chromophore molecules as well as the macro alignment of the chromophores in the direction of poling. Greater sensitivity can be obtained by using high r33 chromophores, and by aligning more of them in the same direction.
  - limitations: The chemistry of the EO polymer(APC/AJL8 limited to $\approx 50pm/V$), Our ability to align the Chromophore molecules
  - Independent variables:
    * Packaging for Corona Poling
      · Low index epoxy
      · Thickness of Low Index Epoxy
      · Uniformity of Thickness
      · Age of low index Epoxy - how does age affect conductivity
      · Is the Low index epoxy premixed well?
      · Chemical Compatibility with EO polymer
      · Glass slide
      · Thickness of Glass Slide - Leave it on during poling or not?
      · Ground electrode - copper, aluminum
    * Corona Needle Poling - this is the method that we use most often
      · Independent Variables:

· Corona Needle Radius

· Corona Voltage

· Corona Current

· Gas Environment during poling

· Height of Corona Needles

· Number of Corona Needles

* Presence of Light During Poling

* Contact - We have attempted this without success in the past

* Electron Beam - This is not a common method nor is it easy, but it could provide results if the other methods will not work.

* Temperature Profile During Poling

· Steps

· Ramps

· Temperatures

– Dependent Variables: r_{33} value, E_π

D.3 Confinement

- Confinement - How much of the light is traveling in the polymer determines how much effect a given electric field will have on the phase change.

  – Limitations: The Waveguide must be single mode, so the etch depth and polymer thickness must be balanced to maintain single mode

  – Independent Variables: Etch Depth, Polymer Thickness, Index of Polymer

  – Dependent Variables: Percent of Mode traveling in the polymer region, E_π

D.4 Length of Polymer Region

- The Phase change of these devices is distributed over the whole length of the core replaced region. A longer polymer region produces a greater phase change under a constant field.
  - Independent Variables: Etch Length,
  - Dependent Variables: E_π

D.5 Loss

- The sensors must be fairly low loss (less than 10dB including splices). The sensitivity of the device is dependent upon the SNR of the device and the higher the signal the more sensitive the device can be.
  - Independent Variables: Etch Length, Etch Depth, Polymer Thickness, Transition Regions
  - Dependent Variables: Total Transmitted Power, Insertion Loss

Appendix E

RIE In-situ Polymer Etching

E.1 The Concept

In the fabrication of a hybrid waveguide an EO polymer is deposited so that it becomes part of the guiding region of the waveguide. While several methods for depositing polymer exist, so far all methods result in a layer of polymer on the flat of the D-fiber. The optimal hybrid waveguide structure would include polymer of just the right thickness in the core of the fiber, with no residual polymer on the flat of the fiber.

In-fiber devices can often be monitored during the various fabrication steps. As an example, the fiber etching process uses in-situ monitoring to determine when to remove the fiber from the HF bath. Extending this concept to the removal of the polymer from the flat of the fiber, a method called RIE In-Situ Monitoring was developed. The fiber sample is connected to fiber feedthroughs which are bolted to the Anelva RIE. An O_2 plasma etch is done while monitoring transmitted power through the fiber. The fiber is removed from the RIE when the desired power is obtained.

Figure E.1 illustrates the hypothetical transmitted power response for an RIE In-Situ Monitored fiber sample. The power starts out very low, since the polymer thickness is much too large, and the light is no confined well to a single mode operating point. Then as the polymer thickness is decreased the transmitted power increases and level out at the optimal transmitted power level. At the optimal thickness the polymer is just the exact thickness necessary to operate in single mode, and increase the modal confinement that was lost during etching. Finally, as all of the polymer

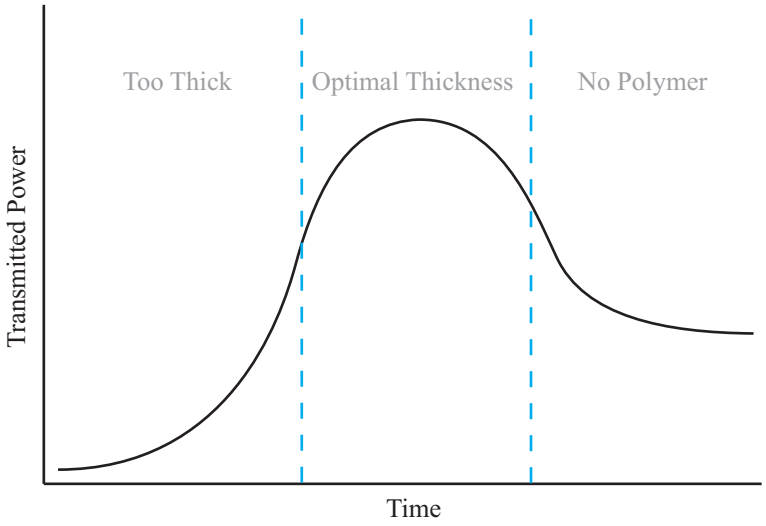

Figure E.1: Plot of the hypothetical results from RIE in-situ monitoring

is removed, the fiber returns to a power level higher than it was with thick polymer, but lower than the transmitted power at the optimal thickness.

This hypothesis was tested with a series of experiments. Information about these experiments will be included in the following sections. First, the process used for RIE In-Situ Monitoring will be detailed, then the experimental results presented, and finally future work will be outlined.

E.2 Detailed Process for RIE In-Situ Monitoring

A fiber was spin-coated with a thick layer of polymer, and the following process was followed:

1. Equipment Cart
   (a) Bring equipment cart into the cleanroom
   (b) Plug in power strip into the outlet below the PE II. Leave the PE II plugged in.
2. Preparing the RIE

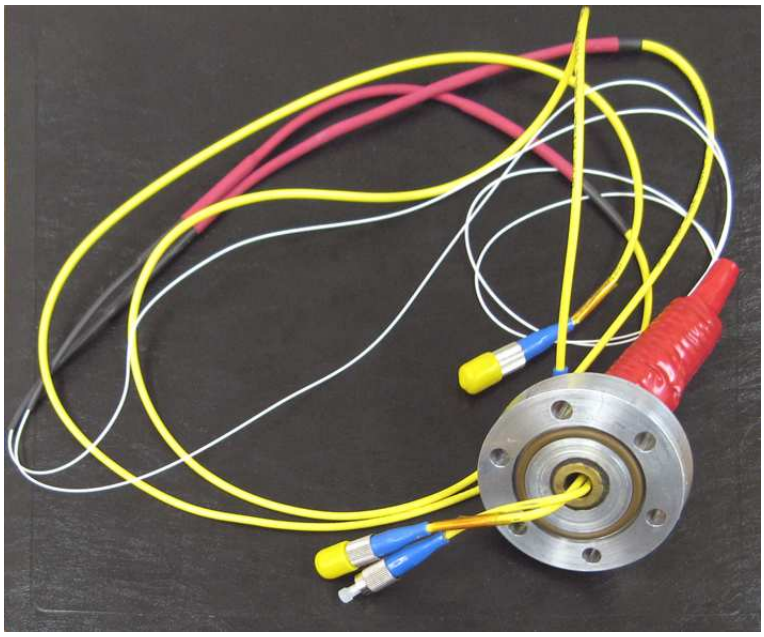

Figure E.2: Photo of fiber feedthroughs which are connceted to the Anelva RIE for in-situ RIE monitoring

(a) Initialization

i. Vent the Chamber

ii. Turn on the Pump in back

iii. Turn on the O2 in back

iv. Adjust the RF Setpoint to 250 Watts

v. Adjust Timer to 45 minutes

(b) Fiber Feedthroughs

i. Remove the O-Ring Plate from the access hole using a size 5 metric allen wrench

ii. In its place screw in the fiber feed-through plate using the same bolts. Figure E.2 is a photo of the fiber feed-through that was made for this process.

A. Tighten the bolts only snug, not overly tight. The o-ring doesn't need too much pressure to make a seal.

3. Connecting the Sample

    (a) Place the sample in the RIE

    (b) Using FC to FC connectors connect the sample to the fiber feed-throughs

    (c) Place glass slides under the bare fiber adapters, to insulate them, ensuring that reflected power stays consistent.

    (d) Place glass slides over the bare fiber adapters, to protect them from etching.

4. Power Check

    (a) Ensure that the 1550 laser is connected to the EDFA

    (b) Connect the EDFA Output to one Fiber Feed-through

    (c) Connect the other Fiber Feed-through to the Detector head

    (d) Turn on the 1550 Laser

    (e) Turn on the EDFA to 200mA

    (f) Verify that power is received (hopefully at least a few nW)

5. Pump Down

    (a) Close the RIE Lid

    (b) Slowly open the pump valve to let the pump begin to pump down the chamber.

    (c) When the needle gauge reaches 15, open the valve all the way

    (d) Open the baratron valve when the roughing gauge reaches 500 mTorr

    (e) Continue pumping until the chamber reached 20mTorr on the baratron gauge

        i. These fiber feed-through may take a little longer to pump down to 20 than normal.

ii. If it doesn't pump down quite to 20, that's ok, you may turn on the oxygen a pump a few times to purge the chamber.

(f) Flip the two O2 switches to their proper position.

i. O2 Level should be showing about 31.

(g) Close the pump until the Baratron valve reaches 80 mTorr

(h) Turn on the Chiller

6. Power Monitoring

(a) Open Labview tracking program

(b) Begin program

(c) Save file

i. Power will start to be registered on the graph

7. Etching the Fiber

(a) Start the Timer

(b) Press the RF On button

(c) Adjust pressure to 100 mTorr

(d) Adjust reflected power to 1

(e) Repeat c and d until done with etch

8. Power vs. Time

(a) The power through put vs. time should be registered on the graph in labview

(b) The scale may need to be changed periodically to get the best idea of what is happening.

(c) There is no real need to watch the power during the etch because the data will be saved, but it's informative.

9. Terminating the Etch

   (a) Press the RF off button when finished etching.

   (b) Press Reset on the timer.

   (c) Turn off the gases.

   (d) Open the pump valve, pumping the chamber down to 20 mTorr

   (e) Close the Baratron Valve

   (f) Close the pump valve

   (g) Vent the Chamber

10. Putting things back together/ Removing the sample

   (a) Turn off the Labview program

   (b) Turn off the Computer.

   (c) Turn off the Laser

   (d) Turn off the EDFA

   (e) Turn off the Detector

   (f) Disconnect the fiber feed-throughs from the sample

   (g) Cap the fiber feedthrough inputs with protectors.

   (h) Remove glass slides from chamber

   (i) Place connector and bare fiber adapter on RIE, allowing it to cool

   (j) Un-bolt the fiber feed-throughs

   (k) Disconnect fiber feed-throughs from the EDFA and from the detector

(l) Cap the fiber feedthrough outputs with protectors.

(m) Bolt the O-Ring Plate back onto the RIE

(n) Remove FC-FC connectors from bare fiber adapters

(o) Cap the bare fiber adapters with protectors.

(p) Remove sample from chamber

(q) Turn off Chiller

(r) Close Lid

(s) Pump down chamber to 500 mTorr on Roughing gauge

(t) Open baratron valve

(u) Pump down to 20 mTorr

(v) Close baratoron valve

(w) Close pump valve

(x) Turn off RIE

(y) Sign Log

(z) Turn off O2 and pump in back

11. Equipment cart Cleanup

(a) Unplug Power strip

(b) Take cart out into the yellow room.

(c) Degown in Gowning room

(d) Roll Cart back to optics lab

E.3 Experimental Results

Many fiber samples were etched using the RIE In-situ Monitoring setup. Figure E.3 shows the transmitted power of one such fiber during the etching process.

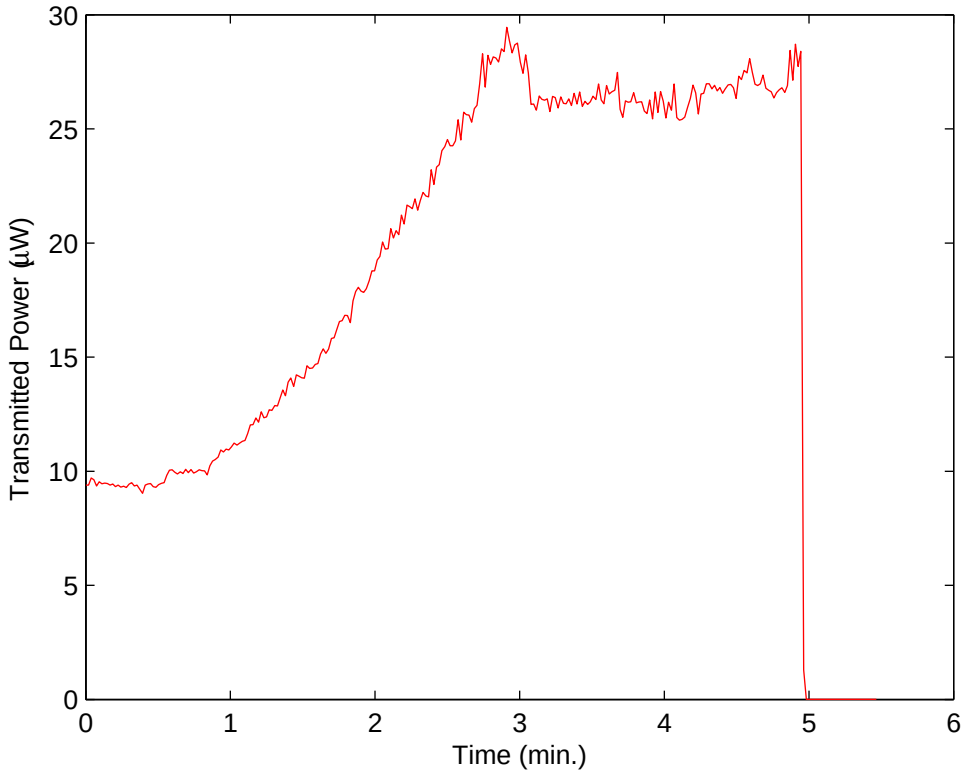

Figure E.3: Plot of transmitted power during RIE in-situ etching

The fiber was connected to the laser source and power monitor and etched with an O_2 plasma. The power was turned off when the transmitted power had reached a maximum of about 29 μW. The transmitted power increased by about 5 dB from the initial level after etching. The laser was turned off at 5 minutes, and the sample was removed from the chamber.

Figure E.4 shows an SEM cross-sectional image of this fiber after etching. The polymer isn't as thick as expected, but it does show that the flat of the fiber is fairly clear of any polymer.

E.4 Tilted RIE Etching

Besides the in-situ RIE etching method of removing polymer from the flat of a D-fiber, another method was attempted. This method was to tilt a vertical core

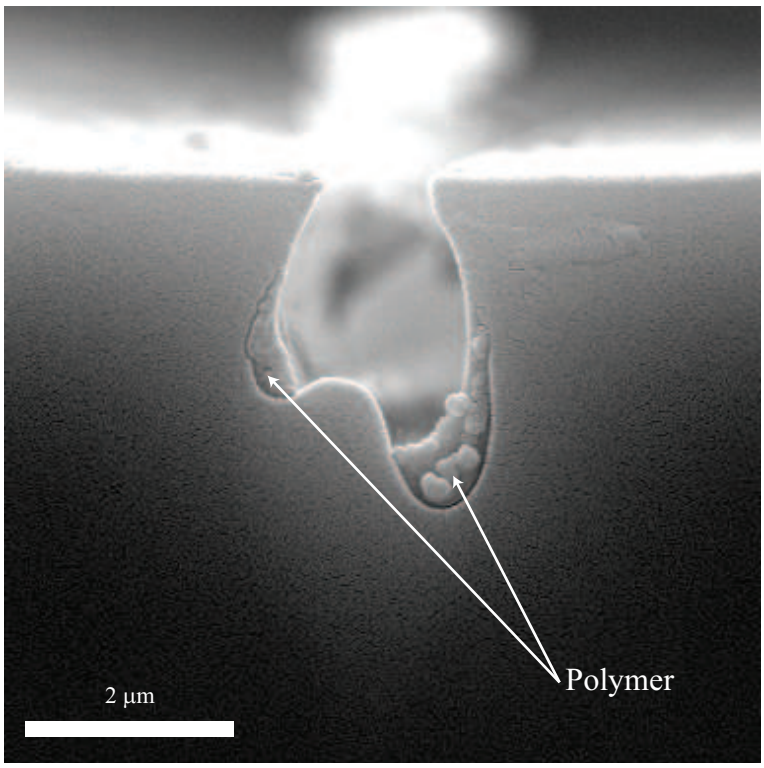

Figure E.4: SEM image of an RIE in-situ etched fiber

D-fiber to about 70 degrees and mount it on a silicon wafer. Then a highly anisotropic etch recipe in the ICP-RIE was used to remove the polymer from the flat, while the deeply etched core topography masks the polymer in the core. Figure E.5 illustrates this method showing how the tilt and the anisotropic etch result in a shadowing of the core. Figure E.6 is a cross-sectional SEM image of a fiber that was etched using the tilted-RIE etching method. The fiber flat is completely clean of polymer, and the polymer is very thick in the core of the fiber.

E.5 Future Work

While preliminary results were promising, several challenges prevented this experiment from producing consistent results. Eventually, research efforts moved toward other methods of creating low loss hybrid waveguides. If there is a future need to re-initiate this experimental effort, a few points should be noted.

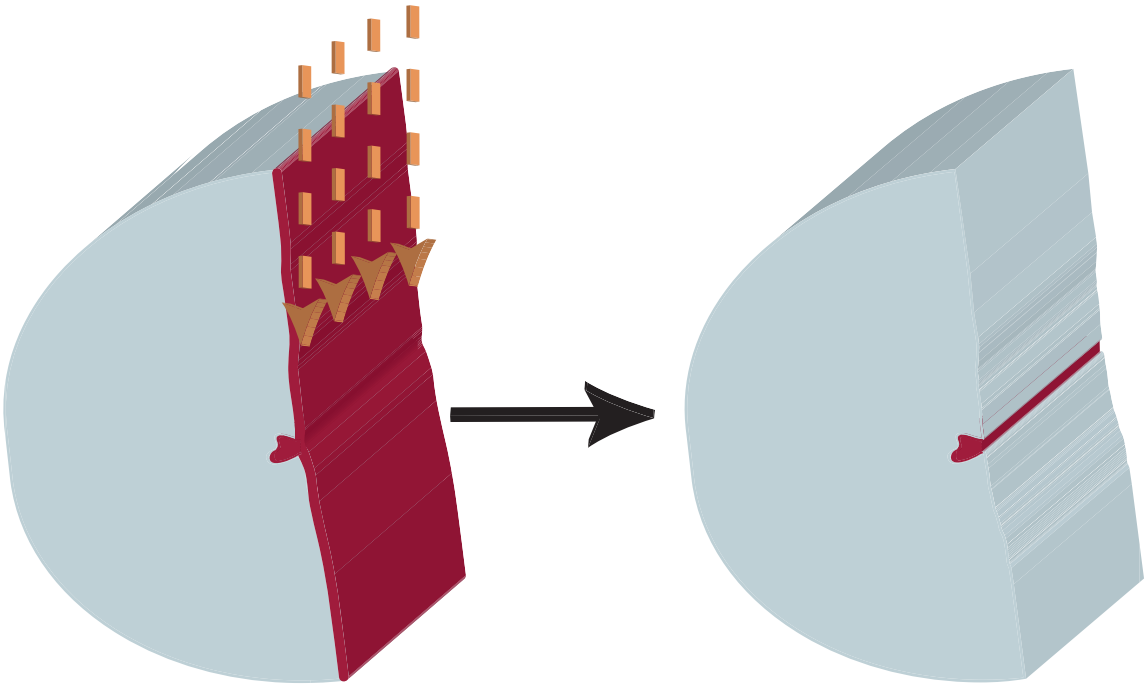

Figure E.5: The polymer on the flat of the D-fiber is removed using an ICP-RIE while leaving the polymer in the core.

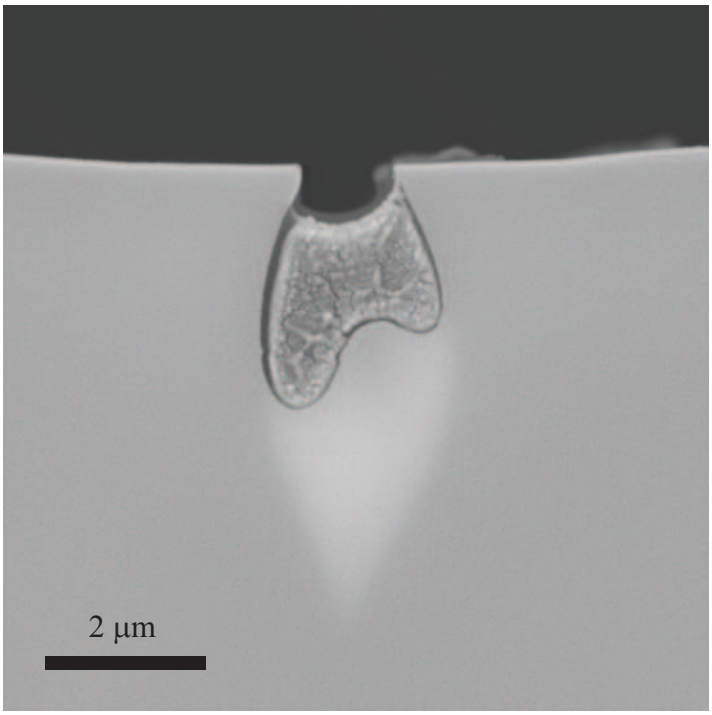

Figure E.6: SEM image of a fiber with polymer on the flat of the D-fiber removed using an ICP-RIE

First, at the time of this experiment, the method of depositing polymer on the fiber resulted in inconsistent polymer thicknesses along the length of the fiber. That inconsistency made it difficult to uniformly etch the polymer of the flat, since it was thicker on the flat in some places and thinner in other. Currently, polymer thickness uniformity is well established through both polymer printing, and spin casting a fiber which has been hot-glued to the substrate.

Second, the fiber feed-throughs were made from SMF28 fiber. Since D-fiber is PM the transmitted power often oscillated irregularly during etching, depending on the polarization launching angle into the D-fiber. If further work much be done, PM fibers should be used for the fiber feed-throughs.

Third, D-fiber connection to other types of fiber was not consistent at the time of this experiment. Fusion splicing, connectorizing or using bare fiber adapters all resulted in significant losses. It is now straightforward to use PANDA to E-fiber to D-fiber splicing for low loss connections.